

## Chapter 10

# IONOSPHERIC RADIO WAVE PROPAGATION

Section 10.1	S. Basu, J. Buchau, F.J. Rich and E.J. Weber
Section 10.2	E.C. Field, J.L. Heckscher, P.A. Kossey, and E.A. Lewis
Section 10.3	B.S. Dandekar
Section 10.4	L.F. McNamara
Section 10.5	E.W. Cliver
Section 10.6	G.H. Millman
Section 10.7	J. Aarons and S. Basu
Section 10.8	J.A. Klobuchar
Section 10.9	J.A. Klobuchar
Section 10.10	S. Basu, M.F. Mendillo

The series of reviews presented is an attempt to introduce ionospheric radio wave propagation of interest to system users. Although the attempt is made to summarize the field, the individuals writing each section have oriented the work in the direction judged to be most important.

We cover areas such as HF and VLF propagation where the ionosphere is essentially a “black box”, that is, a vital part of the system. We also cover areas where the ionosphere is essentially a nuisance, such as the scintillations of trans-ionospheric radio signals.

Finally, we have included a summary of the main features of the models being used at the time of writing these reviews. [J. Aarons]

## 10.1 MEASURING TECHNIQUES

### 10.1.1 Ionosonde

For more than four decades, sounding the ionosphere with ionospheric sounders or ionosondes has been the most important technique developed for the investigation of the global structure of the ionosphere, its diurnal, seasonal and solar cycle changes, and its response to solar disturbances. Even the advent of the extremely powerful incoherent scatter radar technique [Evans, 1975], which permits measurement of the complete electron density profile, electron and ion temperatures, and ionospheric motions, has not made the relatively inexpensive and versatile ionosonde obsolete. On the contrary, modern techniques of complex ionospheric parameter measurements and data processing [Bibl and Reinisch, 1978a; Wright and Pitteway, 1979; Buchau et al., 1978] have led to a resurgence of interest in ionospheric sounding as a basic research tool, while a renewed interest

in HF communications is leading to a rejuvenation of the global ionosonde network.

**10.1.1.1 Ionogram.** Ionospheric sounders or ionosondes are, in principle, HF radars that record the time of flight or travel of a transmitted HF signal as a measure of its ionospheric reflection height. By sweeping in frequency, typically from 0.5 to 20 MHz, an ionosonde obtains a measurement of the ionospheric reflection height as a function of frequency. A recording of this reflection height measurement as a function of frequency is called an ionogram. Ionograms can be used to determine the electron density distribution as a function of height,  $N_e(h)$ , from a height that is approximately the bottom of the E layer to generally the peak of the F2 layer, except under spread F conditions or under conditions when the underlying ionization prevents measurement of the F2 layer peak density. More directly, ionosondes can be used to determine propagation conditions on HF communications links.

Two typical ionograms produced by a standard analog ionospheric sounder using film recording techniques are shown in Figure 10-1. The frequency range is 0.25 to 20 MHz (horizontal axis), and the displayed height range is 600 km, with 100 km height markers. The bottom ionogram is typical for daytime, showing the signatures of reflections from the E, F1 and F2 layers. The cusps, seen at various frequencies (where the trace tends to become vertical) indicate the so-called critical frequencies, foE, foF1, and foF2. The critical frequencies are those frequencies at which the ionospheric sounder signals penetrate the respective layers. These frequencies are a measure of the maximum electron densities of the respective layers. Since the densities vary with time, ionospheric sounding is used to obtain information on changes in the critical frequency and other parameters of the electron density vs height profile.

## CHAPTER 10

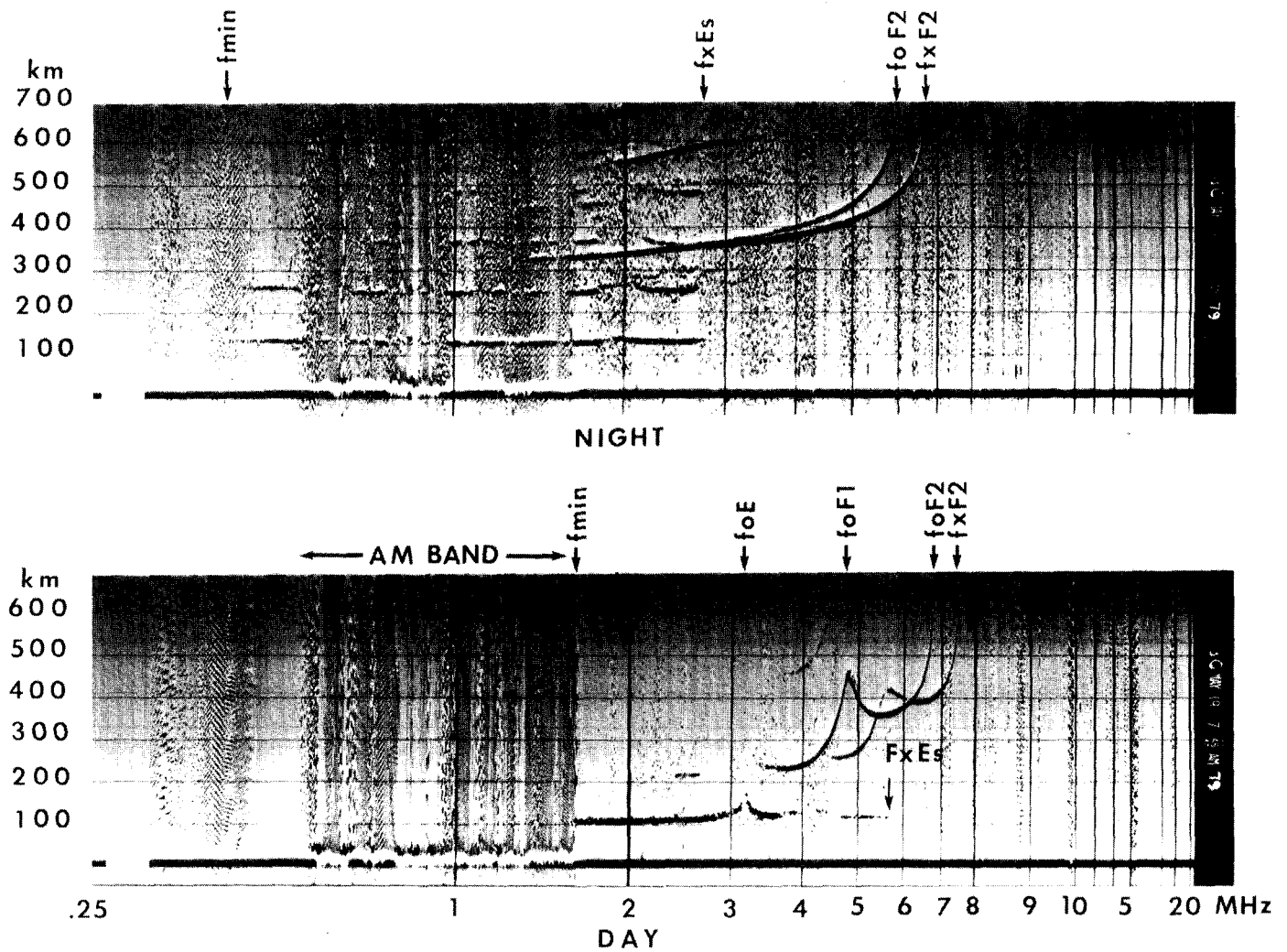


Figure 10-1. Typical midlatitude day and nighttime ionograms, recorded by a C-4 ionosonde at Boulder, Colorado. The daytime ionogram shows reflections from E, Es, F1 and F2 layers; the nighttime ionogram those from Es and F2 layers.

The ionogram (Figure 10-1) shows signatures of various phenomena that complicate the process of ionospheric sounding or the ionogram analysis. Superimposed on the primary F layer echo trace is a similar but not identical trace, shifted up in frequency: the so-called extraordinary or X component. The primary trace is called the ordinary or O component. The echo trace is split into two traces due to effects of the earth's magnetic field. A second trace similar to the primary trace is seen at twice the range, a multiple reflection. Only a small fraction of the wave energy is received by the antenna after it has returned from the ionosphere. Most of the returned energy is reflected back from the ground and provides the first multiple (second order echo) at twice the range. If the ionosphere is a good reflector, and losses in the D region are low, additional reflections can be observed. Figure 10-1 (Night) shows a second multiple (third order echo) for part of the Es trace. It is easy to see that slopes increase by a factor that corresponds to the order of the echo.

### 10-2

Finally, we see vertical bands in the frequency range from 0.5 to 1.7 MHz, the signature of radio frequency interference (RFI) in an ionogram, here from the AM band. RFI can become severe enough to prevent the recording of ionospheric echoes; for example, interference masks part or all of the E layer trace below 1.7 MHz.

The top of Figure 10-1 shows a typical nighttime ionogram. The E and F1 traces have disappeared because these layers dissipate after sunset. (Residual nighttime E region ionization of low density can be observed in the absence of low sporadic E layers at stations with low RFI and large antennas.) Echoes from a sporadic E layer (Es) and F2 layer echoes and their multiples are clearly visible in Figure 10-1. At times a brushlike spreading of the F2 layer cusps is observed. It is called spread F and is caused by small scale irregularities embedded in the ionosphere and ripples in the equidensity contours on the order of hundreds of meters to kilometers. For a detailed discussion of spread F see Davies [1966] and Rawer and Suchy [1967]; for a dis-

## IONOSPHERIC RADIO WAVE PROPAGATION

cussion of the occurrence and global distribution see Herman [1966]. The nighttime ionogram also shows increased RFI bands at higher frequencies. Because the D layer disappears at night, HF propagation over large distances is possible. This long distance propagation is heavily used for broadcasting by commercial users and for shortwave radio communications by government services and radio amateurs. Fortunately the ionosonde's own echoes also increase in amplitude due to the disappearance of the D layer, reducing to some extent the effect of increased propagated noise on the systems overall signal-to-noise ratio.

**10.1.1.2 Principles of Ionospheric Sounding.** The concept of ionospheric sounding was born as early as 1924, when Breit and Tuve [1926] proved the existence of an ionized layer with the reception of ionospheric echoes of HF pulses transmitted at 4.3 MHz from a remote transmitter (distance 13.8 km). This, during the next decade, led to the development of monostatic ionospheric sounders by the National Bureau of Standards and the Carnegie Institution. Even today the principles used by Breit and Tuves constitute the principles on which most ionospheric sounders are based. These are the transmission of HF pulses and the measurement of their time of flight to the reflection level. For a short historical review of the development of ionospheric sounders see Villard [1976].

Ionospheric sounding takes advantage of the refractive properties of the ionosphere. A radio wave propagating into the ionospheric plasma encounters a medium with the refractive index (in the absence of the earth's magnetic field  $B$ , and ignoring collisions between electrons and the neutral atmosphere)

$$\mu^2 = 1 - X = 1 - \left(\frac{f_N}{f}\right)^2 \quad (10.1)$$

where

$$X = \frac{N_e e^2}{4 \pi^2 \epsilon_0 m f^2}, \quad (10.2)$$

$e$ ,  $\epsilon_0$  and  $m$  are natural constants,  $N_e$  is the electron density, and  $f$  is the wave frequency. Below the ionosphere,  $N_e = 0$ , and  $\mu = 1$ . Within the ionosphere,  $N_e > 0$ , and  $\mu < 1$ . At a level where  $X = 1$ ,

$$f_N^2 = \frac{N_e e^2}{4 \pi^2 \epsilon_0 m} = f^2 \quad (10.3)$$

the refractive index  $\mu$  becomes zero. The wave cannot propagate any farther and is reflected. The quantity  $f_N$ , which relates the electron density to the frequency being reflected, is called the plasma frequency. Inserting the natural constants into Equation (10.3) permits us to deduce the useful relation between electron density and plasma frequency (which is identical to the probing frequency being reflected)

$$f_N = 0.009 \sqrt{N_e} \quad (10.4)$$

$$N_e = 1.24 \times 10^4 f_N^2 \quad (10.5)$$

where  $f_N$  is in MHz and  $N_e$  in electrons/cm<sup>3</sup>. The plasma frequency is the natural frequency of oscillation for a slab of neutral plasma with the density  $N_e$  after the electrons have been displaced from the ions and are allowed to move freely. For further discussions of the relation of  $\mu$  to the wave propagation see Davies [1966].

Peak densities of the ionospheric layers vary between  $10^4$  and  $> 10^6$  el/cm<sup>3</sup>. Inserting these numbers into Equation (10.4) gives a plasma frequency range from 1 to  $> 9$  MHz; this is the reason for the frequency range ( $0.5 \text{ MHz} \leq f \leq 20 \text{ MHz}$ ) covered by a typical ionosonde. The low densities of the D layer can only be probed with low frequencies  $< 250 \text{ Hz}$ , requiring large antennas and complex processing/analysis techniques and are not directly measurable by the standard ionosondes (for details see Kelso [1964] and references therein). Indirectly the D region ionization is measured by the integral absorption effects that it imposes on the HF waves propagating through it to the E or F region reflection levels (see discussion of  $f_{min}$ ).

The inclusion of the magnetic field in the formula for the refractive index leads to the well known Appleton dispersion formula (dispersion means that the refractive index depends on the propagating frequency) for a magnetized plasma, here given for the case of no collisions, generally valid for frequencies  $> 2 \text{ MHz}$ , in the E and F regions.

$$\mu^2 = \frac{2X(1 - X)}{2(1 - X) - Y_T^2 \pm \sqrt{Y_T^4 + 4(1 - X)^2 Y_L^2}} \quad (10.6)$$

with

$$Y_{L,T} = \frac{e B_{L,T}}{2\pi m f} \quad (10.7)$$

and

$$\frac{e B}{2\pi m} = f_H \quad (10.8)$$

where  $f_H$  is the gyrofrequency, the natural frequency at which free electrons circle around the magnetic field lines.  $B_{L,T}$  are the components of the magnetic field in the direction of (longitudinal) or perpendicular to (transverse) the wave normal. Inserting the constants into Equation (10.8) leads to the useful relation for the gyrofrequency

$$f_H = 2.8 \times 10^4 B, \quad (10.9)$$

where  $f_H$  is in MHz and  $B$  in gauss ( $1 \text{ gauss} = 10^{-4} \text{ tesla}$ ).

The refractive index given in Equation (10.6) shows, by the  $\pm$  solution to the square root, that in a magnetized

## CHAPTER 10

plasma two and only two “characteristic” waves can propagate. These two characteristic waves are called the ordinary or o-component and the extraordinary or x-component seen in the ionogram shown in Figure 10-1. A radio wave with arbitrary (often linear) polarization will split in the ionospheric medium into two characteristic or o-and x-components, which in general propagate independently.

The reflection condition  $\mu = 0$  gives two solutions for  $X$ ; for the + sign (o-component)

$$X = 1 \quad (10.10)$$

as in the no-field case, Equation (10.3); for the - sign (x-component)

$$X = 1 - Y. \quad (10.11)$$

At the reflection level for the O-component the plasma frequency equals the probing frequency,  $f_N = f$ . The x-component is reflected at a lower level that depends on the local magnetic field strength. It can be shown that the critical frequencies  $f_o$  and  $f_x$ , for  $f_o \gg f_H$ , are related by

$$f_x - f_o \approx \frac{f_H}{2}, \quad (10.12)$$

that is, the magneto-ionic splitting (due to the presence of the magnetic field in the ionospheric plasma) depends on the local magnetic field strength and therefore varies, from station to station. For a typical midlatitude station,  $B = 0.5G$  and from Equation (10.9) we determine  $f_H = 1.4$  MHz, leading to the  $f_o$ - $f_x$  separation of  $\sim 0.7$  MHz seen in Figure 10-1. A solution  $X = 1 + Y$  exists for frequencies below the gyrofrequency  $f_H$ . For details see Davies [1966].

Using ionograms to determine the true height electron density profile  $N_e(h)$  is further complicated by the slowing-down effect that the ionization below the reflection level has on the group velocity of the pulse. While the phase velocity  $v$  of the wave is

$$v = \frac{c_o}{\mu(h,f)} \quad (10.13)$$

it can be shown that the group velocity  $u$ , defined as the propagation velocity of the pulse envelope, is given for the no-magnetic field case by

$$u = \frac{c_o}{\mu'(h,f)} = \mu(h,f)c_o, \quad (10.14)$$

where  $\mu'(h,f)$  is the group refractive index. Therefore, while the phase velocity increases above the speed of light in a plasma, the group velocity, the velocity at which the energy propagates, slows down ( $\mu < 1$  in a plasma). For a more

detailed discussion see Davies [1966] and Chapter 10 of Budden [1961].

As a result, the actual reflection height  $h$  is smaller than the so-called virtual height  $h'$ , which is derived, assuming propagation in the medium with the speed of light from

$$h' = \frac{c_o t}{2} \quad (10.15)$$

with  $t$  the round trip travel time of the pulse. Or since

$$u < c_o, \quad (10.16)$$

then

$$h' > h. \quad (10.17)$$

As stated before, one of the main objectives of ionospheric sounding is the determination of  $h(f)$ , which through the relation between  $f$  and  $N_e$ , Equations (10.3) and (10.4) represents the desired function  $N_e(h)$ . Since the group travel time is

$$t = \frac{2}{c_o} \int_0^h \frac{dz}{\mu} = \frac{2}{c_o} \int_0^h \mu' dz, \quad (10.18)$$

the virtual height is related to the group refractive index by

$$h'(f) = \int_0^{h(f)} \mu' [f_N(z), f] dz. \quad (10.19)$$

If the electron density  $N_e(h)$  is considered as a function of the height  $h$  above the ground,  $\mu'$  is also a function of  $h$  and the problem is now to solve the integral equation (10.19), for given values of  $h'(f)$  obtained from the ionogram. The techniques used to solve this equation are known as true height analysis for which in general numerical methods are used; they are discussed in detail in a 1967 special issue of *Radio Science*.

**10.1.1.3 Analog Ionosonde.** The general principle of an ionospheric pulse sounder is shown in Figure 10-2 [Rawer and Suchy, 1967]. A superheterodyne technique is used to both generate the transmitted pulse of frequency  $f_T$  and to mix the received signals back to an intermediate frequency or IF for further amplification. Tuning the receiver mixer stage so that its output frequency is equal to the frequency of the fixed frequency (pulsed) oscillator  $f_c$ , and using a common variable local oscillator  $f_o$ , ensures that the receiver and transmitter are automatically tuned for every value of

## IONOSPHERIC RADIO WAVE PROPAGATION

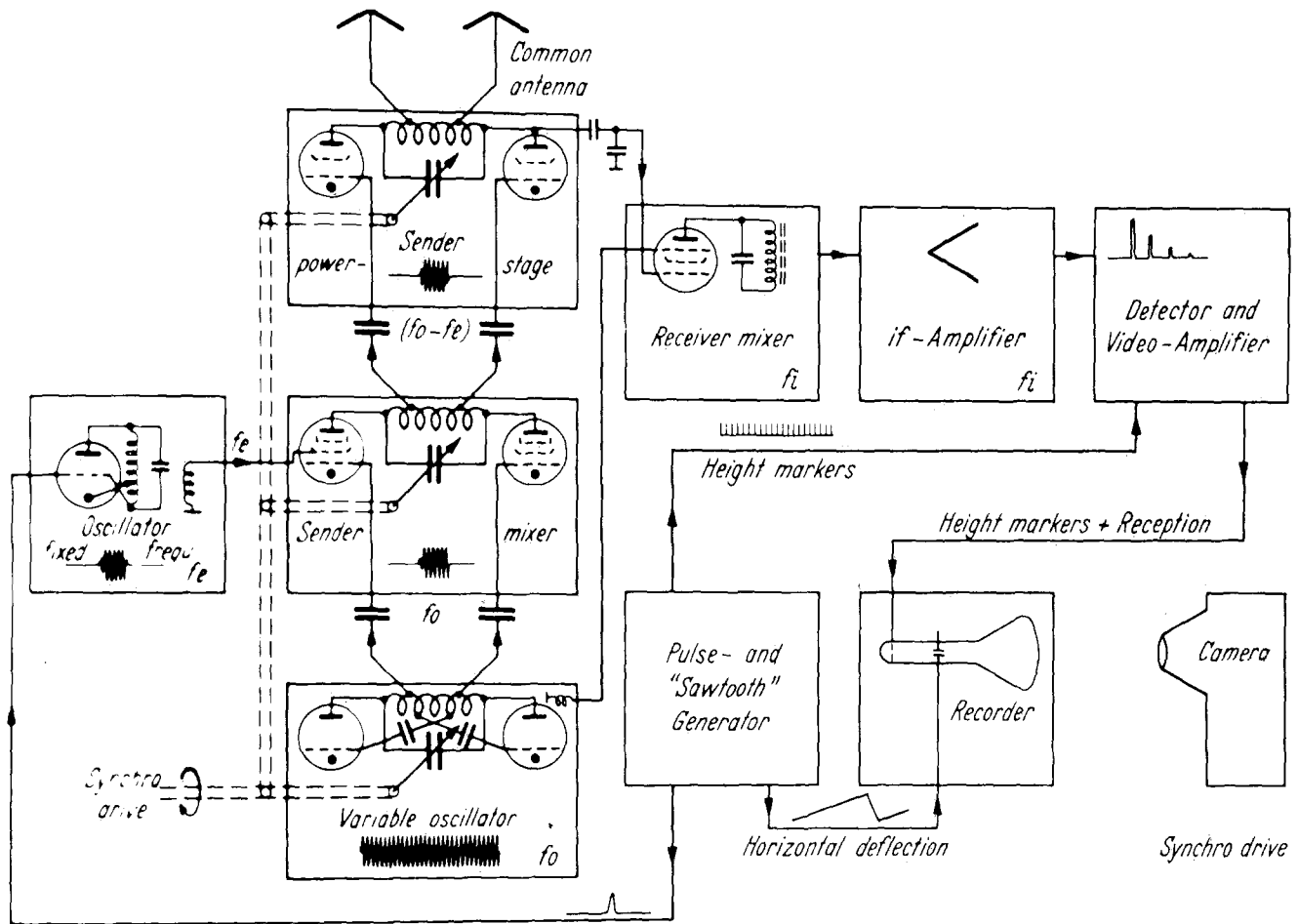


Figure 10-2. Schematic presentation of the major components of an Ionospheric Pulse Sounder.

the oscillator frequency  $f_o$ . The transmit pulse is amplified in one or several power stages and transmitted, using a suitable wide-band antenna with a vertical radiation pattern. The same antenna can be used for reception using either a tap (voltage divider) of the transmitter tank circuit or a Transmit/Receive or T/R switch, which protects the receiver input from overloading during transmission of the pulse, especially problematic for transistorized receivers. More recently separate antennas for transmission and reception have become commonplace. This permits the use of smaller and therefore less costly receiver antennas in phased arrays for angle-of-arrival measurements and as polarized antennas for polarization or mode identification [Bibl and Reinisch, 1978a,b; Wright and Pitteway, 1979].

The received signals are mixed down (or up) to the intermediate frequency and amplified in an IF amplifier, that is matched in bandwidth to the pulse width (overall bandwidth  $B = 1/P$ , with  $P$  the width of the transmitted pulse). After detection and amplification, the video signal modulates the intensity of the CRT's electron beam (Z-axis modulation). Deflecting the beam in the Y-axis with a sawtooth voltage

in synchronism with the transmission and pulling a film slowly in the direction of the X-axis in the focal plane of an imaging optic results in an ionogram recording such as that shown in Figure 10-1. Since sounders based on the general concepts shown in Figure 10-2 rely completely on analog techniques for signal generation, reception, and processing, they have more recently become known as analog sounders, in contrast to the digital sounders developed in several places during the last decade. Analog sounders are still operated at many ionospheric observatories, especially the well-known C3 and C4 ionosondes, which were developed by NBS and which were distributed worldwide as the primary ionosonde for the International Geophysical Year 1957/58.

**10.1.1.4 Analog/Digital Hybrid Ionosonde.** While vertical sounding with the transmitter and receiver and their respective antennas collocated made synchronization of transmitter and receiver relatively easy, a much more de-

## CHAPTER 10

manding task arose when investigators attempted to sound the ionosphere over paths of varying distances to determine the mode structure and the propagation conditions directly.

If the transmitted signal is to be received within the receiver bandwidth, the systems must be started at a precise time, and must have perfectly aligned frequency scans. This was achieved using linear frequency scans and synchronous motor drives, which derived their A/C voltage from crystal oscillators [Bibl, 1963]. A large step forward was the development of frequency stepping sounders such as the Granger Path Sounder [Gowell and Whidden, 1968] which combined digital and analog techniques. Digital techniques generated ionograms by stepping synthesizer/transmitter and receiver through the desired frequency range, providing selectable frequency spacing (for example, 25, 50, or 100 kHz, linear or linear over octave bands). The frequency synthesis itself and the data processing/recording however, used the standard analog techniques. All digital and hybrid pulse sounders currently available use these frequency stepping techniques.

**10.1.1.5 Digital Ionosonde.** The rapid development of integrated circuits, microprocessors and especially Read-Only-Memories, and of inexpensive storage of large capacity, has led to the development of digital ionospheric sounders. These systems have some analog components, but use digital techniques for frequency synthesis, receiver tuning, signal processing, recording, and displaying of the ionograms. However, to the modern sounder, the digital control of all sounder functions, the ability to digitally control the antenna configuration, and above all, the immense power of digital real time processing of the data prior to recording on magnetic tape or printing with digital printers are of special importance.

A digital amplitude ionogram, recorded by a Digisonde 128 PS at the AFGL Goose Bay Ionospheric Observatory is shown in Figure 10-3. This system developed at the University of Lowell [Bibl and Reinisch, 1978a,b] uses phase coding, spectral integration, polarized receive antennas for o/x component identification, and fixed angle beam steering of the receive antenna array for coarse angle of arrival measurements to provide a rather complete description of the properties and origin of the reflected echoes. Using a standard set of 128 range bins for each frequency, the sounder integrates the sampled receiver output signals for a selectable number of integrations, improving the signal-to-noise ratio and providing the samples for spectral analysis. Since for each frequency-range-bin or FRB only one return is recorded, a search algorithm determines from the set of separate signals (o, x, several antenna directions, Doppler lines) the signal with the largest amplitude and retains amplitude and STATUS, that is, special signal characteristics. Using a special font [Patenaude et al., 1973], the resulting digital amplitudes are printed out providing the analog presentation essential for the recognition of the detailed struc-

ture of an ionogram trace simultaneously with the digital information. Preprocessing has largely eliminated the noise background. The bottom part of Figure 10-3 shows a digital amplitude ionogram, represented by all amplitudes above a noise level determined automatically and separately for each frequency. The noise level on each frequency can be estimated, since the unmodified signals of the lowest four height bins are shown at the bottom of the ionogram. The displayed range starts at 60 km and in 128 height increments with a  $\Delta = 5$  km covers the range to 695 km. Each frequency step is in 100 kHz, which covers the range from (nominally) 0 to 13 MHz in 130 frequency steps. Ionograms of this type can be produced in between 30 s and 2 min, depending on the complexity of signal characterization selected. The number of integrations required to achieve an acceptable signal-to-noise ratio, and the desired spectral resolution of the Doppler measurements also affect the duration of the ionogram sweep. The ionogram is similar in structure to the daytime ionogram in Figure 10-1, showing clearly an E-trace ( $f_oE = 3.25$  MHz), an F1-cusp ( $f_oF1 = 5.0$  MHz), and the F2 trace ( $f_oF2 = 8.2$  MHz). The top part of the figure was produced by printing only those amplitudes which had a STATUS indicating o-polarization, vertical signals only. The resulting suppression of the x-component and of the (obliquely received) noise shows the effectiveness of these techniques.

The digital "HF Radar System" developed at NOAA, Boulder, Colorado [Grubb, 1979] is an ionospheric sounder, built around a minicomputer. Appropriate software allows freedom in generating the transmit signal phase coding and sequence, and in processing procedures. However, instruction execution times of the minicomputer limit this flexibility. The sounder with its present software uses an echo detection scheme rather than a fixed FRB grid to obtain the information on the ionospheric returns. This scheme requires that the return has to be identified beforehand, generally using a selectable level above the noise, and an "a hits out of b samples" criterion. This system, by the use of a receive antenna array, then determines on-line for this initially identified return, the echo amplitude, its polarization, Doppler shift, and reflector location [Wright and Pitte-way, 1979].

The spectral information available in digital ionograms has been used to track moving irregularities in the equatorial [Weber et al., 1982] and polar ionosphere [Buchau et al., 1983]. An example of a Doppler ionogram recorded in the polar cap is shown in Figure 10-4. The right lower panel shows a heavily spread amplitude ionogram and superimposed two oblique backscatter traces. The right upper panel shows the Status or Doppler ionogram: each FRB displays the Doppler bin number instead of an amplitude. FRB's with an amplitude below an automatically determined noise level show neither amplitude nor status. Separating the ionogram into positive and negative Doppler ionograms permits the identification and subsequent tracking of approaching

# IONOSPHERIC RADIO WAVE PROPAGATION

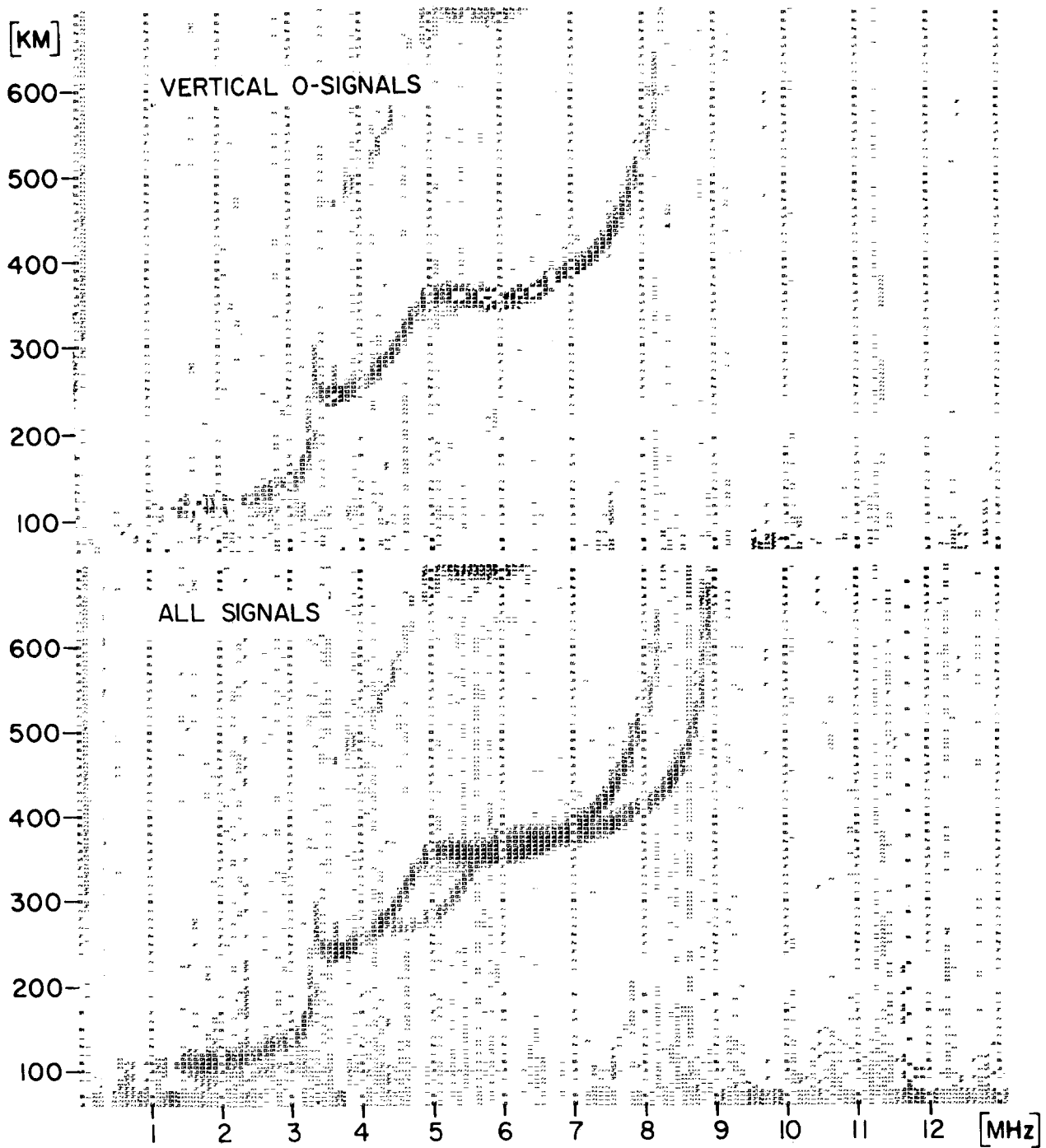


Figure 10-3. Digital daytime amplitude ionogram recorded by a Digisonde 128PS at the AFGL Goose Bay Ionospheric Observatory 16 June 1980 1720 AST. Coarse angle of arrival and polarization information is used to separate the vertical ordinary trace shown in the upper part of the figure.

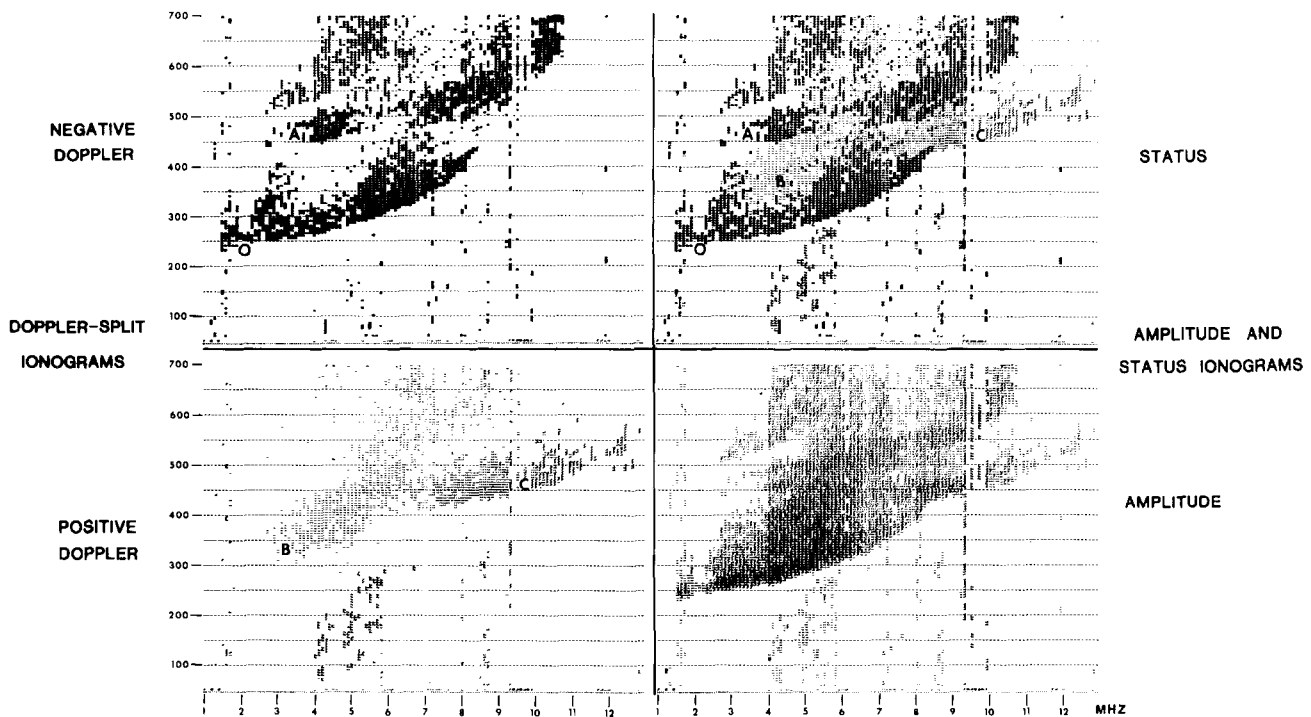


Figure 10-4. Amplitude/status ionogram taken by the AFGL airborne ionospheric observatory with a Digisonde 128PS at Thule, Greenland 9 December 2231 (UT). The lower right panel shows the amplitude ionogram after removal of radio noise. The Doppler ionogram shown in the upper right panel is produced by replacing each amplitude in the ionogram below with a number representing the measured Doppler shift. The separation into positive and negative Doppler traces (approaching and receding reflection regions) is shown in the two panels on the left.

(traces marked B and C) and receding (trace marked A) reflecting or scattering centers. The overhead trace (very low Doppler) is marked 0.

**10.1.1.6 Digital Data Processing.** The availability of ionograms in digital form has finally provided the basis for successful automatic processing of these complex data. Real time monitoring [Buchau et al., 1978], survey of large data bases [Reinisch et al., 1982a], real time analysis of ionospheric parameters [Reinisch et al., 1982b], automatic trace identification and true height analysis [Reinisch and Xuequin, 1982, 1983] have been made possible by the availability of data in digital form. Analysis concepts for angle-of-arrival determination and other parameters for the NOAA/SEL digital sounder have been presented by Wright and Pitteway [1982] and by Paul [1982].

An example of a data survey presentation using digital ionosonde data from Goose Bay is shown in Figure 10-5. The top row shows the integrated height characteristic, obtained by collapsing each ionogram onto its height axis. This characteristic provides the history of E and F layer (minimum) height variations over the course of three days. The middle panel shows the temporal changes of the F layer returns, with the lower envelope determined by foE (day-time) or fmin (nighttime), while the upper envelope is determined generally by foF2. The bottom panel representing

the frequency extent of E and Es traces shows the typical  $\cos X$  ( $X =$  solar zenith angle) pattern of the solar E-layer, maximizing at noon. Sporadic E events observed on all three nights are typically observed at these high latitudes during auroral storms [Buchau et al., 1978].

**10.1.1.7 FM/CW or Chirp Sounder.** The availability of very linear sweep-frequency synthesizers resulted in the development of FM/CW (frequency modulated continuous wave) or Chirp Sounders, initially for oblique incidence and in the 1970s also for monostatic vertical incidence sounding [Barry, 1971]. A linear waveform with the constant sweep rate  $df/dt$  is transmitted. Receiving the waveform after propagation to the ionosphere and back and measuring the time delay of each frequency component against the original waveform permits the determination of the travel time as a function of frequency. This is actually done by mixing the received waveform with the original, resulting in a difference frequency which can be measured by spectrum analysis. The difference frequency as a function of frequency (the "Chirp") is proportional to the travel time of the signal as a function of frequency; therefore, a graph of the difference frequency as a function of time or transmitted frequency, through the known sweep rate  $df/dt$ , forms an ionogram. While initially transmitter and receiver were separated by a substantial distance, to avoid overloading of the re-

# IONOSPHERIC RADIO WAVE PROPAGATION

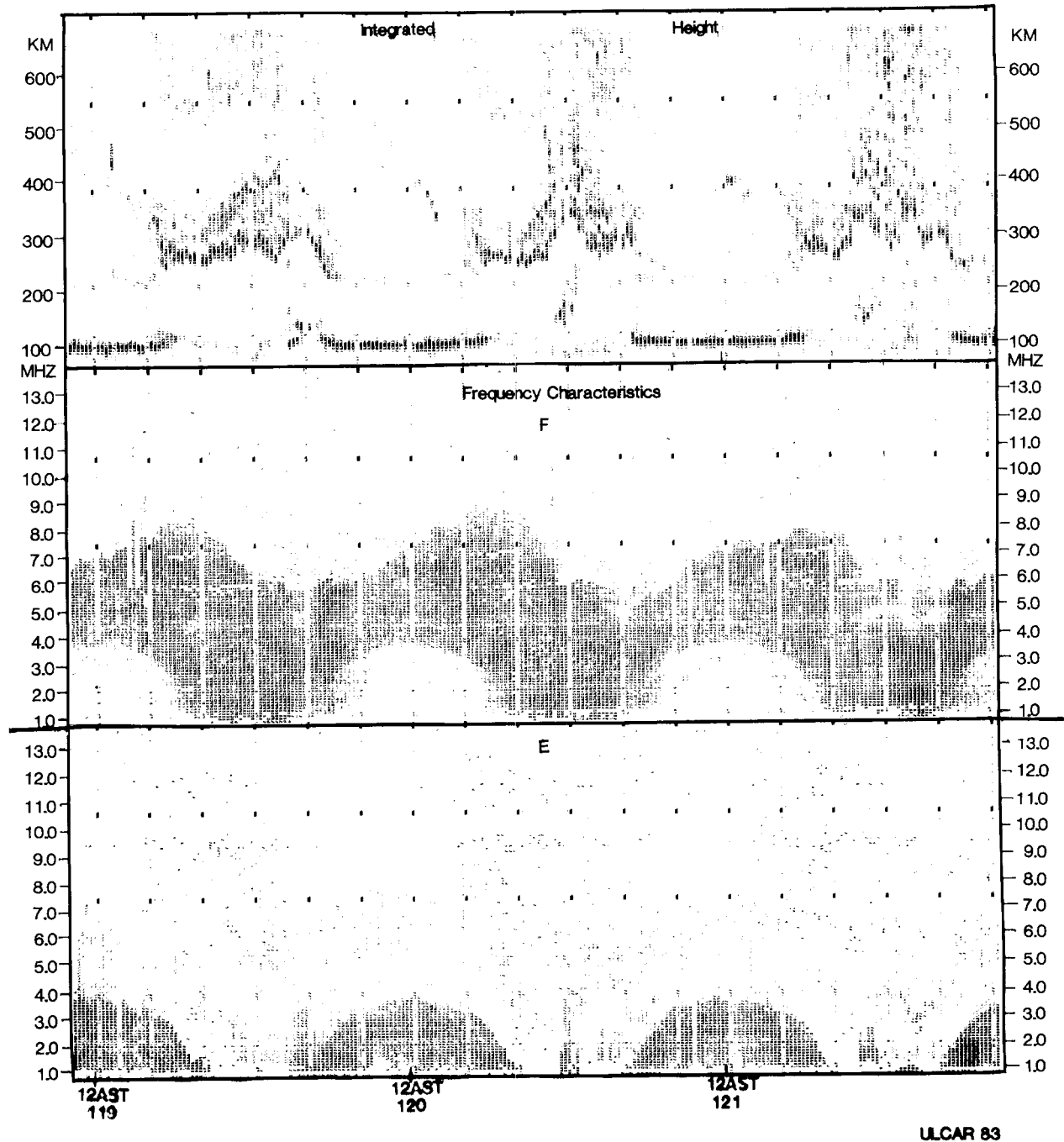


Figure 10-5. Ionospheric characteristics spanning three days produced from digital ionograms recorded at Goose Bay 28–30 April 1980. The integrated height characteristic shows the dynamic changes of the minimum height of the F layer and the appearance of the solar and sporadic E layers. The F and E frequency characteristics show the diurnal variability of these layers as well as evidence of some auroral events.

ceivers with the unwanted direct signal, a monostatic system was developed, using a T/R switch and a quasi-random interruption of the linear waveform transmission. The main advantage of the FM/CW system is the very narrow instantaneous bandwidth of the transmitted signal, allowing a similarly narrow receiver bandwidth (nominal 100 Hz at

sweep rates of 20 kHz/s). This bandwidth is further reduced by spectrum analysis to an effective bandwidth of the order of 1 Hz.

Although the digital integration and spectral analysis used in the modern digital pulsed ionosondes decreases the effective bandwidth of a pulse receiver significantly (by a

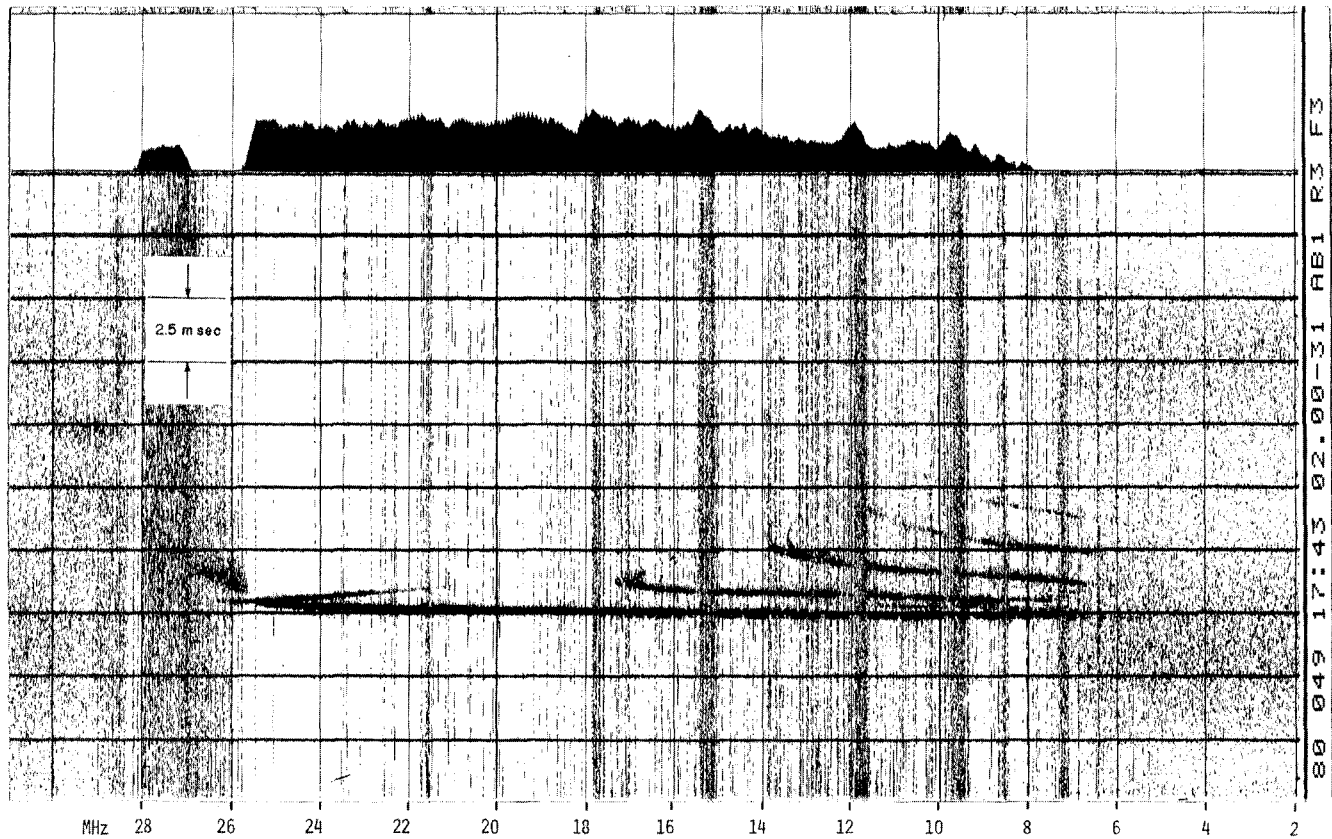


Figure 10-6. FM/CW or chirp-oblique propagation ionogram over a 2400 km path. Transmitted from an aircraft over the North Atlantic and recorded at a receiver site in Maine.

factor between 10 and 100, depending on the integration time and processing procedures) from the original 20 kHz bandwidth for a typical 50  $\mu$ s pulse and makes the actual signal-to-noise ratio comparable to that of a chirp sounder, the FM/CW system allows a substantial reduction of the peak power of the transmission. Good FM/CW ionograms have been obtained with transmit power as low as 1W (CW). The FM/CW system is definitely a good solution for the already strained occupancy of the HF spectrum. However, several drawbacks have limited its application as a vertical sounder: motion of the reflecting region imposes a Doppler shift, which introduces range errors that are intolerable under arctic conditions. The important Doppler shift of the echoes cannot be obtained. However, due to their low transmit power and superior S/N characteristics, many FM/CW systems are used as backscatter sounders and as oblique incidence or propagation sounders. A typical propagation ionogram showing extensive multihop structure is shown in Figure 10-6. The ionogram was obtained over a 2400 km path with the transmitter located on board an aircraft and the receiver located at the AF OTH-B radar site at Columbia Falls, Maine, U.S.A.

**10.1.1.8 Topside Sounders.** Shortly after the onset of the satellite era, an ionospheric topside sounder satellite,

Alouette I, was launched into space on 29 September 1962. Since then a series of follow-on improved topside sounders were launched, either as orbiting ionospheric sounders (Alouette II, 1965) or integrated with a complement of *in situ* measuring geophysical instruments (ISIS I, 1969 and ISIS II, 1971). For details on these sounders see Franklin and MacLean [1969].

Since groundbased ionosondes obtain ionospheric echoes only up to the peak of the layer with the highest electron density (generally the F2 layer), knowledge about the topside ionosphere was based on theory, the few incoherent scatter facilities, and sporadic high-altitude rocket flights. The topside sounders therefore filled a gap in the techniques available to measure the global ionosphere in its entirety. During the approximately 15 years that these topside sounders have provided continuous data, the many millions of ionograms that have been accumulated have contributed substantially to our picture of the global ionosphere [Chan and Colin, 1969; Thomas and Rycroft, 1970] and of its subregions, such as the high-latitude ionosphere [Jelly and Petrie, 1969; Thomas and Andrews, 1968], the F region trough [Muldrew, 1965; Pike, 1976], and the equatorial ionosphere [Eccles and King, 1969]. The topside sounder provides an h'f trace from the satellite altitude down to the peak of the F layer (except for those rare occasions where

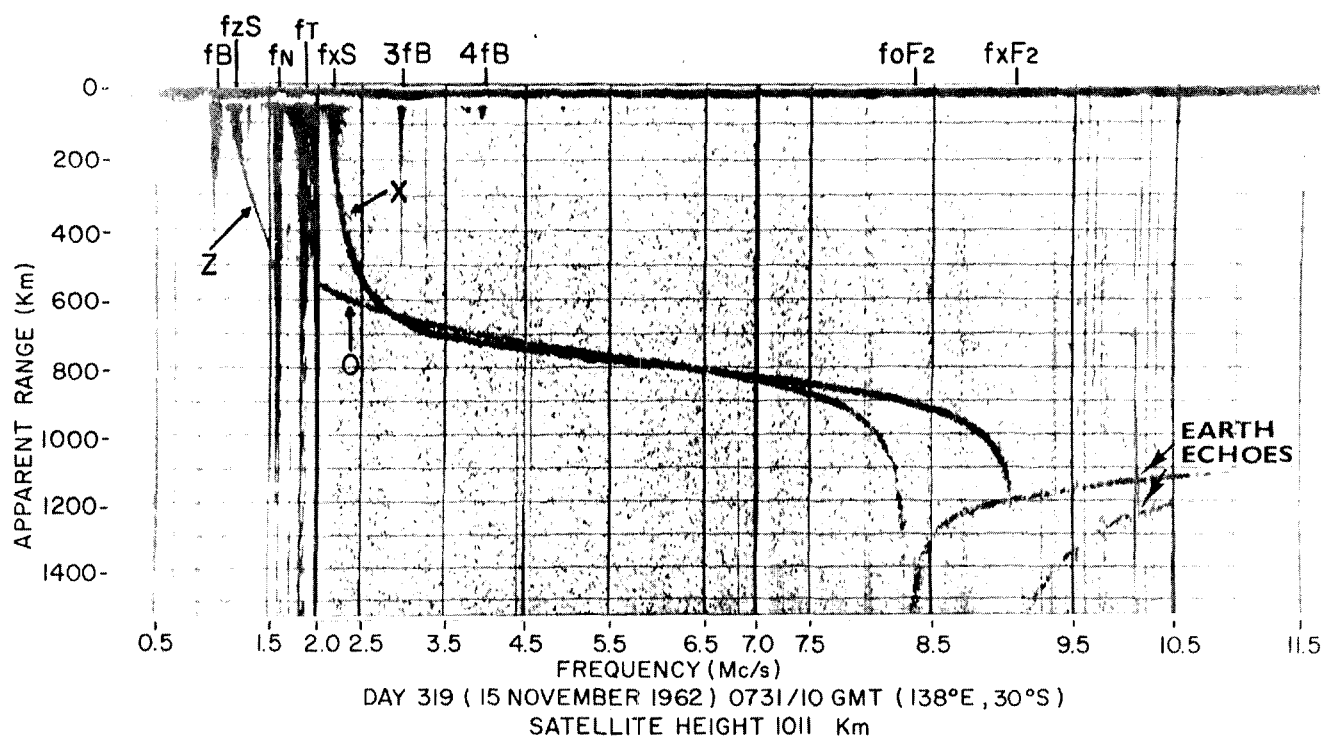


Figure 10-7. An Alouette I topside ionogram illustrating Z-, O- and X-wave traces, cutoffs, resonance spikes, and earth echoes.

ionization of lower layers exceeds the maximum density of the F2-layer). A typical topside ionogram is shown in Figure 10-7 from the *URSI Handbook of Ionogram Interpretation and Reduction* [UAG-23, 1972]. A unique phenomenon observed in topside ionograms are the ionospheric resonance spikes due to the excitation of the ambient plasma by the transmissions. The most frequently observed resonance spikes occur at the (local) plasma frequency  $f_N$ , at the local gyrofrequency  $f_H$  (labeled  $f_B$  in Figure 10-7), at the hybrid frequency

$$f_T = \sqrt{f_N^2 + f_H^2} \quad (10.20)$$

and at certain harmonics of these frequencies [Hagg et al., 1969].

Many of the references given here and a large amount of further material can be found in the special issue on topside sounding of the *Proceedings of the IEEE* [1969].

**10.1.1.9 Ionogram Interpretation.** The behavior of the ionosphere is often very dynamic. This fact and the large range of electron densities, over which the ionospheric layers change from day to day, from day to night, with season and with solar cycle result in a large variety of ionograms. There are also extreme differences in ionospheric variations and structures from the equators to the poles and in the regular or sporadic appearance and disappearance of the lower layers. Dynamic effects that shape the profile along the ray path and specifically in the vicinity of the reflection region also affect the group delay at each frequency and

therefore the final appearance of the h'f-trace. This trace is sometimes further complicated by ionospheric irregularities and oblique returns. All these factors combined ensure an incredible variety of ionograms. To capture their geophysically significant parameters, a large number of rules and definitions have evolved over the decades, which after acceptance by the International Radio Science Union (URSI) have been published as the *URSI Handbook of Ionogram Interpretation and Reduction*, [UAG-23, 1972] governing the analysis of ionograms at all ionospheric stations. This set of rules, resulting from the still continuing or terminated operation of more than 300 ionosonde stations distributed over the whole globe, has produced a rather uniform analyzed data base which is archived at the World Data Centers for Solar Terrestrial Research located at Boulder, Colorado (WDC A), Izmiran, USSR (WDC B), Tokyo, Japan (WDC C1) and Slough, UK (WDC C2). With some exceptions, the individual world data centers store data originating in their respective regions. WDC A stores the data from the western hemisphere and also data from France and India.

To provide special instructions for the analysis of the extremely complex ionograms from high latitude stations, a *High-Latitude Supplement to the URSI Handbook on Ionogram Interpretation and Reduction* has been published [UAG-50, 1975].

For special research efforts, it is often essential to go back to the source data, the ionospheric films of a specific station(s). For the western hemisphere, these films are stored

## CHAPTER 10

at the World Data Center A for Solar Terrestrial Physics, NOAA/NGSDC, Boulder, Colorado. A *Catalogue of Ionosphere Soundings Data* [UAG-85, 1982] provides access to this data base, which spans the period from 1930 through today. The longest and still continuing operation of an ionosonde station started at Slough, UK in January 1930. Continuous operation starting before 1940 is still ongoing at Canberra, Australia (1937); Heiss Island, USSR (1938); Huancayo, Peru (1937); Leningrad, USSR (1939); Tomsk, USSR (1937); and Tromso, Norway (1932).

To provide an overview of some of the more important ionospheric parameters that can be derived from an ionogram and introduce their geophysical meaning, two ionograms are provided in the form of a sketch (Figure 10-8), and the parameters are identified. Both ionograms depict the same ionospheric conditions (taken from Figure 10-1) with the exception of an Es layer that can suddenly appear, possibly as the result of a windshear at E layer heights. This Es layer can obscure parts of the trace from reflections at higher regions of the ionosphere. A list of parameters and their identification and interpretation is provided here as a general reference and not as a guide for ionogram analysis. For detailed instructions in the evaluation of ionograms please refer to the *URSI Handbooks UAG-23 and UAG-50*.

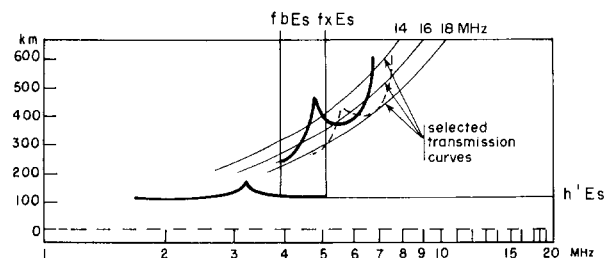
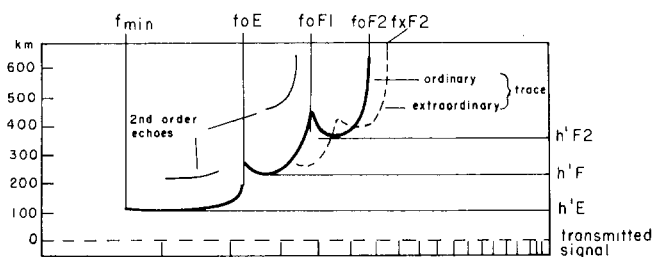


Figure 10-8. Line sketch of daytime ionogram shows definition of important ionogram parameters.

Parameter	Meaning/Comments
a) Critical and characteristic frequencies	
foF2	F2 layer ordinary wave critical frequency. A measure of the maximum density $N_{e_{max}}$ of this layer [see Equation (10.5)].
fxF2	F2 layer extraordinary wave critical frequency. Can be used to infer foF2 using Equation (10.12) if foF2 is obscured by interference.
foF1	F1 layer ordinary wave critical frequency. This layer is often smoothly merging with the F2 layer resulting in the absence of a distinct cusp and in difficulties of determining the exact frequency (L condition).
foE	solar produced E layer ordinary wave critical frequency. <i>Comment:</i> Extraordinary wave returns exist for all layers. However, absorption of the extraordinary component is stronger than that of the o-component and the x-trace of the E layer is rarely, that of the F1 layers not always observed.
fbEs	Es layer blanketing frequency. Returns from higher layers are obscured by the Es layer up to this frequency. This frequency corresponds closely to the maximum plasma density in the (thin) Es-layer [Reddy and Rao, 1968].
fxEs	Highest frequency at which a continuous Es trace is observed.
foEs	foEs can be inferred, applying Equation (10.12). If $fbEs < foEs$ , the layer is semitransparent. Es and higher layers are both observable. The determination of foEs and fxEs for all cases is subject to a complex set of rules beyond the scope of this outline (see URSI Handbook on Ionogram Interpretation). Modern Sounders, using polarized receive antennas, permit unambiguous foEs determination.

## IONOSPHERIC RADIO WAVE PROPAGATION

<i>Parameter</i>	<i>Meaning/Comments</i>
$f_{\min}$	Minimum frequency at which returns are observed on the ionogram. Since radio wave energy is absorbed in the D region according to an inverse square law (Absorption $\sim 1/f^2$ ), the variation of $f_{\min}$ is often used as a coarse indicator of the variation of D region ionization. $f_{\min}$ is not an absolute value (as for example foF2), but depends directly on the transmitted power and the antenna gain. Comparison between stations, therefore, can be only qualitative.
b) Virtual heights	
h'F	The minimum virtual height of the ordinary wave F trace taken as a whole. Due to the effects of underlying ionization and profile shape on the travel time of the pulse, these minimum virtual heights are only useful as coarse and "relative" height classifiers (high, average, or low layer, compared to a reference day). True height analysis must be made to give more meaningful height parameters, such as the height of the layer maximum ( $h_{\max}F2$ ).
h'F2	The minimum virtual height of the ordinary wave F2 layer trace during the daytime presence of the F1 layer. When an F1 layer is absent, the minimum virtual height of the F2 layer is h'F, defined above.
h'E	The minimum virtual height of the normal E layer, taken as a whole.
h'Es	The minimum virtual height of the trace, used to determine foEs.
hpF2	The virtual height of the ordinary wave mode F trace at the frequency $0.834 \times \text{foF2}$ . For a single parabolic layer with no underlying ionization this is equal to the height of the maximum of the layer, $h_{\max}$ . In practice hpF2 is usually higher than the true height of the layer maximum. Useful as a rough estimator of $h_{\max}$ but strongly affected by a low foF2/foF1 ratio ( $\leq 1.3$ ).
MUF(3000)F	A set of "transmission curves" [Davies, 1966 and 1969] developed for a selected propagation link distance (the URSI standard is 3000 km) permits the determination of the <i>Maximum Usable Frequency</i> , which the overhead ionosphere will permit to propagate over the selected distance. The MUF is determined from the estimated transmission curve tangential to the F-trace. For this ionogram MUF(3000)F would be 17.0 MHz.

**10.1.1.10 Ionosonde Network.** Even though the routinely operating ionosondes forming the worldwide network are independent, generally operated as subchains or as individual stations by national or private organizations, their operation is coordinated by the "Ionospheric Network Advisory Group (INAG)", working under the auspices of Commission G (On the Ionosphere), a Working Group of the International Union of Radio Science (URSI). INAG publishes the "Ionospheric Station Information Bulletin" at varying intervals. The Bulletin provides a means of exchanging experiences gained at the various ionospheric stations, discusses in detail difficult ionograms for the benefit of all participants, and disperses information on new systems, new techniques, special events (for example, eclipses), relevant meetings, and general network news. URSI's International Digital Ionosonde Group (IDIG), which provides a forum for the discussion of standardization proposals, for the exchange of software, and for the general exchange of experiences with these rather new and still maturing systems

has been incorporated into INAG as of September 1984. The INAG bulletin can be obtained from the World Data Center A, Boulder, Colorado, 80303.

With the advent of modern digital ionosondes and on-site automated processing, a carefully planned network of remotely controllable ionosondes can provide ionospheric data and electron density profiles to a control location for real time monitoring of ionospheric and geophysical conditions. Automatic oblique propagation measurements between stations of the link can increase manyfold the number of ionospheric points that can be monitored. Considerations for the deployment of a modern ionosonde network have recently been presented by Wright and Paul [1981]. Operational and technical information on the individual stations of the world wide network of ionosondes, as well as their respective affiliations and addresses, are available in the *Directory of Solar Terrestrial Physics Monitoring Stations* [Shea et al., 1984]. Figure 10-9, taken from the report in preparation, shows the locations of all ionosondes reported

## CHAPTER 10

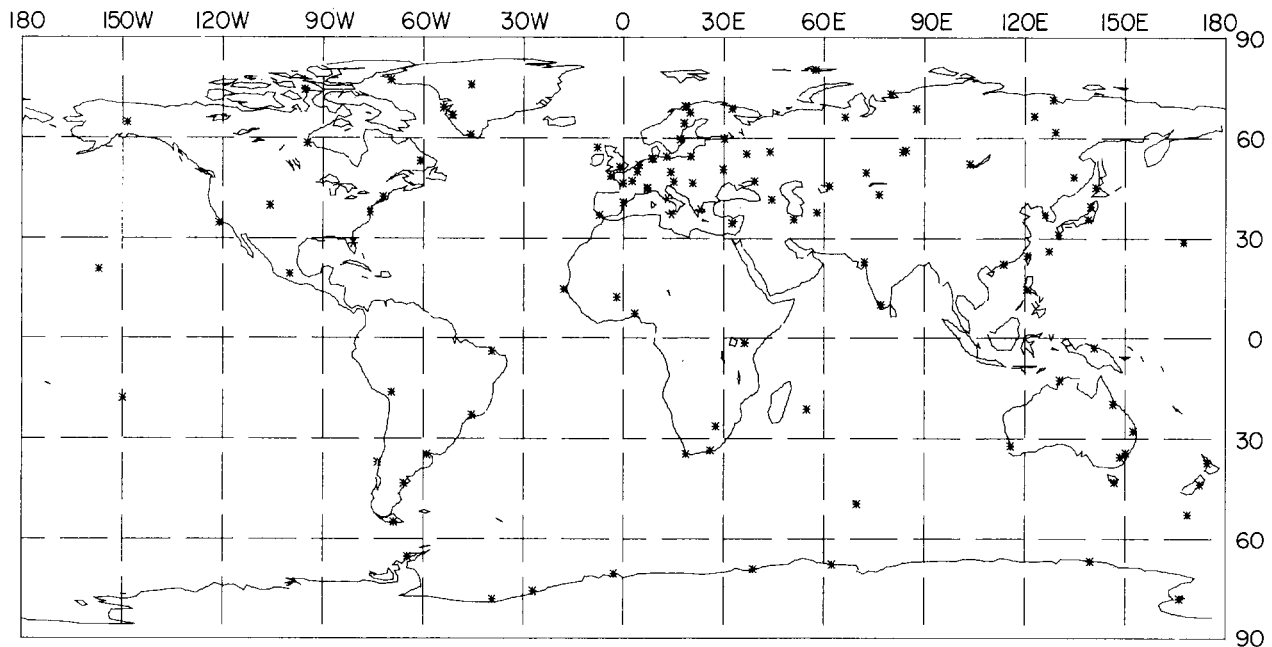


Figure 10-9. Map of vertical incidence ionospheric sounder stations 1984.

as operational or operating in 1984. World Data Center A Report, UAG-85, lists all past and present ionospheric observatories.

### 10.1.2 Incoherent Scatter

J.J. Thomson [1906] showed that single electrons can scatter electromagnetic waves, and that the energy scattered by an electron into unit solid angle per unit incident flux is given by  $(r_e \sin\psi)^2$  where  $r_e$  is the classical electron radius ( $= e^2/\epsilon_0 m_e c^2 = 2.82 \times 10^{-15}$  m) and  $\psi$  is the polarization angle, that is, the angle between the direction of the incident electric field and the direction of the observer. Thus the radar backscatter ( $\psi = \pi/2$ ) cross-section of a single electron will be  $\sigma_e = 4\pi r_e^2$ . Gordon [1958] first proposed that by the use of a powerful radar operating at a frequency  $f \gg f_{oF2}$  where  $f_{oF2}$  is the plasma frequency at the peak of the F2 layer, the backscattered power from the electrons in the upper atmosphere should be detectable. The measurement of scattered power and its characteristics as a function of altitude was expected to provide a measurement of the various geophysical parameters both in the bottomside and the topside ionosphere. Gordon assumed that the electrons were in random thermal motion of the same type as the motion executed by neutral particles so that the radar would detect scattering from individual electrons that are random in phase or incoherent. This is known as incoherent scatter or Thomson scatter (for a comprehensive review, see Evans [1969]). Gordon calculated the backscattered power

per unit volume to be  $N\sigma_e$ , where  $N$  is the electron number density. He also predicted that the spectrum of the scattered signal will be Doppler broadened by the random electron thermal motion. The spectrum of the scattered signal was expected to be Gaussian with center to half-power width of  $0.71 \Delta f_c$  where  $\Delta f_c$  is the Doppler shift of an electron approaching the radar at mean thermal speed so that

$$\Delta f_c = \frac{1}{\lambda} \left( \frac{8kT_e}{m_e} \right)^{1/2} \text{ Hz}, \quad (10.21)$$

where  $\lambda$  is the radar wavelength (m),  $k$  is Boltzmann's constant ( $= 1.38 \times 10^{-23}$  J/K),  $T_e$  is the electron temperature, and  $m_e$  is the mass of an electron ( $= 9.1 \times 10^{-31}$  kg). At a wavelength  $\lambda = 1$  m, and  $T_e = 1600$  K,  $0.71 \Delta f_c \approx 200$  kHz. Soon after Gordon [1958] proposed the feasibility of the incoherent scatter radar experiment to study the upper atmosphere, Bowles [1958] was able to detect radar echoes from the ionosphere. The echoes resembled the predicted ionospheric scatter signal except that the bandwidth of the signal was considerably less than the predicted value. The decrease of the bandwidth of the scatter signals contributing a larger signal power per unit bandwidth obviously made it easier to detect the signal. Bowles [1958] correctly surmised that the presence of ions causes a reduction of the bandwidth of the scattered signal. Later theoretical work [Fejer, 1960; Dougherty and Farley, 1960; Salpeter, 1960; Hagfors, 1961] showed that the spectral form of the scattered signal is dictated by the radar wave-

# IONOSPHERIC RADIO WAVE PROPAGATION

length in relation to the Debye length in the upper atmosphere. The Debye length ( $D$ ) for electrons is defined as

$$D = (\epsilon_0 kT_e / 4\pi N_e^2)^{1/2} \text{ m} \quad (10.22)$$

where  $\epsilon_0$  is the permittivity of free space ( $= 8.85 \times 10^{-12}$  F/m),  $e$  is the charge on an electron ( $= 1.6 \times 10^{-19}$  C),  $k$  is the Boltzmann's constant,  $N_e$  is the electron density ( $\text{m}^{-3}$ ) and  $T_e$  is the electron temperature (K). The Debye length for the electrons in the ionosphere is typically of the order of 1 cm or less below 1000 km and it is not possible to sustain organized motion at scales smaller than these values.

It was shown that, in general, the spectrum of the scattered signal consists of two parts, one due to the ions and the other to electrons. If the radar wavelength is much smaller than the Debye length, the scattered energy is entirely due to the electronic component and the initial predictions of Gordon [1958] for the scattered power ( $N\sigma_e$ ) and its spectrum ( $\Delta f_e$ ) are valid. On the other hand, for radar wavelengths much larger than the Debye length, which represents the experimental situation, the electronic component decreases and appear as a single plasma line at a Doppler shift approximately equal to the plasma frequency of the medium. Under this condition, the largest part of the scattered energy resides in the ionic component and the spectral width is controlled by the Doppler shift  $\Delta f_i$  for an ion approaching the radar at the mean thermal speed of the ions, given by

$$\Delta f_i = \frac{1}{\lambda} \left( \frac{8kT_i}{m_i} \right)^{1/2} \text{ Hz}, \quad (10.23)$$

where  $m_i$  is the mass of the dominant positive ion and  $T_i$  is the ion temperature. Considering  $T_e \approx T_i$ , and the dominant ion to be  $\text{O}^+$ ,  $\Delta f_i \approx 2 \times 10^{-2} \Delta f_e$ . The echo energy is, therefore, mainly concentrated in a relatively narrow spectral window rendering the radar investigation feasible with apparatus of much lower sensitivity than initially envisaged. Figure 10-10 shows how the spectral shape depends on a parameter  $\alpha = 4\pi D/\lambda$  for the case  $T_e = T_i$ . For  $\alpha \geq 10$ , the scattered energy is entirely due to the electronic component, whereas for very small values of  $\alpha$ , the electronic component decreases and the energy appears mainly in the ionic component with a much smaller bandwidth. The electronic component now appears as a single line, known as the plasma line, at a Doppler shift approximately equal to the plasma frequency of the medium.

In the ionosphere, the electrons and the ions are at different temperatures and the spectrum of the ionic component changes for different values of the ratio  $T_e/T_i$  at a given value of  $\alpha$ . This is shown in Figure 10-11 for the case  $\alpha = 0.1$  for  $\text{O}^+$  ions which illustrates the double-humped form of the spectrum. By measuring the height of the hump at the wing relative to the center of the spectrum, it is possible to estimate  $T_e/T_i$  and the total scattering cross-section due to the ionic component is simply obtained from the area under the curves. For small values of  $T_e/T_i$ , which

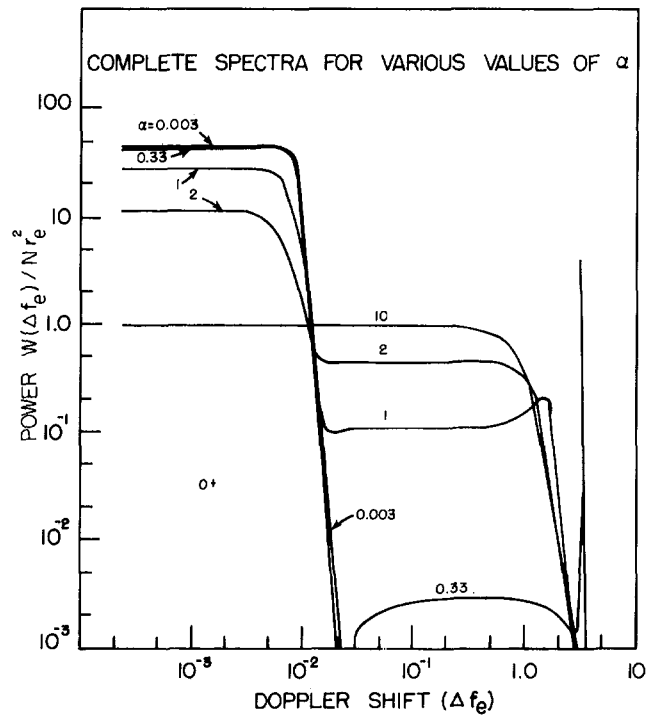


Figure 10-10. The variation of the overall spectrum for different values of the ratio  $\alpha (= 4\pi D/\lambda)$ . The ion has been assumed  $\text{O}^+$ . These curves assume that collisions are negligible and that  $T_e = T_i$  [Hagfors, 1961].

is encountered in the ionosphere, the total scattering cross-section ( $\sigma$ ) may approximately be given by

$$\sigma = \frac{\sigma_e}{(1 + \alpha^2)(1 + \frac{T_e}{T_i} + \alpha^2)} \quad (10.24)$$

The incoherent scatter radar technique opened up the possibility of *in situ* sampling of a wide range of upper atmospheric parameters by the use of a powerful ground-

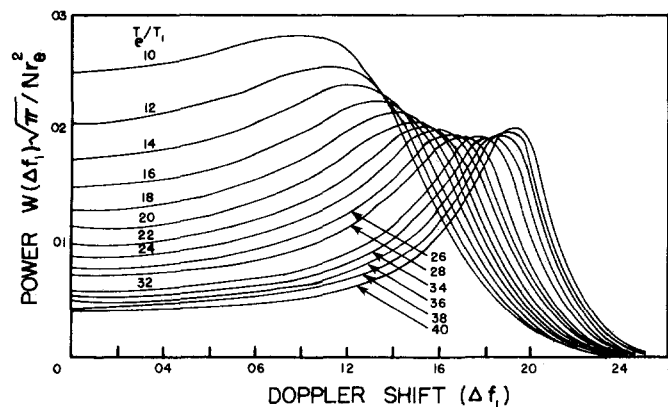


Figure 10-11. Spectra of the ionic component for the case of  $\alpha (= 4\pi D/\lambda) = 0.1$  [Evans, 1969]. (Reprinted with permission from IEEE © 1969.)

## CHAPTER 10

based radar system [Evans, 1969]. The most obvious measurement is the electron density ( $N$ ) versus altitude ( $h$ ) profile made by recording the variation of echo power  $P_s$  as a function of delay by using a vertically directed pulsed radar. The echo power is given by

$$P_s = C \frac{N(h) \sigma(h)}{h^2}, \quad (10.25)$$

where  $C$  is a constant. The constant  $C$  can be determined either by a careful determination of the radar parameters or by an absolute determination of  $N$  at an altitude by an ionosonde or other techniques. However, as mentioned earlier (Equation 10.24), the scattering cross-section  $\sigma(h)$  depends both on  $\alpha$  and  $T_e/T_i$  which are both functions of altitude. From a measurement of the scattered energy spectrum, these corrections can be introduced and electron density profiles are determined. It has also been possible to obviate this difficulty entirely by the use of Faraday rotation technique. Figure 10-12 illustrates the electron density profile extending to almost one earth radius obtained at Jicamarca by this technique. In addition to the rather straightforward measurement of electron density profiles, electron and ion temperatures, ion composition, and photoelectron flux, the ionospheric electric field and a variety of other upper atmospheric parameters have been successfully measured at various locations extending from the magnetic equator to the auroral zone [Radio Science, special issue, 1974].

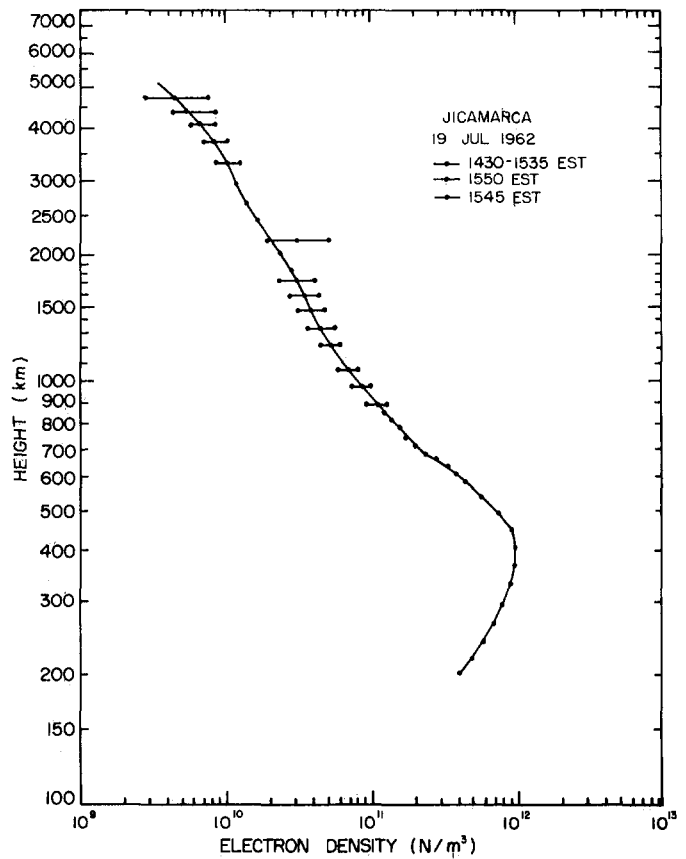


Figure 10-12. An electron density profile obtained at Jicamarca that extends to almost one earth radius [Bowles, 1963].

Table 10-1. Incoherent scatter facilities.

Location	Frequency (MHz)	Power (MW)	Antenna	Dip latitude (°N)
Jicamarca, Peru	50	6 Pulsed	290 m × 290 m array	1
Arecibo, Puerto Rico	430	2 Pulsed	300 m spherical reflector	30
St. Santin, France	935	0.15 Continuous	20 m × 100 m reflector	47
Millstone Hill, USA	440 1300	3 4 Pulsed	68 m 25 m parabola	57
Sondreström, Greenland	1300	5 Pulsed	32 m parabola	71
EISCAT* Transmitter: Tromso, Norway	224 (monostatic) 933.5 (tristatic)	5 2	30 m × 40 m parabola cylinder 32 m parabola	67
Receiver: Tromso, Norway Kiruna, Sweden Sodankyla, Finland			32 m parabola	

\*European Incoherent SCATter facility

## IONOSPHERIC RADIO WAVE PROPAGATION

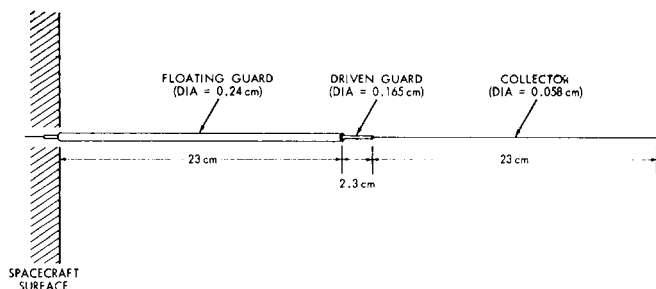


Figure 10-13. Cylindrical Langmuir Probe.

Table 10-1 adopted from Hargreaves [1979] gives a list of the incoherent scatter facilities now in operation and the characteristics of the radar system.

### 10.1.3 Langmuir Probes

One of the simplest devices used on rockets or satellites to measure the ionospheric density *in situ* is the Langmuir probe, named for Irving Langmuir, who pioneered the method at General Electric in the 1920s. The density is determined from a measurement of electric current passing between two conducting surfaces in contact with the environment. A varying electrostatic potential placed between the two surfaces causes the current to vary. The magnitude of the current indicates the density of the ionospheric plasma, and the change in current with respect to changes in the potential between the surfaces indicates the ion and electron temperatures. The double-floating-probe, which is the closest version to an idealized Langmuir probe, usually consists of a conductor at each end of a dipole antenna flown on a rocket or satellite for other purposes. The major disadvantage of a double-floating-probe is that ion thermal velocity is much lower than the electron thermal velocity and the rocket or satellite speeds. Therefore, the usual Langmuir probe is a single probe to measure only electrons; the other

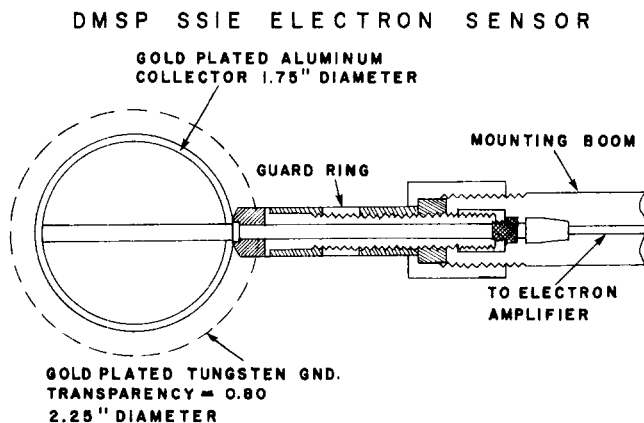


Figure 10-14. The Spherical Langmuir Probe on the DMSP Satellite.

probe is replaced with the entire exposure conducting surface of the rocket or satellite. If the exposed conducting surface of the rocket or satellite is much greater than the area of the probe, the potential of the surfaces will remain fixed as the potential on the probe is swept. As a minimum, the area of the conducting surfaces should be 100 times greater than the area of the probe, and ideally the area should be 10 000 times greater than the area of the probe. By setting the potential of the probe very positive (+1.5v to +20v), all electrons within a few Debye lengths of the probe will be drawn in and measured; this allows a direct measurement of plasma density oscillations which are directly related to plasma turbulence.

The two most common shapes for Langmuir probes are the cylindrical probe (Figure 10-13) and the spherical probe (Figure 10-14). Any shape probe is possible, but these shapes are the easiest to analyze mathematically.

### 10.1.4 Faraday Cups for Rockets and Satellites

The most commonly used device for measuring the thermal ions is the Faraday cup (see Figure 10-15). It is usually an aperture that is a section of a flat, infinite surface in contact with a plasma. A screen across the aperture shields electrostatic potentials inside the sensor from the outside environment. The arrangement of grids or screens inside the sensor is determined by the function of the sensor. Most Faraday cups use a suppressor screen in front of the collector. This screen has a large negative potential (-10V to -100V) to repel electrons from the environment away from the collector and to drive secondary and photoelectrons from the collector back to the collector.

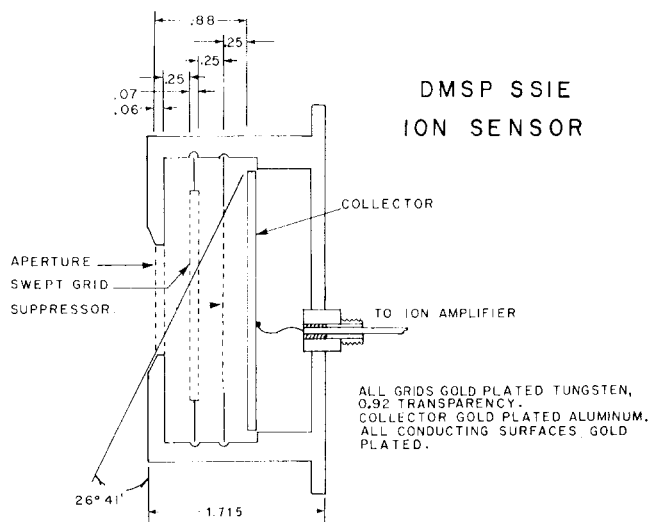


Figure 10-15. The Faraday Cup used on the DMSP Satellite.

## CHAPTER 10

### 10.1.5 Optical Measurements

Ground, airborne, satellite, and rocket based optical measurements are commonly used to determine ionospheric structure and dynamics. While a number of different instruments are employed, all analysis techniques must relate spectral emission features to ionospheric structure and dynamic processes. This is done through a knowledge of the atmosphere/ionosphere chemistry that leads to the measured photon emission. Ionospheric domains are conveniently divided into regions that are produced or influenced by energetic particle precipitation (auroral regions) and those controlled mainly by solar ionizing radiation (equatorial and midlatitude). Optical measurements have played important roles in both regions in defining the spatial and temporal characteristics of ionospheric plasma. Commonly used observing techniques will be discussed followed by a section describing important results.

**10.1.5.1 Observing Techniques.** Optical instruments can be classified according to spectral resolution as low, medium, and high.

*Low Resolution Systems:* The all sky camera has historically been used to measure auroral structure. This is perhaps the lowest resolution system, measuring all wavelengths over the sensitivity range for the type of film used (typically Kodak TRI X). The system uses a 160° field of view lens to measure auroras over a circle of 1000 km diameter in the lower ionosphere (110 km altitude). All sky cameras typically measure only bright auroral features, primarily at E region altitudes.

Photometers are low resolution systems. They rely on narrow band interference filters to isolate spectral lines and bands of interest. Meridian scanning photometers use a narrow (0.5° to 2.5°) field of view and ~2 Å filters to measure absolute intensity of auroral and airglow along a vertical circle, commonly aligned along a magnetic meridian. Tilting filters use the change in transmitted wavelength versus tilt angle to perform a limited wavelength scan. This allows separation of non-spectral continuum from the line or band emission.

More recently, all-sky imaging photometers have been developed to perform all-sky (155°) monochromatic measurements at high sensitivity (20 Rayleighs). These employ slightly wider (~20 Å) interference filters because of the lack of convergence of the extreme optical rays at large zenith angles. Image intensifiers are employed to achieve the high sensitivity. Data are recorded either on a photographic image or by using a TV system to produce a video signal. Typical system parameters are shown in Table 10-2.

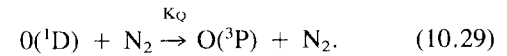
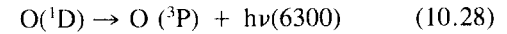
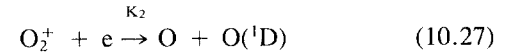
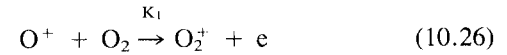
*Medium Resolution Systems:* Ebert-Fastie type scanning spectrometers are used as medium resolution optical systems. These are effectively used over the (visible) wavelength range of 3800 to 7900 Å with variable spectral resolution

from 2-18 Å. They can be scanned across the sky or operated in the zenith. When properly calibrated, spectrometers provide the absolute intensity of auroral and airglow features as well as some measure of spectral character.

*High Resolution Systems:* Fabry-Perot interferometers use multiple path interference to achieve high spectral resolution. These instruments are primarily used to measure spectral line broadening and Doppler shift. From these parameters, atmospheric temperatures and drift velocities can be derived. Primary spectral features of interest are 6300 Å [OI], 5577 Å [OI] for neutral winds, and 7320 Å [OII] for plasma drift.

**10.1.5.2 Ionospheric Structure from Optical Measurements.** Ionospheric structure at mid and equatorial latitudes is controlled by solar ionizing radiation, electric fields, and neutral atmosphere dynamics. Airglow observations of equatorial plasma depletions are one example of optical measurements used to define ionospheric processes. A brief review of equatorial airglow chemical production mechanisms is presented to illustrate the techniques used to infer ionospheric plasma density variations from remote optical measurements.

Two primary airglow spectral emission features are of interest for nighttime, F region phenomena 6300 Å [OI] and 7774 Å OI. The 6300Å atomic oxygen emission results from the following sequence of reaction:



Since  $K_2 \gg K_1$ , and in regions where  $O^+$  is the dominant ion ( $O^+ = N_e$ ) the 6300Å volume emission rate is given by

$$dI(6300) = \left[ 0.75 K_2 E [N_e][O_2] / \left( 1 + \frac{K_Q N_2}{A} \right) \right] dh \quad (10.30)$$

where  $K_2 E = 1.4 \times 10^{-11} \text{ cm}^3 \text{ s}^{-1}$

$$K_Q = 7.0 \times 10^{-11} \text{ cm}^3 \text{ s}^{-1}$$

$$A = 10^{-2} \text{ s}^{-1}$$

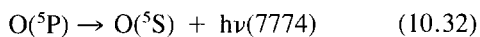
(See Weber et al., [1980] and Noxon and Johanson [1970] for a more complete discussion).

The 7774 Å OI results from radiative recombination of  $O^+$ :

# IONOSPHERIC RADIO WAVE PROPAGATION

Table 10-2. Summary of system specifications.

Field of View	155°
Pass Band	25 Å at f 1.4; 5 Å at f 8
Resolution	1/2° zenith, 2° horizon
Spectral Response	S-20, exceeding 100 μA/lumen
Picture Storage	No detectable degradation for up to 3 s
Tube Gain	Photon noise granularity visible above tube noise
Threshold Sensitivity	20 R at 2 s exposure 1 kR at 30 frames/s
Dynamic Range	20 R to 10 kR covered by 3 preset HV settings
Flatness of Field	30 percent loss at edge of field
Repetition Rate	Typically 20 s for complete filter cycle
Temporary Storage	Video disc, three video tracks + one sync track
Permanent Storage	Video tape deck, time-lapse type (9 h recording time on a single reel); 16 mm color movie camera
Process Controller	In-field programming capability
Display Systems	Four black and white monitors, 9 in. diagonal; Color monitor, RGB and A-B input, 12 in. diagonal
Real-Time Display	Simultaneous fully registered display of three filter channels. Capability of displaying difference of any two pictures. Display of two or three filters as pseudo-color on RGB monitor
Character Generators	Date/time display on each frame for frame identification
Digital Encoding	Digital encoding of time and housekeeping data for computer-controlled data handling



and the volume emission rate is given by

$$dI(7774) = K_3 [O^+][N_e] dh. \quad (10.33)$$

To illustrate the altitude dependence, 6300 Å and 7774 Å airglow volume emission rates were calculated for an electron density profile representative of the Appleton anomaly region, and are shown in Figure 10-16. The bottomside profile was obtained from true height analysis of a digital ionogram. This was matched to a modified Chapman function [Tinsley et al. 1973] to represent the topside profile from hmax F<sub>2</sub> to 690 km. Because of the exponentially

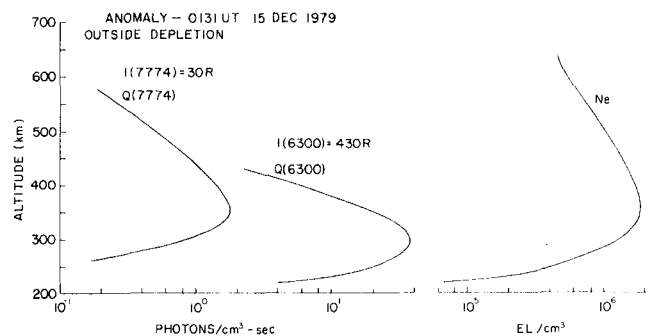


Figure 10-16. Electron density profile derived from true height analysis of bottomside ionogram matched to a modified Chapman function for the topside. Also shown are calculated 6300 and 7774 Å volume emission rates and column intensities in Rayleighs.

## CHAPTER 10

decreasing  $O_2$  concentration, the 6300 Å volume emission rate is confined to the bottomside and reaches a maximum value at 300 km, below  $h_{max}$  F2 (360 km). The 7774 Å volume emission rate is proportional to  $[Ne]^2$  and attains its maximum value at  $h_{max}$  F2. Because of the broad altitude extent of the equatorial electron density profile the 7774 Å volume emission rate displays a similar broad extent and falls to 50% of the maximum value at 300 km and 450 km. Thus the 7774 Å airglow measurements provide information over a broad altitude range, with approximately one half of the emission produced above the F layer peak.

All sky imaging photometer measurements conducted within a few degrees of the magnetic equator and near the Appleton Anomaly region ( $\sim 18^\circ$  ML) have established the two-dimensional horizontal extent of equatorial plasma depletions. These are also the regions of post-sunset equatorial spread F, VHF radar backscatter plumes, and amplitude and phase scintillation on transionospheric radio propagation. Figure 10-17 shows an example of all sky images at 6300 Å and 7774 Å near the equatorial edge of the Appleton Anomaly. The bright region over the southern two-thirds of the image is airglow from the high-density anomaly region. The North-South aligned dark band is a region of decreased airglow emission. Comparison with simultaneous *in situ* measurements from the Atmosphere Explorer satellite (AE-E) shows this airglow depletion to be collocated with a region of significantly decreased ion density. Having established the relation between airglow emission processes and F layer density, the all sky images provide a two-dimensional map of these depleted regions. In addition, the dynamics of these regions can be monitored over extended

periods in the absence of "snapshot" satellite measurements. Optical measurements coordinated with VHF radar, ionosonde, *in situ* density, and satellite radio beacon scintillation observations have helped to provide a detailed description of the development, structure, drift, and decay of these important equatorial ionospheric features.

Optical measurements have improved our understanding of auroral zone and polar cap ionospheric structure and magnetosphere-ionosphere coupling processes. In this region dominated by the effect of precipitating electrons and ions over a wide energy range (few eV to 100's of keV), optical measurements of impact excitation and chemical recombination aid in understanding a wide variety of processes. In this section, several examples of all-sky monochromatic images are shown, primarily to demonstrate the use of optical measurements, especially when coordinated with other ionospheric diagnostics. Figure 10-18 shows a montage of auroral images at 10-min intervals at 6300 Å [OI] and 4278 Å  $N_2^+$ . These images were recorded on an aircraft which flew North-South legs along the Chatanika, Alaska Incoherent Scatter Radar magnetic meridian. The images provide a map of the instantaneous particle precipitation patterns separately for the E (4278 Å) and F (6300 Å) layers. Measurements with the radar mapped electron density structure and satellite UHF radio beacon scintillation measurements mapped regions of ionospheric irregularities (from tens of meters to a few kilometers). In this experiment, optical measurements provide a continuous map of particle precipitation regions over a large area (1200 km diameter at F-region altitudes) for interpretation of magnetosphere-ionosphere coupling and ionospheric dynamics.

Measurements in the polar cap have recently clarified local particle precipitation effects from plasma transport (E-field) effects. Local precipitation of low energy (100's of eV) electrons, during IMF Bz north conditions, leads to the production of sun-aligned F region auroras. Some of these auroras are characterized by F region plasma density enhancement and structuring within these auroras leads to amplitude and phase scintillation.

During Bz south conditions, large patches of F region plasma are observed to drift across the polar cap in the anti-sunward direction. Coordinated satellite measurements show that these patches are not locally produced by precipitating particles, but are convected from a source region at or equatorward of the dayside cusp. These patches are also subject to structuring processes that lead to scintillation.

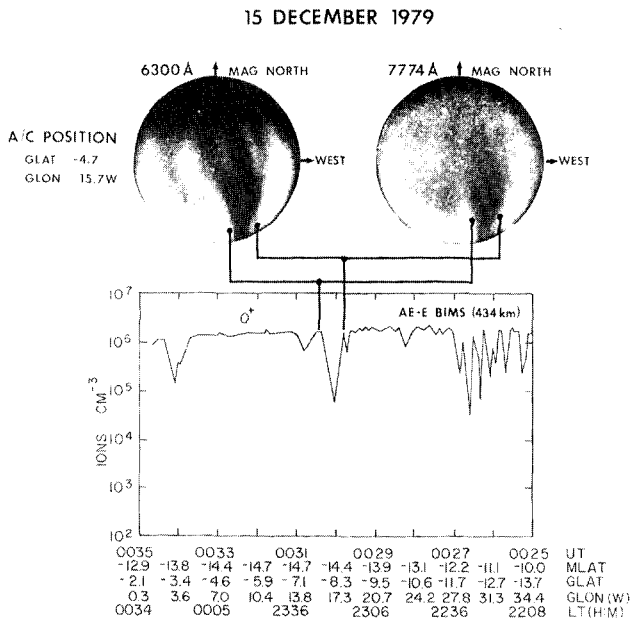


Figure 10-17. All sky images at 6300 and 7774 Å recorded near the equatorial edge of the Appleton Anomaly.

### 10.2 SOME ASPECTS OF LONG WAVE PROPAGATION

It is convenient to refer to radio waves having frequencies below 3000 kHz as "long waves". These include Extremely Low Frequencies (ELF), Very Low Frequencies (VLF), Low Frequencies (LF), and Medium Frequencies (MF), as outlined in Table 10-3. ELF has had very little

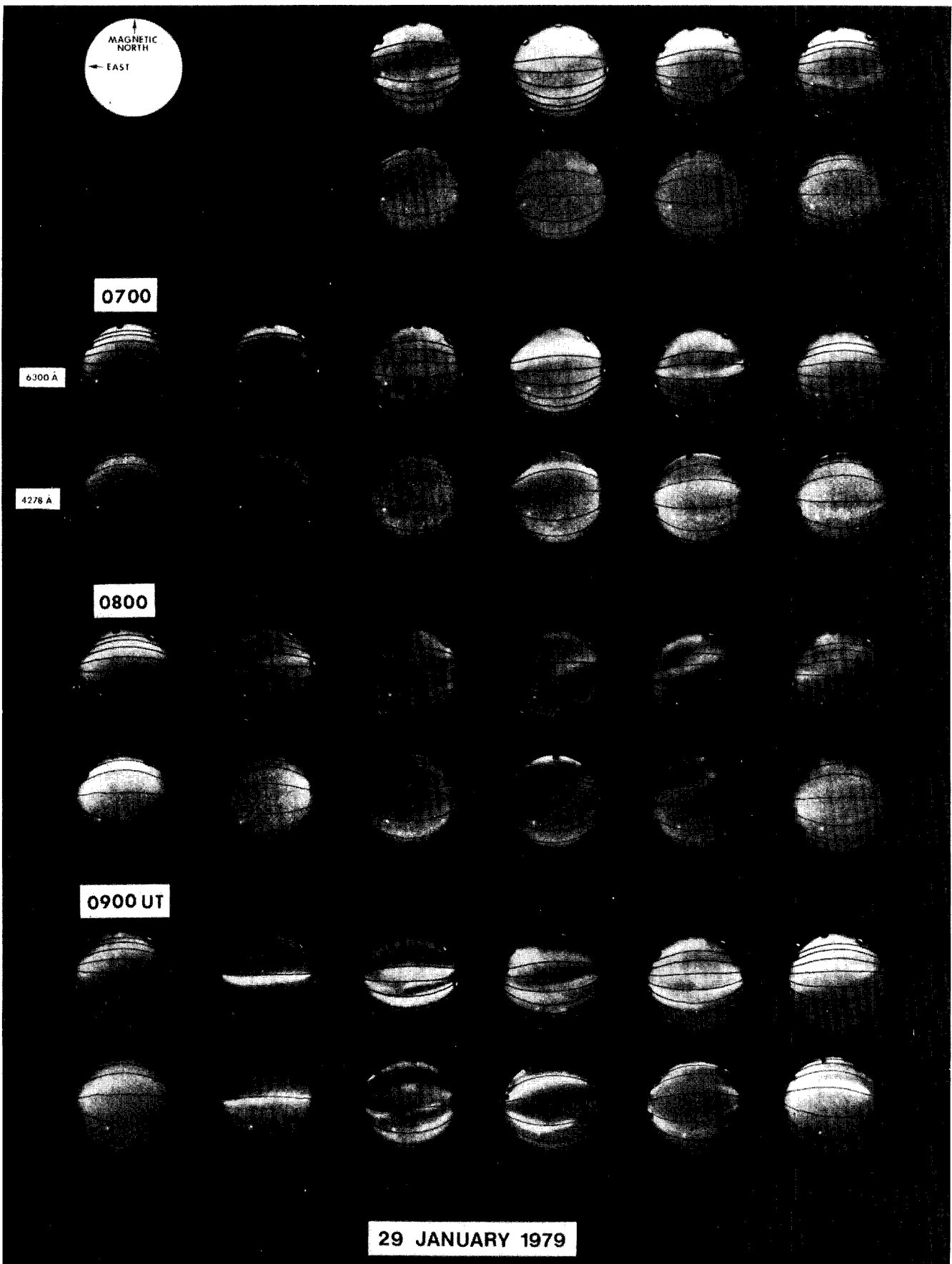


Figure 10-18. Auroral images taken at 10 minute intervals from 0620 to 0950 UT on 29 January 1979. The upper row under each hour shows the 6300 Å images; the lower row, the 4278 Å images.

## CHAPTER 10

Table 10-3. Long wave frequency bands.

Designation	Abbreviation	Frequency Range	Wavelengths
Extremely Low Frequency	ELF	0.003–3 kHz	$10^5$ – $10^2$ km
Very Low Frequency	VLF	3–30 kHz	$10^2$ – $10^1$ km
Low Frequency	LF	30–300 kHz	10–1 km
Medium Frequency	MF	300–3000 kHz	1–0.1 km

use, except for communications that require wave penetration beneath the surface of the ocean or earth. The VLF/LF bands are used extensively for navigation and military communication. The standard AM broadcast systems utilize part of the MF band (535–1606 kHz). Long radio waves are also used in basic ionospheric research, meteorology and thunderstorm study and tracking, standard frequency and time distribution, geological studies, and minerals exploration.

Long waves propagate by a number of different modes. These include propagation over the surface of the earth by diffraction modes, ELF propagation by transmission-line type modes, propagation by ionospheric reflection (or earth-ionosphere waveguide modes) and propagation through the ionosphere by so-called “whistler” modes. Each type of mode requires a separate physical description and mathematical formulation.

### 10.2.1 Groundwave Propagation

The most general definition of the groundwave is the wave that would be excited by an antenna at or near the air-earth boundary if there were no wave reflections from the upper atmosphere. At long wavelengths ionospheric reflections are important, and for continuous wave (CW) transmissions it is necessary to regard the total wave field as a vector sum of the groundwave and skywaves. If an antenna radiates a very short pulse, however, it may be possible for a distant receiver to resolve the groundwave and skywaves individually. The time interval between the onsets of the groundwave and the first-hop skywave is given by

$$\Delta t = (2\sqrt{h^2 + 4a(a+h)\sin^2(d/4a)} - d) (1/c), \quad (10.34)$$

providing

$$d \leq 2a \cos^{-1}\{a/(a+h)\}, \quad (10.35)$$

where  $d$  is the distance between the transmitter and receiver,  $h$  is the effective height of reflection in the ionosphere,  $a$  is the earth’s radius ( $\approx 6370$  km) and  $c$  is the wave velocity ( $3 \times 10^5$  km/s). If the transmitted pulse is short enough,  $\Delta t$  may be long enough (for example,  $\Delta t = 93 \mu\text{s}$  for  $d = 500$  km and  $h = 80$  km) to permit very accurate measurements of the groundwave, especially its arrival time or

phase. The latter is the basis of the long-range 100 kHz groundwave navigation system, Loran-C.

If the transmitted signal is a continuous wave, the amplitude and phase of the composite signal received at a fixed distance vary with time as the ionosphere changes. On the other hand, at a given moment the signal amplitude is a function of distance [Hollingworth, 1926], having maxima and minima typical of an interference pattern. The groundwave component is stronger than the skywaves out to a distance that depends on the wave frequency, among other factors. This region of groundwave dominance is the most stable, or primary, coverage area of MF broadcast transmitters.

As defined above, the groundwave exists at all radio frequencies, but at wavelengths comparable to the height of the ionosphere or greater, the usefulness of the concept begins to fade. Also, for transmitters high above the ground, or at high frequencies where quasi-optical propagation analysis is appropriate, the term groundwave is seldom used.

The earth often acts as a fairly good conductor for long waves, in which case the electromagnetic boundary conditions permit electric fields perpendicular to the surface, while tending to suppress electric fields tangential to the surface. It follows that groundwave fields near the earth’s surface tend to have transverse magnetic (TM) polarization rather than transverse electric (TE) polarization. In common usage the unqualified term “groundwave” implies TM polarization.

**10.2.1.1 Idealized Flat-Earth Models.** In a simple model the earth’s surface is regarded as a flat perfect conductor, and the air is homogeneous with refractive index 1. The most elementary source is a vertically-directed current  $I(t) = I_0 \exp(i\omega t)$ , at frequency  $f = \omega/2\pi$ , of infinitesimal length  $d\ell$ , which has an electric dipole moment  $M(t) = I(t) d\ell$  (Note: complex antennas can be regarded as distributions of such elementary currents). The fields of such a source may be found readily by the method of images. When the current element is just above the surface, the fields in air are simply twice the homogeneous free-space fields. Because of symmetry the magnetic field is everywhere in the azimuthal direction  $\phi$  (see Figure 10-19), while the electric field on the surface is constrained by the boundary conditions to be strictly in the vertical direction  $z$ . In mks units the magnetic and electric fields at a distance,  $d$ , on the flat perfectly-conducting surface are, respectively,

# IONOSPHERIC RADIO WAVE PROPAGATION

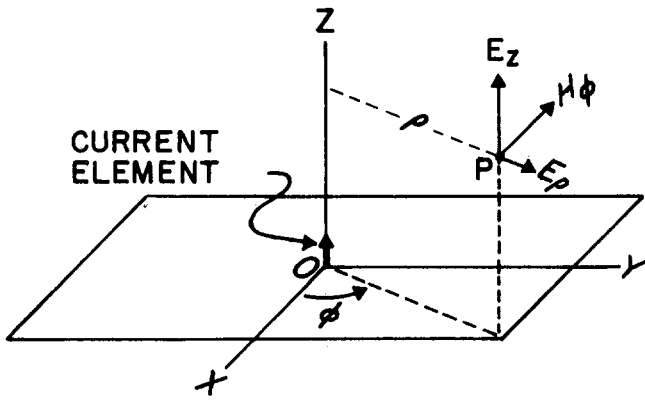


Figure 10-19. Vector field-components at a point P in a cylindrical coordinate system. The plane XOY represents the surface of the earth.

$$H_\phi = \frac{M(t')}{2\pi} \left[ \frac{1}{d^2} + \frac{i2\pi}{\lambda d} \right] \text{ At/m,} \quad (10.36)$$

$$E_z = -\frac{M(t')}{2\pi} \left[ \frac{1}{i^2 \epsilon_0 \omega d^3} + \frac{120\pi}{d^2} + \frac{i\mu_0 \omega}{d} \right] \text{ V/m,} \quad (10.37)$$

$$E_\rho = 0, \quad (10.38)$$

where  $t' = (t - d/c)$ ,  $\lambda$  is the vacuum wavelength ( $\approx 3 \times 10^8/f$  m),  $\epsilon_0$  is the permittivity of free space ( $= 8.854 \times 10^{-12}$  F/m), and  $\mu_0$  is the free space permeability ( $= 4\pi \times 10^{-7}$  H/m). The far-field components are related by

$$E_z = -Z_0 H_\phi \quad (10.39)$$

where  $Z_0$  is the impedance of free-space ( $\approx 120\pi$  ohm).

In a more realistic model, the plane earth is allowed to have finite conductivity  $\sigma$  and permittivity  $\epsilon$ . The solution of this boundary-value problem was given by Sommerfeld [1909] in terms of an infinite complex integral [see Stratton, 1941]. A more complex problem, that of an elevated dipole, was solved by Weyl [1919], who expressed the free-space field as a sum of plane waves that reflected at the earth's surface in accordance with the Fresnel formulas. Norton [1941] and others have calculated numerical values from the formal solutions. Height variations of the fields are shown in Figure 10-20 for a source on a plane earth surface [Heckscher and Tichovolsky, 1981], and curves illustrating groundwave field amplitudes along the surface are given in Figure 10-21 for both plane and spherical earth models.

A type of groundwave, the Zenneck surface wave, has fields expressed exactly in simple closed forms. Although the Zenneck wave is important historically and conceptually, it is generally difficult to excite because of its rather slow decay with height. In fact, the excitation of a pure

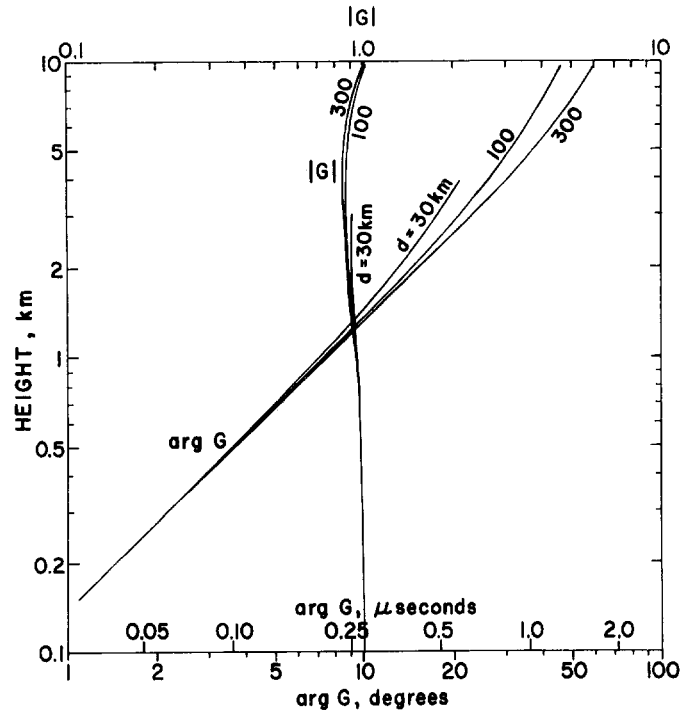


Figure 10-20. Height variations in the amplitudes and phases of 100 kHz groundwave fields for a source on a plane earth. Values are shown at distances of 30, 100, and 300 km, for propagation over fresh water,  $\sigma = 10^{-3}$  S/m,  $\epsilon/\epsilon_0 = 80$  [Heckscher and Tichovolsky, 1981].

Zenneck wave, without any radiation field, requires an infinitely long source distribution [Hill and Wait, 1978].

For a finitely conducting earth, Equation (10.39) is still true approximately, but the radial electric field component  $E_\rho$  has a finite value related to the loss of wave power into

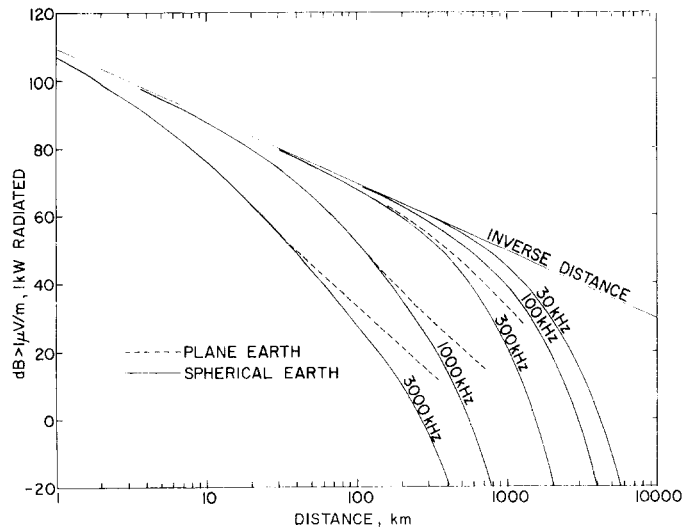


Figure 10-21. Long wave groundwave field amplitudes as a function of distance over plane and spherical earths, for propagation over good earth,  $\sigma = 10^{-2}$  S/m,  $\epsilon/\epsilon_0 = 20$ .

## CHAPTER 10

Table 10-4. Ratio of groundwave radial and vertical electric fields for various earth surfaces and 100 kHz.

SURFACE TYPE	$\sigma$ (S/m)	$\epsilon/\epsilon_0$	$E_\rho/E_z$
Perfect Conductor	$\infty$	—	0
Sea Water	4	80	0.00118  44.99°
Good Soil	$10^{-2}$	20	0.0236  44.66°
Fresh Water	$10^{-3}$	80	0.0713  32.89°
Poor Soil	$10^{-3}$	10	0.0745  43.25°
Thick Ice	$2 \times 10^{-5}$	5	0.403  14.76°

the ground. The ratio of the radial and vertical electric fields at the surface is given by

$$E_\rho/E_z \approx \sqrt{(1 - 1/p)/p}, \quad (10.40)$$

where

$$p \cong \epsilon/\epsilon_0 - i\sigma/\omega\epsilon_0. \quad (10.41)$$

Starting just below the surface of the assumed uniform earth,  $E_\rho$  and  $H_\phi$  decrease exponentially with depth. The fields are  $1/e$  of their values on the surface at the "skin depth"  $\delta$ , which may be estimated from

$$\delta = -\frac{c}{\omega} \sqrt{\frac{\epsilon_0}{\epsilon}} \frac{1}{\text{Im}(p/\sqrt{1+p})} \quad (10.42)$$

$$\approx 503/\sqrt{\sigma f} \text{ when } \arg p \approx -\pi/2. \quad (10.43)$$

Sample values of  $E_\rho/E_z$  are given in Table 10-4 for various earth surfaces at a frequency of 100 kHz, and Figure 10-22 shows skin depths over the long wave spectrum.

The magnetic field of the groundwave  $H_\phi$  may be sensed with a loop antenna having its axis parallel to the surface and perpendicular to the direction of propagation.  $E_z$  may

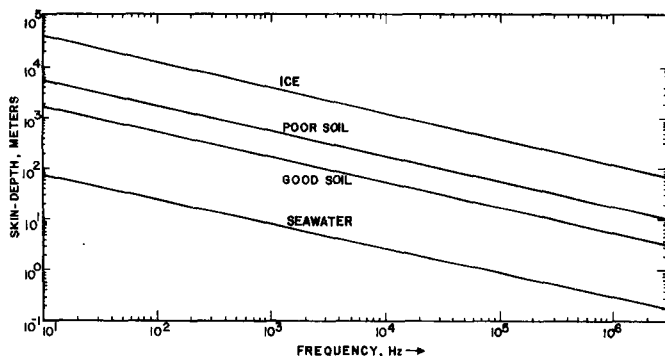


Figure 10-22. Long wave skin-depths for various earth surfaces.

be sensed with a vertical monopole antenna, or a vertical dipole. The radial component  $E_\rho$  may be sensed by a horizontal dipole with its axis in the direction of propagation. It follows from the principle of reciprocity that if a horizontal dipole on the earth is driven with RF current, a TM-polarized groundwave is radiated in directions along its axis. The fields produced by horizontal and vertical current elements have been discussed in mathematical detail by Wait [1954, 1957, 1961, 1971].

**10.2.1.2 Idealized Spherical-Earth Models.** A mathematical treatment of the groundwave on a smooth spherical earth of homogeneous, isotropic material was undertaken by Watson [1919] to determine if an atmospheric reflecting layer (ionosphere) was required to explain the large fields produced by distant transmitters. Such early theoretical analyses were handicapped by the poor convergence of the infinite series contained in the solutions. That difficulty was largely overcome by Van der Pol and Bremmer's [1938] "residue series" solution, which has become a basis for modern numerical analysis of the groundwave.

Figure 10-21 shows examples of field-strength vs distance curves for waves of selected frequencies propagating over "good soil," assuming a vertical source on the surface. The earth-curvature causes the wave amplitude to decrease with distance more rapidly than it would on a flat earth of the same material, but near the source the flat- and round-earth models give essentially the same fields.

One way to present both amplitude and phase data is in terms of the complex factor  $W$ , which is the ratio of the actual field component to an idealized one calculated as if the earth were flat and perfectly conducting. The flat earth propagation distance is taken to be the same as the curvilinear distance on the sphere. Figure 10-23 shows curves of  $W$  in the complex plane, for 100 kHz propagation over sea water and good soil.

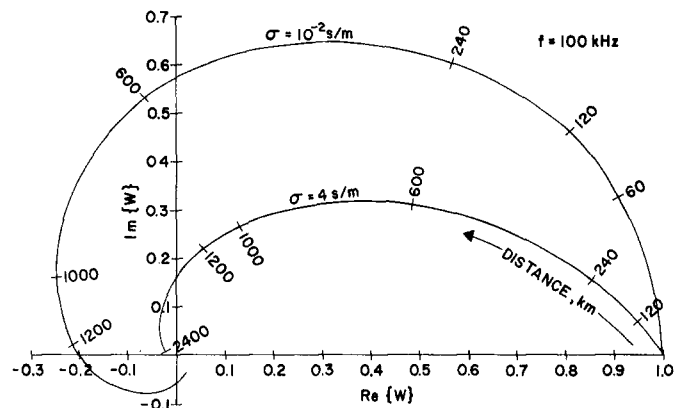


Figure 10-23. Complex values of the ratio  $W$  of actual groundwave field components and ones obtained assuming a flat, perfectly-conducting earth, for 100 kHz over sea water ( $\sigma = 4$  S/m) and good soil ( $\sigma = 10^{-2}$  S/m). Derived from Wait and Howe [1956].

**10.2.1.3 Models with Earth-Properties Gently Varying Along the Propagation Path.** Except for large bodies of water, the earth's surface is too uneven, both in electrical properties and in topology, to be represented well by the idealized models discussed above. However, if the earth's electrical properties and curvature do not vary much in a wavelength, the groundwave amplitude and phase can be approximated by the solution of an integral equation for  $W$  [Hufford, 1952]. The two-dimensional integral equation—the most general form—is valid provided, first, impedance boundary conditions can be applied; and second, terrain irregularities are not too severe.

A much simpler, one-dimensional, integral equation is more commonly used. It is derived by a stationary-phase integration that reduces the dimensionality of the general version; being an approximation, it is not valid for all terrain types, particularly at low frequencies where wave lengths and Fresnel zones have sizes comparable with terrain features. Field [1982a] compared solutions of the one- and two-dimensional equations to quantify the errors incurred by using the one-dimensional equation for terrain features narrower than a Fresnel zone. For a frequency of 100 kHz and on-path features narrower than about 10 km, the two-dimensional equation is needed to properly account for the signal's dependence on obstacle width, recovery at long distances, and transverse diffraction patterns. The one- and two-dimensional solutions approach one another far beyond wide terrain features.

Considerable error can be incurred at low frequencies by applying the one-dimensional equation, even for large terrain features. For example, for a path-length of 500 km, that equation overstates by a factor of about four the effect of an obstacle 6 km in diameter. It cannot give accurate results unless the diameter approaches a Fresnel zone width, which for this example is several tens of kilometers. However, because numerical solution of the two-dimensional integral equation is costly, its use has been limited to highly idealized irregularities. An alternate approach given by King and Wait [1976] obtains an equivalent one-dimensional model by averaging the terrain over the Fresnel zone.

If, instead of being homogeneous, the earth were comprised of layers of different conductivity and dielectric constant, it could still be characterized by a (frequency dependent) surface impedance, so that the integral equation for  $W$  can be formulated. Some progress has been made in this and other ways of estimating earth-constants for ground-wave phase prediction at 100 kHz, but uncertainties in these constants remain a major source of prediction error.

Special models of non-uniform terrain exist for which solution of the integral equation is unnecessary. Ground-wave propagation from land to sea, and vice versa, has been modeled with an earth having a sharp discontinuity of conductivity along a horizontal straight line. A useful approximate solution was given by Millington [1949] based on reciprocity arguments, and mathematical solutions have been given by Wait [1956] and Wait and Walters [1963].

Groundwave perturbations caused by hills have been studied with models having semielliptical bosses on otherwise smooth surfaces [Wait and Murphy, 1957, 1958]. In the electrostatic case, the vertical electric field at the summit of a hemispherical boss is exactly 3 times that on a flat plane, and for a semicylindrical ridge the factor is 2 times. This field-enhancement effect carries over (with modifications) to VLF groundwaves, and has been demonstrated experimentally [Harrison et al., 1971].

## 10.2.2 ELF Propagation

ELF propagation has been the subject of theoretical study for many years. The texts by Wait [1970], Galejs [1972] and Burrows [1978], along with review papers by Bernstein et al. [1974], Wait [1974 and 1977] and Bannister, [1980], provide comprehensive descriptions of the propagation characteristics of ELF waves. Much of the discussion that follows is based on a review paper by Bannister [1982].

ELF waves below a few hundred hertz propagate with little attenuation, penetrate well into lossy media and are very stable compared with higher frequencies. Nevertheless, ELF has limitations relative to conventional radio communication bands. Its restricted bandwidth allows only very low data rates, and because of the great wavelengths, ELF transmitting antennas are very inefficient (less than 0.5% is typical).

The energy of an ELF wave is confined principally to the waveguide that exists between the earth and the ionosphere. At ELF the effective height  $h$  of the waveguide is much less than the wavelength  $\lambda$  of the wave and the waveguide is below cut-off for all but the lowest order mode, the transverse electromagnetic (TEM) mode. On the other hand, at VLF the waveguide height exceeds the wavelength and several modes propagate. At LF the number of significant propagating modes may exceed 20.

The principal TEM fields are the vertical electric field  $E_v$ , and the horizontal magnetic field,  $H_h$ . Secondary field components arise because the surface impedance  $\eta_g$  of the ground—albeit small—is not zero; hence the term “quasi TEM” mode. The secondary fields are small compared with the principal fields, but are important because horizontal antennas would not radiate if the secondary fields were zero [Burrows, 1978].

Attenuation of the ELF quasi-TEM mode in the earth-ionosphere waveguide is low, on the order of 1 or 2 dB/Mm. The attenuation is caused mainly by power absorption in the ionosphere, since the surface impedance of the ionosphere is typically much larger than the surface impedance of the ground. That effect is evidenced in the expression for the waveguide attenuation rate  $\alpha$ , which is inversely proportional to  $h$ . That behavior indicates that the rate of power leakage from the guide is proportional to the field intensity at the surface, whereas the rate of power flow along the guide is proportional to the guide's volume. Thus, as

## CHAPTER 10

the guide's height decreases, the ratio of power leakage to total power flow increases [Burrows, 1978].

ELF attenuation is low enough to support very long-range propagation, and a planar model of the earth is inadequate if the path length exceeds the earth's radius. The most important effect of earth curvature is the closure of the guide, which allows the field to return to the source point after one complete encirclement. Therefore, the total field is the sum of the field arising from propagation over the shorter great-circle path from the source, and that arising from propagation over the longer one. The local effect of the curvature is small, however, and the wave propagates in the curved guide with nearly the same parameters as it would in a planar one.

The geomagnetic field interacts with the charged particles of the ionosphere to produce an anisotropic conducting medium. However, the electrical mismatch between the atmosphere and the ionosphere is large at ELF, and the transition between them abrupt, so the ionosphere acts much like a perfect reflector. The effect of the anisotropy is therefore small, and ELF attenuation and phase velocity depend only slightly on the direction of propagation.

**10.2.2.1 ELF Field-Strength Calculations.** The expressions most often employed for calculating ELF fields in the earth-ionosphere waveguide are based upon an idealized model that assumes the earth and the ionosphere to be sharply bounded and homogeneous. Experimental measurements of the waveguide properties at ELF have shown consistently that they can be represented accurately by formulas based on such a simple model. Complicated calculations that account for vertical structure of the ionosphere [Field, 1969 and Pappert and Moler, 1978] also confirm that the simple model is adequate for many purposes.

For the idealized model, the magnitude of the magnetic field of the signal from a horizontal dipole is approximately

$$|H| \sim Id\ell\Lambda \left[ \frac{k_o}{2\mu_o} \left( \frac{\omega\mu_o}{2\pi} \right)^{1/2} \right] \left( \frac{\rho/a}{\sin \rho/a} \right)^{1/2} \times \frac{10^{-\alpha\rho/2\pi \times 10^7}}{(k_o\rho)^{1/2}} \cos \phi, \quad (10.44)$$

where

$$\Lambda = \frac{\eta_g}{h\sqrt{\omega\mu_o c/\nu}} \quad (10.45)$$

is an excitation factor,  $\eta_g$  is the surface impedance of the ground,  $c$  is the speed of light,  $\nu$  is the phase velocity of the TEM mode and  $a$  is the radius of the earth.

There are six distinct factors in Equation (10.44): (1) the source strength  $Id\ell$  (2) the excitation factor  $\Lambda$ ; (3) a collection of free space parameters, all of which are known once the frequency is specified; (4) a spherical focusing factor; (5) the radial propagation loss factor, including both

the exponential decay due to absorption and the  $\rho^{-1/2}$  decay due to spreading; and (6) the directional dependence of the radiated field. Once the current moment  $Id\ell$ , angular frequency  $\omega$ , and coordinates  $\rho$ ,  $\phi$  of the field point are specified, only two parameters are left undetermined,  $\Lambda$  and the attenuation rate,  $\alpha$ . Both depend on the ionosphere.

Greifinger and Greifinger [1978, 1979], derived simple approximate expressions for ELF propagation constants that agree well with full wave numerical calculations. For daytime propagation, the approximate expressions for  $c/\nu$  and  $\alpha$  are

$$c/\nu \sim 0.985 \sqrt{h_1/h_o} \quad (10.46)$$

and

$$\alpha \sim 0.143f \sqrt{h_1/h_o} \left( \frac{\zeta_o}{h_o} + \frac{\zeta_1}{h_1} \right), \quad (10.47)$$

where  $h_o$  is the altitude where  $\sigma_1 = \omega\epsilon_o$ ;  $h_1$  is the altitude where  $4\omega\mu_o\zeta_1^2 = 1$ ;  $\zeta_o$  and  $\zeta_1$  are the conductivity scale heights at altitudes  $h_o$  and  $h_1$ , respectively; and  $\sigma_1$  is the conductivity of the ionosphere, which varies with altitude.

Equations (10.46) and (10.47) show that the phase constant depends primarily on the two reflecting heights and is nearly independent of the conductivity scale heights. On the other hand, the attenuation rate depends on the scale heights as well as the reflection heights.

A simple exponential fit to the ionospheric conductivity profile is given by Wait [1970] for determining propagation parameters:

$$\sigma_1(z)/\epsilon_o = 2.5 \times 10^5 \exp [(z - H)/\zeta_o], \quad (10.48)$$

where  $H$  is an (arbitrary) reference height. The corresponding values for  $h_o$  and  $h_1$  are

$$h_o = H - \zeta_o \text{Ln} \left( \frac{2.5 \times 10^5}{2\pi f} \right) \quad (10.49)$$

and

$$h_1 = h_o + 2\zeta_o \text{Ln} \left( \frac{2.39 \times 10^4}{f\zeta_o} \right). \quad (10.50)$$

Note that all heights are in kilometers.

**10.2.2.2 Theoretical and Measured ELF Propagation Constants.** It can be shown that the effective waveguide height of reflection is roughly  $h_o$ , rather than the higher reflecting height  $h_1$ . This is in excellent agreement with the effective reflection heights inferred from ELF propagation measurements [Bannister, 1975].

The most common values of  $H$  and  $\zeta_o$  employed in interpreting VLF daytime propagation measurements are  $H = 70$  km and  $\zeta_o = 3.33$  km. By using these values the values of  $h_o$ ,  $h_1$ ,  $c/\nu$  and  $\alpha$  can be determined readily at ELF.

## IONOSPHERIC RADIO WAVE PROPAGATION

Under nighttime propagation conditions, an E region bottom where the electron density increases very sharply is usually encountered below the altitude  $h_1$ . For a simple model that assumes the density above the E region bottom to vary slowly on the scale of the local wavelength, the propagation constant is [Greifinger and Greifinger, 1979]

$$c/v \sim \sqrt{h_E/h_0}, \quad (10.51)$$

and the attenuation rate is

$$\alpha \sim 0.143f \sqrt{h_E/h_0} \left( \frac{\zeta_0}{h_0} + \frac{1}{\pi k_0 n_E h_E} \right), \quad (10.52)$$

where  $h_E$  is the altitude of the E region bottom and  $k_0 n_E$  is the local wave number.

Nighttime ELF attenuation rates are plotted in Figure 10-26 for frequencies from 40 Hz to 1000 Hz. The calculated values were obtained using Wait's nighttime ionospheric conductivity model (with a reference height of 90 km and scale height of 2.5 km) in conjunction with Equations (10.51) and (10.52), and assuming the height of the E region bottom to be 90 km and its conductivity to be  $8 \times 10^{-6}$  S/m. Also plotted are various measured values of  $\alpha$ . Figure 10-26 shows that, for frequencies from 45 Hz to 800 Hz, there is excellent agreement between the theoretical and the measured values.

In addition to their very low attenuation rates, ELF radio waves below about 200 Hz can penetrate lossy media and retain usable strengths to substantial depths. Those features make them attractive for communicating over great distances to sub-surface locations. For example, even for sea water, with a conductivity of 4 S/m, the skin depth is about 36 m at a frequency of 50 Hz.

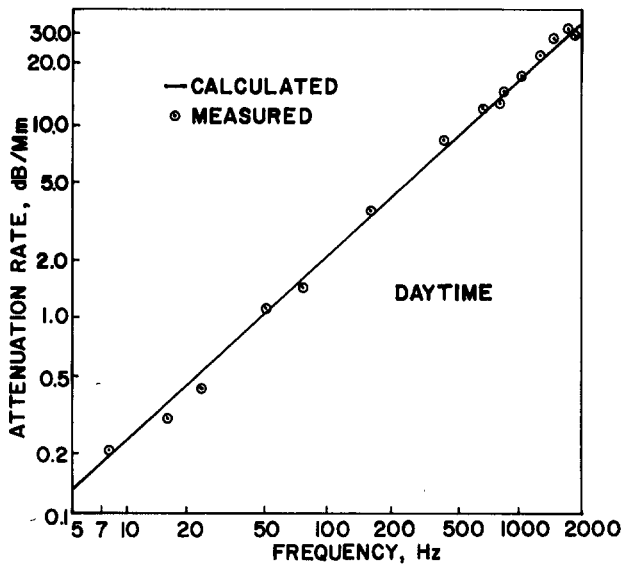


Figure 10-24. Calculated and measured ELF daytime attenuation rates [Bannister, 1982].

Theoretical values of ELF daytime attenuation rates are plotted in Figure 10-24 for frequencies from 5 Hz to 2000 Hz. Also plotted are values of  $\alpha$  determined from controlled source measurements [Bannister, 1982], or inferred from Schumann resonance measurements [Chapman et al., 1966]. Figure 10-24 shows that the agreement between the theoretical and measured values of ELF daytime attenuation rates is excellent.

Theoretical values of ELF daytime relative phase velocity are plotted in Figure 10-25 for frequencies from 5 Hz to 1000 Hz. Also plotted are various values of  $c/v$  determined from measurements of atmospherics. Figure 10-25 shows excellent agreement between the theoretical and measured values of  $c/v$  for frequencies above 50 Hz, and fair agreement for frequencies below 50 Hz.

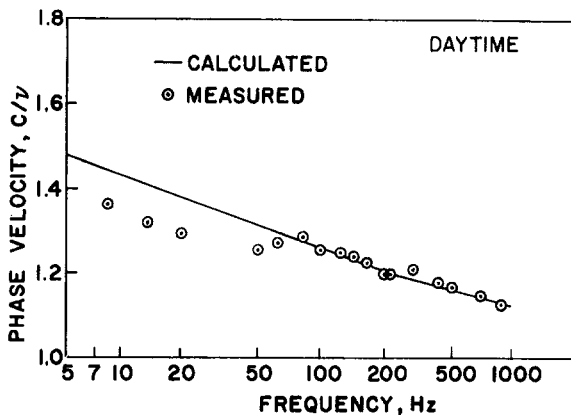


Figure 10-25. Calculated and measured daytime ELF phase velocities [Bannister, 1982].

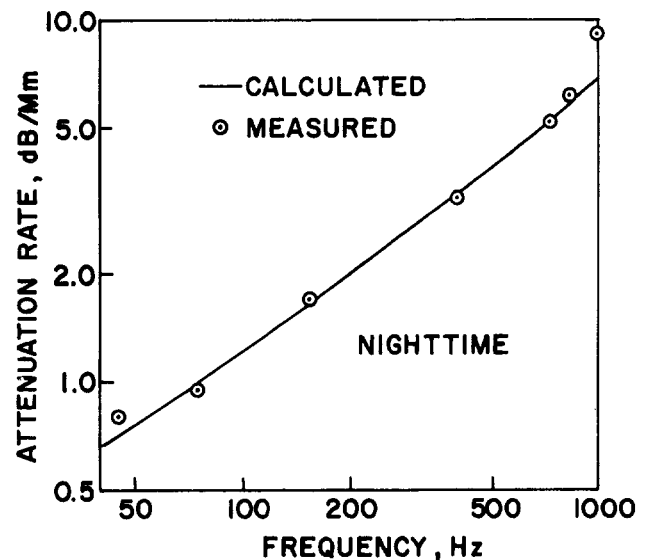


Figure 10-26. Calculated and measured ELF nighttime attenuation rates [Bannister, 1982].

## CHAPTER 10

**10.2.2.3 Anomalous ELF Propagation** Occasionally the nighttime field strengths measured at 40 Hz to 80 Hz have decreased by 4 dB to 8 dB in the northeastern United States [Bannister, 1975, 1980]. Those relatively severe nighttime fades sometimes occurred during the several days following magnetic storms, when similar (but less pronounced) behavior was found to coincide with phase disturbances on VLF paths across the northern United States. These short-path (~1.6 Mm) field strength reductions might have been caused by enhanced ionospheric ionization due to precipitating electrons from the radiation belts. However, attempts to correlate the fades with geomagnetic indices have met with limited success. Simultaneous measurements taken in Connecticut and the North Atlantic area during the magnetically quiet period of early March 1977 have indicated some of these anomalies might have been caused by a moving nocturnal sporadic E layer.

Calculations by Barr [1977] and Pappert and Moler [1978] show that nocturnal sporadic E can produce marked maxima and minima in the propagation characteristics of ELF radio waves. One physical explanation for the effect is interference between waves reflected from the normal E region and from the sporadic E region. Pappert [1980] showed that a sporadic E patch one square megameter in extent could account for the 6-8 dB fades that have been observed. Similarly, patches 0.5 Mm<sup>2</sup> in extent could account for the more commonly observed 3-4 dB fades.

Many other ionospheric disturbances can cause ELF propagation anomalies, including those associated with solar x-ray flares, energetic electrons, protons from solar particle events (SPEs) in the polar cap, and high-altitude nuclear bursts. The attenuation rate can increase easily by 1 or 2 dB/Mm relative to normal daytime conditions during such disturbances, depending on the wave frequency and severity of the disturbance, and certain moderate solar proton events can cause the attenuation rate to approach 4 dB/Mm at 75 Hz [Field, 1982b].

**10.2.2.4 Analysis of Laterally Non-Uniform Ionospheric Disturbances.** Most predictions of ELF fields in the earth-ionosphere waveguide have used a WKB method described by Pappert and Moler [1978]. To find E-fields along any particular radial from the transmitter, that method assumes the properties of the guide to depend only on distance from the transmitter. However, even such large inhomogeneities as sporadic E patches, the polar cap boundary, and the day/night terminator can cause the properties of the earth-ionosphere waveguide to change markedly over the huge wavelength, or Fresnel zone, of an ELF signal. Such inhomogeneities can cause lateral reflection, diffraction, and focusing of ELF modes. Those phenomena are usually unimportant at higher frequencies where the earth-ionosphere waveguide can be assumed to vary slowly in the lateral directions.

To handle such situations, Field and Joiner [1979, 1982] employed an integral equation approach for analyzing prop-

agation in the earth-ionosphere waveguide where conditions change over transverse distances comparable with a Fresnel zone. They derived an expression for the relative errors introduced by neglecting transverse ionospheric gradients over the path and found that the WKB method is inaccurate when the width of a disturbance is less than two thirds of the width of the first Fresnel zone. Further, the WKB approximation significantly overestimates the propagation anomaly when the disturbance is centered near the propagation path and underestimates the anomaly when the disturbance is centered far off path.

Strong localized disturbances behave like a cylindrical lens filling a narrow aperture. Lateral diffraction, focusing, and reflection cause the transverse electromagnetic (TEM) mode to exhibit a transverse pattern of maxima and minima beyond the disturbance and a standing-wave pattern in front of it. The focusing and diffraction diminish when the transverse dimension of the disturbance approaches the width of the first Fresnel zone, typically, several megameters. Reflection from widespread inhomogeneities can be important in two situations: first, for great-circle propagation paths that are nearly tangential to the boundary of the disturbed polar cap; and second, when the TEM mode is obliquely incident on the day/night terminator, in which case a phenomenon analogous to internal reflection can occur.

### 10.2.3 Long-Range VLF/LF Propagation

Very low and low frequency (VLF/LF) waves are reflected from the lowest regions of the ionosphere (the D region during daylight and the lower E region at night), and apart from the sunrise and sunset periods, exhibit propagation characteristics that are very stable in both phase and amplitude. The LF band (30–300 kHz) is useful for communications to distances ranging from hundreds to several thousand kilometers, shorter than the almost global ranges achievable at VLF but much longer than the groundwave distances normally associated with the MF band.

Beginning in 1911 with Austin, various empirical formulas, deduced from numerous measurements, have been used to estimate the field strengths of these long waves. For example, Pierce derived a semiempirical formula to describe VLF propagation over water during the day. That formula, which gives the vertical electric field strength at a distance  $d$  from a transmitter having a radiated power  $P$  (kw) at frequency  $f$  (kHz), is [Watt, 1967]

$$E(\mu\text{V/m}) = \frac{210 \sqrt{P}}{\sqrt{(\sin d/a)}} \exp[-0.2(d/a) f^{0.75}], \quad (10.53)$$

where  $a$  is the radius of the earth and the absorption term is the exponential.

Modern mathematical approaches for predicting the propagation characteristics of VLF/LF waves are formulated

## IONOSPHERIC RADIO WAVE PROPAGATION

in terms of a conducting spherical earth surrounded by a concentric electron-ion plasma (the ionosphere) into which waves are launched from a Hertzian dipole source. The application of Maxwell's equations and the appropriate boundary conditions allow the electromagnetic field to be calculated everywhere. In doing this the earth and the ionosphere can be regarded as forming a waveguide (without side-walls) in which propagation may be viewed either as a series of wave reflections (wave-hops), or by the mathematical equivalent—traveling wave modes. Generally, it is more convenient to apply the waveguide mode approach to the VLF and lower LF band, and the wave-hop approach to the higher LF band, as described below. In addition to the references cited under the specific topics that follow, more detailed descriptions of the features of VLF/LF propagation can be found in the works by Budden [1961], Wait and Spies [1964], Watt [1967], Pappert [1968], Wait [1970], Galejs [1972], Field et al. [1976], and the AGARD proceedings on long waves edited by Belrose [1982].

**10.2.3.1 Waveguide Modes.** In the waveguide-mode formulation for VLF/LF propagation an arbitrary propagating field is regarded as being composed of a series of modal patterns that propagate with characteristic phase velocities, little change in pattern shape, and gradually decreasing amplitudes. Generally, the more complex (or higher-order) modal patterns attenuate more rapidly: at great distances only the simpler (lower-order) modes may be important. The earth-ionosphere cavity exhibits such waveguide features as cut-off frequencies, and reflections from mismatched sections caused by abrupt changes in the electrical properties along its boundaries.

The field at a point in the waveguide depends on how strongly the various modes are excited, and upon their relative amplitudes and phases at the observation point. Although there is evidence of wave focusing in the vicinity of the point antipodal to the transmitter, typical field strength versus distance curves generally show a decreasing trend, upon which are superimposed local variations due to modal interference.

A transmitting antenna modeled by a vertical current-element produces transverse magnetic (TM) polarized waves, which have a magnetic field parallel with the earth's surface, while the electric field is perpendicular to the magnetic field and not quite vertical. For TM waves, the earth-ionosphere waveguide has a quasi cutoff frequency during the daytime at about 2 kHz. Figure 10-27 illustrates idealized TM wave vectors and mode patterns.

Airborne VLF/LF transmitting antennas with horizontal current elements excite transverse electric (TE) waves with horizontal electric fields, and magnetic fields in the vertical plane. Figure 10-27 illustrates idealized TE wave vectors and waveguide patterns. In general, TE fields are very small at the ground, and the modes are difficult to excite with groundbased transmitters.

Because of the presence of the geomagnetic field in the

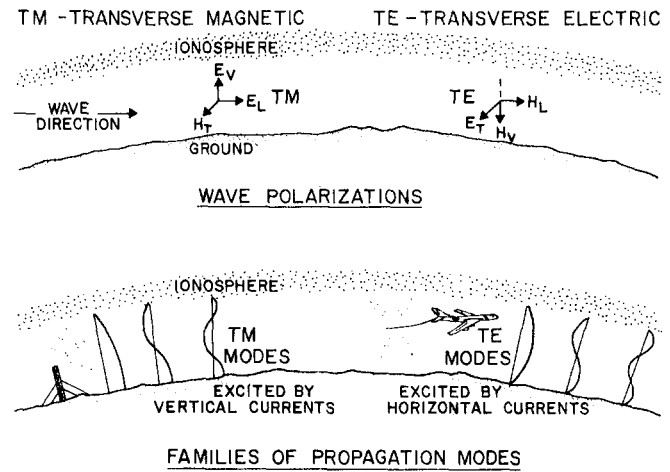


Figure 10-27. Characteristics of transverse magnetic (TM) and transverse electric (TE) waves [Kossey et al., 1982].

ionosphere, the TM and TE modes are not entirely independent, but are coupled. In general, when an electron acquires a velocity from the electric field of the wave the magnetic forces cause it to have a component of motion perpendicular to the electric field, thus causing polarization conversion. The interaction is described by the Appleton-Hartree equation (for example, see Ratcliffe [1959]), and the polarization conversion has been demonstrated experimentally (as reported by Bracewell, et al., [1951] Lewis, et al., [1973] among others). The coupling effect is most pronounced at night when the waves reflect higher in the ionosphere, where the electron-neutral collision frequency is smaller than the electron gyrofrequency.

**10.2.3.2 Waveguide Propagation Equations.** The detailed equations for VLF/LF waveguide propagation are described, for example, by Wait [1970], Pappert and Bickel [1970], Galejs [1972], and Field et al., [1976]. To illustrate the key dependencies and to define the commonly used notations, they are given here for the case when geomagnetic anisotropy (that is, polarization conversion) effects can be neglected. That approximation is fairly accurate for long-range VLF/LF propagation under normal daytime conditions.

### *Transverse Magnetic (TM) Modes*

Conventional ground-based VLF/LF transmitters are vertical and their fields are composed of a superposition of TM waveguide modes. Following Field [1982c] the vertical electric field is given by

$$E_v = -120\pi i \exp\left(-\frac{i\pi}{4}\right) \frac{I L \cos \psi}{\sqrt{\lambda d}} \sqrt{\frac{d/a}{\sin d/a}} \sum_j S_j^{3/2} \Lambda_j \exp\left(-\frac{\alpha_j d}{8.7}\right) \exp\left(-\frac{2\pi i}{\lambda} \frac{c}{v_j} d\right) G_j(h_T) G_j(h_R) \text{ V/m}, \quad (10.54)$$

## CHAPTER 10

where the subscript  $j$  denotes quantities associated with the  $j$ th TM mode,  $IL$  is the effective electric dipole moment of the transmitting antenna;  $\lambda$  is the free-space wavelength;  $d$  is the distance from the transmitter;  $a$  is the earth's radius; and  $c$  is the speed of light. Included is a factor  $\cos \psi$ —where  $\psi$  is the angle between the dipole orientation and the vertical—to account for inclined transmitting antennas ( $\cos \psi = 1$  for a vertical electric dipole). Although most quantities are in mks units, all distances ( $L, \lambda, d, a$ ) are expressed in megameters.

The quantity  $S_j$  is essentially the eigenvalue of the  $j$ th TM mode and must be computed numerically. At VLF, however,  $S$  has a magnitude close to unity, so the term  $S_j^{3/2}$  in Equation (10.54) does not appreciably influence the field. The magnitude of the vertical electric field depends on the state of the ionosphere through three parameters:  $\Lambda_j$ , the excitation factor for the TM mode;  $\alpha_j$ , the attenuation rate in decibels per megameter of propagation (dB/Mm); and  $G_j$ , the height gain function for transmitter and receiver heights  $h_T$  and  $h_R$ , respectively. The phase of the  $j$ th mode is governed by the relative phase velocity,  $c/v_j$ . These propagation parameters must all be computed numerically for model ionospheres having arbitrary height profiles.

### Transverse Electric (TE) Modes

Airborne VLF/LF transmitters use long trailing-wire antennas that radiate a complicated superposition of TM and TE modes. Here much of that complexity is avoided by considering broadside propagation, where the great-circle path connecting transmitter and receiver is perpendicular to the plane containing the inclined electric-dipole transmitting antenna. The vertical electric field produced by the vertical component of the inclined transmitting antenna is given by Equation (10.55). The broadside horizontal electric field produced by the horizontal component is given by

$$E_H = -120\pi i \exp\left(-\frac{i\pi}{4}\right) \frac{IL \sin \psi}{\sqrt{\lambda d}} \sqrt{\frac{d/a}{\sin d/a}} \sum_m S_m^{-1/2} \Lambda_m \exp\left(-\frac{\alpha_m d}{8.7}\right) \exp\left(-\frac{2\pi i}{\lambda} \frac{c}{v_m} d\right) G_m(h_T) G_m(h_R) \text{ V/m.} \quad (10.55)$$

The symbols are the same as in Equation (10.54), except that  $m$  denotes the  $m$ th TE mode.

**10.2.3.3 TE/TM Mode Structure.** Equations (10.54) and (10.55) show that each mode's contribution to the field is proportional to the product of four quantities: the excitation factor  $\Lambda$ , the transmitter height-gain function  $G(h_T)$ , the receiver height-gain function  $G(h_R)$ , and the propagation factor  $\exp(-\alpha d/8.7)$ . This section gives calculated values of these four quantities for a nominal ambient daytime ionosphere and an assumed ground conductivity of  $10^{-3}$  S/m.

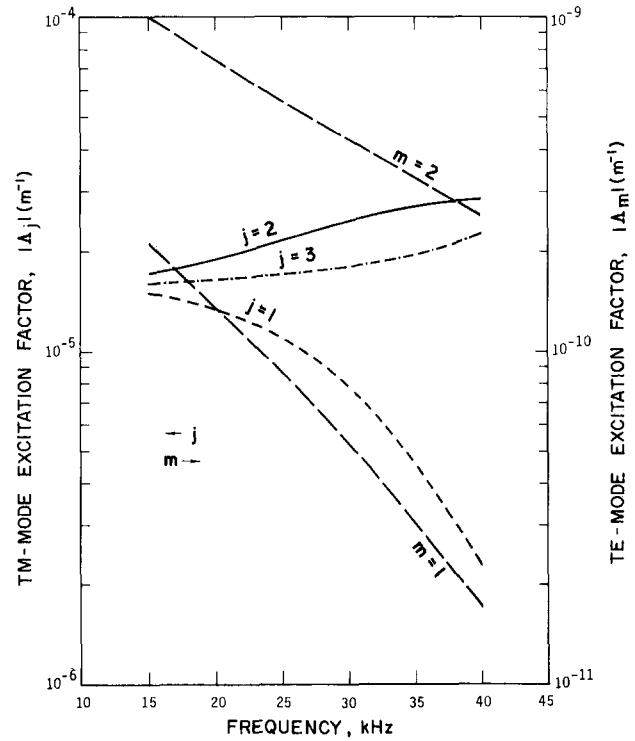


Figure 10-28. Excitation factors vs frequency for lowest three TM modes ( $j = 1, 2, 3$ ) and lowest two TE modes ( $m = 1, 2$ ); ambient day,  $\sigma = 10^{-3}$  S/m [Field et al., 1976].

### TE/TM Excitation Factors

Figure 10-28 shows the frequency dependence of the excitation-factor magnitudes of the first three TM modes and the first two TE modes. The first three TM modes are excited equally at the lower VLF frequencies, but above about 30 kHz the higher-order TM modes are much more effectively excited than the first one. The TE modes are excited much more poorly than the TM modes, by four or five orders of magnitude, as shown in Figure 10-28. The efficiency of TE mode excitation relative to TM mode excitation improves as the ground conductivity is reduced. For example, at 20 kHz the TE mode excitation factors are nearly two orders of magnitude greater for a  $10^{-5}$  S/m conductivity than for  $10^{-3}$  S/m. On the other hand, the excitation factor for the lowest TM mode is less by almost an order of magnitude if the conductivity is changed in the same fashion.

The excitation factors also depend on the state of the ionosphere. The excitation factors as defined here and shown in Figure 10-28 are inversely proportional to a quantity that becomes the "height of the ionosphere" in the limit of a sharply bounded ionosphere. For the diffuse ionospheres the excitation factors at the lower VLF frequencies are roughly proportional to the inverse of the average height at which important reflections occur. Thus, one would expect these factors to become somewhat larger under disturbed conditions.

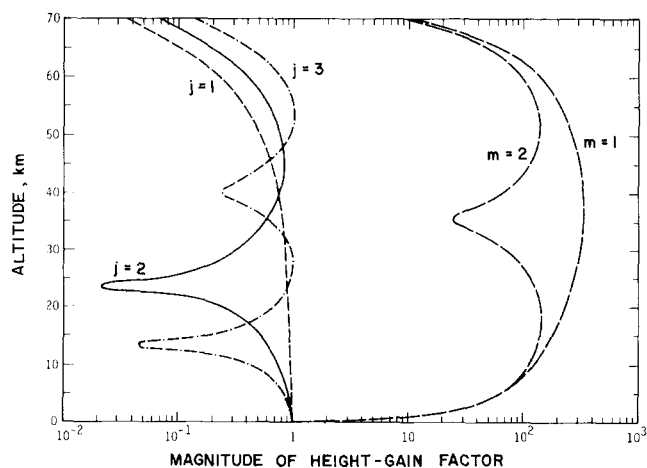


Figure 10-29. Height-gain factors for lowest three TM modes ( $j = 1, 2, 3$ ) and lowest two TE modes ( $m = 1, 2$ ): ambient day, 20 kHz,  $\sigma = 10^{-3}$  S/m [Field et al., 1976].

### TE/TM Height-Gain Factors

The height-gain factor of the waveguide mode accounts for the effects of non-zero transmitter and receiver heights. The transmitter and receiver height-gain factors for a given mode are identical and, therefore, are equal when the transmitter and receiver are at the same altitude. Figure 10-29 shows computed height-gain factors for the first three TM modes and first two TE modes for a frequency of 20 kHz. These height-gain factors exhibit the classic height-dependences for antennas over a highly conductive ground; the TM mode height-gain factors are of the order of unity over most of the waveguide, except for some rather sharp nulls; and, above a few kilometers, the TE mode height-gain factors increase sharply to values well in excess of one-hundred. For elevated antennas, the large TE mode height-gain factor mitigates the effects of the small excitation factor, and these modes can be excited about as effectively as TM modes.

At frequencies above about 30 kHz the first TM mode develops a broad maximum in its height-gain factor in the 40–60 km altitude range. Such “whispering gallery” behavior is not important for ground-based or airborne terminals, but may be significant for very high, balloon-borne, terminals operating at higher frequencies [Videberg and Sales, 1973].

### TE/TM Attenuation Rates

Figure 10-30 shows attenuation rates as a function of frequency for the first three TM modes and the first two TE modes. The higher order modes are more heavily attenuated than the lower, which often allows them to be neglected at VLF for long path-lengths. At the higher frequencies, the attenuation of the higher order modes can be mitigated by efficient excitation. Under normal conditions, therefore, it is usually necessary to retain many terms in the mode sums for frequencies throughout the LF band. In that case, geometric optics is often a more convenient approach to prop-

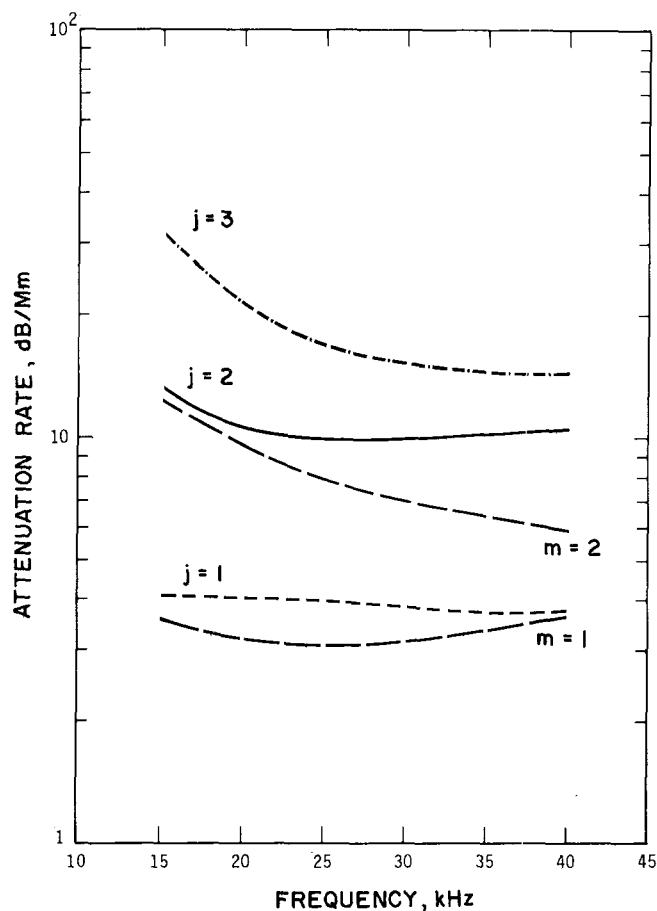


Figure 10-30. Attenuation rates vs frequency for lowest three TM modes ( $j = 1, 2, 3$ ) and lowest two TE modes ( $m = 1, 2$ ): ambient day,  $\sigma = 10^{-3}$  S/m [Field et al., 1976].

agation analysis than is mode theory. In intense disturbances, however, higher order modes are much more severely attenuated than lower, and the mode sum can be used well into the LF regime. Figure 10-30 shows that the first TE mode is slightly less attenuated than the first TM mode, although that result depends on the specific normal daytime conditions and ground conductivity assumed.

Figure 10-31 illustrates the ground conductivity dependence of the attenuation rates of the first TM and TE modes at 20 kHz. Results are given for normal daytime conditions and a moderate ionospheric disturbance, such as a solar proton event (SPE). The disturbance increases the attenuation rate of both polarizations over normal values. However, the TE attenuation rate is virtually independent of ground conductivity, whereas the TM rate exhibits a strong, broad maximum for conductivities between  $10^{-5}$  and  $10^{-4}$  S/m, where the TM eigenangle is near the Brewster’s angle of the ground. The TM mode propagates somewhat better than the TE mode for most common ground conductivities, but propagates much worse over low-conductivity ground, such as occurs throughout Greenland and much of Canada.

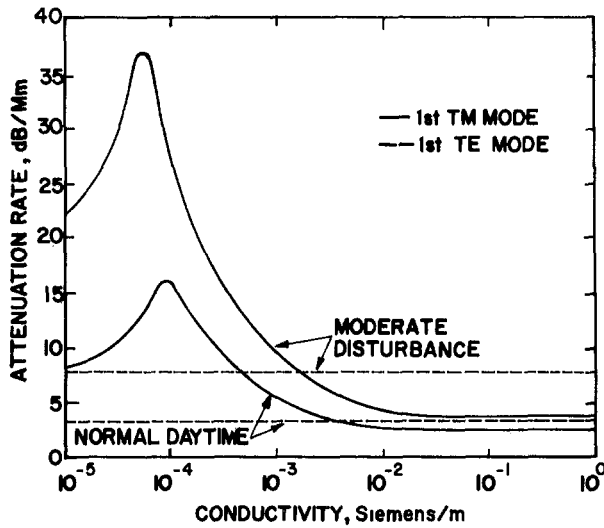


Figure 10-31. Attenuation rates of the lowest order TM and TE modes vs ground conductivity, for 20 kHz under normal daytime and moderately disturbed ionospheric conditions [Field et al., 1976].

Although these results pertain to a frequency of 20 kHz, curves for other frequencies exhibit the same general behavior. The main difference is that the Brewster's angle peak in the TM attenuation rate occurs at higher values of conductivity for higher frequencies, and vice versa.

Except for propagation over very low-conductivity ground, TE modes are more vulnerable than TM mode to degradation in disturbed ionospheric environments. In the VLF band, for example, the TE mode attenuation becomes prohibitive for intense disturbances, as illustrated in Figure 10-32.

*TE/TM Signal Strengths Versus Distance*

Figure 10-33 shows 20 kHz TE and TM signal strengths, computed as a function of distance for ambient and intensely disturbed ionospheric conditions. The curves provide a di-

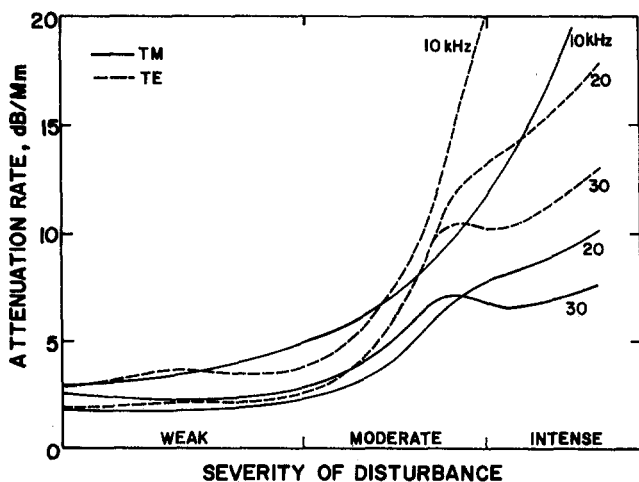


Figure 10-32. Attenuation rates of the lowest order TM and TE modes, for disturbed ionospheric conditions and a perfectly conducting earth [Field et al., 1976].

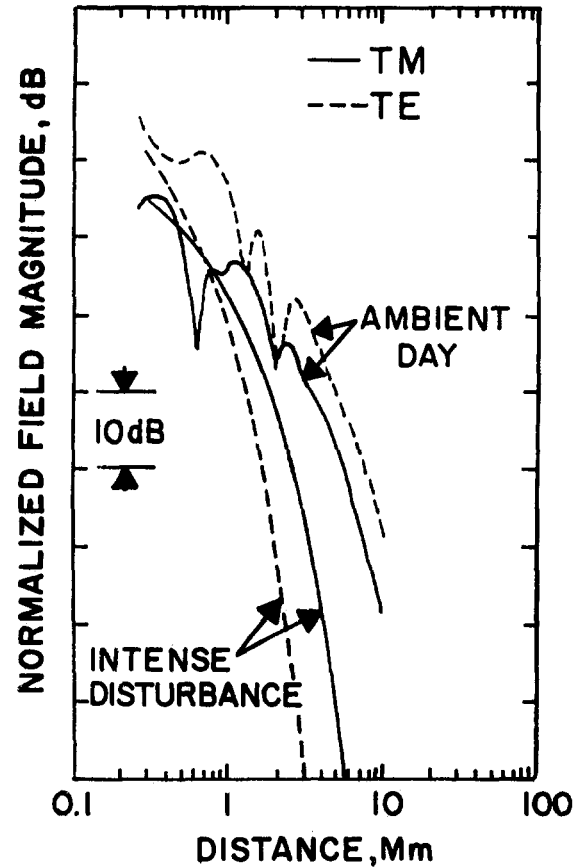


Figure 10-33. TE/TM signal strengths vs distance for ambient day and intensely disturbed ionospheric conditions: 20 kHz,  $\sigma = 10^{-3}$  S/m, 10 degree antenna inclination and transmitter and receiver at 12.2 km [Field, 1982c].

rect comparison of TE and TM polarized signals radiated broadside from a trailing-wire antenna inclined 10 degrees with respect to the horizontal. Both the transmitter and the receiver are assumed to be at an altitude of 12.2 km, and the propagation path is over poorly conducting earth ( $\sigma = 10^{-3}$  S/m).

In Figure 10-33 the ambient signals exhibit nulls and enhancements at ranges up to several megameters, caused by interference among several propagating waveguide modes. At greater distances, the higher order modes, which are more heavily attenuated than the lower order modes, diminish in importance and the signals fall off smoothly with distance. The curves also reveal several differences between signals in ambient and disturbed environments. First, and most important, if at least 2 or 3 Mm of the path are disturbed the disturbed signals fall well below the ambient signals. Such behavior is typical during strong solar proton events in the polar regions, and results when such widespread ionospheric disturbances depress the effective height of reflection in the ionosphere significantly. Second, mode interference patterns are nearly absent in disturbed environments, indicating that heavy attenuation of the higher order modes leaves only the lowest order modes to contribute

## IONOSPHERIC RADIO WAVE PROPAGATION

significantly to the signal strengths. Third, at ranges under approximately 1.5 Mm, the disturbed signals can be stronger than the ambient signals, because the disturbed environment increases the mode excitation factors but destroys interference nulls. However, if the disturbance covers most of the path, but not the transmitter and receiver, the attenuation rates increase but not the the excitations.

In Figure 10-33 the ambient TE signal is stronger than the TM signal at all distances, owing primarily to the relatively high transmitter and receiver altitudes and the nearly horizontal antenna orientation assumed in the calculations. Under the disturbed condition, the TE signal is more adversely affected than the TM signal and falls below it at most distances; however, as indicated by Figure 10-31, if the surface conductivity was reduced sufficiently, the TE signal would again become stronger than the TM signal.

**10.2.3.4 Numerical Modeling of VLF/LF Waveguide Propagation.** Numerous sophisticated computer programs have been developed for making VLF/LF field strength predictions. As described by Morfitt et al. [1982], the model developed at the United States Naval Ocean Systems Center (NOSC) is particularly attractive in that it incorporates (1) arbitrary electron and ion density distributions and collision frequency (with height), and (2) a lower boundary that is a smooth homogeneous earth characterized by an adjustable surface conductivity and dielectric constant. The model also allows for earth curvature, ionospheric inhomogeneity, and anisotropy resulting from the geomagnetic field. In addition, air-to-air, ground-to-air, and air-to-ground TE/TM propagation predictions can be made involving a horizontally inhomogeneous waveguide channel. The NOSC waveguide model can be used for computing long wave fields at fre-

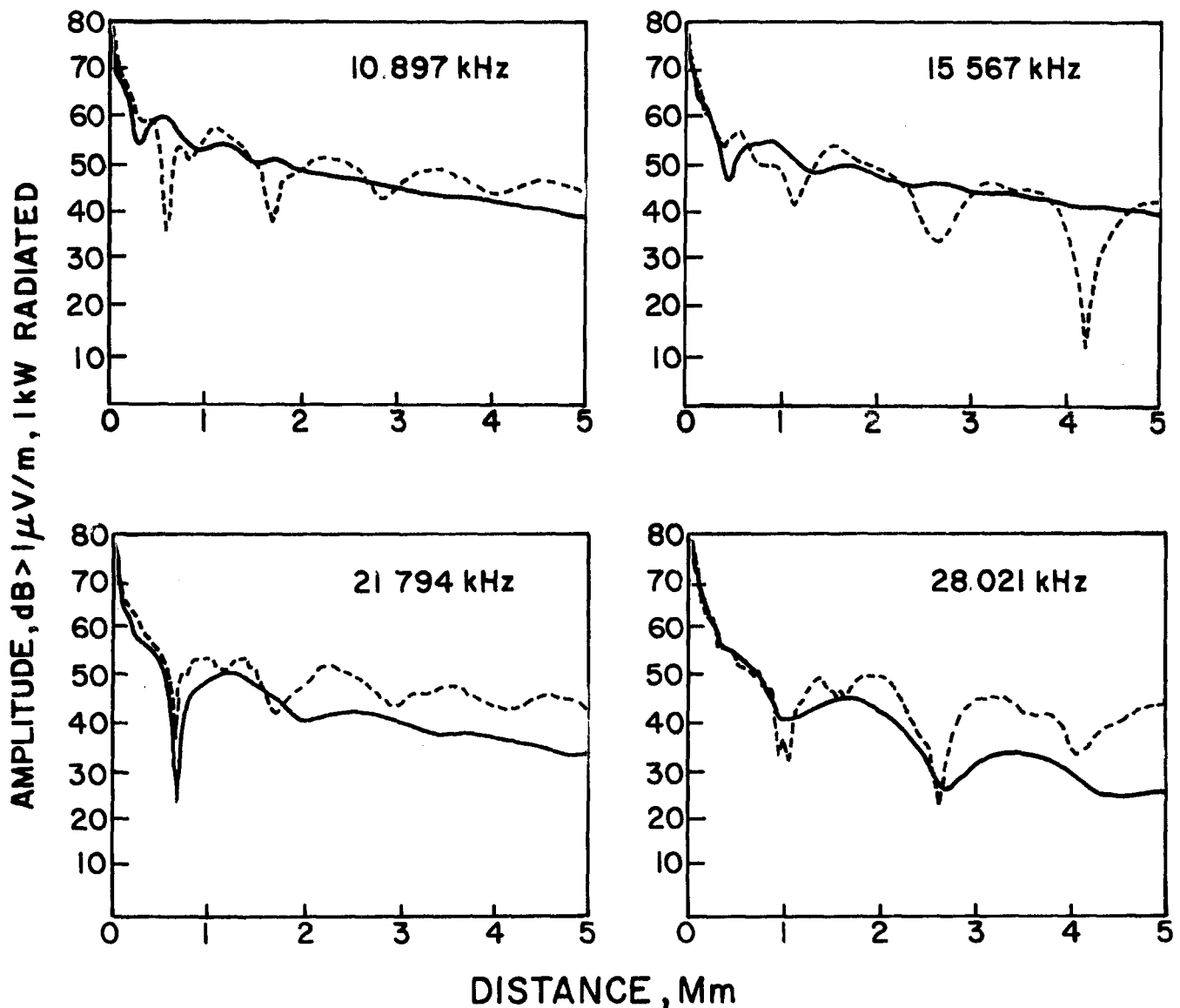


Figure 10-34. VLF signal calculations for a mostly seawater path from Hawaii to Sentinel, Arizona:—daytime,----nighttime [Morfitt, 1977].

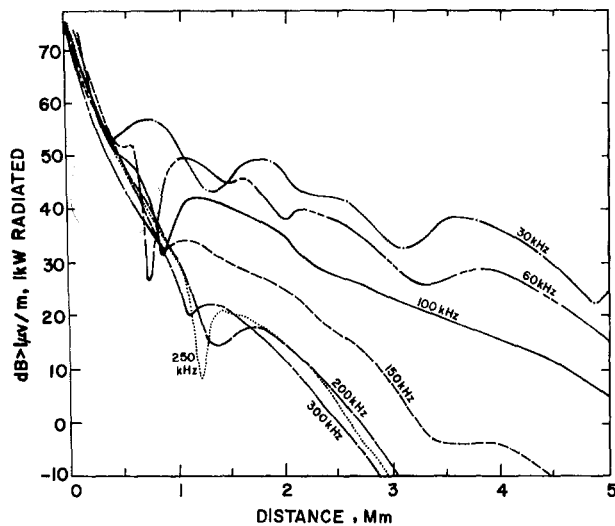


Figure 10-35. LF daytime signal calculations for midlatitude propagation [Pappert, 1981].

quencies as high as 300 kHz for daytime propagation [Pappert, 1981] and as high as 60 kHz for nighttime propagation [Morfit et al., 1982]. Figures 10-34 and 10-35 show representative TM signal strengths computed by NOSC for nominal daytime and nighttime models of the ionosphere appropriate for midlatitudes, and for propagation over water. At VLF, many of the propagation predictions have been validated by NOSC airborne measurements, such as those described by Bickel et al. [1970].

**10.2.3.5 Other VLF/LF Propagation Prediction Techniques.** In addition to the waveguide mode formulations a number of other mathematical techniques have been developed for describing the propagation of VLF/LF waves. These include the zonal harmonic or spherical wave analysis method [Johler, 1964, 1966] and the wave-hop method [Berry, 1964, and Berry and Chrisman, 1965]. The spherical wave technique has the attractive feature that it can model variations in height in the earth-ionosphere cavity, but it requires the use of large-scale, very fast, digital computers for its implementation. For the higher VLF and LF frequencies the wave-hop method requires the least computing time, but it has not been formulated in a way that lends itself to modeling of discontinuities in the earth-ionosphere duct [Jones and Mowforth, 1982].

In the wave-hop approach the field strength at any point is the sum of the groundwave (see Section 10.2.1) and a series of "hops," which represent waves that have been reflected from the ionosphere and/or the ground. The hops are numbered according to the number of times they have been reflected from the ionosphere. Each reflection results in a reduction in hop amplitude so that usually a relatively small number of hops are needed to provide good field-strength estimates. For VLF propagation at distances less than about 1000 km and for LF propagation, in general, the

number of hops required to describe the signal strengths are less than the number of waveguide modes that are required. The most general wave-hop formulations describe the propagation of TE/TM waves excited by an inclined dipole over a spherical earth with an anisotropic ionosphere [Lewis, 1970]. In addition to these sophisticated wave-hop techniques, other (simpler) approaches have been developed that provide good, quick, estimates of VLF/LF signal strengths, but without showing such propagation features as wave interference phenomena or polarization conversion effects [e.g., see Lewis and Kossey, 1975].

**10.2.3.6 VLF/LF Probing of the Ionosphere.** The propagation of long radio waves to great distances is controlled by the lowest regions of the ionosphere (usually the lower E region and the D region). As such, the variations in the amplitudes and phases of propagating long waves are very sensitive indicators of changes in the lower ionosphere. It is not surprising, therefore, that in addition to their uses for long-range communication and navigation long waves are used to assess the state of the lower ionosphere and as a tool for characterizing some of its properties.

Because of the extremely long wavelengths, ELF waves are affected by the electron and ion densities that are present over a very large range of altitudes. At night, for example, that altitude range can extend from below 50 km, to well up into the F region. Similarly, under disturbed conditions the electrons and ions at altitudes appreciably below 50 km can play an important (if not dominant) role in ELF propagation. However, owing to the difficulties involved in interpreting long-path ELF propagation data (which tend to represent an "average" of the state of the ionosphere), ELF has not been used extensively for ionospheric research.

The propagation of VLF/LF radio waves is controlled by the region of the ionosphere below about 90 km at night and below 75 km during the day. Unlike ELF, the observation of the signal characteristics of VLF/LF waves has provided a relatively simple ground-based technique for exploring the state and nature of the lower ionosphere. The technique has proven to be especially sensitive for monitoring ionospheric disturbances, such as those produced by solar x ray flares [for example, see Reder, 1969 and Kossey and Lewis, 1974], geomagnetic storms [Belrose and Thomas, 1968], electron precipitation events [Potemra and Rosenberg, 1973], ionospheric substorms [Svennesson, 1973], polar cap absorption events [Oelbermann, 1970], and high altitude nuclear bursts [Frisius et al., 1964 and Field and Engle, 1965]. The observation of continuous-wave transmissions over very long propagation paths has often been used for monitoring because such paths provide coverage over very large geographical areas. As with ELF, however, a disadvantage of such long path observations is that the effects of relatively localized disturbances are integrated, or smoothed-out, making it difficult to obtain information on the severity, extent, and structure of the disturbed region of the ionosphere.

Steep-incidence (that is, short-path) VLF/LF propagation techniques provide data on more localized regions of the ionosphere. However, with continuous-waves the direct and reflected components (groundwave and skywaves) overlap in space and time and can only be resolved indirectly by observing the interference pattern on the ground [Hollingworth, 1926] or by direct interpretation of diurnal phase and amplitude changes [Bracewell et al., 1951]. For example, the interference patterns produced by the ground-wave and skywave from a 16 kHz transmitter were used by Bracewell and Bain [1952] to first suggest the presence of two ionized layers well below the ionospheric E-region.

Phase and amplitude observations can be used to characterize the steep-incidence VLF/LF reflection properties of the lower ionosphere. Of particular interest is the use of the data to determine effective heights of reflection and effective plane wave reflection coefficients of the ionosphere [Bracewell et al., 1951]. Such experimental data can be compared directly with that obtained theoretically, using full-wave computational techniques in conjunction with electron density and collision frequency models of the ionosphere [for example, see Budden, 1961, Pitteway, 1965 and Inoue and Horowitz, 1968]. Thus, the experimental data can be used to validate theoretical models of the ionosphere, such as those obtained from the chemistry of the upper atmosphere. In addition the data can be used to develop and validate phenomenological models of the lower ionosphere, important for long wave propagation prediction [for example, see Bain, 1982].

More recently, with the advent of high-resolution VLF/LF pulse ionosounding [Lewis et al., 1973] it became possible to observe ionospheric reflections free of the ambiguities of the groundwave and skywave interference phenomena characteristic of continuous-wave measurements. The technique has been used to obtain a variety of steep-incidence reflection data at low-, mid-, and high geomagnetic latitudes [Lewis et al., 1973 and Kossey et al., 1974], and to investigate features of the C-layer of the daytime ionosphere [Rasmussen et al., 1980 and Rasmussen et al., 1982]. The technique provides a relatively direct means for determining VLF/LF ionospheric reflection heights and effective plane wave reflection coefficients, which then can be used to develop electron density models of the lower ionosphere [Kossey et al., 1983].

The inversion of steep-incidence VLF/LF reflection data to obtain electron density models of the lower ionosphere is not an easy task. Under quiet ionospheric conditions it is especially difficult, since usually the polarization conversion effects of the geomagnetic field cannot be ignored. Nevertheless, mathematical approaches that employ full-wave and iterative computational techniques have been developed and applied with some success [for example, see Shellman, 1970 and Field and Warber, 1984]. Under disturbed ionospheric conditions and certain daytime ambient conditions, when the VLF/LF reflections are controlled primarily by ionization below about 70 km, the effects of

the geomagnetic field are greatly diminished and the ionosphere can be assumed isotropic. Under such conditions the mathematical inversion problem becomes somewhat simpler. Field et al. [1983] have developed an inversion technique, appropriate for isotropic propagation, which has been used in conjunction with VLF/LF pulse reflection data to derive conductivity profiles of the severely disturbed polar ionosphere.

A problem with profiles calculated by inversion is that of nonuniqueness, which can be caused by either incompleteness of data or the nonlinear dependence of the reflected signal on the propagation medium. In addition, the profiles characterize narrow regions of the ionosphere, since the propagation data contain information about only those altitudes where the ionosphere interacts appreciably with the reflected wave.

The altitude constraints are even more severe if long path propagation data are used, rather than steep-incidence reflection data. Nevertheless, some effort has been devoted to deducing the structure of the ionosphere from long path data. As described by Crain [1970], the data in this case are the attenuation rates and phase velocities of the propagating waveguide modes, and the analysis is a trial-and-error technique effectively to find an ionospheric conductivity profile which provides a waveguide mode or wave hop structure that agrees with the observed distribution of radio field strength.

In essence the long-path technique is similar to the steep-incidence approach inasmuch as ionospheric reflection coefficients are calculated as an intermediate step in obtaining the mode constants. In order to synthesize the total field as measured, one has to take care to add in as many modes as contribute to the field. This can add a great deal of complexity to the application of the technique. Nevertheless, the technique has been applied with much success to develop phenomenological models of the lower ionosphere. Although such models may not be consistent in all respects with those derived from detailed analyses of the aeronomy of the upper atmosphere, they have found widespread application in long wave propagation prediction codes.

The results obtained by Bickel et al. [1970], Morfitt [1977] and Ferguson [1980] are especially noteworthy in that regard. They have performed detailed analyses of a large volume and a wide variety of VLF/LF propagation data and have derived analytic models of the lower ionosphere for propagation prediction. Those models are simply exponential height-profiles of conductivity, which can be specified by only two parameters, scale height and reference height. Following Wait and Spies [1964] the conductivity parameter,  $\omega_r$ , depends on the ratio of electron density to electron-neutral collision frequency, and is taken to be of the form  $\omega_r(z) = 2.5 \times 10^5 \exp(\beta(z-H'))$ , where  $z$  (km) is altitude,  $\beta$  is the inverse scale-height ( $\text{km}^{-1}$ ) and  $H'$  (km) is a reference height. The value of electron density  $N(z)$ , in electrons/cm<sup>3</sup>, is calculated as a function of height by the equation  $N(z) = 1.43 \times 10^7 \exp(\beta(z-H') - 0.15z)$ . The

## CHAPTER 10

Table 10-5. Suggested exponential profiles for use in long wave propagation prediction codes. Frequencies,  $f$ , are in kHz [Morfitt et al., 1982].

Seasonal-Diurnal Propagation Condition	$H'$ (km)	$\beta$ ( $\text{km}^{-1}$ )	Magnetic Dip ( $^\circ$ )
Summer day	70	0.5	90–75 (high latitudes)  (transition latitudes) <70 (middle latitudes)
Summer night	87	$0.0077f + 0.31$	
Winter day	74	0.3	
Winter night	80	$0.035f - 0.025$ ( $10 < f < 35$ )	
	Linear change between high and middle latitudes	$0.0077f + 0.31$	

collision frequency  $\nu$  (collisions/s) is given by  $\nu(z) = 1.82 \times 10^{11} \exp(-0.15z)$ . Table 10-5 gives exponential profiles, based on VLF/LF propagation data, which are suggested for use in long wave propagation prediction codes [Morfitt et al., 1982].

### 10.2.4 MF Propagation

At night medium frequency skywaves can propagate to considerable distances with relatively little attenuation, but during the day the skywaves are severely attenuated in passing through the ionospheric D-region, so that only the groundwave provides usable signals. Thus, during the daytime MF signals are very stable, while at night they are much less so owing to the variability of the lower E-region of the ionosphere, and to interferences between the groundwave and skywaves.

**10.2.4.1 MF Groundwave Propagation.** The propagation of MF groundwaves can be described using the techniques discussed in Section 10.2.1. Because of the shorter wavelengths, however, such factors as the earth's atmosphere (and hence, the effective radius of curvature of the earth), terrain elevation, conductivity changes, and trees and buildings along the propagation path usually influence MF groundwave characteristics to much larger extents than they do for VLF/LF waves. Most of these effects can produce strong local interference patterns in the amplitudes of MF groundwaves [Knight, 1982 and Hizal and Fer, 1982].

**10.2.4.2 MF Skywave Propagation.** Because there are so many factors that affect the characteristics of MF skywaves, it is difficult to draw a representative set of propagation curves. These factors include the losses associated with an imperfectly conducting earth at the transmitter and receiver, polarization coupling losses that depend on the geomagnetic field, ionospheric absorption losses, and losses

associated with ground-reflections on multi-hop paths (see Figure 10-36). The problem is further compounded in that the ionospheric absorption losses alone show significant short-period and day-to-day variations, as well as diurnal, seasonal, latitudinal, and solar-cycle effects [Knight, 1982].

A number of techniques have been developed to estimate MF field strengths. A relatively simple technique, based on an empirical formula has been adopted by the CCIR [CCIR, 1978]. A more complex wave-hop method has also been developed by Knight [1975]. Figure 10-37 shows computed ionospheric losses over the 500-1500 kHz band for single-hop paths at mid- and low geomagnetic latitudes. In the auroral zones the ionospheric losses are somewhat greater than those shown in the figure, and the estimates do not apply if the waves penetrate the E-layer and are reflected by the F-layer. The latter is most likely to occur at frequencies above 1500 kHz [Knight, 1982].

**10.2.4.3 Effect of MF Waves on the Ionosphere.** Even relatively small electromagnetic fields impart appreciable energies to the electrons in the ionosphere causing their temperatures, and consequently their thermal velocities, increase. This increases the effective electron-neutral collision frequency; as a result, the complex dielectric constant of

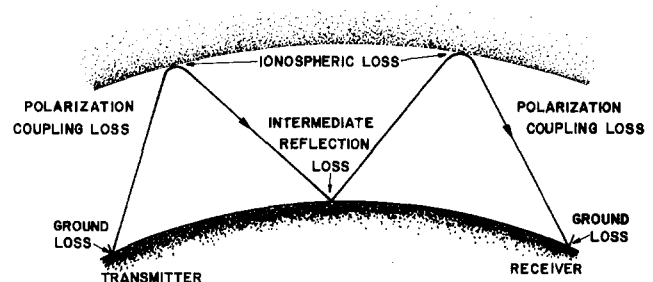


Figure 10-36. Losses associated with MF skywave propagation [Knight, 1982].

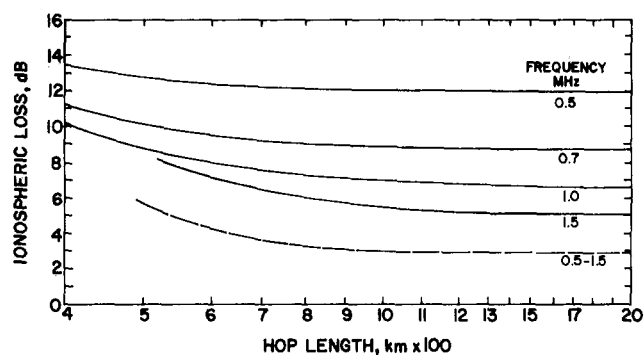


Figure 10-37. Computed MF ionospheric reflection losses:—east-west propagation at all latitudes,---north-south propagation at the magnetic equator [Knight, 1982].

the medium becomes appreciably dependent on the field. Thus, the associated physical processes, and the differential equations which describe the radio wave propagation in the ionosphere, become non-linear. This gives rise to various phenomena, including cross-modulation and de-modulation which, in principle, can be observed experimentally. The effects depend on wave frequency and the collision frequency and are such that they have been mainly observed in the MF band, particularly at night.

The main influence of the non-linear effects on the properties of radio waves reflected from the ionosphere manifest themselves through self-interference of the wave; that is, its influence on itself, and the interaction between a number of waves. These waves can be of the same frequency, or two independent modulated or unmodulated waves of different frequencies. An early observation of such an effect, the so-called Luxemburg effect, was reported by Tellegen [1933] who noted that the signal received in Holland from a 650 kHz Swiss station appeared to be modulated by the signals from a powerful station at Luxemburg (252 kHz). This phenomenon of cross-modulation has been found to be quite common when the unwanted, or disturbing, station is situated near the transmission path of the wanted wave [see Davies, 1969 and Al'pert, 1960].

Although the phenomenon of ionospheric cross-modulation or Luxemburg effect was discovered accidentally, it has been systematically investigated ever since its discovery. The motives of the earliest theoretical and experimental investigations were interest in the effect itself and the possible use of the effect for probing the ionospheric regions in which the cross-modulation occurs [Fejer, 1970]. In the latter case techniques have been developed to obtain D-region parameters such as electron density and collision frequency profiles.

Another MF probing technique, the "partial reflection" experiment, has proven to be a valuable method for obtaining quantitative measurements of electron distributions in the lower ionosphere. It has been one of the most extensively employed techniques for synoptic studies of the ionosphere below 100 km [Belrose, 1970, 1972].

## 10.2.5 Long Wave Propagation Through the Ionosphere

Electromagnetic waves cannot propagate in an ideal plasma unless the wave frequency is less than the plasma frequency, or approximately  $8980 N$ , where  $N$  is the number of electrons per cubic centimeter. Thus, a density only slightly more than  $1 \text{ el/cm}^3$  would suffice to completely reflect a 9 kHz wave. The well-known "whistler" phenomenon, however, demonstrates that under certain conditions long waves can penetrate even through the F-max region of the ionosphere, where the electron density is one hundred thousand times larger than would produce complete opacity if the ionosphere were a simple plasma. The long wave ionospheric transmission window is due to the geomagnetic field of the earth, which constrains the electron motion produced by electromagnetic waves incident on the ionosphere. As such the magnetic field provides a propagation mechanism.

The term "whistler" refers to an audio-frequency phenomenon associated with lightning discharges in the lower atmosphere. Electromagnetic energy at audio frequencies emitted by such discharges propagate in the ionosphere in a highly dispersive manner. The higher frequencies travel faster than the lower ones with the result that the signal, which was originally impulsive, is received over a relatively long time interval with the frequency generally descending with time (hence, a whistling sound).

Extensive studies have been made to determine the properties of whistlers [for example, see Storey, 1953, Ratcliffe, 1959, Pitteway, 1965 and Helliwell, 1965]. Their results [Watt, 1967] show that from the complete expression of the Appleton-Hartree equations for the refractive index, approximate expressions can be developed which give insight into the nature of the whistler mode. For example, the energy transmitted through the ionosphere is well-coupled to the whistler mode when the direction of propagation is in the same direction as the earth's magnetic field. For transverse propagation, this coupling is very poor. Also, the coupling is increased for sharp gradients of refractive index at the ionosphere boundary. When collisions are included, there is a finite range of angles between the wave normal and the direction of the earth's magnetic field for coupling to the whistler mode. In an anisotropic ionosphere, the wave normal and the direction of energy flow along the field lines are different depending upon the magnitude of the refractive index and the static magnetic field. If ducts of ionization that are aligned with the earth's magnetic field exist, the waves can be guided in them.

VLF signals from terrestrial transmitters have been observed at satellite altitudes [Leiphart et al., 1962], and have been tracked from ground level to altitudes of 500 km or more [Orsak et al., 1965 and Harvey et al., 1973]. Such probes showed that the polarization changes from linear to circular as the wave penetrates the ionosphere, and that very significant delays in the signals occur.

Such phenomena can be calculated using full-wave tech-

## CHAPTER 10

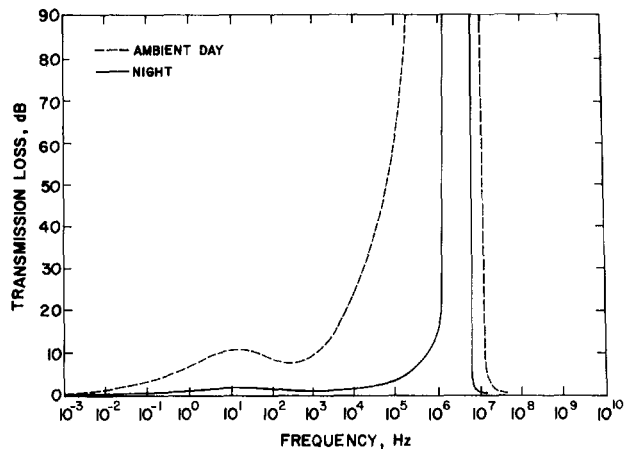


Figure 10-38. Computed long wave transmission losses through ambient day and night ionospheres [Booker et al., 1970].

niques [Pitteway, 1965] or WKB methods [Booker et al., 1970], in conjunction with appropriate models of the ionosphere. Figure 10-38 gives computed long wave transmission losses for plane waves incident on the ionosphere in a direction parallel to the geomagnetic field. The results are representative of those expected for ambient ionospheric conditions at mid- and high geomagnetic latitudes. Under disturbed conditions or at very low geomagnetic latitudes the penetration losses are much more severe, especially for frequencies above a few kilohertz [Booker et al., 1970 and Harvey et al., 1973].

### 10.3 IONOSPHERIC MODELING

For successful radio communication, it is essential to predict the behavior of the ionospheric region that will affect a given radio communication circuit. Such a prediction will identify the time periods, the path regions and the sections of high frequency bands that will allow or disrupt the use of the selected high frequency communication circuit. This need for prediction leads to modeling of the ionosphere.

A model is a numerical statistical description of the ionosphere in terms of location (geographic or geomagnetic latitudes and longitudes), time (solar zenith angle), seasons, and other factors such as the solar activity (10.7 cm flux, sunspot number). The empirical equations are derived from the dependence of the observed phenomena on variables mentioned above. These observed phenomena include: the behavior of critical frequencies\*  $f_oE$ ,  $f_oF1$ ,  $f_oF2$ , and  $f_oEs$  for the E, F1, F2, and sporadic E layers; the altitudes ( $h_mE$ ,  $h_mF1$ , and  $h_mF2$ ) for peak (maximum electron densities for

\*The critical frequency is the limiting radio frequency below which a radio wave is reflected by, and above which it penetrates and passes through, the ionized medium (an ionospheric layer) at vertical incidence.

the layers, and the half-thickness widths\*\*  $y_mE$ ,  $y_mF1$ ; and  $y_mF2$ . These models are called phenomenological models [Barghausen et al., 1969; Bent et al., 1972; Ching and Chiu, 1973; Chiu, 1975; and Kohnlein, 1978].

The ITS-78 model [Barghausen et al., 1969] based on the analysis by Jones et al. [1966] of world-wide, ground based ionosonde data, predicts only the bottomside of the ionosphere. The Bent model [Bent et al., 1972] predicts the total electron content of the ionosphere in the altitude range from 150 to 2000 km, without a direct consideration of the bottomside E and F1 layers. The Ching and Chiu [1973] model covers the altitude range from 110 to 1000 km. Instead of parabolic layers [Barghausen et al., 1969] they assume Chapman functions for the electron density distributions in the E, F1, and F2 layers. Later Chiu [1975] modified the Ching-Chiu model to incorporate the polar ionosphere. Their models are useful only for studying the large scale phenomena such as global thermospheric and ionospheric calculations.

Using ionospheric data from ESRO satellites, Kohnlein [1978] extended the altitude range up to 3500 km. He suggested a "differential approach" for the ionospheric modeling. He separated small scale spatial structures such as the equatorial trough, the midlatitude trough and the polar ionosphere, from the large scale global structure. He modeled these individual structures and added them into the global structure. His method reduces the number of coefficients otherwise needed to model the complicated ionospheric behavior.

The other approach for ionospheric predictions is to use theoretical models [Stubbe, 1970; Strobel and McElroy, 1970; Nisbet, 1971; Oran et al., 1974; and Oran and Young, 1977]. These are based on the physical processes responsible for the production, maintenance and decay of the ionosphere. A theoretical model would thus rely on the process of ionization of neutral atmospheric constituents by the incident solar extreme ultraviolet radiation, the transport processes such as diffusion and neutral winds, and also on the effect of electric and magnetic fields on the transport processes. Essentially the theoretical model tries to explain the experimental observations in terms of known physical processes. In addition, this approach seeks new physical processes to explain the differences between the observational results and the predictions based on the theoretical considerations.

Radio communication can be divided in two main categories. Ground-to-ground radio communication is based on the reflection and scattering characteristics of the ionospheric layers. On the other hand, ground to satellite, satellite to ground, or satellite to satellite radio communications depend on the transmission and refraction characteristics of

\*\*The half-thickness width  $y_m$  of the ionospheric layer is determined with the assumption that the layer has a parabolic shape [Appleton and Beynon, 1940].

the ionosphere. The main goal of any modeling effort is to predict the periods of good or poor radio communications for the selected paths to enable a continuous uninterrupted communication through the ionosphere or by some other means.

We will consider several ionospheric models that are routinely used (or are available) for the prediction and specification of the ionosphere. The emphasis here is on acquainting the user with the modeling programs and their limitations. We do not attempt to review the scientific literature for a determination of the state of the art of modeling efforts. Therefore only the essential references will be cited.

First, we will consider the numerical-phenomenological models. Then we will consider the theoretical models. This will be followed by the modifications to models to take into account high latitude phenomena such as the auroral E layer and the midlatitude F region trough. In the concluding section, we will look at the limitations of these models and a possible approach to overcome these limitations.

### 10.3.1 The Numerical-Phenomenological Models

At present the three most widely used numerical models for ionospheric predictions are (1) The ITS-78 model, (2) The Bent model, and (3) the *Ionospheric Communications Analysis and Prediction Program* (IONCAP). In addition, the 4-D model of the Air Force Global Weather Central and the Bradley model will be considered. We will also look at the International Reference Ionosphere-IRI 79.

**10.3.1.1 The ITS-78 Model.** The main purpose of this model [Barghausen et al., 1969] is to predict long term performance of communication systems operating in the 2–30 MHz frequency range. The ITS-78 model and its computer program was developed by the Institute of Telecommunication Sciences, ESSA, Boulder, Colorado. The model is based on the presentation of the ionospheric characteristics in a form of synoptic numerical coefficients developed by Jones and Gallet [1960] and improved by Jones et al. [1966]. The important features of the ITS-78 model are the parameters for the D, E, Es (sporadic), and F2 layers of the ionosphere.

The model provides (output) circuit operational parameters such as the maximum usable frequency (MUF), optimum traffic frequency (FOT), and the lowest usable frequency (LUF). In addition to the regular E-layer propagation mode, it takes into account propagation via the sporadic E layer. The program computes all the probable modes. It computes the system performance. For that purpose it calculates the antenna patterns and gains for 10 most commonly used antennas. It also has a program to determine MUF as a function of the magnetic activity index  $K_p$ .

The inputs for the ITS-78 model are the date, Universal

Time, geographical location (latitude and longitude) of the transmitter and receiver, and sunspot number. To compute the system performance the model needs the antenna parameters, the radiation power of the transmitter, and the signal to noise ratio of the receiver.

For the D region the model considers only the absorption losses. The non-deviative absorption is in the form of a semi-empirical expression. It enables the user to compute the losses for the HF frequencies penetrating the D layer. The deviative absorption losses are included in the loss calculations as uncertainty factors.

For the E region the model computes the parameter foE. It assumes a constant height of 110 km for the maximum (peak) electron density of the E layer, with a constant semi-thickness of 20 km. The numerical coefficients for foE are based on the experimental ground ionosonde data during high solar activity phase in 1958, and the low solar activity phase in 1964.

For the F2 region the model computes the parameters foF2, the height of maximum electron density  $h_mF2$  and the semi-thickness  $y_mF2$  of the F layer. These are in the form of numerical coefficients for the high (1958) and low (1964) phases of the solar activity. Both the E and F2 layers are assumed to be parabolic in shape.

The sporadic E (Es) layer could be very helpful or harmful to radio communications depending on the nature of the Es layer. A blanketing, totally reflecting Es layer extends the frequency range of the E-mode communications. However a semi-transparent or partly reflecting Es layer would cause serious multipath and mode interference and would be detrimental to communication systems. Using numerical coefficients, the ITS-78 model computes foEs only for the ordinary ray. (The earth's magnetic field splits the incident ray into the ordinary and the extraordinary rays.) The numerical coefficients are for both the high (1958) and low (1964) phases of solar activity. As the model does not predict the occurrence of Es, the foEs maps are used only when propagation via regular E layer is not possible. To compute the system performance, the model incorporates three kinds of noise: galactic, atmospheric, and manmade.

To determine the operational parameters such as the maximum usable frequency (MUF), the model computes the path geometry (between the transmitter and the receiver). The parameters computed in the path geometry are the path length, path bearing (azimuth), and the solar zenith angle  $\chi$  of the sun. The model computes paths for reflections from E, Es, and F2 layers. These are called the E, Es, and F2 modes. The paths could involve more layers (multiple modes) and more reflections (multihop).

To determine wave propagation the electron density distribution with altitude is needed. Both the E and F layers are assumed to have parabolic shapes. The maximum usable frequency (MUF) is obtained by multiplying the critical frequency of the layer by the MUF factor  $M(3000)$ . The term in parentheses refers to the standard ground distance

## CHAPTER 10

of 3000 km between the (hypothetical) transmitter and the receiver. The experimental data for the numerical factor  $M(3000)$  (in terms of coefficients) come from 13 ionosonde stations covering the geomagnetic latitude range from  $71^\circ\text{S}$  to  $88^\circ\text{N}$ .

The stability and predictability of the E layer results in a 99% probability (highest) of supporting radio propagation and communication via the E layer. The next highest probability is via the regular F layer. When neither of the above modes is possible, the Es mode is considered for communication.

For computing the system performance the program allows a selection from 10 antenna patterns. The program takes into account the ground losses, ionospheric losses, free space losses, and the excess losses. The program computes the radio communication circuit reliability, service reliability, and the multipath evaluations.

The ITS-78 model has several limitations. The results from the model are useful only when the operating frequency is below the maximum usable frequency. The model assumes that transmission will be by reflection from the ionosphere. For this the transmitter and the receiver must be on the same side of the ionospheric layer (for example, ground-to-ground communication). The model does not take into account the daytime F1 layer which usually develops between the E and F2 layers. The model does not adequately account for the electron density above the altitude of  $h_mF2$ . Finally, the model does not take into account the dependence of absorption on the operating frequency in considering the D layer absorption.

**10.3.1.2 The Bent Model.** The Bent Model [Bent et al., 1972; Llewellyn and Bent, 1973] is basically for ground-to-satellite communication but can be adapted for ground-to-ground or satellite-to-satellite communication. The main purpose of the Bent model is to determine the total electron content (TEC) of the ionosphere as accurately as possible in order to obtain high precision values of the delay and directional changes of a wave due to refraction. Ground-to-satellite communication demands operating frequencies which are higher than the MUF. Thus the mode involves the transmission refraction characteristics of the F2 layer and the electron density distribution above the height of the F2 peak must be known.

The model provides (output) the vertical total electron content above the transmitter, the profile of vertical electron density with altitude, and the total electron content along the path between the satellite and the ground. It also provides the refraction corrections to the elevation angle, the range, and the range rate.

The input parameters to the model are the date, Universal Time, locations of the transmitter and receiver (ground and satellite), rate of change in elevation and altitude of the satellite, operating frequency, the solar flux (10.7 cm flux), and sunspot number.

The data base of the Bent model consists of 50 000 topside ionospheric soundings, 6000 satellite measurements of electron density and 400 000 bottomside soundings of the ionosphere. The data extend from 1962 to 1969 to cover the maximum and the minimum of the solar cycle.

The bottomside data are foF2 hourly values from 14 stations in the American sector covering geographic latitudes  $76^\circ\text{N}$  to  $12^\circ\text{S}$  or geomagnetic latitudes from  $85^\circ$  to  $0^\circ$ . The topside soundings cover the period 1962 to 1966, with geomagnetic latitude range  $85^\circ$  to  $-75^\circ$ , and the electron density profiles are from 1000 km down to the altitudes of the foF2 peak ( $h_mF2$ ). The satellite data are from the Ariel 3 satellite covering the period May 1967 to April 1968 and are linked with real time foF2 from 13 ground stations. Thus the data base of the Bent model refers to solar cycle 20, while the data base of the ITS-78 model is from solar cycle 19.

The Bent model uses foF2 from the ITS-78 model. Instead of the monthly median values, the Bent model computes average values for every 10-day interval of the month from the 10.7 cm solar flux input. For the height  $h_mF2$ , it uses  $M(3000)$  factors of NOAA (ITS-78) in terms of the sunspot number. It uses an empirical polynomial for  $M$  in computing  $h_mF2$ , in place of the Shimazaki equation [1955] used by ITS-78.

The distribution of electron density with altitude, assumed by the Bent model for the computation of the total electron density is shown schematically in Figure 10-39. Starting from the bottom, it divides the profile into five sections; a bottom bi-parabolic F2 layer; a parabolic F2 layer above the peak; and three exponential sections to cover the altitude above  $h_o$  ( $h_mF2$  to 1000 km). The construction of the profile needs the parameters  $k_1$ ,  $k_2$ ,  $k_3$ ,  $Y_1$ ,  $Y_m$ , foF2, and  $h_mF2$ . The last two have already been explained. The dependence of the other parameters on geomagnetic latitude, solar flux, foF2, and the season is from work of Bent [Llewellyn and Bent, 1973]. The topside and the first adjoining exponential section are matched at a height  $d$  (above  $h_m$ ) by the equation

$$d = h_o - h_m = \frac{1}{k_1} \left[ \sqrt{1 + Y_1^2 k_1^3} - 1 \right], \quad (10.56)$$

where  $Y_1$  is the half thickness of the F<sub>2</sub> layer and  $k_1$  is the exponential constant.

The remaining profile above the F2 peak [of altitude range ( $h_m + d$  to 1012) km] is divided in three equal intervals of altitude.

The model can predict with an accuracy of 75%–80%. If the model is updated with observed recent data within a range of 2000 km radius (from the transmitters), the predictability is improved to 90%.

Though the model predicts total electron content (TEC) with good accuracy, the model does not have separate E and F1 layers. As the model was constructed for the TEC,

# IONOSPHERIC RADIO WAVE PROPAGATION

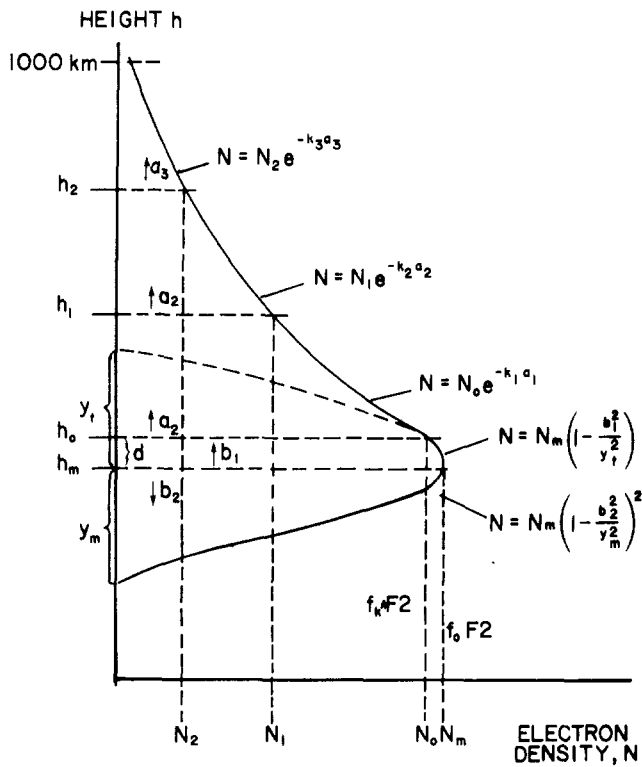


Figure 10-39. Schematic for exponential and bi-parabolic profiles for the electron density distribution with altitude for the Bent model.

the E and F1 layers are included as the bi-parabolic bottomsides of the F2 layer. Also, the program does not take into account the non-deviative absorption in the underlying D layer.

**10.3.1.3 The Ionospheric Communications Analysis and Prediction Program (IONCAP).** The IONCAP [Lloyd et al., 1978] is essentially the latest, improved, and more versatile and flexible version of the ITS-78 model.

It provides 30 output options which can be divided into four categories, (1) ionospheric description, (2) antenna patterns, (3) MUF predictions, and (4) system performance predictions.

For ionospheric predictions it provides monthly median values for the parameters foE, foF1, foF2, hmE, hmF1, hmF2, YmE, YmF1, and YmF2. It also provides the lower, median, and upper decile values of the minimum foE or foEs. It can also provide a prediction in the form of a plot of operating frequency with virtual height and also with true height.

The MUF option of the output provides the minimum radiation angle and the M factors for all four modes, E, F1, F2, and Es. The plots for the diurnal variation of the MUFs are also available. The MUFs provide the description of the state of the ionosphere and do not include any system parameters. The operating frequency for a given radio communication circuit is the critical frequency of the layer multiplied by the MUF factor.

In the system performance options, 22 performance parameters are available. The program for the antenna output option computes the elevation angles and the operating frequencies for optimum antenna geometry and its gain.

Inputs for the program are the date, Universal Time, geographical locations of the transmitter and the receiver, and sunspot number. The program can accept external ionospheric parameters as input to the program. For antenna pattern, one can select the antenna from 17 antennas in the program (7 antennas from ITS-78 have been modified). For the system performance additional inputs such as radiation power of the transmitter, and the S/N ratio of the receiver are needed.

The schematic for the electron density distribution with altitude for the IONCAP program is shown in Figure 10-40. The model has 3 parabolic layers, E, F1, and F2. The altitudes for the peak electron densities are hmE, hmF1, and hmF2. The half thickness widths for the layers are YmE, YmF1, and YmF2 respectively. For the F1 layer, hmF1/YmF1 is assumed to be 4. The E layer has fixed altitudes hmE = 110 km and YmE = 20 km. IONCAP improves on the ITS-78 model by incorporating D and F1 layers. The D layer contribution is considered indirectly by adding an exponential tail for the E layer down to the altitude of 70 km. In the transition region between the E and F1 (or F2 if F1 is absent)

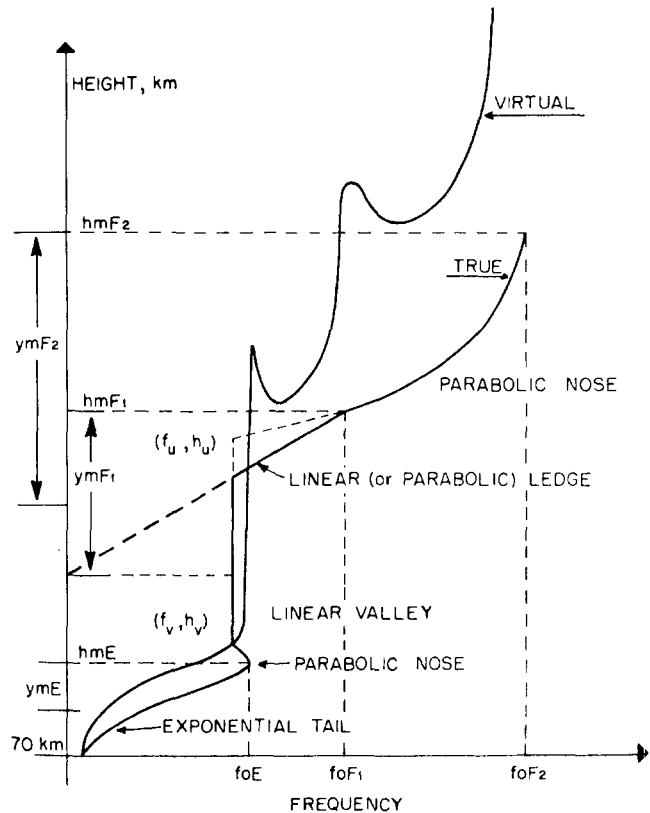


Figure 10-40. Schematic for the electron density profile and virtual height for the IONCAP model.

## CHAPTER 10

layers, the electron density is assumed to be linear for the frequency range  $f_v$  to  $f_u$  where  $f_v = x_v \times \text{foE}$  and  $f_u = x_u \times \text{foE}$ . Typical values for  $x_v$  and  $x_u$  are 0.85 and 0.98 respectively. Thus the electron density decreases above the parabolic nose 0.85 foE ( $< \text{foE}$ ) and continues upwards up to 0.98 foE ( $< \text{foE}$ ) producing a linear valley in the transition region. When the  $x_u = x_v = 1$  the valley is absent in the transition region and the curve is a vertical line starting at the tip of the parabolic nose of the E layer. The F1 layer forms a linear or parabolic ledge depending on the magnitudes of  $h_m\text{F1}$ ,  $h_m\text{F2}$ ,  $\text{foF1}$ , and  $\text{foF2}$ . In the ITS-78 model, the F1 layer is assumed to be absent. In the IONCAP model the numerical coefficients for foE are functions of geographic latitude for both solar maximum and minimum from the work of Leftin [1976]. The model uses foF1 maps of Rosich and Jones [1973]. It also takes into account the retardation below the F2 layer.

For the MUF computations the model uses the corrected form of Martyn's theorem. As the absorption equations using the secant law do not work for lower frequencies at altitudes below 90 km, these equations have been modified in the IONCAP program. The IONCAP provides two programs (1) the ITS-78 short path geometry and (2) the long path ( $> 10\,000$  km) geometry. In addition to the ITS-78 model, the path computations now include the F1 mode, the over-the-MUF mode, D and E region absorption losses, and sporadic E losses. A correction to frequency dependence is added for low frequencies reflected from altitudes below  $< 90$  km.

The improvements over ITS-78 can be summarized (see IONCAP) as follows:

1. The description of the ionosphere is now more complete.
2. The loss equations have been supplemented. This includes E mode adjustments, sporadic E effects, over-the-MUF losses, and losses for low reflection heights.
3. The ray path geometry calculations have been revised. This was an empirical adjustment to Martyn's theorem.
4. The loss statistics were revised to include the effects of the sporadic E layer and of over-the-MUF modes.
5. A separate long path model was developed.
6. The antenna gain package was revised.

All models predict only the quiet ionosphere, which shows a large systematic dependence on latitude, longitude, season, time, and sunspot activity.

**10.3.1.4 The Bradley Model.** The Bradley model contains two modifications to the existing models: (1) the filling of the valley between the E and F layers (F1, or F2 if F1 is absent), by parabolic layers [Bradley and Dudeney, 1973] and (2) a simple formulation of the prediction of the probability of the high-frequency propagation [Bradley and Bedford, 1976].

The assumption that the electron density distribution in the E and F layers is parabolic in shape, results in a valley—

a reduction in electron density between the two peak values,  $N_m\text{E}$  and  $N_m\text{F}$ —at altitudes  $h_m\text{E}$  and  $h_m\text{F}$ , respectively. The rocket observations have shown that in reality the electron density at any altitude between the altitudes  $h_m\text{E}$  and  $h_m\text{F}$  is rarely smaller than the peak electron density  $N_m\text{E}$ . Thus the assumption of the parabolic shapes for E and F layers underestimates the electron density in the altitude region between  $h_m\text{E}$  and  $h_m\text{F}$ . To correct such an underestimation Bradley and Dudeney [1973] suggested a linear distribution of electron density from foE to 1.7 foE. The lower end is at  $h_m\text{E}$ . At the upper end, the F layer is parabolic in shape down the altitude where the plasma frequency is 1.7 foE. This linear interpolation has not yet been incorporated in the IONCAP model (see Figure 10-40) of Lloyd et al. [1978].

In high frequency prediction it is essential to know the probability of communication at any particular operating frequency  $f$ . For convenience the observed data are expressed as follows:  $F_u$  is the upper decile,  $f_m$  is the median, and  $F_\ell$  is the lower decile of the ratios of  $f/f_m$ . The distribution functions of  $F_u$  and  $F_\ell$  are not simple Gaussian distributions ( $F_u - \text{MUF} = \text{MUF} - F_\ell$  for Gaussian). The distributions are  $\chi^2$ -distributions of  $F_u$  and  $F_\ell$ . For probability determinations these two  $\chi^2$ -distributions (of  $F_u$  and  $F_\ell$ ) have to be used. Two variables  $F_u$  and  $F_\ell$  with their associated degrees of freedom, and the need to integrate the  $\chi^2$ -distribution curve makes the process of determining the probability distribution very cumbersome. Bradley and Bedford [1976] derived simple empirical equations for this probability distribution. The equations are

$$Q = 130 - \frac{80}{1 - \frac{1 - (f/f_m)}{1 - F_\ell}} \quad (10.57)$$

or 100, whichever is smaller for  $f \leq f_m$ .

and

$$Q = \frac{80}{1 - \frac{(f/f_m) - 1}{F_u - 1}} - 30 \quad (10.58)$$

or 0, whichever is larger for  $f > f_m$ .

where

- Q - is the cumulative probability,
- f - is the operating frequency,
- $f_m$  - is the predicted median frequency,
- $F_\ell$  - is the lower decile (of  $f/f_m$ ),
- $F_u$  - is the upper decile (of  $f/f_m$ ).

They note that the probability distribution from their simple empirical equation is as good as, though not always better than, that from the  $\chi^2$  distribution. Therefore they highly recommend a replacement of  $\chi^2$  distribution proce-

ture by these equations for a determination of the present probability that signals will propagate at a given hour over a given sky-wave path.

The latest computer model like the IONCAP has not incorporated “Bradley Features” in its program.

**10.3.1.5 The Air Force Global Weather Central 4-D Model.** The input data to the 4-D numerical model [Flatery et al., personal communication] are the critical frequencies for the layers and  $M(3000)$ , real time or near real time observations from 40 ground stations around the world, and total electron content (TEC) from eleven stations. The frequency of observations varies from hourly (best) at one end to weekly (worst) at the other end. The desired purpose of the 4-D model is to produce a consistent ionospheric specification anywhere in the northern hemisphere for a 24-h period. In that sense it is not a forecasting model like the other models mentioned above.

This model has three ionospheric layers, E, F1, and F2. Each layer is represented by a Chapman distribution function

$$N_e(h) = N_{e_{\max}} \exp \{a[1 - z - \exp(-z)]\}, \quad (10.59)$$

where  $a$  refers to the loss mechanism and  $z$  is given by  $z = \frac{h - h_{\max}}{h_s}$  and  $h_s$  is the scale height for the layer. At a given altitude the total contribution to electron density is the sum of contributions by all three layers.

For any height the electron density is approximated by

$$N_e(\ell) = \sum_{k=1}^N a_k W_k(\ell),$$

where  $a$  is the weighting factor and  $W(\ell)$  is an empirically derived set of discrete orthogonal functions for the altitude interval  $\ell$ . The 95 to 2000 km range is divided into 127 intervals. The widths of the intervals range from 5 km at the lowest altitudes to 50 km at highest altitudes. The empirically derived function  $W(\ell)$  is in two parts, spherical harmonic functions for spatial dependence and trigonometric functions (sine, cosine) for temporal dependence.

With the help of these variables  $a_k$  and  $W_k$ , the entire data base for the ionosphere is reduced to a limited number of coefficients. These can be used to construct the electron density profile for any location in the Northern Hemisphere valid for a 24-h specification period. The model is still being developed. The specification accuracy of the model will depend strongly on the frequency and reliability of the input data—real-time experimental observations from the 40 ground stations of the northern hemisphere. Also the quality of specifications interpolated for locations inside the network will be better than those extrapolated outside the observational network.

**10.3.1.6 International Reference Ionosphere—IRI 79.**

The IRI 79 [Rawer, 1981] is the latest addition to the continued efforts of ionospheric modeling. The emphasis of IRI 79 is to summarize the experimental data from rockets and satellites to provide true height profiles of the ionosphere. The model serves as a standard reference for various purposes such as design of experiments, estimation of environmental and other effects, and testing theories. The model gives the altitude dependence of four parameters: electron density, electron and ion temperatures, and the composition of positive ions. It computes the density for atomic ions  $O^+$ ,  $H^+$ ,  $He^+$  and for molecular ions  $O_2^+$  and  $NO^+$ .

For the worldwide description of the peak electron density, the model uses foF2 from CCIR [1967] coefficients, with modified dip coordinates [Rawer, 1963]. As the foF2s are from the ground based ionosonde stations, the model really computes a relative distribution of electron density with true height, with respect to that of the foF2 peak. For a true peak height the model uses an empirical relation [Bilitza et al., 1971] with  $M(3000)foF2$  coefficients from CCIR [1967]. This empirical relation is based on the incoherent scattering measurements which yield electron density with true height. The model has an alternate procedure based on the results of Chiu [1975] to replace the foF2 and  $M(3000)foF2$  coefficients from CCIR. This procedure when used limits the ability of reproducing the complex ionospheric features available from the CCIR coefficients. The IRI 79 can also use direct data of the peak electron density and the peak altitude for computing the profiles.

The schematic for the altitude dependence of the electron density for the IRI 79 model is shown in Figure 10-41. The altitude range from 80 to 1000 km is divided into six sections: topside, F2 bottomside, F1, intermediate, valley, and E/D regions respectively. The topside region is modeled with the use of ‘harmonized Bent’ model [Ramakrishnan et al., 1979]. The bottomside F2 is expressed as the sum of Epstein Transition Functions [Rawer, 1981]. The F1 region is based on the work of Eyfrig [1955] and Ducharme et al. [1973]. The intermediate region fills the gap between the valley region and the F1 layer. The rocket measurements compiled by Maeda [1971] determine the shape and the depth of the valley region. The foE is from Kouris and Muggleton [1973a,b]. The model also takes into account the contribution from the D layer. The model does not account for the highly variable Es layer.

The IRI 79 is the only numerical model with information on additional parameters such as the electron and ion temperatures and the composition of positive ions. The composition is determined with the assumption that the plasma is electrically neutral above 84 km. The model also computes the distribution of cluster ions in the altitude range 80 to 90 km.

The inputs for the program are location (latitude and longitude), sunspot number and time. The optional inputs are the peak altitude and peak electron density. The output consists of 11 parameters: absolute electron density, relative

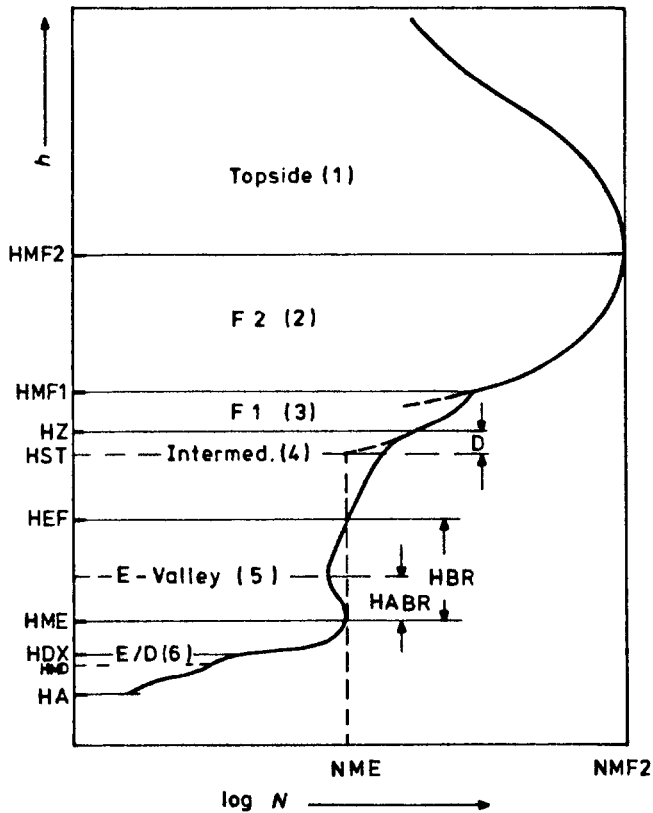


Figure 10-41. The IRI 79 model profile. For details refer to Rawer [1981].

electron density, neutral temperature, electron temperature, ion temperature, ratio of electron to ion temperature, percent concentrations of  $O^+$  (and  $N^+$ ),  $H^+$ ,  $He^+$ ,  $O_2^+$  and  $NO^+$  ions. The accuracy ( $\sigma$ ) of predictions is as below:

	Height	Peak Density	Temperature
F region	$\pm 15\%$	$\pm 30\%$	$\pm 30\%$
E region	$\pm 5\%$	$\pm 10\%$	$\pm 10\%$

The programs are in FORTRAN-4 and ALGOL-60 computer codes. These programs are available from the World Data Center, Boulder, Colorado.

### 10.3.2 The Theoretical Models

The theoretical models for the ionosphere are based on the physical processes responsible for the observed ionospheric phenomena. The processes responsible for the ionosphere are production, maintenance, and decay of the ionosphere. As the approach deals directly with the physical processes, and not with the observed phenomena, the emerging model is called a physical model.

Four models are summarized in Table 10-6 to show several variations in the same processes considered by different workers. Strobel and McElroy [1970] considered only the F2 region (200 to 700 km), whereas others took into account the altitude range from 120 to 1200 km. Nisbet [1971] constructed the first computer-based simple physical model MK-1 for the ionosphere. He considered only three neutral constituents  $N_2$ ,  $O_2$  and  $O$ , whereas Stubbe [1970] and Oran and Young [1977] also considered the minor constituents  $He$  and  $H$ . For the dissociation and ionization of the neutral species, the incident solar EUV radiation in the range 30 to 1912 Å is used, along with the wavelength dependent absorption and ionization cross sections for the neutral species. Nisbet considered three basic predominant ionic species:  $O^+$ ,  $NO^+$ , and  $O_2^+$ . Oran and Young [1977] took into account the additional ionic species  $H_2^+$ ,  $Ne^+$ ,  $N^+$  and  $H^+$ . One has to consider the chemical reactions that produce ions by charge exchange processes. Nisbet [1971] used 5 reactions whereas Oran and Young [1977] used 24 chemical reactions [see Strobel and McElroy, 1970]. For maintenance of the ionosphere, the processes of diffusion and photoionization are assumed. The processes of dissociative recombination and radiative recombination are

Table 10-6. Variations in the physical processes used in the theoretical models

Processes	Nisbet [1971]	Stubbe [1970]	Strobel and McElroy [1970]	Oran and Young [1977]
In the Altitude Region (km)	120-1250	120-1500	200-700	120-1200
Neutral Constituents for Ionization	$N_2$ , $O_2$ , $O$	$N_2$ , $O_2$ , $O$ , $He$ , $H$	$N_2$ , $O_2$ , $O$ , $He$	$N_2$ , $O_2$ , $O$ , $He$ , $H$
Chemical Reactions (Charge-Exchange)	5 Reactions	10 Reactions	4 Reactions	24 Reactions
Ionized Constituents	$O^+$ , $NO^+$ , $O_2^+$	$O^+$ , $NO^+$ , $O_2^+$ , $H^+$	$O^+$	$O^+$ , $NO^+$ , $O_2^+$ , $H^+$ , $N^+$ , $He^+$ , $N_2^+$
Neutral Winds	—	Horizontal Winds	Horizontal Winds	Horizontal Winds
Electric Fields	—	Yes	—	—
Magnetic Fields	—	Yes	—	—
Additional Features	—	—	—	Solar Flare Effects

responsible for the decay of the ionosphere. For his simple model, Nisbet neglected the transport processes such as neutral winds, electric fields, and magnetic fields. The procedure is further complicated because coupled simultaneous equations must be solved for neutral winds, mass transport, and energy transport. For determining electron density in the ionosphere, the gas consisting of both ions and electrons, is considered electrically neutral. Thus, in every elementary volume, the number of electrons is equal to the number of ions. All the models reproduce many of the observed features such as the diurnal variation, seasonal variation, and solar cycle dependence of the midlatitude ionosphere under quiet conditions. The accuracy of the theoretical models depends upon the understanding of the physical processes considered in the models. For accurate predictions from the theoretical models, precise information on the large number of variables used in the models is necessary. Also, the models use several observed average boundary conditions which could have a large variability dependent on other geophysical parameters such as solar activity and magnetic activity. The results from the models are adequate for long term planning of science and engineering applications. Though these models reproduce main observed average features of the ionosphere, they are unable to specify the ionosphere within an accuracy of  $\pm 20\%$  needed by the systems in operation. At present, the main input information of solar EUV radiation needed for the theoretical models is not routinely available for predicting the ionosphere.

### 10.3.3 Comparison of the Phenomenological Models, Their Limitations and Ability

In comparing the models one must note that IONCAP is the modified and more flexible version which replaces the ITS-78 model. As the ITS-78/IONCAP and the Bent models serve entirely different purposes, it is essential to understand the difference in their approaches and final output parameters computed by the models. These are summarized in Table 10-7. The left-hand column in Table 10-7 lists the parameter under consideration. The next four columns summarize the features in each of the models, ITS-78, IONCAP, the Bent, and the IRI 79 models, respectively. From the table it is seen that the selection of a model will depend more upon the information sought under the parameter headings, than on accuracy. The IONCAP model is basically useful for wave propagation using operating frequencies which would be reflected by the E, Es, F1, and F2 layers. On the other hand, the Bent model relies on the transmission, refraction, and absorption characteristics of the ionosphere, with the operating frequency much larger than the foF2 frequency. The IRI 79 model basically provides a distribution of electron density with altitude. All the models predict quiet ionospheric conditions only. The models do not hold for disturbed ionospheric conditions.

The additional limitations of these models are

1. All the models are poor in predicting the high latitude ionosphere.
2. None of the models take into account the effects of particle precipitation in the auroral region which enhance the E(Es) and F layers.
3. The mid-latitude trough which exhibits large horizontal gradients in electron density is not incorporated in these models.
4. These models are good for latitudes  $\pm 20^\circ$  to  $\pm 60^\circ$ , and are poor predictors for the equatorial region and the high latitude region.

Nonetheless these models serve two useful functions: (1) to predict ionospheric parameters, and (2) to determine physical phenomena and/or to modify existing coefficients for explaining the deviations between the experimentally observed value and the predictions from these models.

The computer programs for the ITS-78 [Barghausen et al., 1969] and the IONCAP program [Lloyd et al., 1978] are available from the Institute for Telecommunications Sciences, Boulder, Colorado 80303. The computer programs for the Bent model [Llewellyn and Bent, 1973] are available from the Atlantic Science Corporation, P.O. Box 3201, Indianapolis, Florida 32903. The computer programs for IRI 79 are available from World Data Center A, Boulder, Colorado 80303.

### 10.4 HIGH FREQUENCY RADIO PROPAGATION

The high frequency (HF) band of the electromagnetic spectrum extends from 3 to 30 MHz, corresponding to a wavelength range of 100 to 10 m. Many services have frequencies allocated in this band—Local/International Broadcast, Amateurs, Standard Frequencies, Maritime and Land Mobile, Point-to-point Communications, Industrial, Scientific, Medical Diathermy, Aero Fixed, Citizens' Band, and so on. The band is also used for ionospheric sounding and over-the-horizon surveillance. Its use in most applications depends on the fact that HF waves are reflected by the ionosphere.

HF is used for broadcasting because of its greater area coverage relative to the bands on either side, which are restricted to either ground wave or line-of-sight propagation. Its use for communications stems mainly from the fact that it is often the only means of communication. It is also very often the simplest and least expensive form of communication.

With the advent of satellite communications, which use signals of such high frequency that the normal ionosphere has little effect on them, and improvements to submarine cables, the proportion of traffic that goes by HF is significantly smaller than it used to be. However, the *total* use of HF radio circuits is actually greater now than ever before, and a substantial research effort is still being devoted to

## CHAPTER 10

Table 10-7. Intercomparison of the empirical-computer based ionospheric models.

Parameter	Ionospheric Models			
	ITS-78	IONCAP	Bent	IRI 79
D Region	Non-deviative and deviative absorptions only	Same as ITS-78 + E Layer exponential extension down to 70 km	Not modeled	Modeled
E Region foE	Modeled by Leftin et al. [1968]	Same as ITS-78 + exponential down to 70 km	Not modeled	Modeled
h <sub>m</sub> E Y <sub>m</sub> E	110 km fixed 20 km parabolic shape	Leftin [1976] coefficients		Kouris and Muggleton [1973a,b]
F1 Region foF1	Not modeled	Rosich & Jones coefficients [1973]	Not modeled	Modeled Eyfrig [1955] Ducharme et al. [1973]
h <sub>m</sub> F1 Y <sub>m</sub> F1		h <sub>m</sub> F1/y <sub>m</sub> F1 = 4 (fixed)		
F2 Region Bottomside foF2 h <sub>m</sub> F2 Y <sub>m</sub> F2	Haydon-Lucas coefficients [1968] Shimazaki eq [1955] + E layer retardation Kelso [1964]	Same as ITS-78	Bi-parabolic  Bent coefficients	Modeled Rawer [1981]
F2 Region Topside	Not modeled	Not modeled	Up to 1000 km	Modeled Rawer [1981]
E-F Transition Region	Not modeled	Modeled	Not modeled	Maeda [1971]
Electron-Density Profile	Not computed	Available up to h <sub>m</sub> F2	Available up to 3500 km	Available up to 1000 km
Electron, Ion Temperatures	Not modeled	Not modeled	Not modeled	Modeled
Ion Composition	Not modeled	Not modeled	Not modeled	Modeled
Total Electron Content (TEC)	Not computed	Not computed	Computed	Not computed
MUF	For short path only	Also for long path (>10,000 km)	Not modeled	Not modeled
Short-Term Prediction of MUF	Function of Kp	Not modeled	Not modeled	Not modeled
Input Parameters required	Sunspot number	Sunspot number	Sunspot number and 10.7 cm solar flux	Sunspot number

# IONOSPHERIC RADIO WAVE PROPAGATION

Table 10-7. (Continued)

Parameter	Ionospheric Models			
Noise Parameters	Galactic Atmospheric Manmade	Same Modified Same	Not modeled	Not modeled
MUF 50% FOT 90% HPF 10%	Modeled	Modeled	Not modeled	Not modeled
System Performance	Modeled for short path (<3000 km)	Also has a long path option $\geq$ 10,000 km	Not modeled	Not modeled
Antenna Patterns	Uses ITSA-1 Package with 10 antenna options	Modified ITS-78 package with 17 antenna options	Not modeled	Not modeled
Sporadic E	Modeled in terms of occurrence frequency	Same as ITS-78	Not modeled	Not modeled
Circuit Reliability Service Probability Multipath Evaluation	Modeled	Modeled as ITS-78	Not modeled	Not modeled

improving our knowledge of the ionosphere and HF propagation.

Some of the difficulties associated with using HF for communications, broadcasting, or surveillance stem from the ionosphere itself and success in any of these fields demands a good knowledge of the ionosphere and its vagaries. Irreducible difficulties associated with HF propagation can usually be traced to characteristics of the ionosphere or of radio waves propagating through any lightly ionized medium. Thus it is essential for the professional user of HF to have a good knowledge of both the ionosphere and radio wave propagation.

Much has already been written about the ionosphere and radio wave propagation and the reader should look elsewhere for details. See, for example, the books by Davies [1966, 1969], David and Voge [1969], Rishbeth and Garriot [1969], Hargreaves [1979], Ratcliffe [1970], Lied [1967], and Picquenard [1974]. The four volume report "Solar Terrestrial Predictions Proceedings" [Donnelly, 1979, 1980] is an excellent supplement to these books, providing more recent reports on the general problem of forecasting the solar-terrestrial environment. The reports of Study Group 6 of the Consultative Committee for International Radio (CCIR) are also a very useful source of information, and are particularly valuable because they are regularly updated. AGARD

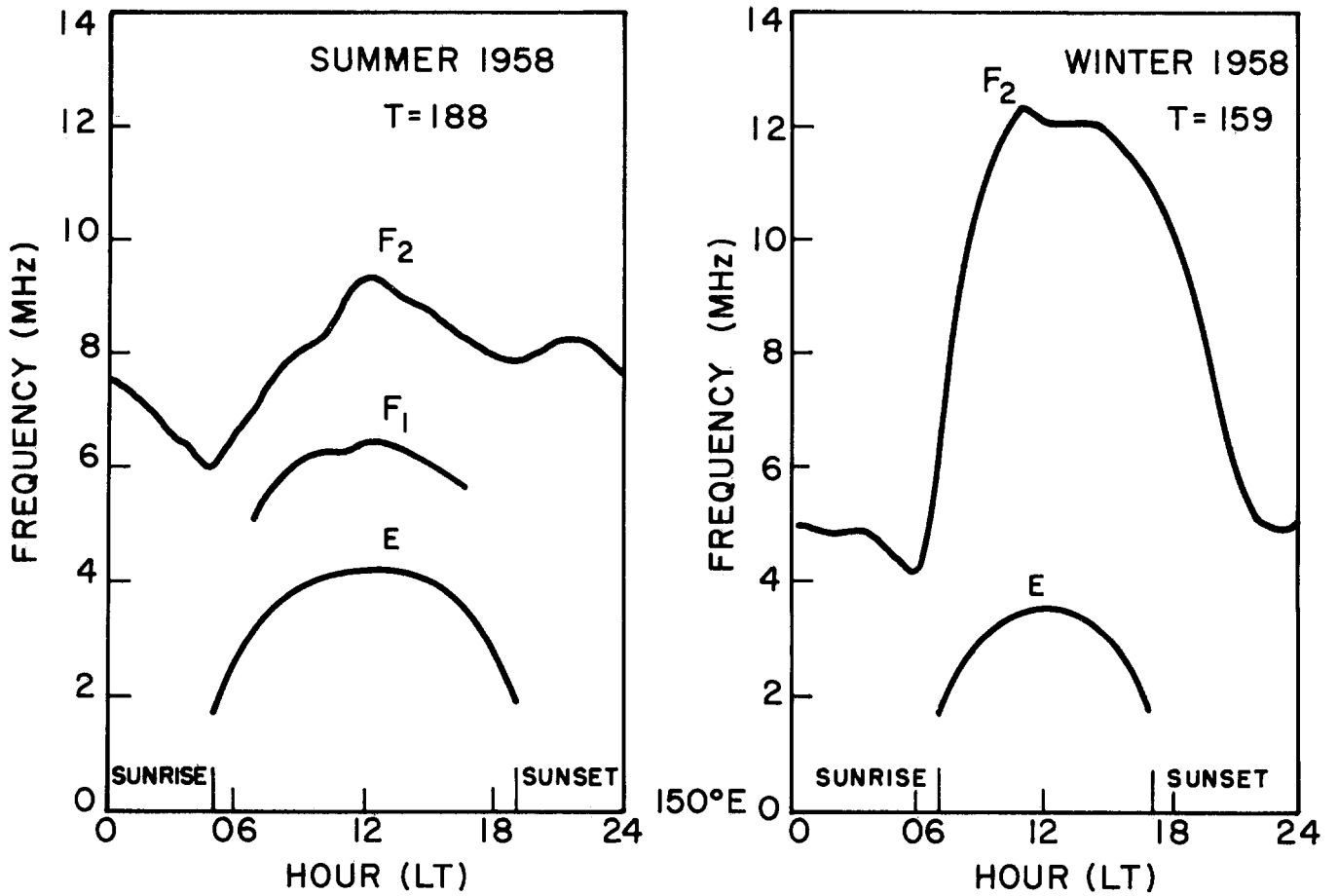
Lecture Series No. 127 on "Modern HF Communications" is also a valuable source of information [AGARD, 1983].

It is the intention of this section to provide a broad overview of HF propagation, its relationship to the ionosphere, its problems, and to indicate those areas of current interest to users of HF. A basic knowledge of the ionosphere itself is assumed (see Chapter 9 of the present volume). Emphasis will be placed on the use of HF for communications. The same concepts and problems also apply to the use of HF for broadcasting and surveillance (over-the-horizon radar). Section 10.6 covers the effects of over-the-horizon radars in the HF band.

## 10.4.1 Morphology of the Ionosphere

An understanding of the morphology of the ionosphere is an essential prerequisite for its successful use as a communications medium. The basic theory of the ionosphere and its variations has been outlined in Chapter 9 of this volume—here we are concerned mainly with how the ionosphere varies, rather than why it does.

There are five main variations of the electron density of the ionosphere that must be taken into account:



SOLAR MAXIMUM

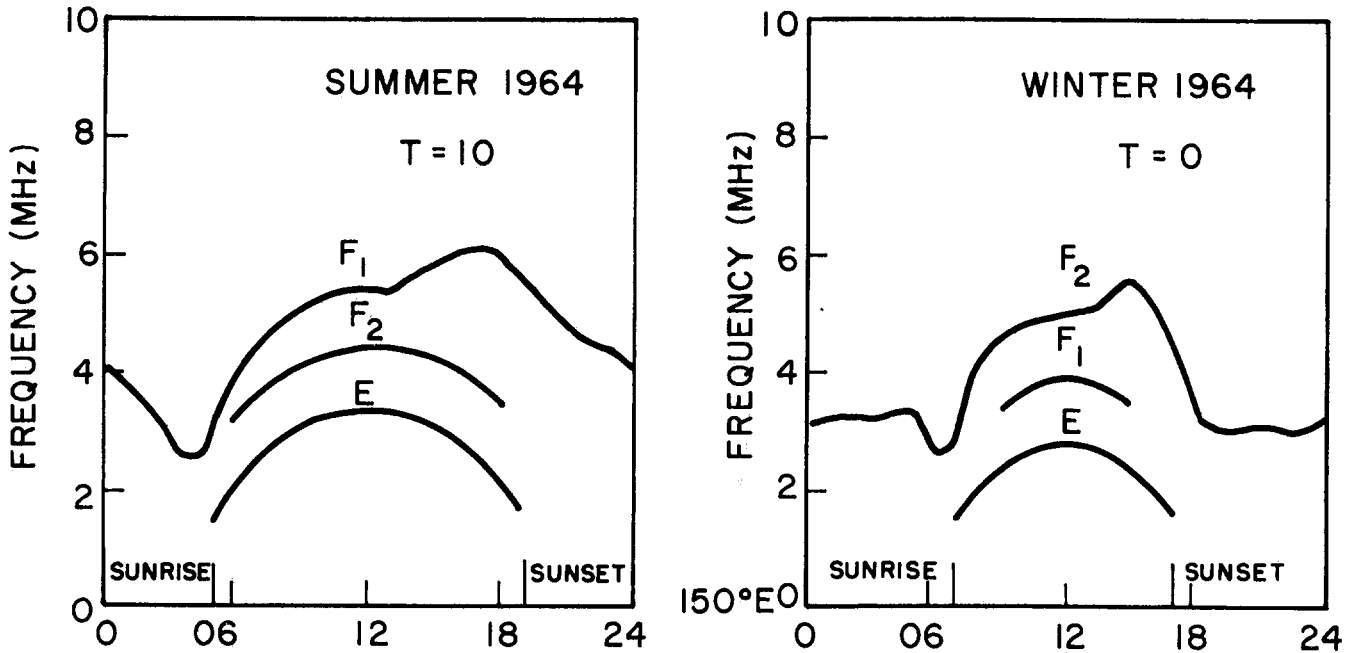


Figure 10-42. Diurnal variations of the critical frequencies of the E, F<sub>1</sub>, and F<sub>2</sub> layers for solar maximum (1958) and solar minimum (1964) and for summer (January) and winter (June), at a typical midlatitude station (Canberra). The parameter T is an ionospheric index related to the level of solar activity.

# IONOSPHERIC RADIO WAVE PROPAGATION

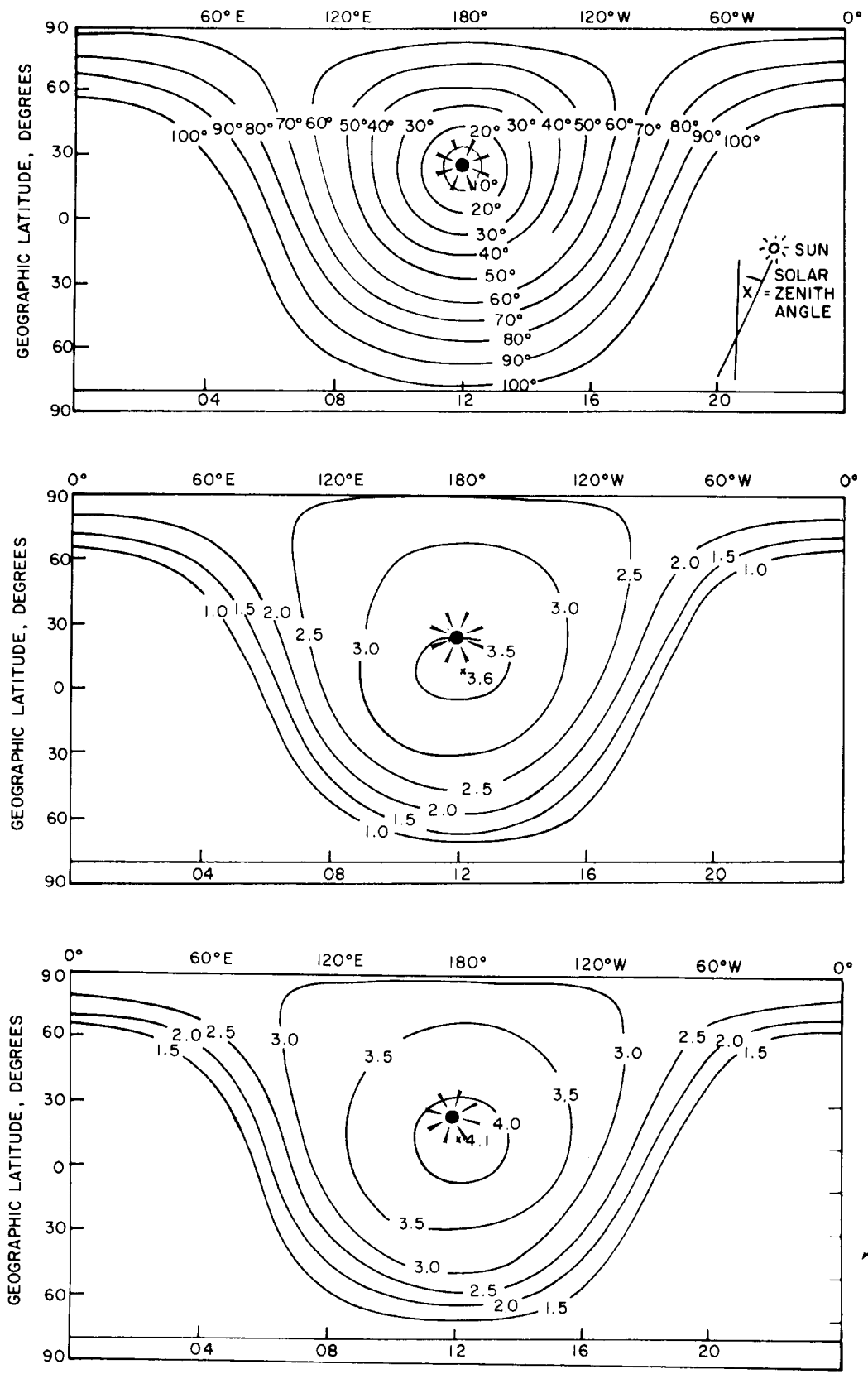


Figure 10-43. The geographical variation of the critical frequency of the E layer as a function of local time for June at solar minimum (center panel) and solar maximum (bottom panel). The top panel shows the variation of the solar zenith angle for the same month.

## CHAPTER 10

1. DIURNAL-variation throughout the day, which is largely due to the variation of the solar zenith angle.
2. SEASONAL-throughout the year.
3. LOCATION-both geographic and geomagnetic.
4. SOLAR ACTIVITY-both long term and disturbances
5. HEIGHT-the different layers.

These variations have all been deduced experimentally, by world-wide observations of the ionosphere over the past few decades. The reader may refer to Davies [1966, Chapter 3] and Hargreaves [1979, Chapter 5] for details. The diurnal, seasonal, solar cycle and height variations of the ionosphere may all be deduced by routine monitoring of the ionosphere at one location. Figure 10-42 shows these four variations for a typical midlatitude station. 1958 was a period of high solar activity, as indicated by the high values of the ionospheric index, T (see Section 10.4.4). The figure also illustrates the mid-latitude seasonal anomaly, the name given to the initially unexpected fact that foF2 is higher in the winter than in the summer, in spite of the larger solar zenith angle. This anomaly and others are described by Hargreaves [1979, Chapter 5].

Once the diurnal, seasonal, solar cycle and height variations of the ionosphere at a given location have been deduced, the next step is to measure and understand the variation with location. This has been achieved through an international effort of observations and data exchange, and we now have reliable maps of the world-wide distribution of the important ionospheric parameters. The accuracy of these maps over the ocean areas, where no observations are available, still remains somewhat limited [Rush et al., 1983].

The easiest part of the ionosphere to model on a world-wide basis is the E layer. Figure 10-43 shows the variation of foE, the critical frequency for the E layer, for June at solar minimum and solar maximum. The figure also shows the variation of the solar zenith angle for the month, and it can be seen that the variation of foE follows closely that of the solar zenith angle. In fact, the variations are so close, indicating that foE is very largely solar controlled, that it is possible to use a simple empirical representation to deduce foE for a given zenith angle,  $\chi$  [for example, Hargreaves 1979; Muggleton, 1971]:

$$foE = 3.3 [(1 + 0.008R) \cos \chi]^{1/4} \text{ MHz} .$$

Note that foE also varies linearly with sunspot number, R, increasing by about 20% over a typical slow cycle for a zenith angle of zero.

Sporadic E (Es) layers also occur in the height range of the normal E region. These layers are patchy and only a few kilometers thick at mid latitudes. They tend to appear and disappear almost at random (hence the name), but have well-defined gross seasonal and latitudinal variations. See, for example, Hargreaves [1979, p.90].

The F1 layer is similar to the E layer (see Figure

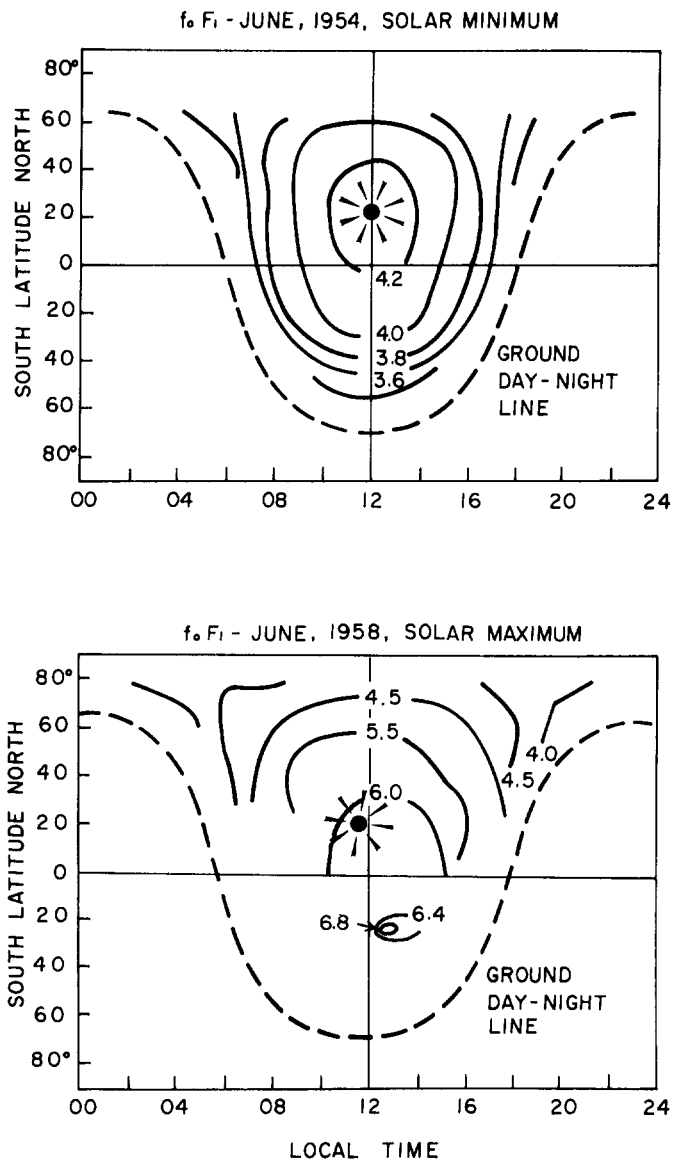


Figure 10-44. The geographical variation of the critical frequency of the F1 layer as a function of local time for June at solar minimum and maximum.

10-44), except that the F1 layer tends to disappear in winter. Hargreaves [1979] gives the following formula for foF1:

$$foF1 = 4.25 [(1 + 0.0015R) \cos \chi]^{1/4} \text{ MHz} .$$

The variations of foE and foF1 with  $(\cos \chi)^{1/4}$  identify both the E and F layers as well behaved Chapman layers. Other, more accurate, world-wide representations of foF1 have been given by Rosich and Jones [1973] and Ducharme et al. [1971].

Moving on to the F2 layer, due to its large height and electron density the most important layer as far as HF propagation is concerned, we find that the simple situation that holds for the E and F1 layers does not hold very well for

## IONOSPHERIC RADIO WAVE PROPAGATION

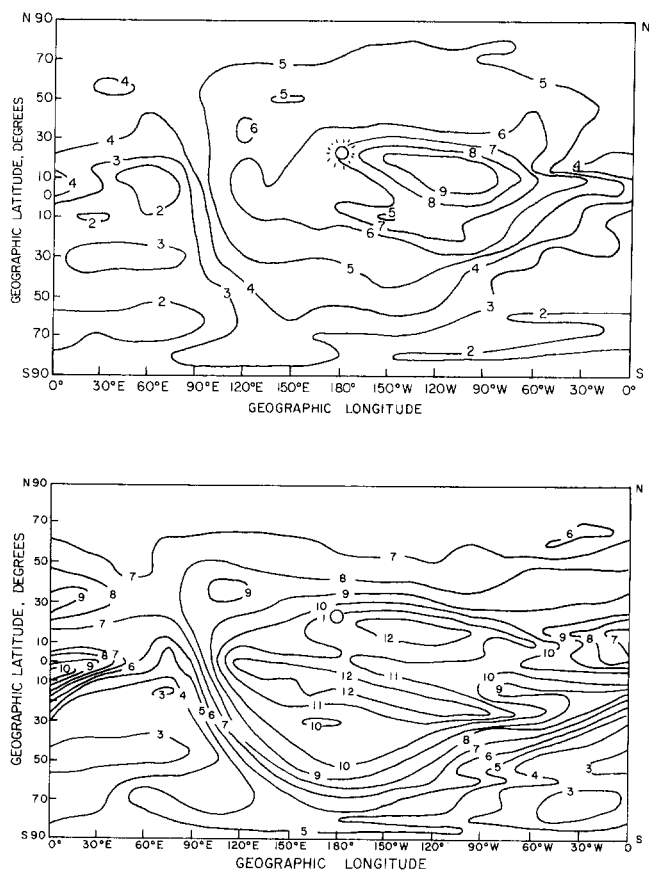


Figure 10-45. The geographical variation of the critical frequency of the F2 layer for June at solar minimum and maximum, for 00 UT. World maps such as these are made for each hour of each month (576 maps).

the F2 layer. Figure 10-45 shows, for example, how the F2 layer critical frequency, foF2, varies over the earth at 00 UT in June, for low and high solar activities. It can be seen that the simple structure obtained for the E and F1 layers, with the contours of foE and foF1 closely following the contours of the solar zenith angle, no longer applies although a clear zenith angle dependence can be seen around sunrise ( $\sim 90$  to  $\sim 120^\circ\text{E}$ ). In fact, the departures of foF2 from a simple  $R \cos^{1/4}\chi$  dependence are so great that it is necessary to make world-wide observations to determine the actual variations of foF2. Detailed studies of foF2 have shown that as well as depending on  $R$  and  $\cos \chi$ , foF2 also depends on other factors such as electric fields, and neutral winds to name a few, and its large scale morphology is controlled by the geomagnetic field.

foF2 is also found to have variations with latitude which are not seen in foE and foF1. For example, Figure 10-45 shows that foF2 exhibits two afternoon peaks ( $\sim 12$  MHz in the solar maximum portion of the figure) situated on either side of the equator. This feature is known as the equatorial anomaly and is due to electrodynamic lifting of the layer at the equator under the combined influence of horizontal elec-

tric and magnetic fields. Theoretical modeling studies of the equatorial ionosphere have been performed by Anderson [1981], among others. Empirical maps of foF2 and other ionospheric parameters have been published by CCIR [1966].

The morphology of the high latitude ionosphere is even more complicated than that of the equatorial ionosphere and much remains unknown about it. Probably the most important feature of the high latitude ionosphere is the mid-latitude ionosphere trough, which lies equatorwards of the auroral oval. The trough is a narrow feature that moves in step with geomagnetic activity and thus fails to appear in monthly median maps of foF2. However, it can have very serious effects on HF communications at high latitudes because of the strong horizontal gradients associated with it. The morphology of the high latitude ionosphere has been reviewed, for example, by Hunsucker [1979], Hunsucker et al. [1979] and CCIR [1981a].

Lastly, we must consider the D region. This region is of no direct concern for HF radio propagation since the electron densities are always too low to reflect HF waves. However, the D region is very important from the point of view of absorption of the energy of an HF wave, especially at the lower end of the HF band. A review of the D region and the prediction of its effects on radio propagation has been presented by Thrane [1979]. Synoptic models of the D region electron density are unreliable because of the complexities of the D region and the difficulties encountered in measurement of the electron density profiles.

Absorption of HF waves occurs mainly in the D and lower E regions of the ionosphere. The free electrons absorb energy from the incident wave and reradiate it in a continuous process. However, if an energetic electron collides with a neutral particle before it can reradiate its energy, this energy will be taken up by the neutral particle as kinetic energy and will be lost to the HF wave, that is, energy will be absorbed by the medium.

This type of absorption is known as non-deviative absorption and is roughly proportional to  $1/f^2$  where  $f$  is the wave frequency. Extra absorption, known as deviative absorption, also occurs near the reflection level. The non-deviative term usually dominates for oblique propagation. If the operational frequency,  $f$ , becomes too low, the absorption will increase to the point where the signal disappears below the level of the noise at the receiver site and becomes unusable. This frequency is known as the lowest usable frequency, or LUF. A good treatment of absorption is given by Davies [1969, Chapter 6] while the variations of absorption are discussed by Davies [1966, Chapter 3].

### 10.4.2 Simple Ray Propagation

Many of the operational aspects of HF propagation may be studied using simple ray concepts. Figure 10-46 illustrates the basic geometry of a one-hop HF circuit. Note that

# CHAPTER 10

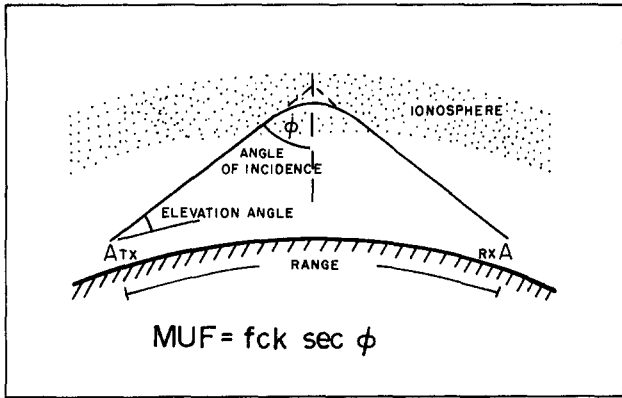


Figure 10-46. Simple geometry of an HF oblique circuit, illustrating the essential elements of the circuit. The formula for the maximum usable frequency (MUF) is all that is required in many calculations for HF propagation.

the diagram ignores the ground wave which is usable for ranges up to about 50–100 km, depending on the frequency, antenna, ground conductivity, etc. The reflected ray is continuously refracted as it passes through the ionosphere and if sufficient refraction occurs the ray will be bent down sufficiently to reach the receiver. Figure 10-46 also shows one of the most basic formulas of ray propagation:

$$MUF = f_c \times \text{obliquity factor} = f_c \times k \times \sec \phi,$$

that is, the maximum usable frequency (MUF) is equal to the product of the critical frequency,  $f_c$ , of the reflecting layer and an obliquity factor related to the geometry of the circuit. For a flat earth/ionosphere approximation, this factor is  $\sec \phi$ , where  $\phi$  is the angle of incidence. For a curved earth and ionosphere, the factor  $k$  is introduced to allow for the different geometry. This factor is typically of the order 1.1.

In practice, the obliquity factor for a given circuit relying on reflection from the F2 layer for example, is obtained from

FOR A 1000km CIRCUIT: -

	E - MODE		F - MODE	
	1-hop	2-hop	1-hop	2-hop
elevation angle	9.0	20.5	28.1	48.4
$k \times \sec(\phi)$	4.4	2.6	1.9	1.3

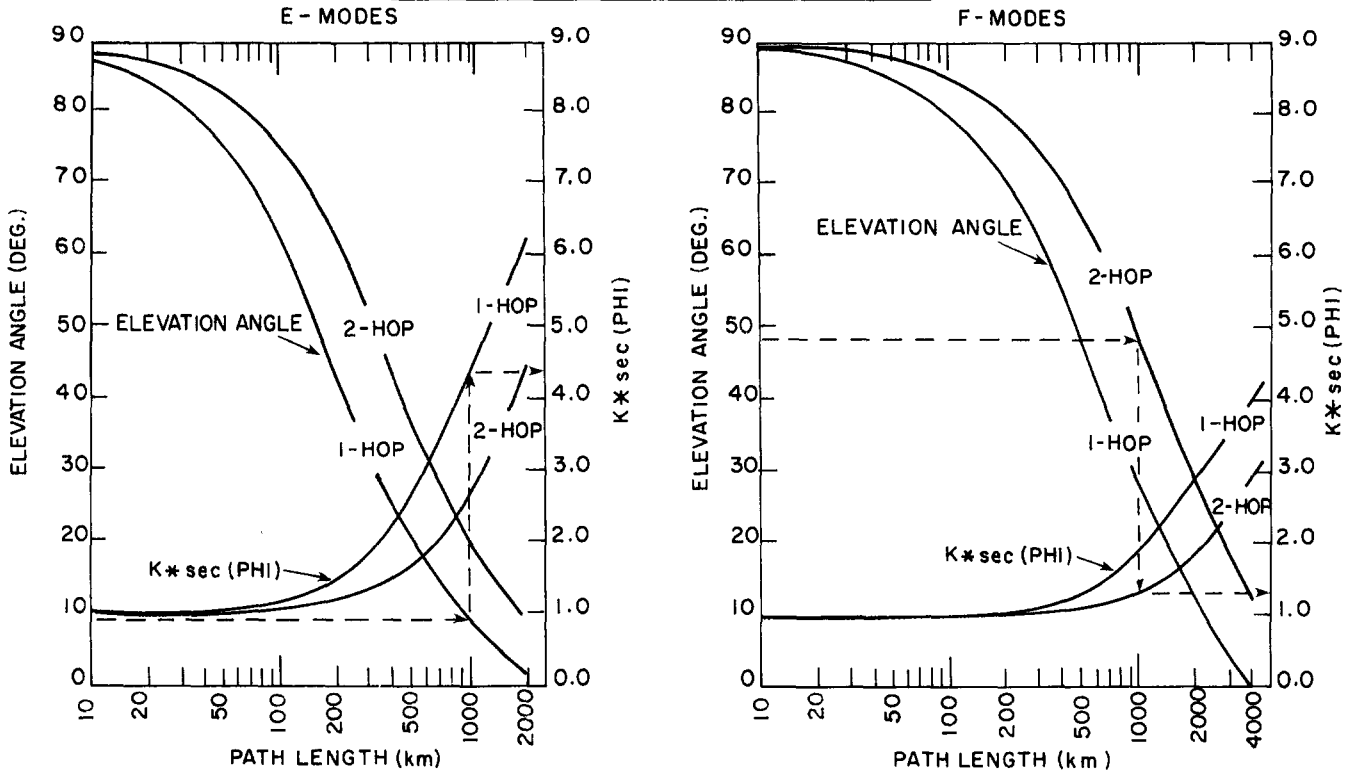


Figure 10-47. Plots showing the elevation angle and obliquity factor ( $k \sec \phi$ ) for propagation via the E and F layers. For a given circuit length and number of hops, these plots show the required elevation angle (necessary for selecting an appropriate antenna) and obliquity factor for the two layers (useful, among other things, for consideration of possible E layer screening).

## IONOSPHERIC RADIO WAVE PROPAGATION

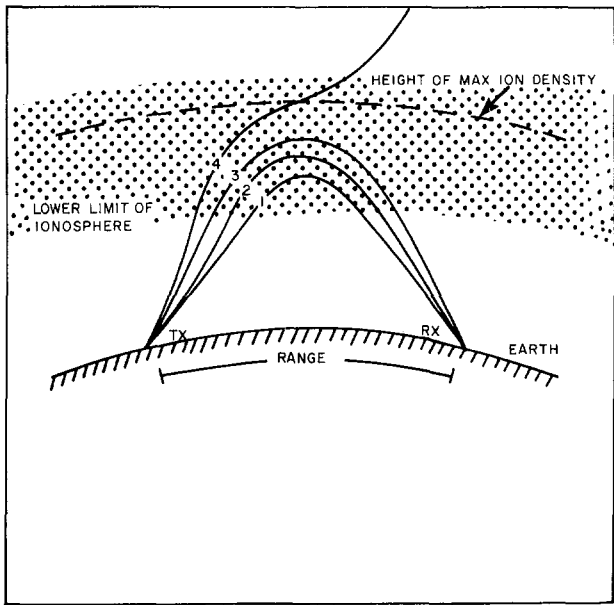


Figure 10-48. Sample ray paths for a fixed distance but different frequencies. As the frequency increases, the ray must penetrate further into the ionosphere. If the frequency is too high, that is, above the MUF for the circuit, the ray penetrates.

values of the obliquity factor for a 3000 km hop,  $M(3000)F_2$ , which is scaled routinely from vertical incidence ionograms [Piggott and Rawer, 1972]. The obliquity factor for a distance  $D$  is related in an empirical fashion to  $M(3000)F_2$ . Figure 10-47 shows how the value of  $k \sec \phi$  varies with circuit length for one and two hop E and F layer modes. Typical values for the E and F one-hop modes are  $\sim 5$  and  $\sim 3$ . Figure 10-47 also shows the elevation angles corresponding to the different propagation modes.

Figure 10-48 illustrates ray propagation for different frequencies on a fixed circuit. As the frequency increases, the ray must penetrate further into the ionosphere before it is refracted to the horizontal and thence back to the ground. The highest frequency that can be reflected back to the ground is the MUF for that circuit. Note that the ray corresponding to the MUF does not reach the altitude of the peak density of the layer,  $h_{max}$ . It is only for vertical incidence that the ray actually reaches  $h_{max}$ .

Figure 10-49 illustrates the concept of the skip zone, which is a zone into which an ionospherically reflected signal cannot propagate. The figure illustrates the effect of different elevation angles for a fixed frequency. As the elevation angle increases, corresponding to a shorter circuit length, the ray must penetrate deeper into the ionosphere in order to be reflected. However, as the elevation angle increases the obliquity factor  $k \sec \phi$  decreases. While the product  $f_oF_2 \cdot k \sec \phi$  remains greater than the operating frequency  $f$ , the signal will be reflected. When  $f$  exceeds  $f_oF_2 \cdot k \sec \phi$ , the signal will penetrate the ionosphere.

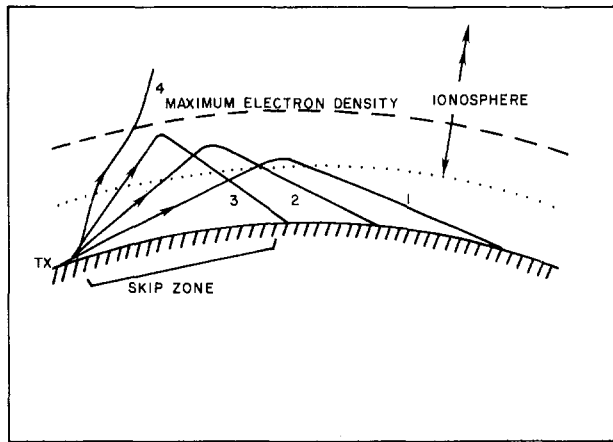


Figure 10-49. Sample ray path for a fixed frequency but varying elevation angle. If the operating frequency is above the local critical frequency, high elevation rays will penetrate and there will be a "skip zone" around the transmitter which cannot be reached by an ionospherically propagated ray.

The area surrounding the transmitter, which is defined by  $k \sec \phi \leq f/f_oF_2$ , is known as the skip zone for that frequency (and location and time). Signals at the frequency  $f$  cannot penetrate into the skip zone, although the ground wave would propagate out to about 50–80 km. This phenomenon can also be used to advantage by ensuring that an unwanted receiver lies in the skip zone of the transmitter. When the value of  $f_oF_2$  above the transmitter exceeds the operating frequency there is, of course, no skip zone.

HF-communication via ground wave is important in many areas, particularly over sea and flat land with high conductivities, where reliable circuits may be established up to distances of several hundred kilometers. The conductivity of the surface is strongly frequency dependent with rapid attenuation at the higher frequencies. In the past CCIR has published a set of curves of ground wave field strength versus distance. CCIR is in the course of implementing a computer program to estimate ground wave field strengths. Ground wave propagation may be quite complex, particularly over rough terrain and over mixed land-sea paths. There is a need for better charts of ground conductivity, and in some cases terrain modeling may be useful and important. Large topographical features such as mountain ranges and glaciers may cause reflections and strong attenuation, and vegetation, soil humidity and snow cover also influence the propagation characteristics.

We have seen that the MUF for a given circuit is set by the density of the ionosphere at the reflection point and the geometry of the circuit. For a multi-hop circuit, the MUF is set by the lowest of the MUFs for the individual hops. The lowest usable frequency (LUF), on the other hand, is set by absorption of the signal by the ionosphere and by the generally poor performance (low gain) of most HF antennas at low frequencies.

## CHAPTER 10

### 10.4.3 Requirements for Successful Communications

Under normal operating conditions, there are three factors that must be considered to achieve successful communications. These are

1. Choosing a suitable operating frequency.
2. Choosing a suitable antenna system.
3. Ensuring that the wanted signal is at a level above that of the local radio noise at the operating frequency.

The choice of a suitable operating frequency is the subject of main concern in the present context since this is where a knowledge of ionospheric physics and radio wave propagation is required. This choice will be discussed in Section 10.4.4. The choice of a suitable antenna system will require matching the antenna pattern to the propagation angles of the HF signals—these can be deduced using the ionospheric models developed for choosing a suitable operating frequency. However in many cases practical considerations will intervene and a far from ideal antenna will be used. The ideal antennas tend to be very expensive and mobile operators especially will often be forced to use a random wire hung over a tree. As a general rule of thumb, horizontal antennas are required for short circuits and vertical antennas are required for long circuits. The ubiquitous whip antenna is absolutely the worst (but probably the most common!) choice for short sky-wave circuits since its antenna pattern has a null in the vertical direction. Antenna patterns for the common antennas can be obtained from Lloyd et al. [1978]. Table 10-8 gives a brief summary of

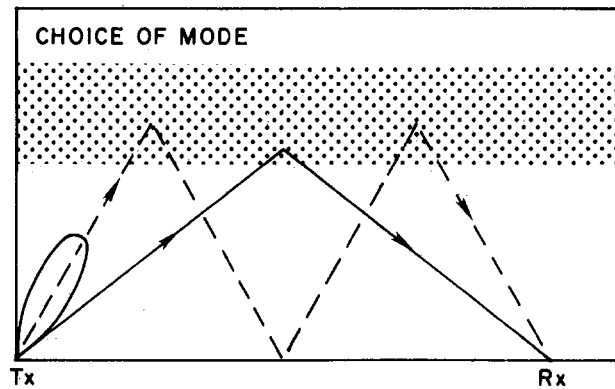


Figure 10-50. Sketch illustrating the fact that the antenna pattern should match the required propagation mode for a given circuit.

the situation. Note that the radiation pattern of an antenna is a function of frequency so that an antenna appropriate for a low HF frequency may have a very poor performance at a higher frequency. Selection of the correct antenna will not only ensure that the bulk of the transmitted power goes at the required elevation angle, but can also be used to select a particular propagation mode and thus avoid multipath interference. Multipath interference arises when the transmitted signal arrives at the receiver over two or more separate propagation paths with different time delays.

Figure 10-50 illustrates propagation via 1F and 2F propagation modes, with an antenna pattern whose lobe favors the higher angle 2F mode and almost completely prohibits

Table 10-8. Suitable simple antennas for use on paths from 0 to more than 3000 km.

Path Length (km)	Required Radiation (Elevation) Angles	Suitable Simple Antenna
0–200	60°–90°	Horizontal dipole: broadside is required azimuth. 0.25 wavelength ( $\lambda$ ) above ground.
200–500	40°–70°	Horizontal dipole: broadside to required azimuth. 0.3 $\lambda$ above ground.
500–1000	25°–50° and 10°–20°	0.25 $\lambda$ vertical monopole, or horizontal dipole, broadside to required azimuth 0.5 $\lambda$ above ground.
1000–2000	10°–30° and low angles	Vertical monopole up to 0.3 $\lambda$ long with ground screen.
2000–3000	5°–15° and 20°–30°	Vertical monopole up to 0.3 $\lambda$ long with ground screen.
> 3000	low angles	Vertical monopole up to 0.6 $\lambda$ long with ground screen.

## IONOSPHERIC RADIO WAVE PROPAGATION

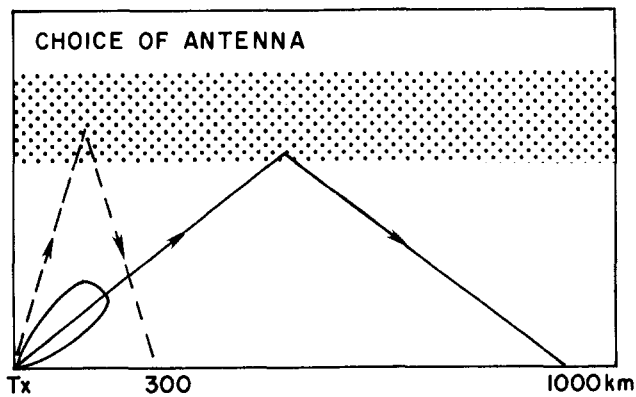


Figure 10-51. Sketch illustrating the fact that the antenna should be chosen to match the circuit length. The antenna pattern illustrated is not appropriate for short circuits ( $R \sim 300$  km).

propagation via the 1F mode. The impact of the choice of an antenna for a given circuit is illustrated in Figure 10-51 for hop lengths of 300 and 1000 km. In this case, the antenna heavily favors the longer circuit and is quite inadequate for short-haul circuits.

Given a frequency that the ionosphere will support and an antenna which emits sufficient power in the direction taken by the signal that arrives at the receiving site, the third thing to ensure is that the signal strength is above the strength of the local radio noise. This noise can be natural or manmade. Below about 20 MHz, natural noise is caused by either distant thunderstorms, which cause a general increase in background noise level, or local thunderstorms which are usually much more obvious causes of poor signal-to-noise ratio. Galactic cosmic noise becomes the dominating natural noise above  $\sim 20$  MHz when it penetrates the ionosphere from above at frequencies above foF2. The worldwide distribution and characteristics of atmospheric radio noise can be obtained from the CCIR Report 332 [CCIR, 1963]. Manmade noise includes such things as industrial noise due to welders, diathermy machines, car ignition, power lines and so on. Interference from other communicators using the same operating frequency can also be regarded as noise.

There are many techniques available to ensure an adequate signal-to-noise ratio. The more environmentally acceptable method is to aim at lowering the noise level. This can be achieved by choosing as a receiver site some location that is remote from the major sources of manmade noise, which usually entails being away from major cities. Some noise rejection is also possible using horizontally polarized antennas which de-select the local noise that tends to be vertically polarized. Careful attention to the azimuth of the main lobe of the receiving antenna can also result in the beam not being aimed at a nearby source of noise. In heavily urbanized areas (Europe, East and West Coast of the United States), the noise level is often set by the large number of other communicators.

If an adequate signal-to-noise ratio cannot be obtained by lowering the noise level, it is necessary to increase the signal level. Some increase in signal level can be achieved by choosing an antenna that has more gain at the given operating frequency and elevation angle. This is one approved solution. An alternate solution is to increase the transmitter power.

### 10.4.4 Predictions for HF Communications

The first step in predicting HF communication conditions is to set up an appropriate model of the ionosphere. To have practical application, this model must include all five main variations of the electron density distribution of the ionosphere (altitude, location, diurnal, seasonal, solar cycle), must include some measure of the remaining variability of the ionosphere after these main variations have been accounted for, must exist as a reasonably efficient and fast computer code, and must possess some method for projection forward in time. Ideally, it should also be capable of a modelled response to short time scale events such as shortwave fadeouts and ionospheric storms. (These are discussed in Section 10.4.6.)

Most of the ionospheric models used for communication predictions are empirical models based on world-wide observations of the ionosphere over the past four decades. Observations of the main parameters of the ionosphere, foE, foF1, foF2, M(3000)F2, and Es have been used to produce worldwide contour maps of monthly median values of these parameters for each hour of each month and for low and high levels of solar activity. An example of such maps is given in Figure 10-45. To calculate the maximum usable frequency (MUF) for a given circuit, hour and month, the values of foF2 and M(3000)F2, for example, are determined by interpolation in the appropriate world map for the expected point(s) of reflection of the signal. For a level of solar activity other than the low or high levels for which the maps are drawn, values of the ionospheric parameters are obtained by interpolating in each of the low and high activity level maps and then interpolating again in these results to find the values appropriate to the given level of activity.

In practice, the only prediction actually performed in making predictions of suitable HF operating frequencies is that of the general level of solar activity that can be expected to pertain at the epoch for which the predictions have been made. This prediction is usually made in the form of some ionospheric or solar index, which is a single parameter describing the gross behavior of the ionosphere, and which is used to drive the computer program. The most common index used for prediction programs such as the U.S. programs IONCAP and ITS-78, and by the CCIR, is the average sunspot number,  $R_{12}$ . However, Wilkinson [1982] has shown

## CHAPTER 10

A PLOT FOR BRISBANE JUNE 00UT

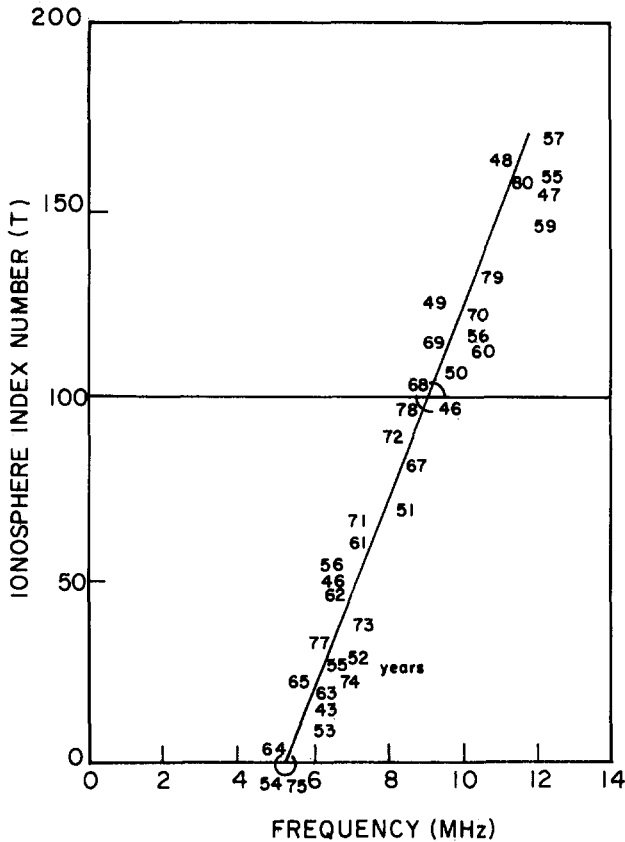


Figure 10-52. The variation of the monthly median value of foF2 for June, 00 UT, at Brisbane, Australia, as a function of the ionospheric index, T. Each data point represents the value for June for years 1943–1980.

that any index based on the ionosphere itself, such as IF2 [Minnis and Bazzard, 1960] is usually preferable to a purely solar index such as  $R_{12}$ . Figure 10-52 illustrates the relationship between the ionospheric index, T [Turner, 1968; Turner and Wilkinson, 1979] and the monthly median values of foF2 at Brisbane, Australia for 00 UT in June (10 LT). Each data point represents data for June in the years 1943 to 1980. The low dispersion of the data points about the regression line indicates the usefulness of the T index for describing ionospheric conditions. The selection of the correct index for some future epoch will become more uncertain as the lead time increases because of our general inability to predict the detailed behavior of the sun.

Predictions of the main critical frequencies and heights of the ionosphere, together with some simple geometry (Section 10.4.2), are adequate for the calculation of the appropriate frequencies to use for communication on a given circuit. It is also possible to determine elevation angles of the possible propagation modes (and thence choose a good antenna) and to determine the conditions under which some adverse propagation conditions will exist.

The calculation of the transmitter power required to yield

an appropriate signal-to-noise level at a receiver site is a much more complicated procedure than the calculation of the MUF. The required transmitter power is of no small matter since the cost of the transmitter increases dramatically with the power. The noise level may be either measured at the site or estimated from empirical data bases such as provided by CCIR. See for example Davies [1966, Chapter 7] and CCIR [1963].

There are two other main concerns here, the antenna and the transmitter, but let us assume that an appropriate antenna with a known gain has already been selected. To calculate the required transmitter power, we need to calculate the losses. These include deviative and non-deviative absorption losses, basic free-space transmission loss, multihop ground reflection loss, polarization coupling loss, sporadic E obscuration loss and horizon focus gain (a negative loss). The largest of them is the free-space loss, and this increases with the length of the propagation path.

Because the circuit losses depend on the propagation path, all possible paths must be considered and compared. Reliable determination of the actual propagation paths requires a reliable model of how the electron density varies with altitude up to the peak of the F2 layer. Suitable models of this  $N(h)$  variation have been developed by Bradley and Dudeney [1973], among others. As well as being an accurate representation of the real  $N(h)$  distribution, such a model must also be computationally simple because it is used many times in the determination of the virtual reflection heights,  $h'$ , and thence the possible propagation modes. The International Reference Ionosphere [Lincoln and Conkright, 1981] may also be used to deduce an  $N(h)$  profile, but this model has not been designed for the speed that is required in routine field strength calculations.

The ionospheric models currently available for use in studies of HF propagation have been reviewed by Dandekar [1982] and Goodman [1982] (see also Section 10.3). Full descriptions of the techniques used to calculate field strengths at a receiving site are given by Davies [1966, Chapter 7], Lloyd et al. [1978] and CCIR [1970, 1978]. A straight forward approach to obtaining MUF's for various modes and their respective path losses which also permits the inclusion of realistic antenna patterns for transmit and receive sites is available in the IONCAP program [Lloyd et al., 1978]. The model computations are based on a three layer (F2, F1, E) representation of the electron density profile with ITS78 coefficients being used to determine the ( $R_x$ -dependent) foF2 value. The ionospheric parameters are evaluated at the reflection points and two dimensional ray tracing is applied, assuming local horizontal stratification. For the most reliable results, simplistic approaches to propagation mode determination must be replaced by ray tracing techniques such as described by Davies [1969, Chapter 7]. These techniques are essential when large horizontal gradients exist in the ionosphere, but are rarely used for routine calculations because they are very time consuming.

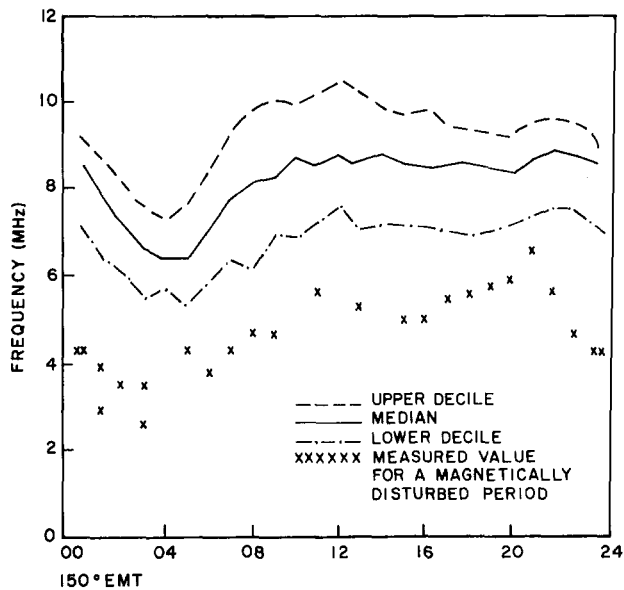


Figure 10-53. Plot of the observed values of foF2 at a midlatitude station, December 1980, as a function of local time. At each hour there are 31 data points. 80% of observations lie within the dashed upper and lower decile curves.

### 10.4.5 Problems with HF Communications

The use of the ionosphere for communication, broadcasting, and surveillance is fraught with difficulties, some of which have already been mentioned. Predictions of the MUF, LUF, and field strengths rely on median models of the ionosphere and can therefore specify only mean propagation conditions. A knowledge of the spread of values about the median is required for successful communication for more than 50% of the time, and such statistics are in fact usually provided by the better prediction programs. For quiet, undisturbed conditions, this spread about the median is typically 15%–20%. See for example Figure 10-53.

Even when conditions are undisturbed and the communicator has chosen an appropriate operating frequency, antenna, and transmitter power, propagation problems are still encountered. Some of these are associated with events on the sun and will be discussed in Section 10.4.6. Here we wish to consider some problems that can occur even when the ionosphere is being cooperative.

**10.4.5.1 Multipath Propagation.** We have already seen in Section 10.4.3 that propagation will normally occur by several paths, for example, the 1F and 2F modes (see Figure 10-50). The received signal will be the vector sum of all waves arriving at the receiver. If the different signal paths change with time in different ways, deep and rapid fading may occur, sometimes causing the signal level to drop below the local noise level. Different modulation techniques are affected in different ways by this multipath fading.

Multipath propagation may sometimes be eliminated from

a circuit by choosing a frequency that is supported by only one propagation mode (for example, use a frequency above the 2F MUF but below the 1F MUF) or by choosing an antenna that heavily favors one propagation mode. Diversity techniques, in which the same information is sent in two or more ways and recombined at the receiver, can also be used to overcome the effects of fading. Example are space (spaced antennas), frequency, angle of arrival, and polarization diversity.

**10.4.5.2 Sporadic E.** Sporadic E is a two-faced phenomenon having both advantages and disadvantages. There is no doubt that when a strong sporadic E layer is present, it presents an ideal propagation mode suitable even for medium speed digital data transfer. However, a dense Es layer can screen the F layer, preventing signals from ever reaching that layer and causing Es-F combination propagation modes that may have none of the desired characteristics—the signals may miss the target or may arrive at an angle not specified in the original receiving antenna design. Many prediction schemes for HF propagation include statistical occurrence rates for Es propagation modes, but the Es layer remains essentially unpredictable.

**10.4.5.3 Problems in High Latitudes.** After major solar flares with particular characteristics, high energy protons penetrate into the lower ionosphere at the poles and causes wide-spread and long-lasting disruptions to HF communications. The polar cap absorption event is discussed briefly in Section 10.4.6. The penetration of electrons with energies in excess of 10 keV into the D region leads to increased absorption in the auroral zone. This auroral absorption may have severe consequences for circuits crossing the auroral zone, but strong absorption is usually limited geographically to patches a few hundred kilometers in extent and the duration is typically half an hour to a few hours.

An important feature of the undisturbed high latitude ionosphere is the great variability in space and time. This variability severely limits the usefulness of a median model of the ionosphere. The F region trough, which marks a transition between the midlatitude and high-latitude ionospheres, can have severe and detrimental effects on signals propagating through it. The sharp gradients at the walls can cause reflections and result in off-great-circle propagation.

Propagation in the auroral region may introduce rapid and severe fading of HF signals. Diversity techniques or some sort of real time channel evaluation technique (see Section 10.4.9) therefore become almost mandatory.

The polar cap ionosphere in darkness, of importance to long distance HF communication between higher latitude stations such as in Canada and northern Europe, is essentially unpredictable for HF purposes. Enhanced F ionization regions resulting from particle precipitation are randomly distributed within a low density background ionization. Especially during slightly disturbed conditions polar cap plasma convection moves high density particles anti-sunward at

## CHAPTER 10

high velocities (Buchau et al, 1983). These changes will result in rapid MUF and mode variations and will in general lead to poor channel performance. MUF variations of typically several MHz from hour to hour and day to day were observed on an arctic link [Petrie and Warren, 1968]. In summertime the F1 mode tends to dominate the mid-morning MUF, and during winter/solar minimum conditions Es modes over transpolar circuits (for example, Andoya, Norway to College, Alaska) have a greater than 50% occurrence [Hunsucker and Bates, 1969].

**10.4.5.4 Problems in Low Latitudes.** HF communication problems at low latitudes due to steep spatial and temporal gradients have been discussed by Lakshmi et al. [1980]. The very steep gradients in foF2 during sunrise hours give rise to several difficulties [Lakshmi et al., 1980]:

1. HF link operators are expected to get their frequencies cleared from the appropriate governmental authority well in advance and it is usual practice to fix one frequency for the daytime and another for the nighttime. The use of the night frequency during sunrise will require much more power than is normally permitted while the frequency allocated for the daytime will be higher than the MUF during the transition period.

2. Point-to-point links normally use inexpensive tuned directional antennas, and frequent change of operational frequency is deleterious from the point of view of antenna efficiency.

3. In the case of long distance circuits in the east-west direction involving multi-hop F region propagation, the problem of the sunrise period will extend to a large number of hours, because the different F region reflection points will fall in the sunrise transition location at different periods.

The steep gradients associated with the equatorial anomaly cause problems with north-south circuits. For example, if we consider the anomaly peak in the northern hemisphere to be at 15°N geomagnetic latitude, if a north-south HF circuit is operating such that the reflection point is on either of the sides of the peak, and if the frequency of the link is very close to the MUF, a peculiar situation arises. If the point of reflection is equatorward of this anomaly peak, the radio waves incident on the ionosphere for the northern circuit will continuously encounter increasing levels of electron density due both to the vertical gradient as the radiowave penetrates higher into the ionosphere and the horizontal gradient as the wave progresses in the direction of increasing electron density. On the other hand for the same link in the return direction, the horizontal gradient is reversed. Thus the real MUF values for the two opposite directions in the same circuit can vary by a large margin depending on the angle of incidence and on the magnitude of the horizontal gradient. In fact, rather frequently, especially when the operating frequency is close to the MUF (calculated ignoring horizontal gradients), only one way communication would be possible. This has been one of the

unusual complaints in the Indian Subcontinent [Lakshmi et al., 1980].

**10.4.5.5 Spread F and Irregularities.** Small scale irregularities of ionization seem to exist at every level of the ionosphere superimposed on the background of ionization discussed in previous sections. They affect the propagation of radio waves and their characteristics may, therefore, be determined by radio techniques (see for example, Rishbeth and Garriott, [1969], Section 6.4). When seen on ionograms, the presence of irregularities is described as “spread F”, the spreading being either in the range or frequency domain. The corresponding descriptions are “range spreading” and “frequency spreading”, and parameters describing this spreading are scaled routinely from ionograms [Piggott and Rawer, 1972]. Many morphological studies of spread F, showing its diurnal, seasonal, solar cycle and latitudinal variations, have been published (see for example Herman, [1966] or Singleton, [1980], and references cited therein). An earlier review of spread F and some of the effects on radio propagation has been given by Newman [1966]. Most morphological studies of spread F have been concerned with frequency spreading. The characteristics of range spreading are, however, quite different and only a few studies of this type of variation have been made (see for example Cole and McNamara, [1974]). At equatorial regions, range spreading is often associated with the large scale electron density depletions known as bubbles or plumes [Basu et al., 1980c; Tsunoda, 1980; and Tsunoda et al., 1982].

The effects of irregularities on radio propagation are most important on paths that cross the equator when propagation actually relies on the presence of the irregularities [Nielson and Crochet, 1974]. Most recent efforts on describing the effects of irregularities on communications have concentrated on the effects of irregularities on trans-ionospheric propagation, where the problem of scintillation is encountered. This subject is covered in Section 10.7, this Chapter.

### 10.4.6 Disturbances to Normal Communications

We have previously seen that HF communications are subject to sudden and often large disturbances due to events that originate on the sun. Solar flares can cause immediate and complete absorption of HF radio waves by greatly enhancing the absorption suffered as the waves pass through the D region. These events, called short-wave fadeouts (SWF), are due to increased ultraviolet and x-ray fluxes, and can therefore occur on only the sunlit side of the earth. Major flares can also eject a stream of protons which can penetrate the ionosphere near the magnetic poles and give rise to complete blackout of HF communications in polar regions. Such events are called polar cap absorption events (PCAs) and can last for days depending on the size of the flare and

## IONOSPHERIC RADIO WAVE PROPAGATION

how well it is connected magnetically to the earth. The SWFs, on the other hand, usually last from a few minutes to a few hours at the greatest and are most severe at low latitudes (see Section 10.5).

Many large flares also eject a cloud of plasma, which if geometrical and interplanetary magnetic field conditions are favorable, can intersect the earth's magnetosphere and cause both geomagnetic and ionospheric storms. The geomagnetic storm, in which the earth's magnetic field is usually depressed below its normal quiet day value, is a result of a strong enhancement of the ring current and of no intrinsic interest to the HF communicator, but is a useful and readily available indicator of an accompanying disturbance to the ionosphere and thus to communicators. The ionospheric storms are of concern, however, especially when the effect of the storm is to decrease the MUF on a circuit to well below the predicted levels.

The physics of ionospheric storms is not yet completely understood, but it is well established that both electric fields and thermospheric winds (see Chapter 17) play a role. See for example Hargreaves [1979, Chapter 11].

The effect of a storm at a given location can be either to increase the value of foF2 (a so-called positive phase or enhancement) or to decrease the value of foF2 (a negative phase or depression), or to do both, a long depression following short enhancement. What actually happens depends on such things as local time of onset of the storm, station latitude, and season. During winter, most storm effects tend to be enhancements, whereas in summer and equinox depressions often follow short-lived enhancements. It is the depression that causes the major communications problems—the enhancements often go unnoticed by communicators. Major depressions last typically for a day and can decrease the MUF by a factor of two. Storm effects are much more marked at higher latitudes (see for example Rishbeth and Garriott, [1969], Chapter 8).

The lower regions of the ionosphere are not usually affected during ionospheric storms and the lower frequency limit for HF communication remains unchanged.

Ionospheric storms due to solar flares are a high solar activity phenomenon. However, ionospheric storms also occur away from the peak of the solar cycle. These are attributed to enhanced solar wind streams emanating from magnetically open features in the corona known as coronal holes. As the stream sweeps over the earth, the electric currents flowing in the magnetosphere and ionosphere are modified, yielding both geomagnetic and ionospheric storms. These storms are called recurrent storms because they tend to recur every 27 days (solar rotation period as seen from the earth) as the solar wind stream passes over the earth again. The effects on the ionosphere are usually less marked than those of a flare-induced storm but can last longer (a few days) because of the time taken for the stream to pass over the earth.

The scientific community keeps a 24-h watch on the sun

through an international effort coordinated through the IUWDS (International Ursigram and World Days Service) and many national agencies issue forecasts of solar and geophysical conditions. This effort has been described, for example, by several authors in Volume 1 of Donnelly [1979], including Heckman [1979]. CCIR Report 727 [CCIR, 1981c] gives a review of the subject and refers to many of the latest available papers.

The USAF Air Weather Service (AWS), through its operational centers of the Air Force Global Weather Central (AFGWC), provides space environmental support to the entire Department of Defense. The overall driving requirement is to minimize system effects caused by impulsive solar/geophysical activity and ionospheric variations. The techniques for geophysical forecasting used at AFGWC have been described by Thompson and Secan [1979]. A major advance in observational equipment during the last decade was the deployment of the new solar observing network (SOON) and radio solar telescope network (RSTN). With the data from SOON, RSTN and x-ray data from satellites, AFGWC can provide a real-time comprehensive analysis of a flare and its effects on the space environment.

The action taken by an HF user to overcome the effects of these disturbances depends on the nature of the disturbance. During a SWF, a move to higher operating frequencies is appropriate since the absorption decreases with increasing frequency. During the negative phase of an ionospheric storm, lower frequencies must be used. The effect of a PCA, on the other hand, is normally so severe that it becomes necessary to reroute the traffic around the disturbed area. This usually requires avoiding the whole high latitude ionosphere.

### 10.4.7 Unusual Propagation Modes

The usual monthly-median HF predictions normally assume simple propagation modes such as the 1F and 2F modes and in general these predictions are quite successful. Some prediction systems also include Es and such propagation modes as 1Es and Es-F. However, it is found in practice that other unusual propagation modes can also exist. In general these unusual modes have one feature in common—they rely for their support on some particular feature of the ionosphere that is restricted in latitude. We shall consider here a few examples of such modes.

Possibly the most useful propagation mode not normally predicted is the F<sup>2</sup> super-mode encountered on transequatorial circuits during periods when the equatorial anomaly is well developed, that is, during the afternoon and early evenings, during equinoxes, at high levels of solar activity. This mode involves two F region reflections without an intervening ground reflection and is characterized by high signal strength, low fading rates and an MUF 10-15 MHz higher than for the normal (2F) mode. It is often described as the afternoon-type TEP (transequatorial propagation) mode.

## CHAPTER 10

A second mode associated with the equatorial ionosphere, and which can coexist with the afternoon-type TEP mode in the early evening, is called the evening-type TEP mode. It is characterized by strong signals, rapid flutter fading and frequencies well above the normal 2F MUF. A propagation frequency of 102 MHz has been regularly observed on a Japan-Australia circuit. The propagation mode in this case is probably a ducted mode, the signals traveling within the walls of equatorial “bubbles” [Heron and McNamara, 1979 and Winkler, 1981]. This mode is also most likely to occur during the equinoxes at solar maximum. A review of TEP has been published by Nielson and Crochet [1974].

Enhancements of the MUF on transequatorial circuits have also been attributed to combination modes in which one hop is via a reflection from the equatorial Es belt which stretches a few degrees either side of the magnetic equator [McNamara, 1974a]. In an Es-F combination mode, the MUF is enhanced because the F layer hop is longer than the usual hop length on a 2F mode. Similar MUF enhancements on nighttime circuits have been attributed to a combination mode in which one hop relies on scatter from F layer irregularities [McNamara, 1974b]. Propagation above the MUF due to scatter by small scale irregularities can routinely be observed [Rawer, 1975].

The high latitude also produces its share of unusual propagation modes, mostly because of the presence of the midlatitude trough. Strictly speaking, the modes are not different from those expected—they are just heavily affected by the presence of the trough.

Another interesting propagation mode is the round-the-world (RTW) propagation mode. This mode relies on aspects of the vertical distribution of electron density rather than on latitudinally localized features of the ionosphere. Consideration of observed elevation angles, signal losses and time delays have led to the conclusion that RTW signals propagate via a chordal mode of propagation, rather than by a uniform multihop mode.

### 10.4.8 Short-Term Forecasting of HF Conditions

Long-term predictions of monthly median parameters of the ionosphere such as described in Section 10.4.4 are the traditional approach to frequency management. Frequencies are selected which should ensure at least a 90% success rate for communications at all times of day, during any season, and at all parts of the solar cycle. Engineering decisions such as transmitter power and antenna configuration are also made at this stage. Optimum working frequencies (OWF) are derived for each hour of the day, usually for a month at a time, using empirically derived frequencies and signal-to-noise ratios. Use of predictions in this manner continues to provide acceptable, though not high quality, communications for many purposes such as voice and telegraph con-

ditions. For a survey of the historical development of forecasting methods for HF propagation see Rawer [1975].

The effects on the ionosphere and communications of solar disturbances which cause ionospheric storms have been discussed in Section 10.4.6. However daily values of foF2 and MUF are known to vary by about 15% to 20% from the monthly median values during quiet times as well as during ionospheric/magnetic storms. See, for example, Figure 10-53. These variations may be superimposed on slower upward or downward drifts in values over several days. It is desirable to predict all of these variations for the purpose of efficient radio communications.

There are several possible approaches to the short-term forecasting of ionospheric parameters.

1. Using associated geophysical parameters.
2. Using the ionospheric parameters themselves.
3. Using ionospheric indices.

The day-to-day variability of foE and foF1 is so small that monthly median values of these parameters can be used to represent the daily variation in the E and F1 regions [Rush and Gibbs, 1973] and therefore offer little difficulty.

Short-term forecasts of foF2 have been made by relating changes in foF2 to corresponding changes in selected solar and geophysical variables such as the 10.7 cm solar flux and the geomagnetic index Kp [Bennett and Friedland, 1970; Ichinose et al, 1980]. The disadvantage of this type of approach is that the independent variables upon which changes in foF2 are assumed to depend must themselves first be predicted. Even if this is done successfully, only limited success is possible because the correlations of these parameters with parameters of the ionosphere are not very high.

A more successful approach to the short-term forecasting of foF2, or alternatively of an operational MUF on a given circuit, is a prediction scheme based directly upon immediate past observations of foF2 or an operational MUF. Such prediction schemes for foF2 are described, for example, by Rush and Gibbs [1973], Lyakhova and Kostina [1973], McNamara [1976], and Wilkinson [1979].

Rush and Gibbs [1973] used a five-day weighted mean value of foF2 to predict daily and hourly values of that parameter. The method of Lyakhova and Kostina [1973] is based on the observation that correlation coefficients between the deviations of foF2 from median values remain greater than 0.5 for up to four hours. The high correlation between hour-to-hour variations of foF2 has been discussed by Lyakhova [1960], Radinov [1963], Gautier and Zacharisen [1965] and Rush [1972].

McNamara [1976] made predictions of foF2 at a particular location up to 3 hours ahead by projecting forward the trend in the departures of the last few hours' observations from a 15-day running median. Wilkinson [1979] on the other hand, simply projected forward in time the deviation of an observed foF2 value from the predicted monthly median value of foF2. He found this technique to be effective for lead times of up to about 3 hours.

Similar techniques have been applied to oblique circuits

by Ames and Egan [1967], Ames et al. [1970], Krause et al. [1970, 1973a,b], D'Accardi [1978], and Uffelman and Harnish [1982].

The success of any of these forecasting schemes will depend on the particular circumstances of its intended use, especially as regards the required accuracy of the forecast and the lead time required. Most schemes are reasonably successful in forecasting an operational MUF that is closer to the actual value than is the predicted monthly median value, but only for lead times of the order of an hour or less.

Forecasts can be made with different lead times, depending on how closely the variations in the ionosphere need to be tracked, and the sampling interval for actual observations must match that lead time. In general, the error in the forecast values will increase with the lead time and if this error becomes too great, the forecasting scheme would offer no advantages over the use of a monthly median value.

To make short-term forecasts for circuits for which no real-time observations exist, the behavior of the ionosphere must be inferred from such data as are available, using these observations to infer the values along the required circuit. Numerous studies have reported correlation coefficients that illustrate the degree to which hourly deviations from median values of ionospheric parameters at two or more locations are related [Gautier and Zacharisen, 1965; Zacharisen, 1965; Zevakina et al., 1967; Rush, 1972]. These correlations may be used to infer values of foF2 at locations remote from the observing site, with an error depending on the separation of the two locations in latitude and longitude, and on the local time and season. Rush [1976] has used the observed correlations to establish the usefulness of, and requirements for, a network of ground-based and satellite-borne ionospheric observations whose measurements are to be used for short-term forecasting of radio propagation conditions. However, it should be noted that the relatively high correlations used by Rush originate from the very disturbed days (that is, ionospheric storm days) and these same high correlations are not always obtained for days when the deviations from the median values are relatively small.

A third approach to short-term forecasting is to use observations at all available ionospheric stations to determine an effective ionospheric index, which can then be used in conjunction with synoptic monthly median maps of foF2 and other parameters (see Section 10.4.4) to predict the values of these parameters at the reflection points of the given circuit. The limitations of this technique are set by the accuracy with which an appropriate index can be determined from a restricted subset of observations and the accuracy with which the ionospheric model, driven by this index, can reproduce the actual ionosphere at the reflection points. An example of the use of ionospheric indices to update models of the ionosphere has been given by McNamara [1979]. Other, more complicated, methods have been described by Thompson and Secan [1979] and Tascione et al. [1979]. Actual forecasts of propagation con-

ditions requires the projection forward in time of the effective ionospheric index. In the limit of zero lead-time, the "forecast" in fact becomes a real-time assessment of the ionosphere.

A brief review of short-term forecasting for HF propagation has been given by CCIR [1981b]. The special case of high latitude propagation is considered in CCIR [1983].

### 10.4.9 Real Time Channel Evaluation

To take full advantage of the HF communications potential of the ionosphere and to overcome its inherent variability, frequency management should be implemented in three stages, namely long-term predictions (Section 10.4.4), short-term forecasting (Section 10.4.8) and real-time channel evaluation (RTCE). It is at the first stage that engineering decisions such as site location, antenna configuration, and transmitter power are made, and suitable operating frequencies applied for from the appropriate regulating body. The second stage, that of short-term forecasting, determines which of the allocated frequencies will actually propagate now or a short time ahead. These two stages are generally all that would be required for voice and low-speed telegraphy circuits.

This two-stage approach has several limitations:

1. The signal-to-noise data are not always reliable and this ratio is not necessarily a useful criterion for choosing frequencies for some forms of communications.
2. Reliable long-term predictions of sporadic E are not available. (Es modes are often the best to use.)
3. No account is taken of interference from other users.
4. The forecast available frequency range will be uncertain to some extent because of inevitable errors in the forecasting models.
5. The approach does not indicate which of the assigned frequencies propagating at a given time would be the best to use for a given form of communication.

RTCE is the third stage of a frequency management system required to maintain reliable high quality HF communications even under the most adverse conditions. It becomes especially important for medium and high speed digital data transfer. With an RTCE system, all channels are sounded in turn to determine which is actually the best to use at a given time for the particular type of communication/modulation system.

Darnell [1978] has given the following definition of RTCE: "Real-time channel evaluation is the term used to describe the processes of measuring appropriate parameters of a set of communication channels in real time and of employing the data thus obtained to describe quantitatively the states of those channels and hence the relative capabilities for passing a given class, or classes, of communication traffic."

A review of RTCE has been prepared by Study Group 6 of CCIR [CCIR, 1981d], and the interested reader is

## CHAPTER 10

referred to that report. One of the more recently developed techniques of RTCE, which can serve as an example of the technique, is that of pilot tone sounding.

In pilot tone sounding [Betts and Darnell, 1975], low level CW tones are either inserted into the data spectrum or transmitted in potentially available alternative channels. At the receiver, simple measurements on the tones enable the relative states of the channels to be specified in terms of predicted (digital) data error rates. In a situation where a multicomponent broadcast is being used to radiate identical data simultaneously on each of several frequencies, this type of RTCE system allows the best component to be selected automatically at the receiver.

One of the main advantages of the pilot-tone RTCE technique is the extreme simplicity of the concept and the implementation when compared with other techniques for RTCE, for example, oblique incidence ionosondes. A further advantage of the technique is that it permits RTCE and data signals to be combined in a simple format, rather than requiring a separate stimulus. The technique also lends itself readily to automation. With an automated system, there will be little difficulty in principle in including into the algorithm for selecting the optimum working frequency any measurements of other pertinent properties of the pilot tone, for example, amplitude, Doppler shift, and spectral width. The noise level in the channel could also be included.

The pilot-tone sounder technique does not permit the determination of the operational MUF or identification of propagation modes. The former may cause difficulties when the MUF is decreasing (for example, due to normal diurnal variation) if the working frequency is just below the MUF. Difficulties could be severe if the MUF changes significantly during the RTCE time (typically 3 min per channel).

The signal optimization problem at HF is potentially very complex and to date RTCE has been used almost exclusively as a frequency selection aid. Darnell [1975b] lists the various parameters on an HF link which could be under the control of the communicator and hence be made adaptive in response to the RTCE data:

- Transmission frequency
- Transmitter power level
- Bandwidth
- Data rate
- Modulation type
- Time at which the transmission is made
- Signal processing algorithm at the receiver
- Elevation angles for antenna array beams
- Diversity type

To this list may be added antenna polarization for near vertical incidence propagation.

The potential advantages accruing from the use of RTCE techniques have been summarized by Darnell [1975a]:

1. The effect of man made noise and interference can be measured and specified quantitatively [Darnell, 1978].
2. The facility for real-time, on line measurement of propagation and interference allows the use of relatively

transient propagation modes, for example, sporadic E layer propagation.

3. RTCE evaluation allows a more efficient use of the frequency spectrum by tending to select frequency channels higher than those which would be chosen via prediction techniques. Thus spectrum congestion is reduced.

4. RTCE will provide a means of automatically selecting the best frequency and simultaneously indicating preferred stand-by channels.

5. Transmitter power can be minimized, consistent with providing an acceptable quality of received traffic.

6. In the longer term, RTCE data can be used to adapt other parameters of a communication system, apart from frequency, optimally for the prevailing path conditions.

### 10.4.10 Conclusion

It has not been possible within the present limitations of space to present more than a cursory overview of the subject of HF propagation. However, it is hoped that most readers will be able to follow up on topics of special interest by going to the references cited. In this regard, the value of the proceedings of the "Boulder Workshop" (Donnelly, 1979; 1980) cannot be stressed too highly. The CCIR documents and the AGARD Lecture Series No. 127 should also prove very useful, but possibly somewhat harder to obtain.

## 10.5 IONOSPHERIC DISTURBANCES

### 10.5.1 Sudden Ionospheric Disturbance (SID)

The SID is caused by x-ray and ultraviolet emissions from solar flares. These emissions produce increased ionization of the sunlit ionosphere. This excess ionization typically lasts for a period of 10 to 60 minutes, depending on the intensity and duration of the responsible flare. SIDs are observed by monitoring manmade and natural High Frequency (HF) or Very Low Frequency (VLF) radio signals that propagate via the ionosphere. The various types of SIDs are named according to the method of their observation:

1. SWF—short wave fadeout: a decrease (either sudden or gradual) in the signal received from a distant HF (2–32 MHz) transmitter,
2. SCNA—sudden cosmic noise absorption: a decrease in the intensity of the constant galactic radio noise as measured by riometers (relative ionospheric opacity meters) operating between 15–60 MHz,
3. SPA—sudden phase anomaly: a change in phase of a received VLF (10–150 kHz) signal relative to a frequency standard at the receiving site,
4. SES—sudden enhancement of signal: an increase in the strength of an incident VLF signal occurring at the same time as an SPA,

5. SEA—sudden enhancement of atmospherics: an increase in the background VLF noise from distant thunderstorms,
6. SFD—sudden frequency deviation: a short-lived increase in the frequency of the signal from a distant HF transmitter,
7. SFE—solar flare effect or geomagnetic crochet: sudden variation in the H component of the earth's magnetic field.

The first five of these effects are all attributable to increased ionization in the D layer, primarily by soft (1–8 Å) flare x-rays. The absorptive effects (SWF and SCNA) are caused by a thickening of the absorbing layer through which the HF waves pass, while the effects on VLF signals are due to the lowering (SPA) and strengthening (SES and SEA) of the D layer from which these lower frequency waves are reflected. In contrast, SFDs arise from the flare associated increase in ionization in the E and F regions produced by extreme ultraviolet (EUV) radiation in the 10–1030 Å range. Finally, the geomagnetic crochet (SFE) appears to be a hybrid effect, having an impulsive component associated with the flare “flash phase” EUV emission, and a more gradual component associated with the flare soft (1–8 Å) x-rays [Richmond and Venkateswaran, 1971]. These ionizing emissions temporarily increase the D and E layer conductivity and alter the normal ionospheric currents to give rise to the SFE. For a comprehensive review of the SID phenomenon, see Mitra [1974].

## 10.5.2 Polar Cap Absorption (PCA)

While SIDs are caused by flare electromagnetic emission, PCAs result from bombardment of the ionosphere by flare-accelerated protons with energies  $\leq 10$  MeV. These particles stream into the earth's polar regions along geomagnetic field lines and produce increased ionization in the D layer (as well as aurora at E layer heights). PCAs are normally observed by means of riometers. In contrast to the SID, the PCA is a long-lived effect, with durations ranging from tens of hours to several days. In general, PCAs follow only the most intense solar flares and begin within a few hours after flare maximum, dependent on the flare longitude. A review of the PCA phenomenon has been published by Hultqvist [1969].

## 10.6 HF RADAR IONOSPHERIC CLUTTER

Backscatter reflections from E layer auroral ionization and F layer electron density irregularities can be an important source of clutter for a radar operating in the high latitudes. The ionospheric clutter can degrade the performance

of an over-the-horizon (OTH) radar designed for the surveillance of aircraft at ranges of approximately 1000 to 3500 km.

The radar reflections are the result of scattering from electron density irregularities aligned along the lines of force of the earth's magnetic field. The characteristics of the field-aligned scatterers are such that the radar echoes originate in a small range of angles about perpendicular incidence to the magnetic field lines and that the amplitude of the auroral echo is aspect-angle sensitive. In addition to the orthogonality condition, it is necessary that this geometric configuration take place at ionospheric altitudes, that is, 80 km and above.

The probability of observing radar reflections from ionization irregularities is also dependent upon the frequency of occurrence of E layer auroral or spread-F irregularity activity in the region of interest. Reflections can be expected to occur in regions where both the conditions of near-perpendicularity at ionospheric heights and high auroral or spread-F irregularity activity are satisfied. The fulfillment of only one requirement is not sufficient to warrant a radar reflection.

An appropriate model to use to define the condition of auroral activity is the Feldstein-Starkov [1967] auroral belt (oval) model. Since the location and extent of the auroral oval are a function of time and geomagnetic activity, E layer auroral echoes can be expected to appear over a wide area during magnetically disturbed periods for an HF backscatter radar located at high latitudes.

The F layer irregularities can be described in terms of the probability of occurrence of spread-F derived by Pennedorf [1962] or in terms of Aarons' [1973] irregularity scintillation region.

In this section, an estimate is made of the characteristics of ionospheric clutter that could be observed by an HF backscatter radar operating in the midlatitude with the antenna beam oriented towards the polar region. The topics to be discussed are the amplitude, the backscatter cross-sectional area, the angular extent, the Doppler frequency variation, the frequency of occurrence, the diurnal and seasonal variation and the correlation with solar-geophysical conditions.

### 10.6.1 Signal Amplitude

The amplitude of E layer auroral clutter that could be encountered by an HF backscatter radar is deduced by extrapolation of radar-auroral data recorded by SRI International at Fraserburgh, Scotland, during 1959 and 1960 [Leadabrand et al., 1965]. The radar measurements were made simultaneously at frequencies of 30, 401 and 800 MHz.

To predict the SRI International auroral data effects on an HF backscatter radar in terms of the corresponding radar, it is necessary to determine the relative sensitivities of the

## CHAPTER 10

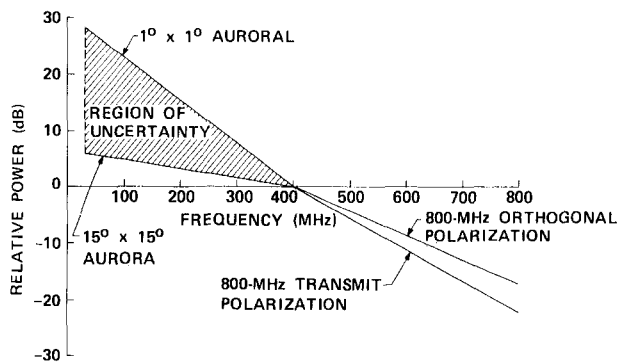


Figure 10-54. Relative signal strength of auroral echoes at 30, 401, and 800 MHz obtained by the SRI International-Scotland radars [Leadabrand et al., 1965].

radars to the aurora. This is accomplished by comparing the various parameters that enter into the radar equation.

According to the radar equation, the signal-to-noise ratio of the received signal is given by

$$\frac{P_r}{N} = \frac{P_t G_t G_r \lambda^2 \sigma}{(4\pi)^3 R^4 KTB \overline{NF} L_s L_p} \quad (10.60)$$

where  $P_t$  is the transmitted power,  $G_t$  and  $G_r$  are the gains of the transmitting and receiving antennas, respectively,  $\lambda$  is the wavelength,  $\sigma$  is the radar-target cross section,  $R$  is the radar range,  $K$  is Boltzmann's constant,  $T$  is the ambient temperature,  $B$  is the receiver noise bandwidth,  $\overline{NF}$  is the receiver noise figure,  $L_s$  is the system loss and  $L_p$  is the two-way loss due to the propagation medium. This relationship is applicable to a point target, that is, the antenna beamwidth is much larger than the dimensions of the target.

For aurora which fills the antenna beam,  $\sigma$  is replaced by the volume scattering coefficient,  $\sigma_v$ , that is, radar cross section per unit volume, such that, for a rectangular antenna,

$$\sigma = \sigma_v V = \sigma_v R^2 \beta_H \beta_V \frac{c \tau}{2}, \quad (10.61)$$

where  $V$  is the volume filled by the scatterers,  $c$  is the free space velocity,  $\tau$  is the pulse length, and  $\beta_H$  and  $\beta_V$  are the horizontal and vertical antenna beamwidth, respectively.

Figure 10-54 is a plot of the relative signal strengths of auroral echoes recorded by SRI International at the three frequencies in April 1960. The region of uncertainty between 30 and 401 MHz results from the fact that there was no way to specify to what degree the auroral scatterers filled the 30-MHz antenna beam. At 401 and 80 MHz, the antenna beamwidth was  $1.2^\circ$ , while at 30 MHz it was  $15^\circ$ . Thus, it was assumed that the scatterers completely filled the beam at the two higher frequencies. However, it was doubtful that the beam was completely filled at 30 MHz. The  $1^\circ \times 1^\circ$  aurora is assumed to be a point target for the 30-MHz antenna.

The data in Figure 10-54 are normalized with respect to 401 MHz. For a filled beam antenna, the relative signal strength of the 30-MHz echoes was 6-dB greater than those at 401 MHz, while, for the point target case, there was a 28-dB difference between the 30- and 401-MHz data.

The absolute magnitude of the 30-MHz auroral echoes can be deduced by comparing the system sensitivities of the 30- and 401-MHz radars. According to Table 10-9, the 401-MHz radar was 48.9-dB more sensitive than the 30-MHz radar assuming that the aurora was a point target and 26.9-dB more sensitive, assuming that the 30-MHz antenna beam was completely filled with scatterers. Thus, it follows that

Table 10-9. Comparison of SRI International-Scotland 30-MHz and 401-MHz radar sensitivities utilized in the April 1960 radar-auroral observations.

Parameter	30-MHz Radar	401-MHz Radar	Point Target (401 MHz/30 MHz) (dB)	Scatterers Fill Antenna Beam (401 MHz/30 MHz) (dB)
$\lambda^2$ (m <sup>2</sup> )	(10.0) <sup>2</sup>	(0.748) <sup>2</sup>	-22.5	-22.5
$P_t$ (Mw)	0.0015	0.12	+19	+19
$G_t G_r$ (dB)	40	84	+44	+44
$\beta_H$ (DEG)	15	1.2	-	-11
$\beta_V$ (DEG)	15	1.2	-	-11
$\tau$ ( $\mu$ s)	300	300	0	0
$B$ (kHz)	6	6	0	0
$\overline{NF}$ (dB)	9	4.5	+4.5	+4.5
$L_s$ (dB)	7	3.1	+3.9	+3.9
			+48.9	+26.9

# IONOSPHERIC RADIO WAVE PROPAGATION

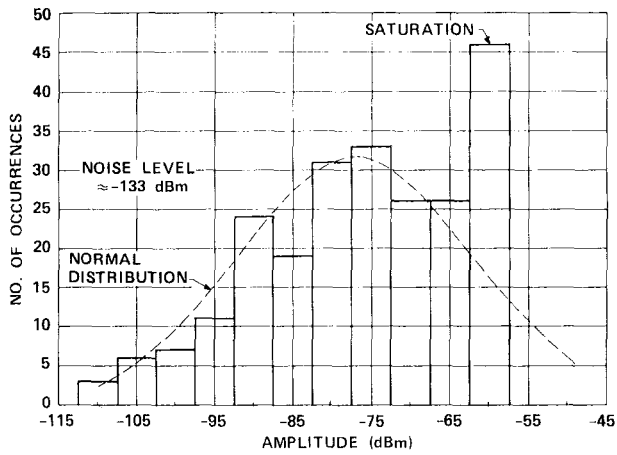


Figure 10-55. Amplitude histogram of SRI International 401-MHz Scotland radar auroral data [Leadabrand et al., 1965].

the magnitude of the 30-MHz radar-auroral data was 20.9-dB less than that of the 401-MHz data.

The amplitude distribution of the 401-MHz radar-auroral echoes is presented as a histogram form in Figure 10-55. The system noise level was approximately  $-133$  dBm and that the system saturated at  $-60$  dBm, which accounts for the large number of echoes at that amplitude.

The histogram data, when replotted as a cumulative distribution on probability paper, shown in Figure 10-56, closely fit a straight line. This characteristic is indicative that the 401-MHz amplitudes are log-normally distributed. The theoretical normal distribution function plotted in Fig-

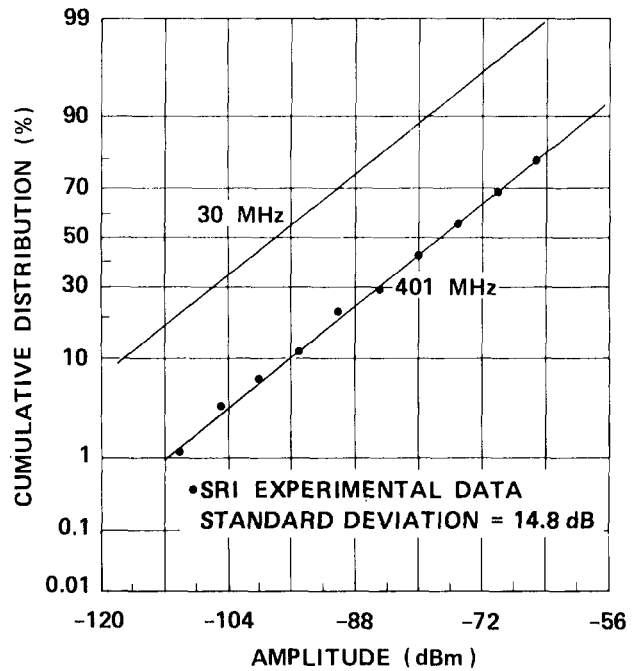


Figure 10-56. Cumulative distribution function of SRI International-Scotland radar auroral data.

ure 10-55 was computed utilizing the value of  $-77.2$  dBm for the mean as obtained from Figure 10-56. The 30-MHz amplitude data, also shown in Figure 10-56, was derived on the basis that the 30-MHz auroral echoes followed a Gaussian distribution and were 20.9-dB less than the 401-MHz results.

Table 10-10. Comparison of the sensitivity of an HF backscatter radar to that of the SRI International-Scotland 30-MHz radar.

Parameter	HF Backscatter Radar	SRI-Scotland Radar	Point Target (HF Radar/SRI) (dB)	Scatters Fill Antenna Beam (HF Radar/SRI) (dB)
$\lambda^2$ (m <sup>2</sup> )	(10.0) <sup>2</sup>	(10.0) <sup>2</sup>	0	0
$P_t$ (MW)	0.8	0.0015	+27.3	+27.3
$G_t G_r$ (dB)	45	40	+5	+5
$\beta_H$ (DEG)	5	15	-	-4.8
$\beta_V$ (DEG)	15	15	-	0
$\tau$ ( $\mu$ s)	400	300	-	+1.2
	10			-14.8
B (kHz)	2.5	6	+3.5	+3.8
	100		-12.2	-12.2
$\overline{NF}$ (dB)	12	9	-3	-3
$L_s$ (dB)	3	7	+4	+4
			( $\tau = 400 \mu$ s) +37.1 dB	+33.5 dB
			( $\tau = 10 \mu$ s) +21.1 dB	+1.5 dB

# CHAPTER 10

Table 10-11. Estimate of radar-auroral clutter levels of a hypothetical HF backscatter radar at 30 MHz based on SRI International data.

Statistical Parameter	Point Target		Scatterers Fill Antenna Beam	
	$\tau = 400 \mu\text{s}$ (dBm)	$\tau = 10 \mu\text{s}$ (dBm)	$\tau = 400 \mu\text{s}$ (dBm)	$\tau = 10 \mu\text{s}$ (dBm)
Upper Decile	-42.0	-58.0	-45.6	-77.6
Upper Quartile	-51.0	-67.0	-54.6	-86.6
Median	-61.0	-77.0	-64.6	-96.6
Lower Quartile	-71.0	-87.0	-74.6	-106.6
Lower Decile	-80.0	-96.0	-83.6	-115.6
Standard Deviation	14.8	14.8	14.8	14.8

To estimate the magnitude of the auroral echoes that could be observed by an HF backscatter radar, it is necessary to compare the sensitivity of the HF backscatter radar to that of the SRI International 30-MHz radar. The parameters of an hypothetical HF radar, considered in this analysis, are given in Table 10-10. For an assumed pulse length of 400  $\mu\text{s}$ , the HF radar is 37.1-dB more sensitive than the SRI International 30-MHz radar for the point target case and 33.5-dB more sensitive for the filled beam case. When the pulse length is decreased to 10  $\mu\text{s}$ , the difference in sensitivities decreases to +21.1 dB and +1.5 dB for the point target and filled beam case, respectively.

The predicted HF backscatter radar-auroral clutter levels at 30 MHz are presented in Table 10-11. The SRI International 30-MHz radar-auroral data given in Figure 10-56 and radar sensitivities in Table 10-10 are used in the calculations.

In deducing the radar-auroral signal levels at other frequencies in the HF band, it is assumed that the auroral echo power is frequency dependent according to the law

$$P = k f^{-n}, \quad (10.62)$$

where  $k$  and  $n$  are constants. Utilizing the data in Figure 10-54, it can be shown that for this power law  $n = 2.5$  for a point target and  $n = 0.5$  for the filled beam case. However, an examination of other radar-auroral data taken at Scotland revealed a value of  $n = 6.8$  for a point target and  $n = 2.7$  for a filled beam [Leadabrand et al., 1965]. An analysis of auroral echoes from simultaneous multiple frequency observations in Alaska by Leadabrand et al., [1967] revealed that  $n = 2$  for frequencies between 50 and 850 MHz and  $n = 5$  between 850 and 3000 MHz.

Radar backscatter measurements of artificial electron clouds in the E region of the ionosphere by Gallagher and Barnes [1963] yielded a constant,  $n$ , of 4 for frequencies between approximately 20 and 50 MHz and -4 between 5 and 20 MHz. At times, however, it was found that the amplitude returns were insensitive to frequency in approx-

imately the 10- to 20-MHz range. From simultaneous auroral echo measurements at frequencies of 49.7, 143.5 and 226 MHz, Flood [1960] has deduced a value of  $n = 3.5$  between 49.7 and 143.5 MHz and  $n = 6.5$  between 143.5 and 226 MHz.

Measurements of E region radar aurora at frequencies in the HF band and at VHF (143.8 MHz) from locations in Finland and Germany indicated a frequency dependency of  $n = 3$  [Oksman et al., 1979].

Since there is a wide discrepancy in the experimental measurements of the frequency dependence of auroral backscatter, which could be due to the characteristics of the auroral ionization, that is, inhomogeneous distribution of auroral electrons, varying scale sizes of ionization irregularities and different scattering altitudes, a value of 4 for the exponent in Equation (10.62) is assumed in this analysis.

The estimated median auroral clutter amplitudes that could confront the hypothetical HF backscatter radar in the 5- to 30-MHz band are shown in Figure 10-57. The external

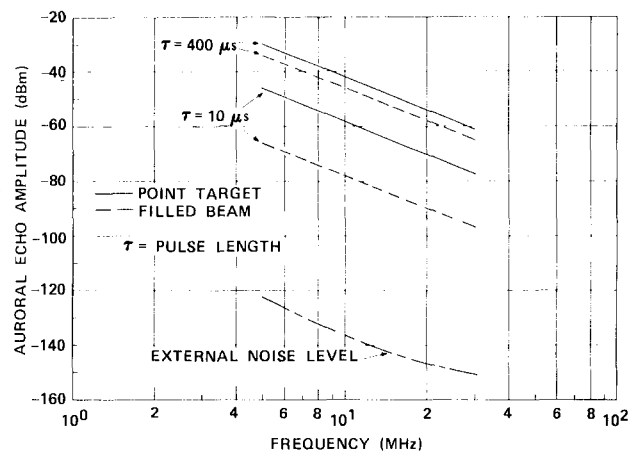


Figure 10-57. Estimated median auroral clutter amplitude based on SRI International-Scotland radar data,  $f^{-4}$  frequency dependency.

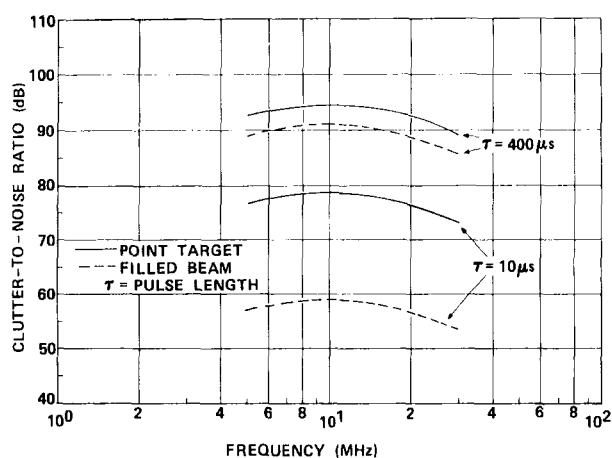


Figure 10-58. Estimated median radar-auroral clutter-to-noise ratio based on SRI International-Scotland radar data,  $f^{-4}$  frequency dependency.

noise level of a rural environment also shown in Figure 10-57 is the average median value as predicted for a location in Maine at an azimuth of  $60^\circ$  for all seasons, all times of day and a sunspot number of 70. It is seen that the auroral clutter amplitude increases with decreasing frequency and bandwidth and that the amplitude of the point target case is greater than that of the filled beam case.

Figure 10-58 is a replot of the data in Figure 10-57 in terms of the auroral clutter-to-noise ratio. It is of interest to note that, for a  $f^{-4}$  frequency dependency, the clutter-to-noise ratio maximizes in the vicinity of 10 MHz. This is due to the fact that the external noise level increases with decreasing frequency.

When a frequency dependency of  $f^{-2}$ , that is,  $n = 2$  in Equation (10.62), is assumed, the ionospheric clutter levels over the HF band are decreased, with respect to the  $f^{-4}$  estimates, by an amount of 15.6, 9.5, 6.0, 3.5 and 1.6 dB at 5, 10, 15, 20 and 25 MHz, respectively. As shown in Figure 10-59, the clutter-to-noise ratio for the  $f^{-2}$  case, monotonically increases with increasing frequency. The clutter-to-noise ratio at 30 MHz is 12.2 dB greater than that at 5 MHz. The upper and lower decile values of the data presented in Figures 10-58 and 10-59 are +19 dB and -19 dB with respect to the median level.

The height distribution of the auroral echoes observed by SRI International in Scotland was peaked at about 100 to 120 km, that is, in the E region, although heights as great as 200 km were observed. Thus, the data presented in Figures 10-58 and 10-59 can be considered to apply only to E region reflections.

It should also be mentioned that the amplitude distribution of the 401-MHz auroral echoes shown in Figure 10-55, which was used as a basis of extrapolation to the HF backscatter radar, was applicable to data obtained when the direction of propagation at the reflection point was perpendicular to the magnetic field lines. When directions of prop-

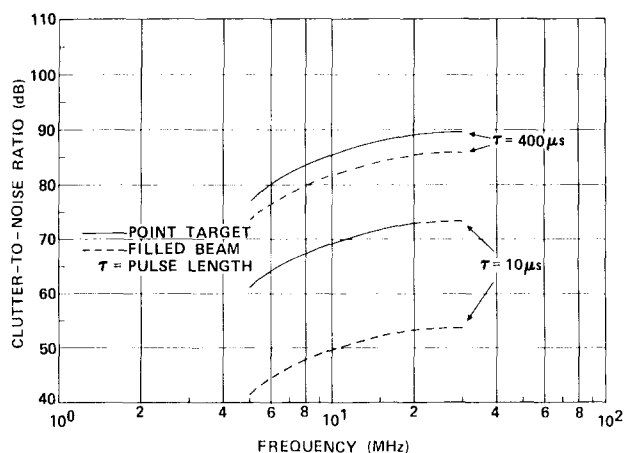


Figure 10-59. Estimated median radar-auroral clutter-to-noise ratio based on SRI International-Scotland radar data,  $f^{-2}$  frequency dependency.

agation and magnetic field lines are not orthogonal, the auroral clutter amplitude should decrease.

Bates and Albee [1969] report that, assuming a simple model of auroral backscatter from the E region that includes ionospheric refraction effects, a lower limit of 6 dB/deg in the 15- to 50-MHz range was observed for the aspect-sensitive decrease in backscatter cross section with off-perpendicular angle from the geomagnetic field. The aspect-sensitive decrease of the cross section of F layer backscatter echoes was found by Bates and Albee [1970] to be on the order of 5 dB/deg of off-perpendicularity from the magnetic field in the 6- to 15-MHz region. An aspect angle decay of 2 dB/deg at 30 MHz was deduced from the Scotland-auroral measurements by Leadabrand et al. [1965].

## 10.6.2 Cross Section

HF radar observations conducted at Caribou, Maine, under the Polar Fox II program, at frequencies of 8.125 and 14.875 MHz, during the period between December 1971 and November 1972 are used to estimate the cross section of ionospheric clutter.

The radar cross section given by Equation (10.61) can also be expressed by

$$\sigma = \sigma_v R \beta_H \frac{c\tau}{2} \Delta h \quad (10.63)$$

where  $\Delta h$  is the thickness of the aurora in the vertical direction. Since  $\Delta h$  was an unknown factor in the Polar Fox II experiment, it was assumed to be unity (1m). Thus, Equation (10-63) can be written as

$$\sigma = \sigma_A A = \sigma_A R \beta_H \frac{c\tau}{2} \quad (10.64)$$

## CHAPTER 10

Table 10-12. Average area scattering coefficient of E layer and F layer irregularities based on Polar Fox II data, January 1972.

Frequency (MHz)	Statistical Parameter	Area Scattering Coefficient (dBsm/m <sup>2</sup> )	
		E Layer	F Layer
8.125	Upper Quartile	-34.2	-27.2
	Median	-47.6	-33.6
14.875	Lower Quartile	-58.6	-42.0
	Upper Quartile	-56.5	-37.1
	Median	-63.9	-47.2
	Lower Quartile	-74.0	-54.3

where  $\sigma_A$  is the area scattering coefficient and A is the area containing the scatterers.

The area scattering coefficients of E layer and F layer irregularities as deduced from the Polar Fox II data are given in Table 10-12. The data show the averages over all times in the month of January 1972, and over all azimuths in the 90° sector between -30° and +60° with respect to true North. It is seen that, for all the statistical parameters, the 8.125-MHz data are from 12- to 21-dB greater than the 14.875-MHz results. The most interesting feature of the basic data, from which Table 10-12 was derived, was the lack of evidence of the influence of the geographic locations of the ionospheric scatterers on the magnitude of the area scattering coefficient. It was hypothesized that the scattering coefficient would be greater in the northerly directions since this is the region encompassed by the auroral oval [Feldstein and Starkov, 1967].

The cross section of ionospheric clutter that could be observed by the HF backscatter radar is presented in Table 10-13. The calculations are based on an assumed radar range of 700 km for the E layer irregularities and 1500 km for the F layer irregularities. These ranges correspond to a ray path oriented at an elevation angle of 5° and intersecting the ionosphere at altitudes of approximately 100 and 300 km, respectively. For this configuration, the E layer scattering area evaluates to 95.6 dBsm and 79.6 dBsm for a pulse length of 400  $\mu$ s and 10  $\mu$ s, respectively. For the corresponding pulse lengths, the F layer scattering area is 99.0 dBsm and 82.9 dBsm. According to Table 10-13, it is evident that the F layer clutter cross section is about 10 to 20 dB greater than the E layer cross section at 8.125 MHz and 20 to 23 dB at 14.875 MHz. The differences between the F layer and E layer cross sections are most likely due to the fact that the F layer ionization level is many times that of the E layer.

It should be noted that the Polar Fox II estimates of the E layer and F layer area scattering cross section contain all the propagation loss terms, that is, the ionospheric propagation losses had not been removed from the calculations. Because of this, it is not possible to use the Polar Fox II data for extrapolation to other frequencies in the HF band.

### 10.6.3 Angular Extent

The angular extent of HF ionospheric clutter was determined from Polar Fox II radar data recorded in January 1972 at six frequencies ranging between 8 and 23 MHz. Figure 10-60 contains plots of the cumulative distribution of the angular extent of E layer, F layer, and the combined E and F layer clutter. According to Table 10-14 which

Table 10-13. HF backscatter radar—estimated average cross-section of E layer and F layer irregularities based on Polar Fox II data, January 1972.

Frequency (MHz)	Pulse Length ( $\mu$ s)	Statistical Parameter	Average Cross Section (dBsm)		Cross Section Ratio (dB)
			E Layer	F Layer	F Layer/E Layer
8.125	400	Upper Quartile	61.2	71.8	10.6
		Median	48.0	65.4	17.4
		Lower Quartile	37.0	57.0	20.0
	10	Upper Quartile	45.4	55.7	10.3
		Median	32.0	49.3	17.3
		Lower Quartile	21.0	40.9	19.9
14.875	400	Upper Quartile	39.1	61.9	22.8
		Median	31.7	51.8	20.1
		Lower Quartile	21.6	44.7	23.1
	10	Upper Quartile	23.1	45.8	22.7
		Median	15.7	35.7	20.0
		Lower Quartile	5.6	28.6	23.0

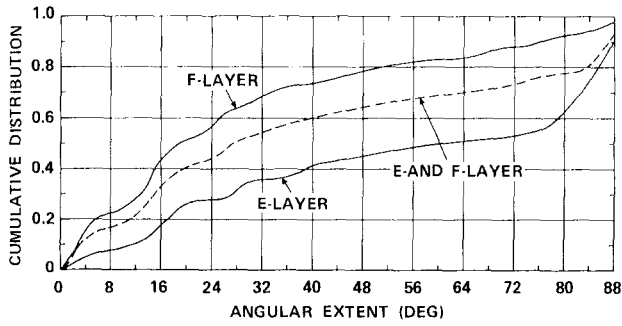


Figure 10-60. Cumulative distribution of the angular extent of ionospheric clutter based on Polar Fox II data.

summarizes the statistical characteristics of the three curves in Figure 10-60, the median values evaluate to 60.2°, 18.8° and 27.6°, respectively. The angular dimensions characterized in Table 10-14 were deduced from ionospheric clutter present only in the 1-hop propagation mode.

**10.6.4 Doppler Frequency Spectrum**

The Doppler spectrum of radar pulses reflected from the aurora differs from that of the original transmitted pulse. The changes that can take place are (1) the center frequency can be shifted, and (2) the spectral width can be increased.

The shift in the center frequency corresponds to a drift motion of the auroral ionization. Radar-auroral data indicate an east-west drift before magnetic midnight and a west-east drift after magnetic midnight [Leadabrand et al., 1965]. Drift velocities of the order of 500 m/s are typical. According to the analysis of E layer radar-auroral echoes recorded in Scotland at a frequency of 401 MHz, the maximum Doppler shift is normally ±2.15 kHz [Larson and Hodges, 1967].

The spread in the Doppler spectrum is due to the random, turbulent motion of the irregularities of electron density in the auroral ionization. According to Larson and Hodges

Table 10-14. Statistical distribution of the angular extent of ionospheric clutter based on Polar Fox II data.

Statistical Parameter	Angular Extent (Deg)		
	E Layer Clutter	F Layer Clutter	E and F Layer Clutter
Upper Decile	87.7	76.0	87.0
Upper Quartile	83.8	42.4	74.4
Median	60.2	18.8	27.6
Lower Quartile	19.0	10.0	13.6
Lower Decile	11.6	2.8	3.4

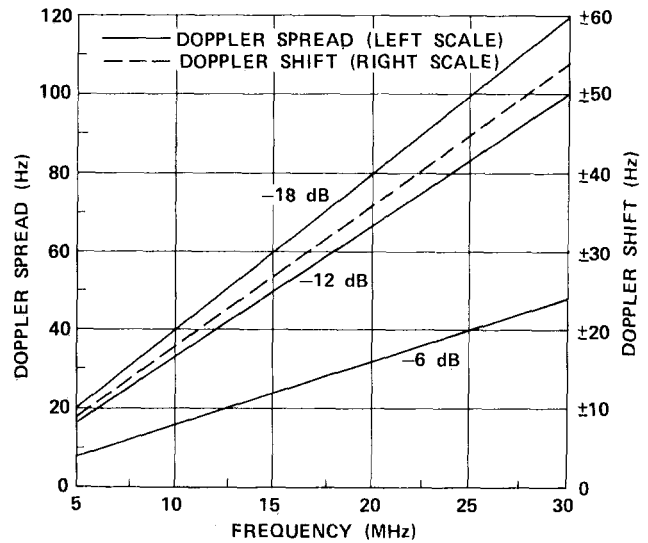


Figure 10-61. Estimate of E layer HF radar-auroral doppler frequency spread and shift based on SRI International-Scotland measurements at 401 MHz.

[1967], the maximum Doppler frequency spread at 401 MHz is on the order of 1.90 kHz at -6 dB below the peak, 4.00 kHz at -12 dB, and 4.75 kHz at -18 dB.

The expected (one standard) deviation of Doppler frequency shift and spread at HF is presented in Figure 10-61. The estimates are based on the fact that the Doppler frequency variations are directly proportional to frequency and on the assumption that shifts and spreads are normally distributed. Thus, the maximum shift and spread are equivalent to the 3-sigma (standard deviation) value of the distribution.

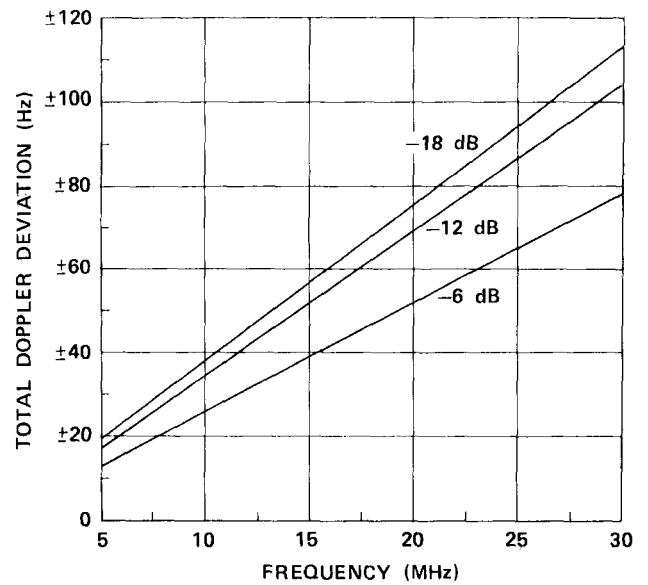


Figure 10-62. Estimate of E layer HF radar-auroral total doppler frequency deviation based on SRI International-Scotland measurements at 401 MHz.

## CHAPTER 10

At 10 MHz, the Doppler frequency shift evaluates to  $\pm 18$  Hz and the Doppler frequency spread becomes 16 Hz at the  $-6$  dB level, 33 Hz at  $-12$  dB and 40 Hz at  $-18$  dB.

The estimates of E layer HF radar-auroral total Doppler frequency deviation are plotted in Figure 10-62. At 10 MHz, it is possible that the 1-sigma value of the total Doppler deviation could be on the order of  $\pm 26$  Hz at the  $-6$  dB level,  $\pm 35$  Hz at  $-12$  dB, and  $\pm 38$  Hz at  $-18$  dB.

E layer radar-auroral echoes, having radial velocities as high as 1450 m/s, have been observed at 17 MHz by Brooks [1966]. This corresponds to a Doppler frequency shift of 164.3 Hz. The maximum radial velocity of F region field-aligned irregularities detected at 17.3 MHz [Baggaley, 1970] was found to be on the order of 165 m/s with a mean of 65 m/s. In terms of the Doppler frequency shift, these velocities evaluate to 19.0 and 7.5 Hz, respectively.

The extrapolation to the HF band of the Doppler measurements of E region irregularities conducted by Hofstee and Forsyth [1969] at a frequency of approximately 40 MHz, Balsley and Ecklund [1972] at 50 MHz, Balsley et al. [1973] at 50 MHz, Greenwald et al. [1975] at 50 MHz and Hal-doupis and Sofko [1976] at 42 MHz are in agreement with the results presented in Figures 10-61 and 10-62.

### 10.6.5 Frequency of Occurrence and Correlation with Solar-Geophysical Conditions

The experimental observations of field-aligned echoes at 19.4 MHz conducted over a three-year period (1961–1963) at a site located in the vicinity of Boston disclosed that the echoes were present for as long as 11 h/day [Malik and Aarons, 1964]. Although a seasonal pattern was clearly defined, there appeared to be a tendency for the reflections to occur on a greater number of days during the summer than during the winter. The correlation of echo activity with sunspot number was found to exist. For example, in 1961 when the sunspot number was 53, echoes appeared on 73% of the days at an average of 3.0 h/day. In 1963 when the sunspot number was 28, the echoes appeared on 55% of the days at an average of 1.5 h/day. Maximum echo activity occurred between 1800 and 2000 h local time.

A more thorough analysis of the 19.4 MHz field-aligned echoes recorded from 1961 through 1965 had been performed by the Air Force Cambridge Research Laboratories [Basu et al., 1973, 1974]. It was found that under quiet magnetic conditions field-aligned E layer echoes showed a summer evening maximum and appeared to be associated with the ground-backscatter echoes from sporadic E [Basu et al., 1973]. A weak secondary maximum existed in the winter with no detectable field-aligned echoes during the daytime. During disturbed magnetic conditions, the field-aligned E layer echoes increased with magnetic activity and appeared during the daytime with a corresponding decrease

in sporadic E. The data did not reveal a seasonal dependence.

Under quiet magnetic conditions, the field-aligned F layer echoes were found to be a sunset phenomenon and correlated with the sunspot cycle [Basu et al., 1974]. In general, the echoes occurred in the range from 1050 to 1500 km. However, during the daytime, long range echoes, at times, were observed at ranges of 3000 to 3300 km. An interesting disclosure was the fact that the occurrence of the F layer field-aligned echoes increased directly with the increase in magnetic activity until the level  $K_{Fr}$  (Fredericksburg, Maryland, three-hour K index) attained a value of four. Beyond this level, there was a decrease in the occurrence of the F layer echoes with no echoes being observed when  $K_{Fr} \geq 7$ . Radar auroral measurements made at Stanford University at a frequency of 17.3 MHz reveal that maximum auroral activity occurred between 1900 and 0400 hours local time [Peterson et al., 1955].

According to the HF radar echo observations conducted at 12 and 18 MHz in the state of Washington, there was a pronounced peak in the frequency of occurrence of the echoes from field-aligned irregularities near the time of local sunset [Hower et al., 1966]. The characteristics of the echoes detected at sunset were different from those occurring at night. It was found that the local sunset echoes appeared at ranges of about 2000 km and were generally spread in range (diffuse). The occurrence of the sunset echoes was relatively independent of magnetic activity. The nighttime echoes, on the other hand, appeared at ranges of about 1000 km and tended to display little spread in range (discrete). The occurrence of nighttime echoes was highly dependent on magnetic activity.

Hower et al., [1966] noted a decreasing echo activity with solar cycle, the maximum percentage occurrences during the nighttime being approximately 80% in December 1958, 37% in December 1963, and 35% in March 1964. The (Zurich) relative sunspot number during the corresponding period was 185.2, 11.8, and 14.5, respectively. Hower and Makhijani [1969] have concluded that HF F layer backscatter echoes arise from the same general irregularity regions in which spread F is detected.

Sprenger and Glöde [1964] have reported that the diurnal variation of the frequency of occurrence of radar-auroral echoes recorded from late 1958 to mid 1962 at 33 MHz at Kuhlungsborn (geographic coordinates: 54°N, 12°E; geomagnetic latitude: 54°N) showed a double maximum at approximately 0100 and 1700 hours local time. The probability of occurrence of E layer auroral echoes was found to be a function of magnetic activity. No auroral echoes were observed at a magnetic index,  $K_p < 5$ , and 100% occurrence at  $K_p = 9$ . With regard to the correlation of auroral echo activity with sunspot cycle, Sprenger and Glöde [1964] have concluded that the maximum of auroral activity occurred in 1960 about two years after the sunspot maximum and that the activity decreased to zero within a period of only one and a half years.

Brooks' [1965, 1966] investigation of radar-auroral echoes at 17 MHz conducted in 1959 and 1960 indicated that, for the discrete echoes, the maximum number appeared between 0000–0300 hours local time, and for the diffuse echoes, between 1900–2100 hours local time.

A maximum number of backscatter echoes at 13.866 MHz from the F region on 75% of the nights for March 1958 was reported by Weaver [1965]. A minimum number of echoes was observed in June, the data being collected during 1957 and 1958 at Ithaca, New York, with the antenna beam oriented in a northward direction.

Backscatter observations of F region field-aligned irregularities made at 17 MHz near Sheffield, England (geographic coordinates: 53.43°N, 1.58°W; geomagnetic latitude: 65.4°N) between mid-October, 1964, and mid-January, 1966, [Baggaley, 1970] which was a period of low sunspot activity, showed that, on the average, the echoes were present on 23.3% of the days while only 1.5% of the total observing time was occupied by the echoes. A summer maximum and a winter minimum were found to exist. This seasonal variation correlates with Malik and Aarons' [1964] results.

Baggaley [1970] noted that there was a correlation between the onset of F layer echoes and the solar zenith angle at the reflection point in the F layer (assuming a height of 300 km). That is, a maximum number of echoes occurred at a solar zenith angle of 90°–95°, and a minimum at angles less than 85° and greater than 125°. In addition, no correlation was found to exist between F layer echo occurrence and magnetic activity. Of the total time for which F layer echo activity was present, only 11% was associated with magnetic index  $K_p \geq 4$ .

Field-aligned echoes from the F region observed at Brisbane, Australia, at 16 MHz occurred preferentially during geomagnetic disturbances and correlated strongly with spread-F and radio star scintillations occurring in the same region of the ionosphere [Swenson, 1972].

An analysis of 29-MHz backscatter measurements carried out in Northern (West) Germany and Scandinavia (geomagnetic latitudes of 55°–77°N) by Czechowsky et al., [1974] confirmed the close correlation between radio-auroral occurrence and geomagnetic activity. Most of the radio auroras appeared in the afternoon and evening hours.

## 10.6.6 Conclusions

The radar-auroral clutter-to-noise ratio in the 5–30 MHz frequency range, as predicted from the SRI International radar data acquired in Scotland, is dependent on the frequency dependence law of the auroral backscatter echo power. Assuming a frequency variation of  $f^{-4}$ , the clutter level maximizes at approximately 10 MHz. When a  $f^{-2}$  law is assumed, the maximum clutter level is shifted to a frequency of 30 MHz.

For an assumed  $f^{-2}$  dependence, the radar-auroral clutter-to-noise ratio at 5 MHz is 15.6-dB less than that derived on the basis of an  $f^{-4}$  law. Assuming that the radar aurora is a point target, the clutter-to-noise ratio for a 400  $\mu$ s pulse is estimated to be 3.6-dB greater than that deduced for auroral scatterers that completely fill the antenna beam. For a 10- $\mu$ s pulse, the corresponding difference is 19.6 dB.

An analysis of the HF ionospheric backscatter data obtained in Maine under the Polar Fox II program reveals that the F layer cross section could be 10 to 20 dB greater than the E layer cross section at 8.125 MHz and 20 to 23 dB at 14.875 MHz.

The median value of the angular extent of E layer, F layer and combined E and F layer ionospheric clutter appears to be on the order of 60.2°, 18.8° and 27.6°, respectively.

Extrapolating from the SRI International-Scotland UHF radar-auroral data, it is estimated that for 5-MHz radar transmissions reflected from E layer auroral ionization, the 1-sigma value of the total Doppler frequency deviation, that is, Doppler frequency shift and spread, could be on the order of  $\pm 13$  Hz at the  $-6$  dB normalized signal level,  $\pm 17$  Hz at  $-12$  dB, and  $\pm 19$  Hz at  $-18$  dB. At 30 MHz, the 1-sigma Doppler deviations should increase to approximately  $\pm 78$  Hz,  $\pm 105$  Hz, and  $\pm 114$  Hz, respectively.

HF field-aligned backscatter echoes usually occurs most often near local sunset. However, experimental observations have shown, at times, peak activity near the midnight hours.

There is a strong correlation of backscatter echoes with the solar cycle. That is, the percentage of days displaying backscatter reflections decreases with decreasing sunspot number.

The characteristics of sunset echoes are found to be different from those occurring during the night. The sunset echoes are generally of the diffuse type, and are independent of magnetic activity while the nighttime echoes are discrete and correlate with magnetic activity.

## 10.7 SCINTILLATION ON TRANS-IONOSPHERIC RADIO SIGNALS

A radio wave traversing the upper and lower atmosphere of the earth suffers a distortion of phase and amplitude. When it traverses ionospheric irregularities, the radio wave experiences fading, phase deviations, and angle of arrival variations. These signal fluctuations, known as ionospheric scintillation, vary widely with frequency, magnetic and solar activity, time of day, season, and latitude.

The irregularities producing scintillations are predominantly in the F layer at altitudes ranging from 200 to 1000 km with the primary disturbance region for high and equatorial latitude irregularities between 250 and 400 km. There are times when E layer irregularities in the 90 to 100 km region produce scintillation, particularly sporadic E and auroral E.

## CHAPTER 10

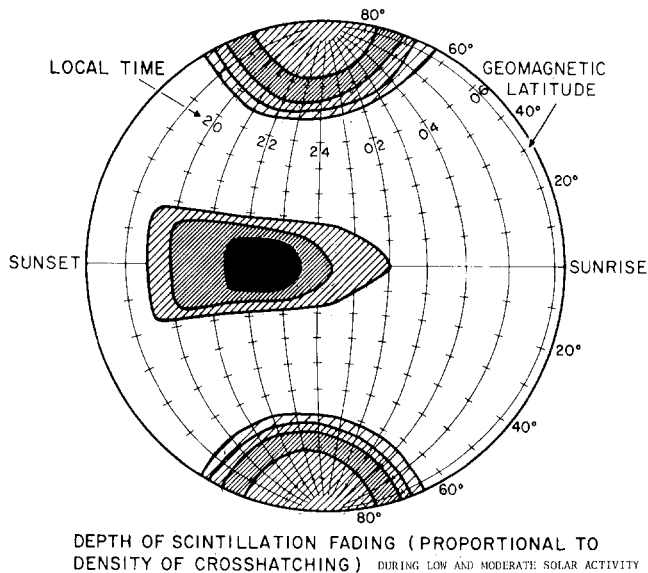


Figure 10-63. Global depth of scintillation fading (proportional to density of crosshatching) during low and moderate solar activity.

### 10.7.1 Global Morphology

From the global point of view there are three major sectors of scintillation activity (Figure 10-63). The equatorial region comprises an area within  $\pm 20^\circ$  of the magnetic equator. The high latitude region, for the purposes of the scintillation description, comprises the area from the high latitude edge of the trapped charged particle boundary into the polar region. We shall term all other regions “middle latitudes”.

In all sectors, there is a pronounced nighttime maximum. At the equator, activity begins only after sunset. Even in the polar region, there appears to be greater scintillation occurrence during the winter months than during the months of continuous solar visibility.

### 10.7.2 Scintillation Examples

The intensity fading can best be characterized by an idealized example such as in Figure 10-64. The mean signal level is modulated by the passage through the irregularities so that the signal level very rapidly increases and decreases. In Figure 10-64 the mean signal level at times fades below the 3 dB level and below the 6 dB level. The number of fades and the fade duration for a typical 15 minute length of signal from a synchronous satellite is shown in Figure 10-64 along with the cumulative probability distribution function (pdf). In this example the signal was above the 6 dB fade level 91.7% of time.

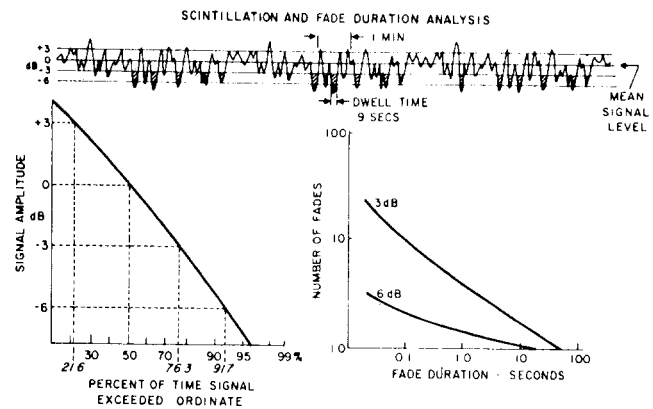


Figure 10-64. Sample of intensity fading produced by signal passing through irregularities. Fade duration and cumulative probability distribution are also shown.

### 10.7.3 Signal Characteristics

The amplitude, phase and angle of arrival of a signal will fluctuate during periods of scintillation. The intensity of the scintillation is characterized by the variance in received power with the  $S_4$  index commonly used for intensity scintillation and defined as the square root of the variance of received power divided by the mean value of the received power that is,  $S_4^2 = \frac{\langle I^2 \rangle - \langle I \rangle^2}{\langle I \rangle^2}$  [Briggs and Parkin, 1963].

An alternative, less rigorous but simple measure of scintillation index has been adopted by many workers in the field [Whitney et al., 1969] for scaling long-term chart records.

The definition is

$$SI = \frac{P_{\max} - P_{\min}}{P_{\max} + P_{\min}} \quad (10.65)$$

where  $P_{\max}$  is the power level of the 3rd peak down from the maximum excursion of the scintillations and  $P_{\min}$  is the level of the 3rd peak up from the minimum excursion, measured in dB [Whitney et al., 1969].

The equivalence of selected values of these indices is indicated below.

$S_4$	dB
0.075	1
0.17	3
0.3	6
0.45	10

Scaling of the chart records is facilitated by simply measuring the decibel change between the  $P_{\max}$  and  $P_{\min}$  levels.

The phase variations are characterized by the standard deviation of phase,  $\sigma_\phi$ , over a given interval of fluctuation frequency.

Attempts have been made to model the observed amplitude pdf. Whitney et al. [1972] and Crane [1977] have constructed model distribution functions based upon the use of the Nakagami-m distribution ( $m = (S_4)^{-2}$ ) and have shown that the empirical models provide a reasonable approximation to the calculated distribution functions. Fremouw et al. [1980] showed that the Nakagami distribution for intensity and the normal distribution for phase may be used to characterize the statistics of the scintillation signal. In addition, the Rayleigh pdf provides a good fit to the data under conditions of very strong scintillation ( $S_4 \sim 1.0$ ).

### 10.7.4 Frequency Dependence

Observations [Fremouw et al., 1978] employing ten frequencies between 138 MHz and 2.9 GHz transmitted from the same satellite, show a consistent wavelength ( $\lambda$ ) dependence of the form  $\lambda^{1.5}$  of  $S_4$  for  $S_4$  less than about 0.6. The frequency dependence becomes less steep for stronger scintillation, as  $S_4$  approaches a maximum value near unity with a few rare exceptions. When  $S_4$  exceeds 0.6 (peak to peak values  $> 10$  dB) the frequency dependence exponent decreases. (If two frequencies are being compared and both experience strong scattering to the extent that each displays Rayleigh fading ( $S_4 \sim 1.0$ ), then there is effectively no wavelength dependence over the frequency interval.) When strong scattering occurs but is not constant over the frequency interval, the wavelength dependence is difficult to determine. The observations [Fremouw et al., 1978] also show that the phase scintillation index,  $\sigma_\phi$ , varies as  $\lambda$  for both weak and strong scattering. However, in extremely strong scattering environment, the frequency dependence of phase scintillation is also weakened.

### 10.7.5 Fading Spectra

During their passage through the ionospheric irregularities of electron density, radio waves from satellites undergo spatial phase fluctuations. As the wave emerges from the irregularity layer and propagates towards the ground, these phase fluctuations cause interference to occur and a diffraction pattern in both intensity and phase develops on the ground. In the presence of a relative motion between the diffraction pattern and the observer, a temporal variation of intensity and phase results. By transforming the temporal pattern to the frequency domain, the frequency spectra of intensity and phase fluctuations are obtained.

If a thin irregularity layer lies in the plane  $z = 0$  of a

cartesian coordinate system ( $x, y, z$ ), and a plane wave of wavelength  $\lambda$  traveling in the  $z$ -direction is incident on the layer, then for weak scattering (rms phase  $\phi_o \ll 1$ ) the spatial spectrum,  $\Phi(\kappa_x, \kappa_y)$ , of phase ( $s$ ) and log amplitude ( $\chi$ ) (Yeh and Liu, 1982) on the ground ( $z = z$ ) is given by

$$\Phi_{\chi, s}(\kappa_x, \kappa_y) = \pi(r_e \lambda)^2 L \left\{ 1 \mp \frac{2k}{\kappa_{\perp}^2 L} \sin\left(\frac{\kappa_{\perp}^2 L}{2k}\right) \right. \quad (10.66)$$

$$\left. \times \cos\left[\frac{\kappa_{\perp}^2}{k}\left(z - \frac{L}{2}\right)\right] \right\} \Phi_{\Delta N}(\kappa_x, \kappa_y, 0)$$

the upper and lower signs within the bracket referring to  $\chi$  and  $s$  respectively. In the above equation,

- $\kappa_x, \kappa_y, \kappa_z$  - spatial wave numbers in  $x, y$  and  $z$  directions
- $\kappa_{\perp}^2$  =  $\kappa_x^2 + \kappa_y^2$
- $\Phi_{\Delta N}(\kappa_x, \kappa_y, \kappa_z)$  - power spectrum of irregularity electron density deviation
- $k$  - the wavenumber of the radio wave  
(=  $\frac{2\pi}{\lambda}$ )
- $r_e$  - the classical electron radius  
(=  $2.818 \times 10^{-15}$  m)
- $L$  - irregularity layer thickness.

In the presence of a relative motion between the propagation path and the irregularities the spatial spectrum  $\Phi(\kappa_x, \kappa_y)$  is convected past the observer and a temporal variation of signal phase and amplitude is observed. If the irregularity structure does not change during the convection ('frozen-in' hypothesis) and the irregularities have a uniform velocity  $u$  in the  $x$ -direction then the power spectra of log amplitude and phase in the frequency domain are given by

$$\Phi_{\chi, s}(\omega) = \frac{1}{u} \int_{-\infty}^{+\infty} \Phi_{\chi, s}\left(\kappa_x = \frac{\omega}{u}, \kappa_y\right) d\kappa_y$$

$$= \pi \frac{(r_e \lambda)^2 L}{u} \int_{-\infty}^{+\infty} \left\{ 1 \mp \frac{2k}{q^2 L} \sin\left(\frac{q^2 L}{2k}\right) \right. \quad (10.67)$$

$$\left. \times \cos\left[\frac{q^2}{k}\left(z - \frac{L}{2}\right)\right] \right\} \cdot \Phi_{\Delta N}\left(\frac{\omega}{u}, \kappa_y, 0\right) d\kappa_y$$

where

$\omega$ —angular frequency of phase and amplitude fluctuation

$$q^2 = \frac{\omega^2}{u^2} + \kappa_y^2.$$

The term within the bracket with the upper sign is known

## CHAPTER 10

as the amplitude or Fresnel filter function and that with the lower sign as the phase filter function. The Fresnel filter function oscillates with the variation of frequency  $f$  and attains its first maximum at the frequency  $f_F = u/\sqrt{2\lambda z}$ . The behavior of the phase filter function is very different from the amplitude filter function as it fails to attenuate the low frequency regime. Equation (10.67) provides a relationship between the irregularity power spectrum in the ionosphere and the amplitude or phase scintillation spectrum obtained on the ground. Since the irregularity power spectrum has a power law variation [Dyson et al., 1974; Phelps and Sagalyn, 1976] of the form  $\kappa^{-p}$ , the power spectrum of amplitude scintillation shows a maximum at the frequency  $f_F$  due to the Fresnel filter function. On the other hand, the phase fluctuations are dominated by the low frequency regime. At  $f \gg f_F$ , both amplitude and phase scintillation spectra show an asymptotic variation  $f^{1-p}$  when the three-dimensional irregularity spectrum is of the form  $\kappa^{-p}$ . Thus from a study of weak scintillation spectra the spectral form of the irregularities causing scintillations may be deduced.

Figures 10-65a and 10-65b show two samples of weak phase and amplitude spectra obtained from 244 MHz scintillation observations made at Goose Bay, Labrador by the use of the Fleetsat geostationary satellite [Basu et al., 1982]. The phase and amplitude scintillation data were detrended by a high pass detrend filter with a cut-off frequency of 0.0067 Hz and the data sample yields an rms phase deviation of 2.4 radians and amplitude scintillation index  $S_4 = 0.51$  conforming to weak scintillation criterion. Both spectra show an asymptotic variation in the high frequency region, the amplitude spectrum showing  $f^{-2.35}$  variation, and the phase spectrum showing  $f^{-2.6}$  variation. If we consider that the scintillation spectra have an average  $f^{-2.5}$  variation, the corresponding three-dimensional irregularity power spectrum is expected to have a power law wavenumber spectrum of the form  $\kappa^{-3.5}$ . The decrease of power spectral density at the low frequency end of the phase spectrum is caused by the detrend filter. It may be noted that in the amplitude scintillation spectrum the high frequency roll-off starts at the Fresnel frequency of about 40 mHz. For an irregularity layer height of 350 km, the observed Fresnel frequency yields the irregularity drift velocity as 37 m/sec.

When scintillations become intense, the theory outlined above does not hold, and strong single scattering as well as multiple scatter theories appropriate to such cases have been developed [Yeh and Liu, 1982 and references therein]. In such cases it becomes difficult to relate in a straightforward manner, the scintillation spectra to the irregularity structures in the ionosphere. Figures 10-65c and 10-65d show a sample of intense amplitude scintillation data and its spectrum ( $S_4 = 0.88$ ) analyzed from 257 Hz scintillation data obtained at Ascension Island near the crest of the equatorial anomaly by the use of transmission from the geostationary satellite, Marisat [Basu and Whitney, 1983]. In contrast to the weak amplitude scintillation spectrum shown earlier, these spectra show a flat low frequency portion and increased

bandwidth of the frequency spectra, implying the development of shorter scales in the diffraction pattern. It is found that the correlation lengths get progressively smaller with increased strength of scattering [Rino and Owen, 1981; Basu and Whitney, 1983]. Under conditions of strong scattering, the phase scintillation spectra are also believed to suffer from the refractive scattering from very large scale irregularities [Booker and MajidiAhi, 1981]. Since wave propagation through a strong irregularity environment has considerable systems applications, intensive work in this area is in progress.

### 10.7.6 Geometrical Considerations

The intensity at which scintillations are observed depends upon the position of the observer relative to the irregularities in the ionosphere that cause the scintillation. Keeping both the thickness of the irregularity region and  $\Delta N$ , the electron density deviation of the irregularity, constant, geometrical factors have to be considered to evaluate data and to predict scintillation effects at a particular location. Among these are:

(a) Zenith distance of the irregularity at the ionospheric layer. One study [Wand and Evans, 1975] found the intensity of scintillation related approximately to the secant of the zenith angle up to  $70^\circ$ ; at angles  $>70^\circ$  the dependence ranges between  $1/2$  and the first power of the secant of the zenith angle.

(b) Propagation angle relative to the earth's magnetic field. Performing this calculation demands the use of an irregularity configuration and the consideration of Gaussian or a power law model for the irregularities. At high latitudes, irregularities in one study were elongated along the earth's magnetic field with a cylindrical form of axial ratio of 5 along the lines of force. Sheet-like irregularities with forms of 10 : 10 : 1 have also been found in recent auroral studies [Rino et al., 1978]. For equatorial latitudes, this elongation along the lines of force may be of the order of 50 to 100 [Koster, 1963].

(c) The distance from the irregularity region to the source and to the observer (near the irregularities, only phase fluctuations are developed). As noted in Mikkelsen et al., [1978] and Crane, [1977] the theoretical scintillation index can be expressed in terms of the above factors when dealing with ionospheric irregularities represented by a Gaussian power spectrum.

Mikkelsen et al. [1978] have attempted to determine the theoretical scintillation index,  $S_4$ , when the irregularities are described by a power-law power spectrum.

Mikkelsen assumed the approximate dividing line between weak and strong scintillation is  $\sim 9$  dB, with  $SI < 9$  dB denoting the weak case.

The geometric variation of  $S_4$  is provided in Mikkelsen et al. [1978].

# IONOSPHERIC RADIO WAVE PROPAGATION

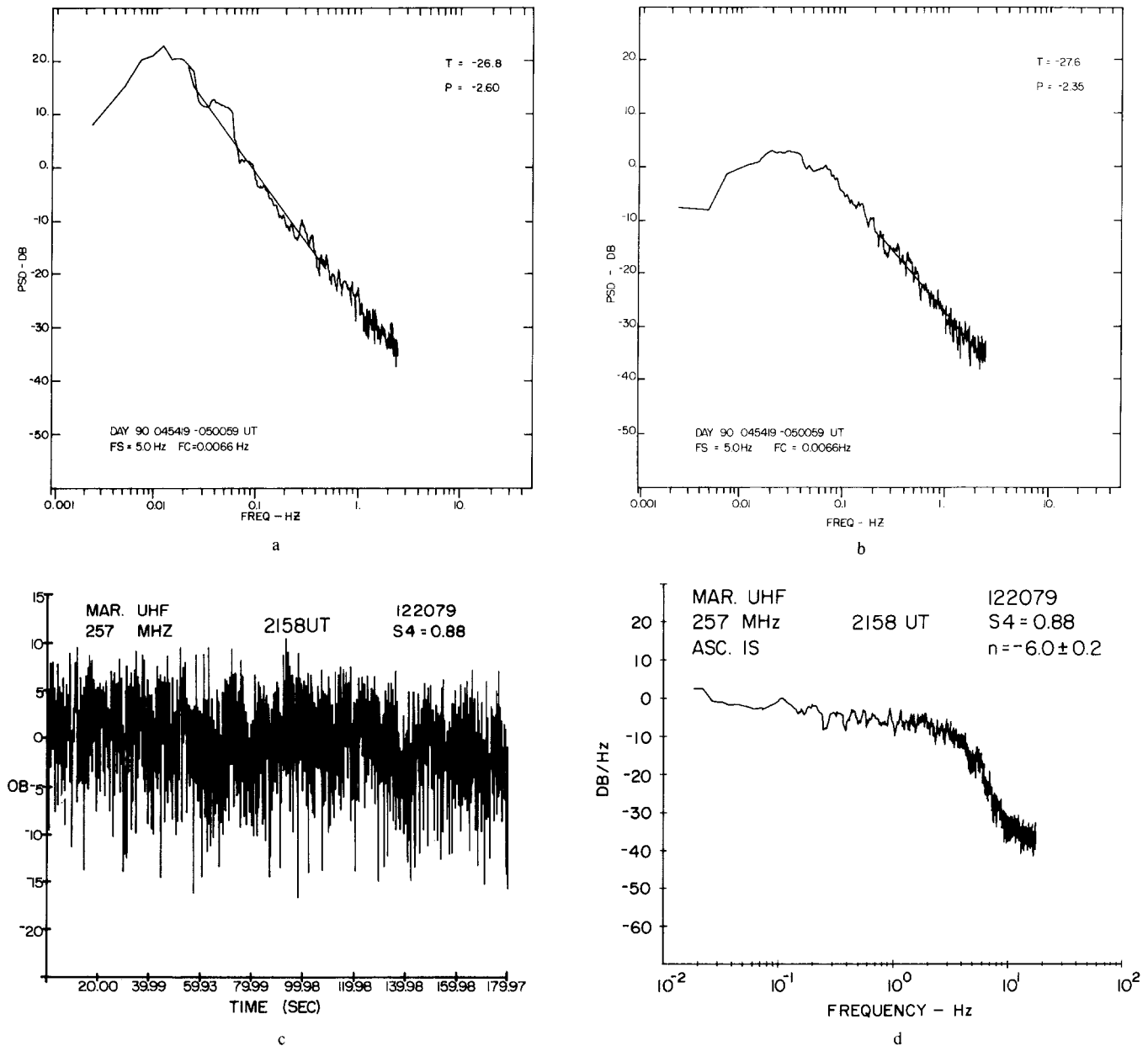


Figure 10-65. Spectra of (a) phase scintillation and (b) intensity scintillation under weak scatter conditions at 244 MHz observed at Goose Bay, Labrador on 31 March, 1979. (c) Data of 257 MHz intensity scintillation and (d) its spectrum under strong scatter conditions observed at Ascension Island on 20 December, 1979.

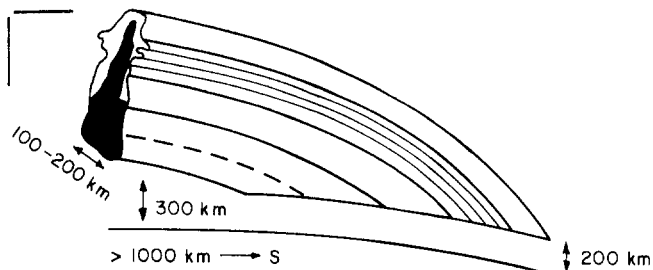
## 10.7.7 Spread F and Scintillation

The evidence from the correlation of scintillation occurrence and spread F [Rastogi, 1980] is that equatorial range spread is associated with scintillation activity and frequency spread is not. Thus the available spread F maps cannot be used for scintillation observations in these regions; they are dramatically misleading in many cases. In the high latitude region no statistical study has been made to correlate types of spread F with scintillation activity. It might be noted that even range spread occurrence and scintillation have important differences.

## 10.7.8 Equatorial Scintillations

**10.7.8.1 Patch Characteristics.** It has been established that nighttime ionospheric equatorial irregularity regions emerging after sunset develop from bottomside instabilities, probably of the Rayleigh-Taylor type. The depleted density bubble rises into the region above the peak of the F2 layer. Steep gradients on the edges of the hole help to generate the smaller-scale irregularities within the patch which produces intense scintillation effects [Basu and Kelley, 1979].

A plume-like irregularity region develops, finally forming a patch of irregularities that has been likened to a banana



THREE DIMENSIONAL  
PATCH MODEL

Figure 10-66. Three dimensional model of an equatorial irregularity patch in the form of a banana or orange segment.

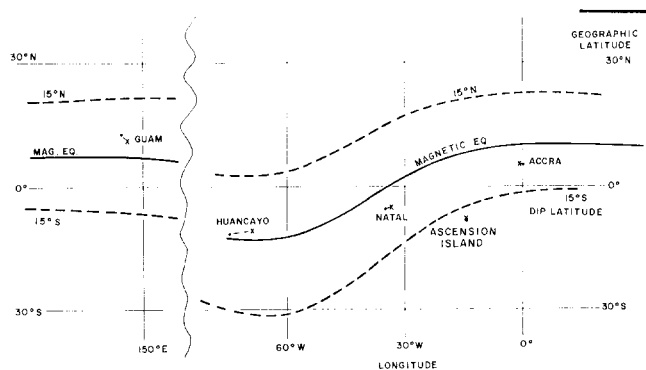


Figure 10-67. Map of equatorial regions using the 1975 epoch of the DMA magnetic inclination map. X marks sub-ionospheric intersection.

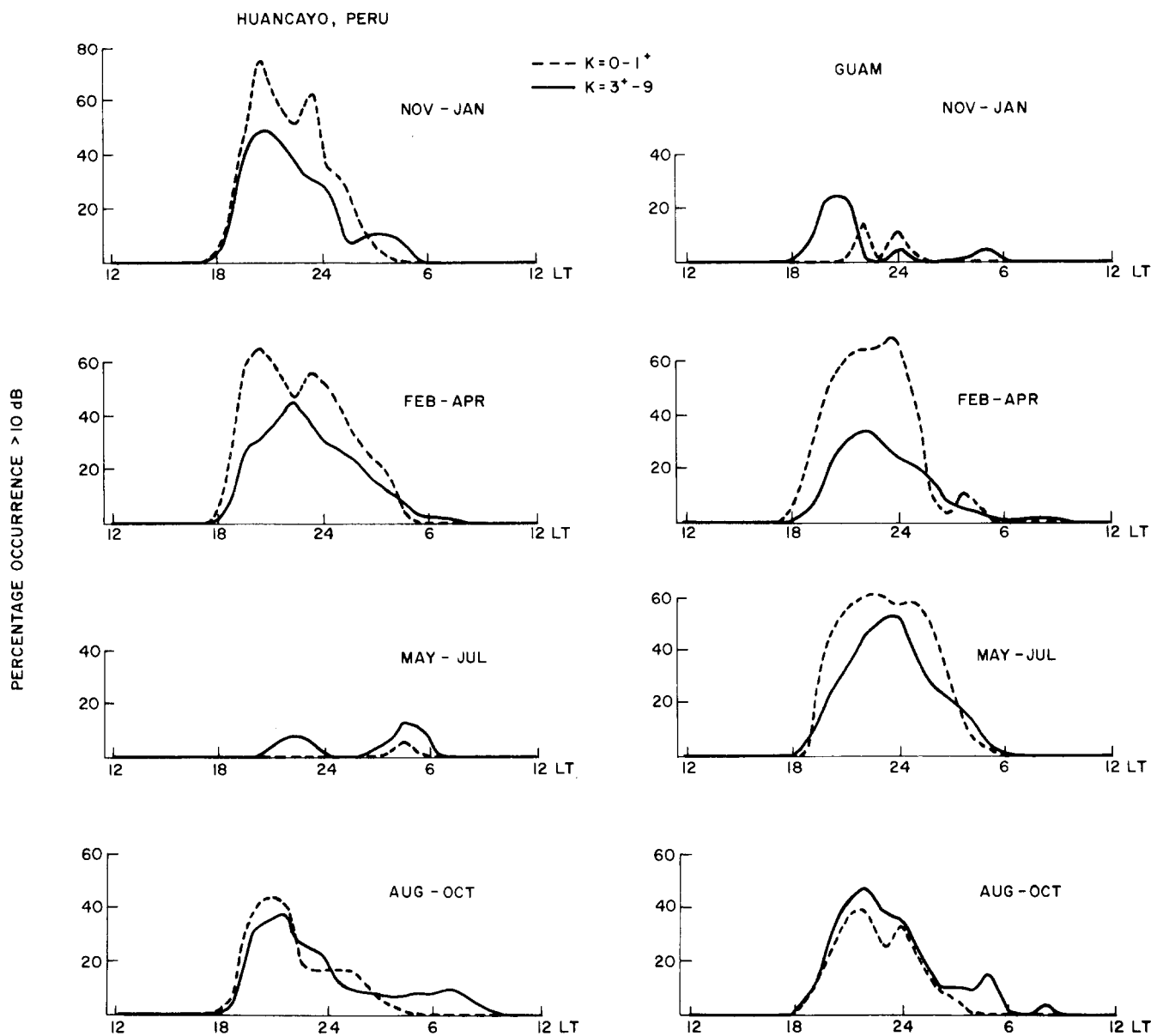


Figure 10-68. Comparison of seasonal patterns of occurrence of scintillation activity  $> 10$  dB at 250 MHz at Guam and Huancayo under very quiet ( $K_p = 0 - 1^+$ ) and disturbed ( $K_p = 3^+ - 9$ ) magnetic conditions.

## IONOSPHERIC RADIO WAVE PROPAGATION

or an orange segment. A cut through the center of the “banana” is shown in Figure 10-66.

The characteristics of the patch development, motion and decay can be summarized as follows:

1. A new patch forms after sunset by expanding westward in the direction of the solar terminator with velocities probably similar to that of the terminator. It comes to an abrupt halt after typically expanding to an east-west dimension of 100 to several hundred kilometers. It appears to have a minimum size of  $\sim 100$  km.

2. It is composed of field-aligned elongated rod or sheet-like irregularities. The vertical thickness of the patch is 50 to several hundred kilometers. The patch has maximum intensity irregularities in a height region from 225 to 450 km, with irregularities extending to over 1000 km.

3. Its north-south dimensions are of the order of 2000 km or greater.

4. Once formed, the patch drifts eastward with velocities ranging from 100 to 200 m/s.

5. The patch duration as measured by scintillation techniques is known to be greater than  $2\frac{1}{2}$  h; individual patches have been tracked by airglow techniques up to 3 hours where they have maintained their integrity [Weber et al., 1978]. Effects have been seen over 8 h.

Studies of the variation in electron content in the patches have been made by measuring the change in relative phase between the two characteristic waves (ordinary and extraordinary modes) with polarimeters. It is found that the patches are regions of depletion in electron content. While the electron content depletions are found to be only of the order of 20%, the satellite *in situ* data may indicate density depletions as large as two or three orders of magnitude at one fixed altitude. In a strong irregularity environment, however, fast fluctuations in polarization are often obtained. Lee et al. [1982] have shown that scattering suffered by each characteristic wave may induce fast polarization fluctuations and obtained expressions for the variance of these fluctuations for irregularities with Gaussian and power law type spectra.

**10.7.8.2 Variation of Scintillation Activity.** A variety of observatories used data taken over the same time period to compare scintillation activity at 250 MHz [Aarons et al., 1980b]. One set of data was taken at Huancayo, Peru, Natal, Brazil, and Accra, Ghana with all observations made at elevation angles greater than  $20^\circ$  and with distance between the most separated stations about  $70^\circ$  of longitude; a map of both geographical and magnetic coordinates is shown on the right side of Figure 10-67.

A second comparison of data at 250 MHz was made between observations from Huancayo and from Guam. The data are shown in Figure 10-68; activity minima occur from May–July in Huancayo and from November–January in Guam. The conclusion is that the occurrence patterns are longitudinally controlled.

It should be noted that in general maximum intensity occurs in the equinoctial months. This can best be illustrated

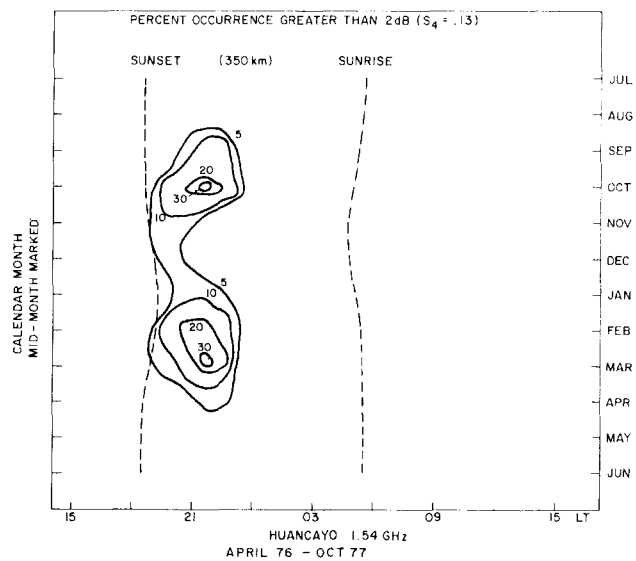


Figure 10-69. Percentage occurrence of 1.5 GHz scintillation  $\geq 2$  dB during Apr 1976–Oct 1977.

by the occurrence of L band, 1500 MHz activity, at Huancayo, Peru. That evidence is shown in Figure 10-69 [Basu et al., 1980b] L-band activity at Huancayo does not suffer from strong scattering or from saturation (as does 136 MHz and 250 MHz data on occasion); the data show clear equinoctial maxima.

From available data it appears as if geomagnetic control of the occurrence of scintillation varies with longitude. The generalization can be made that increased magnetic activity inhibits scintillation activity before midnight—except during those months with very low scintillation activity (May–July for the region  $(0^\circ\text{--}70^\circ\text{W})$  and November–January in the Pacific longitudes  $(135^\circ\text{--}180^\circ\text{E})$ . After midnight the scintillation activity in general increases slightly with the presence of magnetic storms. The data shown in Figures 10-70 and 10-71 are for a year’s observation in each case. The complexities of the magnetic control of scintillation occurrence are illustrated by the variations in the curves of occurrence at each station in each season. For further details see Mullen [1973].

**10.7.8.3 In-Situ Data.** Basu and Basu [1980] have developed a model from *in situ*, theoretical, and scintillation studies. In their morphological model of scintillations, *in situ* measurements of irregularity amplitude,  $\Delta N/N$ , as computed from T secs of data are utilized in conjunction with simultaneous measurement of electron density  $N$ . A combination of  $\Delta N/N$  and  $N$  data provides the required  $\Delta N$  parameter as a function of position and time.

**10.7.8.4 Sunspot Cycle Dependence.** From the viewpoint of electron density variations, the equatorial region around the magnetic equator displays a complex pattern. During the day an increase in maximum electron density occurs away from the equator. The electron density contours

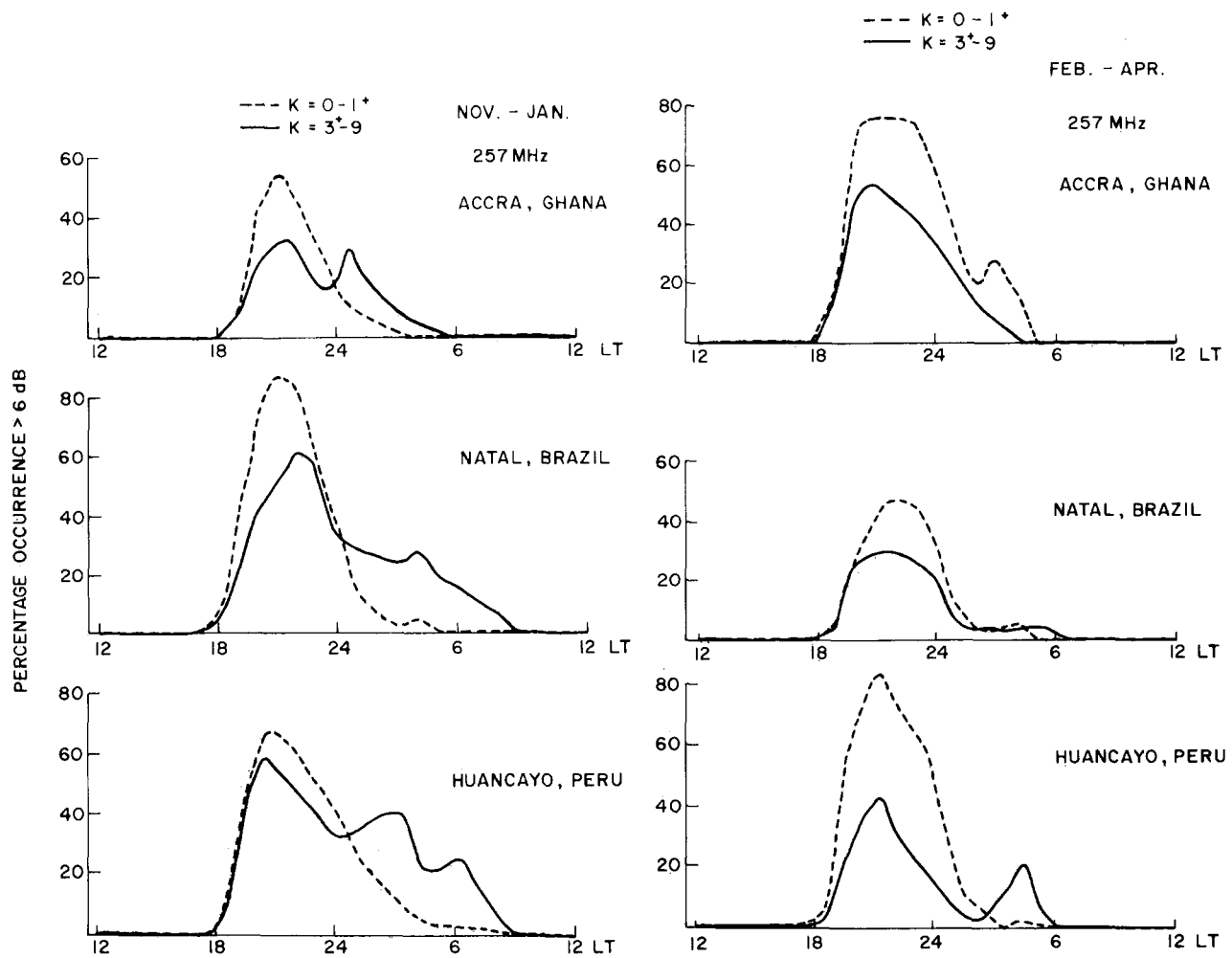


Figure 10-70. Seasonal patterns of occurrence of scintillation activity > 6 dB ( $S_4 = 0.3$ ) at 250 MHz for very quiet ( $K_p = 0 - 1^+$ ) and for disturbed ( $K_p = 3^+ - 9$ ) magnetic conditions for Nov-Apr.

display a distinct trough of electron density in the bottomside and topside ionosphere at the magnetic dip equator with crests of ionization at  $\pm 15^\circ - 20^\circ$  north and south dip latitudes; this is the Appleton anomaly with the region within  $\pm 5^\circ$  dip latitude of the magnetic equator termed the electrojet region.

From the solar cycle minimum in 1974 and maximum in 1969-1970, Aarons [1977] found that there was a higher occurrence of deep scintillations during a year of high solar flux than during a year with low solar flux for observations at both Accra, Ghana and Huancayo, Peru.

Recent observations of L band scintillations from both MARISAT and GPS during the period of maximum solar flux (1979-1981) [DasGupta et al., 1981] have revealed that scintillation intensities maximize in the Appleton anomaly region rather than near the magnetic equator.

The conclusion in the study [Aarons et al., 1981a] was that the intense scintillation activity during years of high solar flux are due to two factors:

1. The equatorial anomaly has considerably higher electron density values in high sunspot number years than in years of low solar activity.
2. The occurrence of maximum electron density for anomaly latitudes is near sunset in the years of high sunspot number and in the afternoon in years of low solar activity. Thus the post sunset irregularity patches attain high  $\Delta N$  levels in the years of high solar flux.

### 10.7.9 Middle Latitude Scintillation

The middle latitude scintillation activity is not as intense as that encountered at equatorial, auroral or polar latitudes. However, activity may reach levels, primarily at VHF and UHF, that will increase error rates of systems with low fade margins. The reader is referred to Aarons [1982] and Bramley [1974].

# IONOSPHERIC RADIO WAVE PROPAGATION

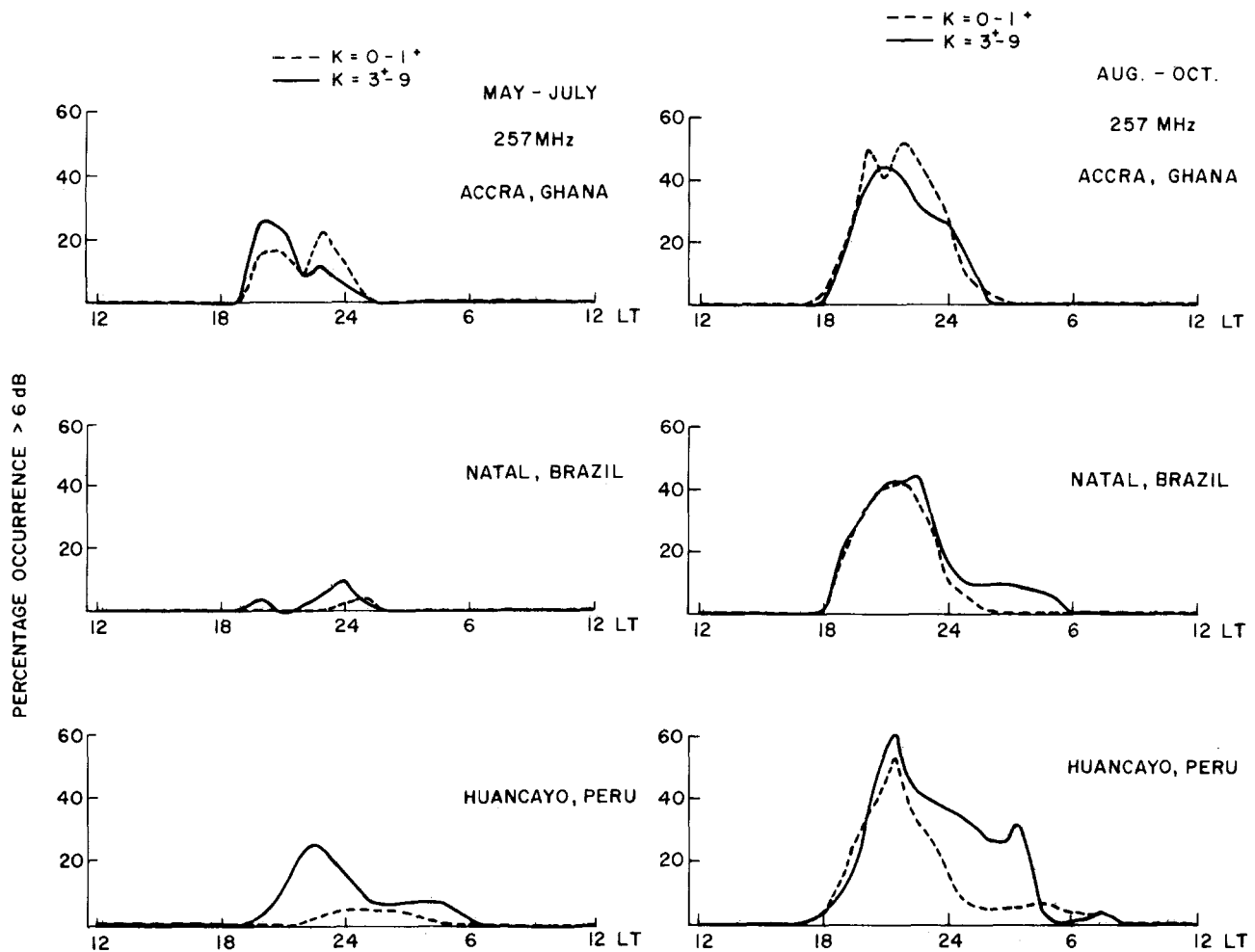


Figure 10-71. Seasonal patterns of occurrence of scintillation activity  $> 6$  dB ( $S_4 = 0.3$ ) for very quiet ( $K_p = 0 - 1^+$ ) and for disturbed ( $K_p = 3^+ - 9$ ) magnetic conditions for May-Oct.

**10.7.9.1 Effect of Magnetic Index on Midlatitude Scintillation.** At latitudes below the auroral oval, various sets of data have yielded behavior indicating little correlation with magnetic conditions. Evans [1973] found no correlation of their 400 MHz radar scintillations with magnetic index south of their station at  $56^\circ$  invariant latitude. Aarons and Martin [1975] found that during the August 4-10, 1972 magnetic storms there was a negative correlation of scintillation and magnetic index for Athens, Greece and Camp Parks, California and little correlation at the  $45^\circ$  invariant latitude intersection for Aberystwyth, Wales. Bramley [1974] found that except for the December 1971 magnetic storm (when the irregularity region probably encompassed the intersection point of  $\sim 45^\circ$ ), there was no correlation between magnetic activity and scintillations.

This type of data essentially corroborates the early radio star observations in the U.K. which found little correlation with magnetic index except in paths to the north (with the exception of some intense magnetic storms).

## 10.7.10 The High Latitude Region

Figure 10-72 depicts the intensity of scintillation at high latitudes in a very broad manner for the period of time around midnight.

**10.7.10.1 The Plasmopause and the Trough.** The present evidence is that there is a boundary at the high latitudes where weak irregularities commence. It is probably a few degrees equatorwards of the plasmopause, between  $45^\circ$ - $55^\circ$  Corrected Geomagnetic Latitude (CGL), the system used at high latitudes in this review.

At night a trough or region of low electron density and total electron content exists between the end of normal ionospheric plasma behavior and the auroral region where energetic electron precipitation and current systems are dominant factors in producing both the normal ionospheric layers and the irregularities.

All observers of irregularities see a dramatic change in

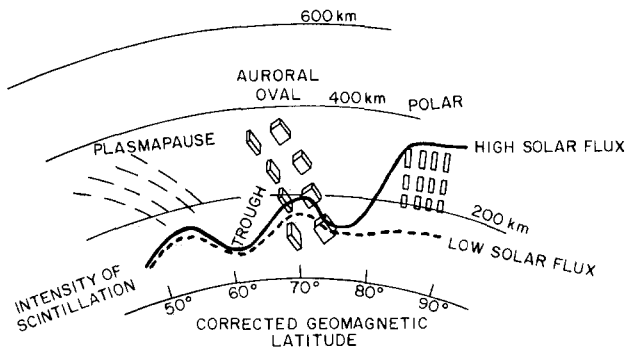


Figure 10-72. Depiction of high latitude irregularities ~22-02 LT. Sheet-like irregularities are seen in the auroral oval, rod irregularities at higher and lower latitudes.

irregularities in the auroral oval at the poleward edge of the trough. In the auroral oval, the intensity of scintillations is a function of local magnetic activity. Poleward of the aurora there may again be a lowering of scintillation activity until the observing path transits the polar region [Aarons et al., 1981b]

**10.7.10.2 Auroral Scintillations.** From studies of radio star and low altitude satellite scintillations, a series of height measurements have pointed to F layer heights as the primary seat of the irregularities producing the signal fading.

Maximum irregularity intensity appears above the region showing maximum intensity aurora [Martin and Aarons, 1977]. Vickrey et al. [1980] have shown that there is a collocation of scintillation patches in the auroral oval and F region ionization enhancements.

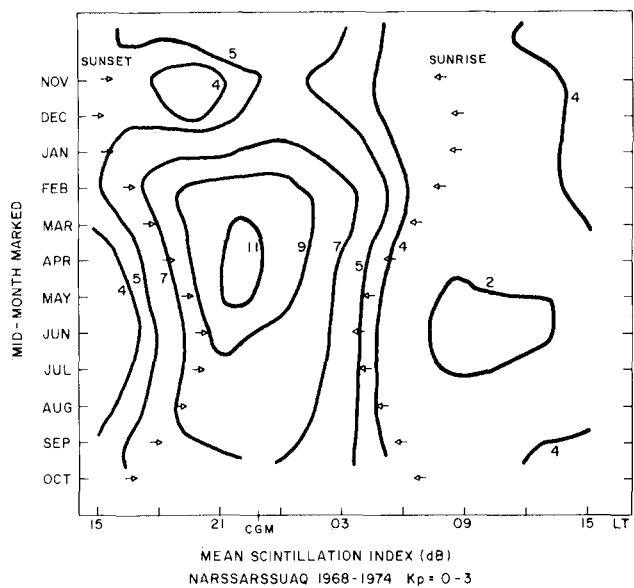


Figure 10-73. Contours of monthly mean scintillation index in dB at 137 MHz as a function of local time for quiet conditions ( $K_p = 0 - 3$ ) obtained at Narssarsuaq during 1968-1974.

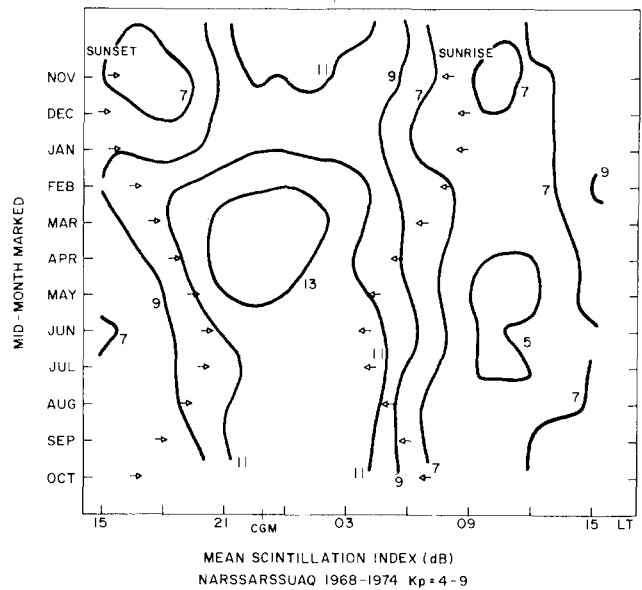


Figure 10-74. Contours of monthly mean scintillation index in dB at 137 MHz as a function of local time for disturbed ( $K_p = 4 - 9$ ) magnetic conditions obtained at Narssarsuaq during 1968-1974.

Perhaps the most consistent studies of long term behavior of scintillations have been made in the auroral zone, at Alaskan longitudes and along the 70°W meridian.

Both the diurnal pattern of scintillation activity and the seasonal behavior as observed from one site can be noted in Figures 10-73 and 10-74. The data used for this long term study [Basu and Aarons, 1980] were taken over a period of 6 years from Narssarsuaq by observing 137 MHz scintillations of the ATS-3 beacon; the propagation path traversed the ionosphere at ~63° CGL.

The long term study used for Figure 10-75 incorporated data from three observatories (Narssarsuaq, Greenland; Goose Bay, Labrador; and Sagamore Hill, Massachusetts). The contours are of reduced data for one season (May-July) for magnetically active periods of time [Basu and Aarons, 1980]. The boundary of active scintillation is pushed equatorwards extending into what was the quiet trough and plasmapause latitudes. Thus during magnetic storms scintillations and

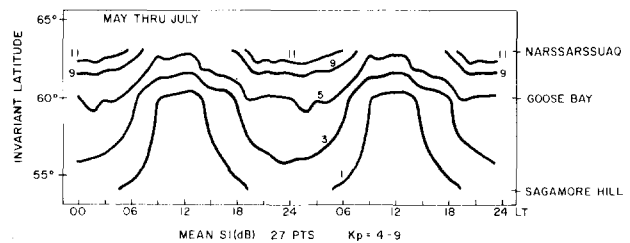


Figure 10-75. Variation of mean scintillation index during the northern solstice in dB at 137 MHz with local time and invariant latitude derived from hourly data at the 3 stations under disturbed magnetic conditions ( $K_p = 4 - 9$ ).

# IONOSPHERIC RADIO WAVE PROPAGATION

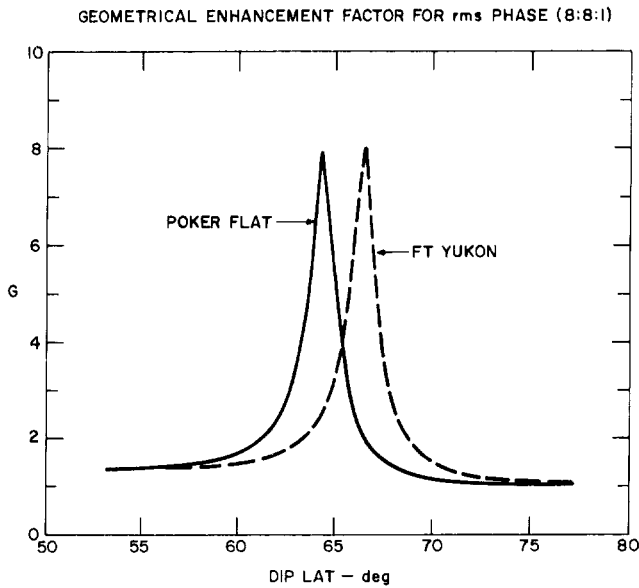


Figure 10-76. Model computations of phase geometrical enhancement factor for sheet-like structures with an 8 : 8 : 1 anisotropy. Because of the meridional pass trajectory, the location of the enhancement is independent of the pass elevation. [Rino and Owen 1980]

optical aurora can be noted farther south than 55°. In the 70°W longitude region this extends below the latitude of Boston.

*Geometry and Enhancement.* Sheet-like irregularities produce strong enhancements when observations are made in specific directions. For two sites in Alaska, Rino and Owen [1980] have constructed the theoretical geometrical enhancement factor for rms phase fluctuations for an 8:8:1 irregularity (Figure 10-76) [Rino and Matthews, 1980]. They found this enhancement in phase fluctuations as can be seen by the data in Figure 10-77. The amplitude enhancement, less dramatic but present, is also shown in Figure 10-77. Daytime scintillation does not show the sheet-like struc-

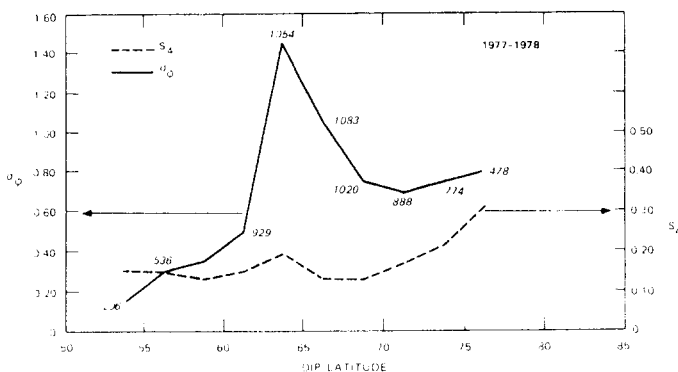


Figure 10-77. RMS phase and  $S_4$  at 50% exceedance level vs magnetic latitude for nighttime data during 1977-1978.

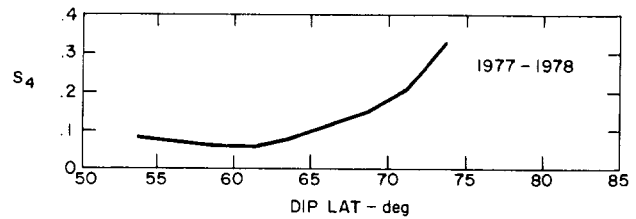


Figure 10-78.  $S_4$  at 50% exceedance level vs magnetic latitude for daytime data during 1977-1978.

ture—at least as observed from Alaska. Figure 10-78 illustrates the daytime increase with increasing latitude.

**10.7.10.3 Polar Scintillations.** A long term consistent series of measurements has been taken at Thule, Greenland with observations at 250 MHz [Aarons et al., 1981b]. The scintillations for this study ranged from very low values of 3-6 dB peak to peak on occasion during a period of low sunspot number to saturation fading of 28 dB peak to peak for hours during winter months of years of high sunspot number.

One set of measurements was taken between April and October 1975. During this period of low solar activity, there was an absence of strong scintillation activity to such an extent that only the occurrence of scintillation greater than 6 dB could be plotted. Figure 10-79 shows the contrast between the 1975 period when solar flux was low (10.7 cm flux was ~75) and the same months in 1979 when the solar flux was high (~150-225).

A contour plot of the percent occurrence of scintillation index greater than 10 dB is shown in Figure 10-80. The plot was developed from hourly average values of the 15 minute SI for each month for low magnetic activity ( $K_p = 0-3$ ). Two patterns emerge: (1) Maximum occurrence of activity takes place in the months of little or no sunlight at F

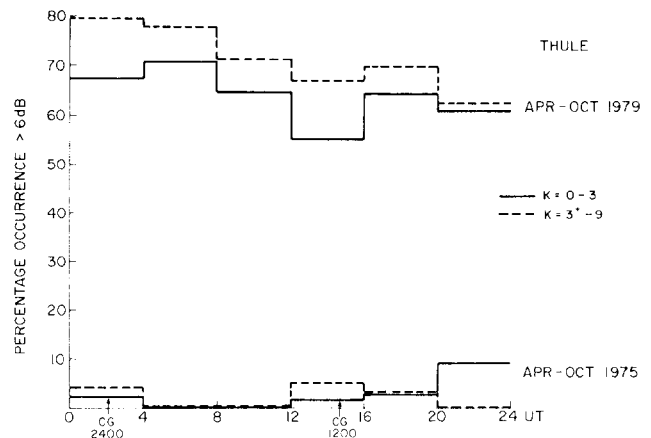


Figure 10-79. Percentage occurrence of scintillation greater than 6 dB for low solar flux period April-October 1975 is contrasted with that for high solar flux period April-October 1979 for both quiet and disturbed magnetic conditions.

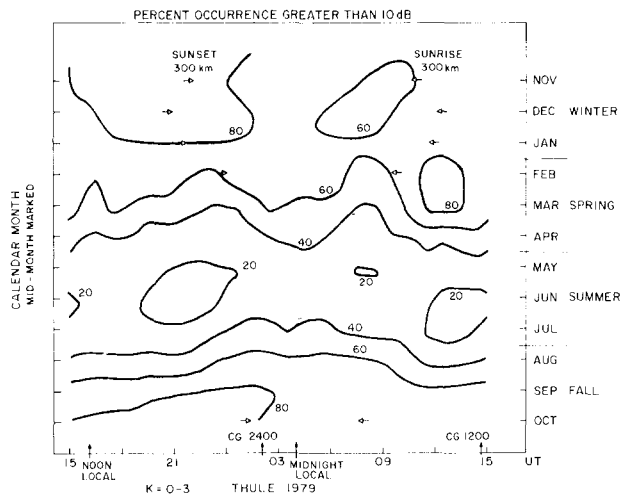


Figure 10-80. Contour plot of diurnal pattern of monthly percent occurrence of scintillation greater than 10 dB for low magnetic activity ( $K_p = 0 - 3$ ). Observations were taken during Mar 1979–Feb 1980.

region heights. Much lower scintillation occurrence takes place in the sunlit months. (2) The diurnal variation is weak, and apparent only during the winter months.

Auroral arcs in the polar cap are approximately aligned with the noon-midnight magnetic meridian [Davis, 1962]. These arcs generally drift in the dawn to dusk direction [Danielson, 1969]; however, reversals have been noted [Akasofu, 1972; Weber and Buchau, 1981]. Recently Weber and Buchau [1981] described the orientation and motion

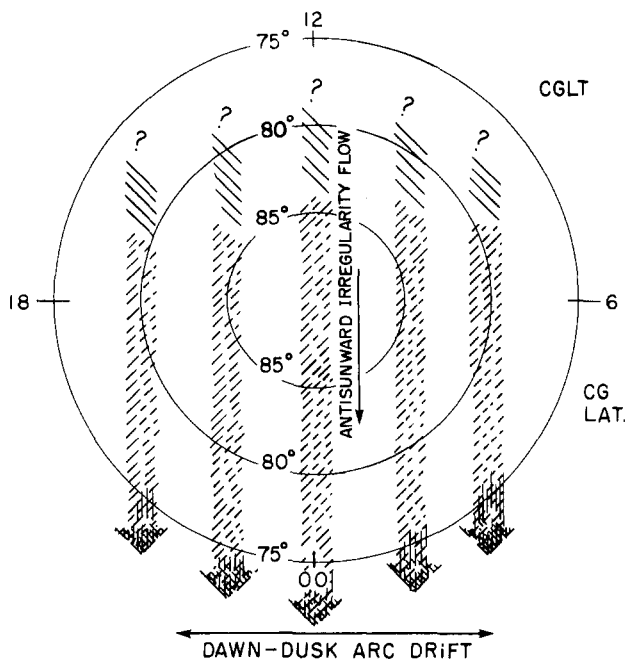


Figure 10-81. Schematic of small scale anti-sunward irregularity drift and the patch motion.

of subvisual F layer ( $\lambda = 6300 \text{ \AA}$  OI) polar cap arcs. Kilometer-size irregularities within the arcs produced intense (saturated) amplitude scintillation at 250 MHz as the arcs drifted through a satellite to ground ray path. Outside the arcs, scintillation frequently persisted at a lower level ( $SI \sim 6 \text{ dB}$ ).

A pictorial representation of both the small scale anti-sunward irregularity drift and the patch motion (predominantly dawn to dusk) is shown in Figure 10-81 (E. Weber, private communication). Results point to two irregularity components in the polar cap; antisunward drifting irregularities which produce a background level of weak to moderate scintillation and intense irregularities within F layer polar cap arcs that produce more discrete ( $\sim 1 \text{ h}$  duration) intense scintillation events as the arcs drift through the ray path.

### 10.7.11 Empirical Model Of Global Scintillation Behavior

**10.7.11.1 WBMOD.** Over a period of years, starting from available data and from weak scintillation theory, a model of scintillation termed WBMOD has been developed [Fremouw and Bates, 1971; Fremouw and Lansinger, 1981; Fremouw and Rino, 1978, 1976; Fremouw, 1980; Fremouw et al., 1977]. The program provides for phase and amplitude information. Input user parameters include frequency, location, local time, sunspot number, and planetary magnetic index,  $K_p$ . The user also must specify the longest time the system needs phase stability. Scintillation indices are the output. A model of the irregularity drift velocity is contained in the program.

Program WBMOD permits a user to specify his operating scenario. The code returns the spectral index  $p$  for power-law phase scintillation, the spectral strength parameter  $T$ , the standard deviation  $\sigma_\phi$  of phase, and the intensity scintillation index,  $S_4$ , as functions of a changing independent variable chosen by the user.

The descriptive irregularity model is based on numerous observations [Fremouw and Bates, 1971; Fremouw and Rino, 1978], but most particularly on observations of phase scintillation performed in the DNA Wideband Satellite Experiment [Sagalyn et al., 1974]. The most significant caveat about use of WBMOD, however, is that it has been calibrated quantitatively against Wideband data from only a single station in the northern auroral zone (Poker Flat, Alaska). The descriptive model was developed by iterative comparison with most of the Wideband data population from Poker Flat, with a portion of the population reserved for final comparative tests.

The basic calculations are made of two central quantities  $T$  and  $p$ .  $T$  is the spectral strength of phase at a fluctuation frequency of 1 Hz,  $p$  is the power-law spectral index of

## IONOSPHERIC RADIO WAVE PROPAGATION

phase;  $T$  is highly variable, unlike  $p$ . The program calculates  $T$  and  $p$  and the two commonly used indices of scintillation activity based on them, one for phase,  $\sigma_\phi$ , and one for intensity,  $S_4$ .

In order to calculate  $T$ ,  $p$ ,  $\sigma_\phi$ , and  $S_4$ , one must have values for eight parameters describing ionospheric irregularities. They are (1) the height,  $h$ ; (2) vector drift velocity,  $V_d$ , of the irregularities; (3) an outer scale,  $\alpha$ ; (4,5,6,7) four "shape" parameters describing the irregularities' three-dimensional configuration and spatial "sharpness",  $a$ ,  $b$ ,  $\delta$ , and  $\nu$ ; and (8) the height integrated strength of turbulence,  $C_sL$ . Program WBMOD contains models for the foregoing eight parameters, but the degree of detail is very much less for some than for others.

The most variable and the most important of the eight is the height-integrated strength of turbulence,  $C_sL$ . The irregularity strength is modeled by

$$\sqrt{C_sL} = E(\lambda_m, \lambda_g, T, D, \bar{R}) + M(\lambda_m, T) + H(\lambda_m, T_m, K_p, \bar{R}) \quad (10.68)$$

where  $\lambda_m$  = geomagnetic invariant latitude,

$\lambda_g$  = geographic latitude,

$T$  = local meridian time,

$D$  = day of the year,

$\bar{R}$  = smoothed Zurich sunspot number,

$T_m$  = geomagnetic time,

$K_p$  = planetary geomagnetic activity index.

The three terms in Equation (10.68) respectively describe the strength of equatorial, midlatitude, and high-latitude irregularities. The first two have not been tested extensively against Wideband data but the high latitude term  $H$  has been.

The high-latitude term is based on the observation that there often is a more-or-less abrupt boundary [Aarons et al., 1969] between the midlatitude region of relatively smooth ionosphere and the highlatitude scintillation region. It is located, typically, equatorward of discrete-arc auroras in the general vicinity of the diffuse auroral boundary.

**10.7.11.2 Formulas In Atlantic Sector.** Since WBMOD has been developed and calibrated against data from only one longitude sector (Alaska), it is appropriate to note empirical formulas that, though not as complex, have been developed for another longitude sector, along the 70°W meridian. These formulations have been made [Aarons et al., 1980a] for Narssarssuaq, Greenland, Goose Bay, Labrador and Sagamore Hill, Massachusetts based on 3–7 years data base of 15-min scintillation indices. The forcing functions are time of day, day of the year, magnetic index and solar flux. However, these individual models are much

more limited than WBMOD as (1) they are applicable only for the frequency of the data base, 137 MHz, (2) there is an equipment-biased limited excursion of the scintillations and, (3) these data have an implicit dependence on the geometry of the observations, namely, observing ATS-3 from the stations detailed above. This does not permit other viewing geometries or taking into consideration the configuration of the irregularities unless correcting factors are included.

With these caveats, the equations for each station are Narssarssuaq (63° CGL intersection)

$$\begin{aligned} SI \text{ (dB)} &= -6.4 + 9.2(1 - 0.2FD)\{1 + 0.23(1 - 0.3FD) \\ &\quad \times \cos(HL + 2.0 + 0.34Kp) + 0.03 \\ &\quad \times \cos[2(HL - 0.6)] + 0.02 \cos[3(HL \\ &\quad + 3.0)]\}2^{[0.14Kp(1 + 0.12FD) + 0.09As(1 + 1.76FD)]} \\ FD &= \cos(DA + 15.6) + 0.56 \cos[2(DA - 22.4)] \end{aligned} \quad (10.69a)$$

Goose Bay (60° CGL intersection)

$$\begin{aligned} SI \text{ (dB)} &= -1.3 + 1.1(1 - 0.77FD)\{1 + 0.5(1 - 0.2FD) \\ &\quad \times \cos(HL + 2.1 - 0.6Kp) + 0.06 \\ &\quad \times \cos[2(HL - 2.1)] + 0.02 \cos[3(HL \\ &\quad + 5.2)]\}2^{[0.3Kp(1 + 0.1FD) + 0.8As(1 + 1.2FD)]} \\ FD &= \cos(DA + 0.5) + 0.2 \cos[2(DA - 99)] \end{aligned} \quad (10.69b)$$

Sagamore Hill (53° CGL intersection)

$$\begin{aligned} SI \text{ (dB)} &= 0.33 + 0.02(1 + 0.2FD)\{1 + 1.2(1 - 0.01FD) \\ &\quad \times \cos(HL - 0.4 - 0.15 Kp) + 0.3 \\ &\quad \times \cos[2(HL - 0.8)] - 0.1 \cos[3(HL \\ &\quad + 6.1)]\}2^{[0.38Kp(1 + 0.3FD) + 3.1As(1 - 0.2FD)]} \\ FD &= \cos(DA + 56) + 0.7 \cos[2(DA - 143)]. \end{aligned} \quad (10.69c)$$

$DA$  is day number,  $As = S_f/100$ ,  $HL$  is local time (hours) at subionospheric point (350 km), and  $S_f$  is solar flux at 2695 MHz in solar flux units; all angles are in radians. Arguments of the cosines with diurnal and yearly terms should be converted by factors of  $2\pi/24$  and  $2\pi/365$ , respectively.

In Aarons et al. [1980a] corrections for frequency dependence are given thus allowing higher frequency scintillations to be estimated. In addition, corrections for geometry are also given similar to those cited in Section 10.7.3.1.

## CHAPTER 10

### 10.8 IONOSPHERIC TIME DELAY EFFECTS ON EARTH-SPACE PROPAGATION

One of the most important effects of the ionosphere on radio waves that traverse it is a retardation, or group delay, on the modulation or information carried on the radio wave, due to its encounter with the free, thermal electrons in the earth's ionosphere. Other effects the ionosphere has on radio waves include (1) RF carrier phase advance (2) Doppler shift of the RF carrier of the radio wave (3) Faraday rotation of the plane of polarization of linearly polarized waves (4) angular refraction or bending of the radio wave path as it travels through the ionosphere (5) distortion of the waveform of transmitted pulses, and (6) amplitude and phase scintillation. With the exception of scintillation effects (see Section 10.7), all the other effects listed here are proportional, at least to first order, to the total number of electrons encountered by the wave on its passage through the ionosphere or to their time rate of change. In fact, phase scintillation also is merely the short term, time rate of change of total electron content (TEC) after the longer term variations have been removed.

In this section a short description is given of each ionospheric TEC effect upon radio waves, along with a representative value of the magnitude of each of these effects under normal ionospheric conditions. This is followed by a discussion of the important characteristics of average ionospheric TEC behavior and the temporal and spatial variability of TEC.

#### 10.8.1 Group Path Delay

The additional time delay, over the free space transit time, of a signal transmitted from above the ionosphere to a user on, or near, the earth's surface is given by

$$\Delta t = \frac{40.3}{cf^2} \times \text{TEC (s)}, \quad (10.70)$$

where the TEC is the total number of electrons along the path from the transmitter to the receiver,  $c$  is the velocity of light in m/sec., and  $f$  is the system operating frequency in hertz. The TEC is generally expressed as the number of electrons in a unit cross section column of one square meter area along this path.

A plot of time delay versus system operating frequency for TEC values from  $10^{16}$  to  $10^{19}$  el/m<sup>2</sup> is given in Figure 10-82. These two values represent the extremes of observed TEC in the earth's ionosphere. Note that, at a system operating frequency of 1 GHz, for example, a TEC of  $10^{18}$ , a value frequently exceeded in many parts of the world, would produce a time delay of 134 ns or 40.2 m of range error. At a system operating frequency of 100 MHz this same TEC values would produce a range error of over 4

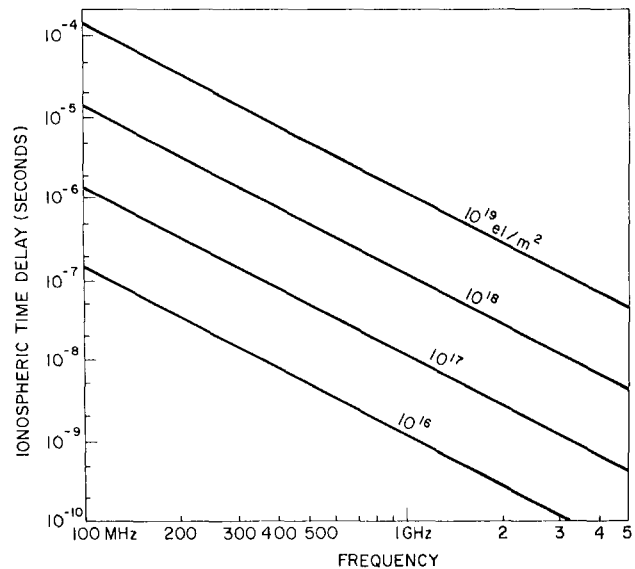


Figure 10-82. Time delay vs frequency for various values of TEC.

km! Obviously, the TEC parameter is of potentially great importance to precision satellite ranging systems.

**10.8.1.1 Two-Frequency Ionospheric Time Delay Corrections.** If the navigation or ranging system bandwidth is large enough so that two, fairly widely spaced bands can be used for ranging, the ionospheric time delay error can be reduced to an acceptable level automatically and can be made transparent to the system user. Because the ionospheric time delay is a function of frequency we can write:

$$\Delta t_1 = \frac{k}{cf_1^2} \times \text{TEC}, \quad \Delta t_2 = \frac{k}{cf_2^2} \times \text{TEC}, \quad (10.71)$$

where  $\Delta t_1$  is the ionospheric error on frequency  $f_1$ , and  $\Delta t_2$  is the ionospheric error on the frequency  $f_2$ . If the normal system operational frequency is  $f_1$  and we choose  $f_2$  at a lower frequency for ionospheric correction purposes, we

$$\begin{aligned} \text{obtain: } \delta(\Delta t) &= \frac{k}{c} \times \text{TEC} (1/f_2^2 - 1/f_1^2) \\ &= \Delta t_1 (f_1^2 - f_2^2) / f_2^2 \end{aligned} \quad (10.72)$$

$$\text{or: } \Delta t_1 = f_2^2 / (f_1^2 - f_2^2) \times \delta(\Delta t)$$

The value  $\delta(\Delta t)$  is obtained from the difference of the simultaneous measurements of the total range, including ionospheric time delay, at the two frequencies,  $f_1$  and  $f_2$ , since the geometric distance is, of course, the same at all frequencies. The quantity  $f_2^2 / (f_1^2 - f_2^2)$  is called the ionospheric scaling factor. For ratios of  $f_2/f_1$  near unity, the required precision of the differential measurement may be unreasonably large. A plot of this quantity, normalized by  $f_1$ , is given in Figure 10-83. In this derivation the contribution of re-

## IONOSPHERIC RADIO WAVE PROPAGATION

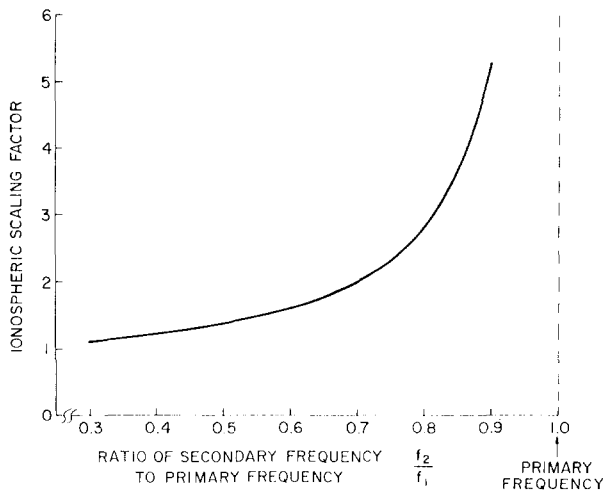


Figure 10-83. Ionospheric scaling factor vs ratio of primary (higher) to secondary (lower) frequency.

ceiver noise to the differential measurement accuracy has not been considered.

**10.8.1.2 An Example of a Two-Frequency Ionospheric Time Delay System.** The Department of Defense is currently testing an advanced navigation system, called the NAVSTAR-Global Positioning System (GPS), [Demaro, 1981; Milliken and Zaller, 1978] which uses coherently derived, identical modulation on two carrier frequencies, called L1 and L2, to measure the ionospheric group path delay directly and thereby correct for ionospheric time delay. The ratio of frequencies used in the GPS system is exactly 154/120, with the higher frequency (L1) at 1575 MHz. The two carrier frequencies transmitted by the GPS system are the 154th and 120th harmonics of 10.23 MHz. This 10 MHz frequency is bi-phase modulated on both carriers with a pseudo random code resulting in a  $[(\sin x)/x]^2$  shaped spectrum of width 20 MHz to the first nulls. A user with knowledge of the transmitted code collapses the received spectrum to equivalent carriers with 10 MHz modulation. The 10 MHz modulation is transmitted with a known phase difference on the two carriers, and the received modulation phase difference is a direct measure of the ionospheric group path delay.

For the GPS carrier and modulation frequencies the ionospheric group path delay at frequency L1, as obtained from Equation 10.73 is

$$\Delta t_1 = -1.5457 \delta(\Delta t), \quad (10.73)$$

where  $\delta(\Delta t)$  is the difference between the ionospheric time delay measured at the two frequencies. This difference in range is directly related to absolute ionospheric time delay as, of course, the satellite is at the same range at both frequencies. The only frequency dependent parameter in range measurements is the ionospheric time delay effect,

assuming the satellite transmitted modulation phase at L1 and L2 is known and the receiving system frequency dispersive characteristics can be independently measured and corrected for.

For a typical daytime high solar activity TEC value of  $10^{18}$  el/m<sup>2</sup> column the  $\delta(\Delta t)$  measured by a GPS receiver would be 35 ns or 10.5 m of ionospheric error. For a direct measure of absolute TEC from the modulation phase delay at L2 minus L1 we have

$$\text{TEC} = 2.852 \times 10^{16} \times \delta(\Delta t), \quad (10.74)$$

where  $\delta(\Delta t)$  is measured in nanoseconds (ns). Since, at 10.23 MHz, one complete cycle of modulation phase of 360° is 97.75 ns, we obtain  $\text{TEC} = 0.7745 \times 10^{16}$  el/m<sup>2</sup> per degree of 10.23 MHz modulation phase difference, or:  $\text{TEC} = 278.8 \times 10^{16}$  el/m<sup>2</sup> per cycle of modulation phase difference. Thus, the cycle ambiguity in absolute values of TEC is trivial to resolve using the GPS system as a means of determining ionospheric time delay.

Absolute ionospheric time delay measurements can be made with an accuracy approaching 1 to 2 ns, depending upon the received signal to noise ratio on both frequencies. For the power levels transmitted by the GPS satellites, an omnidirectional receiving antenna, and a receiver with a modulation tracking bandwidth of approximately 15 Hz, the differential modulation phase has been measured to within approximately  $\pm 2$  ns. The contribution of receiver noise for the two-frequency ionospheric time delay corrections on the GPS system has been considered by Cretcher [1975].

### 10.8.2 RF Carrier Phase Advance

In addition to group path delay, or modulation time delay, over the free space delay, the phase of the carrier of radio frequency transmissions is changed by the ionosphere. The RF phase is advanced with respect to its phase in the absence of an ionosphere. This effect is extremely important in determining space object velocities by means of range rate measurements. The amount of phase increase or phase path decrease can be expressed as

$$\Delta\Phi = \frac{1.34 \times 10^{-7}}{f} \text{TEC (cycles)}, \quad (10.75)$$

where  $f$  is the system operating frequency in hertz, and TEC is in el/m<sup>2</sup> column. In practice, the amount of this phase advance cannot readily be measured on a single frequency and two, coherently derived, frequencies are required for this measurement.

**10.8.2.1 Differential Carrier Phase.** In addition to the dual frequency identical modulation transmitted from the GPS satellites for ionospheric group path correction, these satellites also transmit two, coherently-derived carrier fre-

## CHAPTER 10

quencies for ionospheric differential carrier phase measurements. For the pair of frequencies used by GPS, approximately 1.2 and 1.6 GHz, the differential carrier phase shift, referenced to the lower frequency, is

$$\Delta\phi = \frac{1.34}{L_2} \times 10^{-7} \times \frac{(m^2 - 1)}{m^2} \times \text{TEC (cycles)}, \quad (10.76)$$

where  $m = f_1/f_2 = 1.2833$ ,  $\Delta\phi = 4.31 \times 10^{-17} \times \text{TEC}$  or  $2.32 \times 10^{16} \text{ el/m}^2$  per complete  $2\pi$  cycle of differential carrier phase between L1 and L2, measured at L2. The differential carrier phase [Equation (10.76)] is related to the differential modulation phase, [Equation (10.72)] simply by the ratio of carrier to modulation frequencies. With a reasonable carrier signal to noise ratio, this differential carrier phase can be measured to within a few degrees, or less than approximately  $0.04 \times 10^{16} \text{ el/m}^2$ . Since the TEC is generally much greater than  $2.32 \times 10^{16}$ , corresponding to  $2\pi$  of differential carrier phase, there is a  $2n\pi$  ambiguity in the differential phase measurement.

The differential carrier method of measuring TEC cannot, in practice, be used to measure absolute values of TEC by itself due to the large  $2n\pi$  phase ambiguity in the measurement, but this is not important for navigation systems which require a correction only for range rate errors due to the ionosphere between two measurement times.

The US Navy Navigation Satellite System, NNSS [Black, 1980; Kouba, 1983], determines position for stationary and slowly moving vehicles by measuring satellite transmitted RF carrier phase changes as a function of low-orbit satellite motion across the sky. This method of positioning requires only range rate information. The primary NNSS frequency is 400 MHz. A second RF carrier at 150 MHz is used only for ionospheric range rate corrections. While various techniques have been proposed for determining the absolute TEC from the differential carrier phase information received from the NNSS satellites, they all involve assumptions concerning some *a priori* knowledge of the ionosphere, and they cannot be used in the general case.

As an ionospheric monitoring tool the combination of differential carrier phase and differential modulation phase provides an excellent means of determining ionospheric electron content along the ray path to the satellite. The absolute value of TEC can be determined by the group delay technique and relative TEC changes can be measured with great accuracy by the differential carrier phase technique.

**10.8.2.2 Second Difference of Carrier Phase.** The second difference in phase between an RF carrier and that of its upper and lower sidebands can be used to measure absolute values of TEC, as described by Burns and Fremouw [1970]. If three coherently derived frequencies,  $f - f_m$ ,  $f$ , and  $f + f_m$  are transmitted the second difference of phase is given by

$$\Delta_2\phi = (\phi_u - \phi_c) - (\phi_c - \phi_L) = \phi_u + \phi_L - 2 \times \phi_c$$

from Equation (10.75)

$$\Delta\phi = \frac{1.34}{f} \times 10^{-7} \times \text{TEC (cycles)}$$

thus

$$\Delta_2\phi = \frac{2.68 \times 10^{-7} f_m^2}{f(f^2 - f_m^2)} \text{TEC (cycles)}.$$

When

$$f^2 \gg f_m^2 \quad (10.77)$$

$$\Delta_2\phi = \frac{2.68 \times 10^{-7} f_m^2}{f^3} \text{TEC (cycles)}.$$

For a carrier frequency of 100 MHz a modulation frequency of 1.93 MHz would be required to give  $2\pi$  of second differential phase for a TEC value of  $10^{18} \text{ el/m}^2$ . A value of  $\Delta_2\phi$  of  $2\pi$  for  $10^{18} \text{ el/m}^2$  is a reasonable compromise between the requirement for minimizing chances of an ambiguity in absolute TEC and accuracy in measuring TEC relative changes. The second difference of carrier phase has been used with the DNA-002 satellite to make estimates of the absolute value of TEC [Freemouw et al., 1978].

### 10.8.3 Doppler Shift

Since frequency is simply the time derivative of phase, an additional contribution to geometric Doppler shift results due to changing TEC. This additional frequency shift is generally small compared to the normal geometric Doppler shift, but can be computed by

$$\Delta f = \frac{d\phi}{dt} = \frac{1.34 \times 10^{-7}}{f} \frac{d}{dt} \text{TEC (Hz)}. \quad (10.78)$$

For high orbit satellites where the diurnal changes in TEC are greater than geometric ones, an upper limit to the rate of change of TEC is approximately  $0.1 \times 10^{16} \text{ el m}^{-2}\text{s}^{-1}$ . This value yields an additional frequency shift of less than 0.1 Hz at 1.6 GHz which would not be significant compared with a typical required receiver loop bandwidth of at least a few hertz. At 400 MHz a similar rate of change of TEC would produce a frequency shift of approximately 0.3 Hz, probably still not significant.

During times of severe phase scintillation, which can occur even at GHz frequencies, the TEC likely does not change in a consistent, rapid manner to yield greater ion-

ospheric Doppler shifts, but the phase of the incoming RF signal can have a large random fluctuation superimposed upon the changes associated with the normal rate of change in TEC. This large, random component may actually spread out the spectrum of the received signal sufficiently to cause the receiver to lose phase lock, as the receiver signal phase may have little energy remaining in the carrier, and instead may be spread over several Hz, with little recognizable carrier remaining. A knowledge of phase scintillation rates is required to determine the spread of received signal phase.

**10.8.4 Faraday Polarization Rotation**

When a linearly polarized radio wave traverses the ionosphere the wave undergoes rotation of the plane of polarization. At frequencies of approximately 100 MHz and higher the amount of this polarization rotation can be described by:

$$\Omega = \frac{2.36 \times 10^{-5}}{f^2} \int B \cos \theta Ndl. \quad (10.79a)$$

where the quantity inside the integral is the product of electron density times the longitudinal component of the earth's magnetic field, integrated along the radio wave path. Many ionospheric workers have used this effect, named for Michael Faraday who first observed polarization changes in an optical experiment, to make measurements of the TEC of the ionosphere. Since the longitudinal magnetic field intensity changes much slower with height than the electron density of the ionosphere, the equation can be rewritten as

$$\Omega = \frac{K}{f^2} B_L \times \text{TEC}, \quad (10.79b)$$

where  $B_L = \overline{B \cos \theta}$  is taken at a mean ionospheric height, usually near 400 km,  $K = 2.36 \times 10^{-5}$  and TEC is  $\int Ndl$ . Typical values of polarization rotation for northern midlatitude stations viewing a geostationary satellite near their station meridian are given in Figure 10-84 as a function of system frequency and total electron content. In fact, the largest portion of TEC data available today from stations throughout the world have come from Faraday rotation measurements from geostationary satellite VHF signals of opportunity.

For satellite navigation and communication designers, however, the Faraday polarization rotation effect is a nuisance. If a linearly polarized wave is transmitted from a satellite to an observer on or near the surface of the earth, the amount of polarization rotation may be nearly an odd integral multiple of 90 degrees, thereby giving no signal on the receiver's linearly polarized antenna, unless the user is careful to realign his antenna polarization for maximum received signal.

As shown in Figure 10.84 at 4 GHz, a commercial

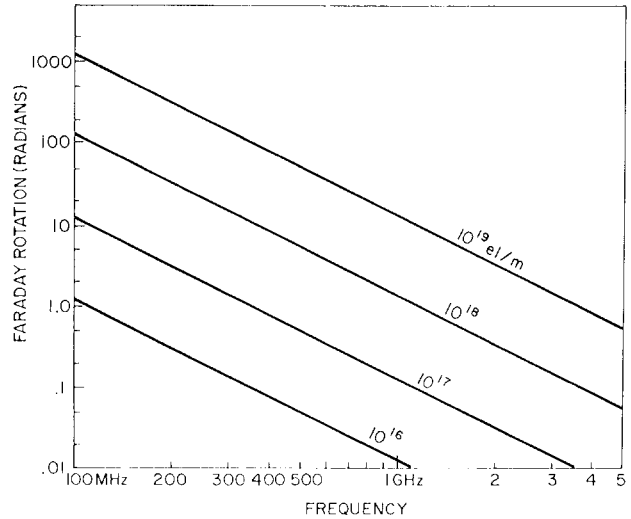


Figure 10-84. Faraday polarization rotation vs frequency for various values of TEC.

satellite transponder frequency band, the amount of Faraday rotation can be a tenth of a radian, well in excess of that required for dual, linear orthogonal channel separation.

The Faraday rotation problem is overcome by the use of circular polarization of the correct sense at both the satellite and at the user's receiver. Generally the mobile user finds it difficult to utilize circular polarization due to the continual vehicle directional changes; thus he settles for a received linear polarization. The 3 dB loss between transmitted circular polarization and received linear polarization is a necessary price to pay for user antenna maneuverability and simplicity.

**10.8.5 Angular Refraction**

The refractive index of the earth's ionosphere is responsible for the bending of radio waves from a straight line geometric path between satellite and ground. This angular refraction or bending produces an apparent higher elevation angle than the geometric elevation. Millman and Reinsmith [1974] have derived expressions relating the refraction to the resultant angular bending. Perhaps the easiest expressions to use, as given by Millman and Reinsmith [1974] relate the ionospheric range error to angular refraction:

$$\Delta E = \frac{R + r_o \sin E_o (r_o \cos E_o)}{h_i (2r_o + h_i) + r_o^2 \sin E_o} \times \frac{\Delta R}{R}, \quad (10.80)$$

where  $E_o$  is the apparent elevation angle,  $R$  is the apparent range,  $\Delta R$  is computed from  $\Delta R = (40.3/f^2) \times \text{TEC}$ ,  $r_o$  is the earth's radius, and  $h_i$  is the height of the centroid of the TEC distribution, generally between 300 and 400 km.

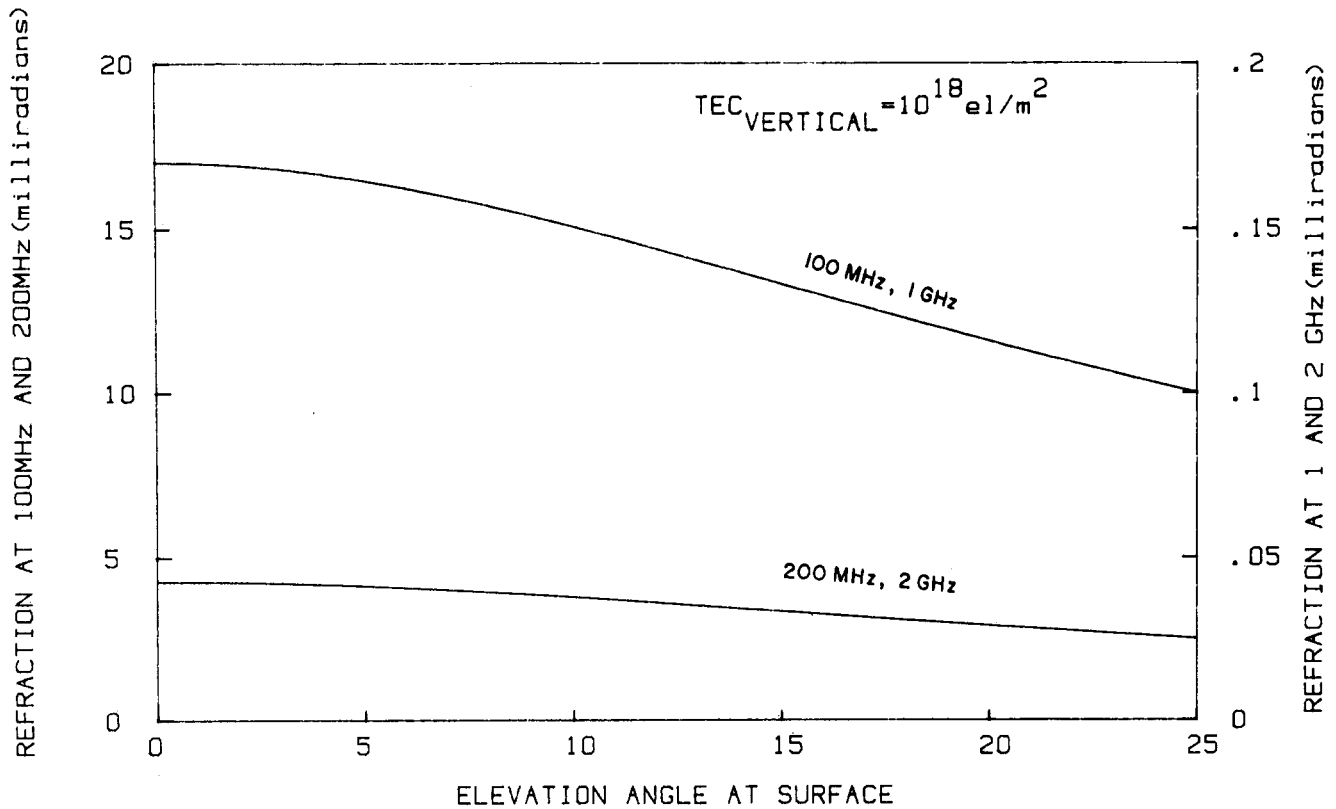


Figure 10-85. Refraction in elevation angle vs elevation angle for indicated frequencies and values of TEC.

For low elevation angles and satellites well above most of the ionization,  $R \gg r_o \sin E_o$ , and the angular refraction can be expressed as:

$$\Delta E = \frac{\cos E_o}{2h_i} \Delta R. \quad (10.81)$$

Typical values of elevation refraction error for a TEC of  $10^{18}$  el/m<sup>2</sup> column are shown in Figure 10-85 for several frequencies. Note that, at the lowest frequency, 100 MHz, near the horizon the refraction is well over 1.5 degrees! The curves shown in Figure 10.85 have been constructed using the approximation derived by Millman and Reinsmith [1974] for low elevation angles given in Equation (10.81).

Generally, the range error itself is the main ionospheric problem for advanced navigation systems, and elevation angle errors are insignificant. Satellite detection radar systems, on the other hand, do have the requirement to know accurate pointing elevation angles for their large aperture arrays, though generally the accurate tracking is done by using range rate information, and elevation angle is of secondary importance as long as the beamwidth of the antenna is large enough to see the target.

Errors in the azimuth of radio waves transmitted through the ionosphere can also occur; they depend upon azimuthal gradients in TEC which are generally small and which can usually be neglected in practical cases.

### 10.8.6 Distortion of Pulse Waveforms

Two characteristics of the ionosphere can produce distortion of pulses of RF energy propagated through it. The dispersion, or differential time delay due to the normal ionosphere, as derived by Millman [1965] is proportional to  $1/f^2$ , and produces a difference in pulse arrival time across a bandwidth  $\Delta f$  of

$$\Delta t = \frac{80.6 \times 10^6}{c f^3} \Delta f \times \text{TEC}, \quad (10.82)$$

where  $c$  is the velocity of light in m/s,  $f$  and  $\Delta f$  are expressed in Hertz, and TEC is in el/m<sup>2</sup> column. The dispersive term for pulse distortion is thus proportional to TEC. When the difference in group delay time across the bandwidth of the pulse is the same magnitude as the width of the pulse it will be significantly disturbed by the ionosphere. Millman and Bell [1971] also derived mathematical relationships for ionospheric dispersive effects on an FM Gaussian shaped pulse.

In addition to pulse distortion by the dispersive effects due to the TEC of the normal background ionosphere, radio pulses are also modified by scattering from ionospheric irregularities. Yeh and Liu [1979] have computed pulse mean arrival time and mean pulsewidth due to both dispersion and scattering.

## IONOSPHERIC RADIO WAVE PROPAGATION

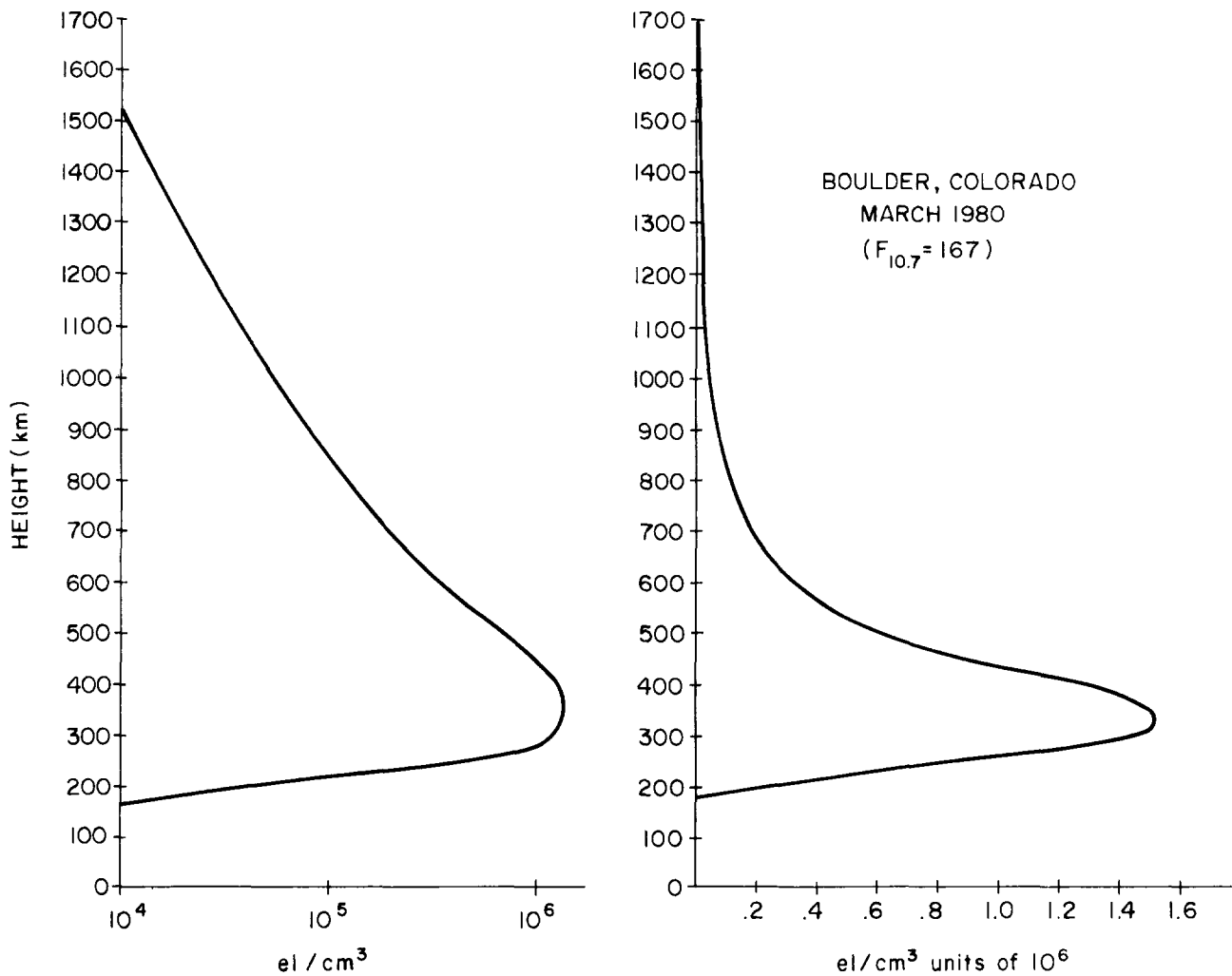


Figure 10-86. Typical profile of electron density vs height. In (a)  $\log N_e$  is plotted; in (b)  $N_e$  is plotted on a linear scale.

### 10.9 IONOSPHERIC TOTAL ELECTRON CONTENT (TEC)

#### 10.9.1 Average TEC Behavior

The ionospheric parameter responsible for the effects described in section 10.8 is the total number of free electrons, TEC, or its rate of change, along the path from a satellite to a ground station. The greatest contribution to TEC comes from the F2 region of the ionosphere. A typical daytime midlatitude, high solar maximum electron density profile is illustrated in Figure 10-86. The curve on the left side of Figure 10-86 is the  $\log$  of  $N_e$  plotted versus height as normally shown by ionospheric workers. Since the TEC is represented by the area under the curve of a linear plot of  $N_e$  versus height, the right hand plot of Figure 10-86 illustrates the actual linear plot. Note that most of the contribution to TEC occurs near the peak of the F2 region. The reason for making this point is as follows: ground-based

ionosondes have been used since the 1930s to make continuous, routine measurements of the density at the peak of the F2 region, measured by ionosondes as foF2, and equated to  $N_{\max}$  by

$$(\text{foF2})^2 = 80.6 N, \quad (10.83)$$

where foF2 is in MHz, and  $N$  is in units of  $10^6$  el/cc.

In the 1950s and 1960s, continuing to a more limited extent even today, upwards of 150 ionosondes were operated to provide improved prediction capability for long distance high frequency propagation by means of ionospheric refraction. Various models of foF2 were developed for this purpose, one of the more popular ones being commonly known as ITS-78 [Barghausen et al., 1969] after the report number which described the model. This model, among other things, characterized the 10 day average worldwide behavior of foF2 by Fourier temporal components and Legendre polynomial geographic coefficients ordered by magnetic, rather than geographic, latitude. The success of this

## CHAPTER 10

experimental, data based, or empirical model, in representing the actual worldwide foF2 is due to the large amount of data available from ionosondes in many regions of the world. Other characteristics of this model are discussed by Dandekar [1982] and in Section 10.3 of this chapter.

For the TEC parameter, data availability have been, and will likely continue to be, much more sparse. First, TEC measurements have generally been calculated from measurements of Faraday polarization rotation using VHF signals of opportunity transmitted from geostationary satellite telemetry transmitters. A few lunar reflected Faraday rotation measurements in the late 1950s and early 1960s and the TEC obtained from a few low orbit satellites did not contribute significantly to our knowledge of world-wide TEC behavior, at least not for modeling average ionospheric conditions. Only since the early to mid-1960s have TEC values been obtained on a more-or-less regular basis. Even today fewer than one dozen stations regularly contribute TEC data, which can be used in TEC modeling purposes, to a world data center.

Fortunately, most of the contribution to TEC comes from near the F2 region density peak where models of foF2 are available. These foF2 models can be combined with some limited knowledge of topside ionospheric thickness obtained from topside sounders, along with topside *in situ* density measurements, to produce a complete ionospheric height profile model. The most well known of these models is the one by Bent [Llewellyn and Bent, 1973] which uses ITS-78 coefficients for foF2, and topside exponentials for com-

puting TEC. A representation of world-wide average behavior of TEC is illustrated in Figure 10-87 for 2000 hours UT. To first order the TEC contours shown in Figure 10-87 move westward along magnetic, rather than geographic, latitude lines, at the earth's rotation rate. The Bent model was constructed using solar maximum data from the 1968-1969 period and had to be adjusted upward somewhat to account for the much higher 1979-1980 solar maximum than that of 1968-1969. This adjustment was necessary to adequately represent the actual TEC values from stations making observations in March 1980, which was near the maximum of the second highest solar cycle ever recorded in the more than 200 year history of solar cycle observations. The Bent model, appropriately adjusted for high solar cycle values, does however, represent fairly well the average behavior of TEC for many locations tested. Other worldwide ionospheric electron density profile models from which average TEC can be obtained include ones by Ching and Chiu [1973], and Chiu [1975], Kohnlein [1978], the 4-D model [VonFlotow, 1978], and the International Reference Ionosphere (IRI)[Rawer, 1981]. The characteristics of some of these models are described in Dandekar [1982] and in Section 10.3.

Other empirical models of TEC have been developed directly from TEC data alone, though these have necessarily been limited in temporal and geographic extent by the available data base. These include models of TEC over Europe and the Mediterranean [Klobuchar, 1973] for low and medium activity portions of the 11 year solar cycle, and a

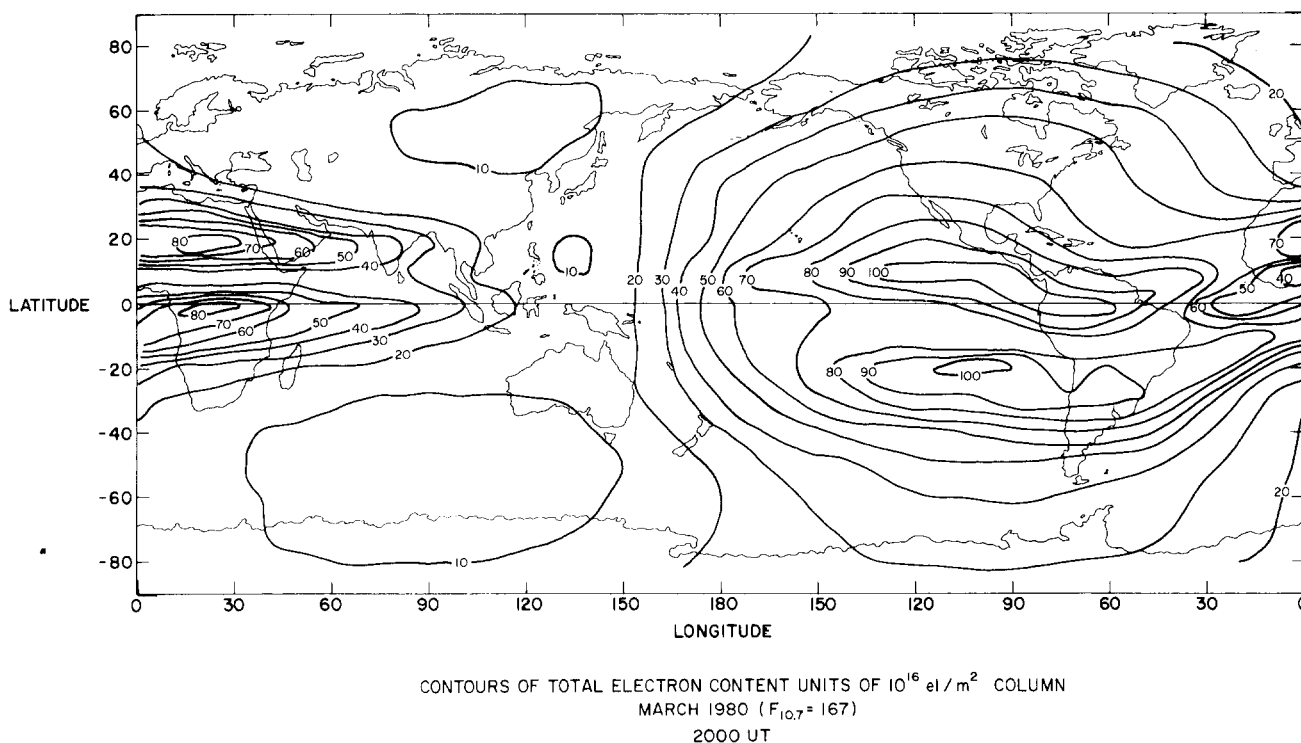


Figure 10-87. Contours of vertical TEC in units of  $10^{16}$   $e_l/m^2$  column for 2000 UT, March 1980.

## IONOSPHERIC RADIO WAVE PROPAGATION

model of TEC over the Indian subcontinent for both solar minimum and for an average solar maximum [Klobuchar, et al.1977]. Models of the slab thickness parameter, the ratio of  $TEC/N_{max}$  have been developed for specific regions such as the one for northern Europe by Kersley [1980], and one for the eastern USA by Klobuchar and Allen [1970], from which TEC can be obtained from a model of foF2. An algorithm designed for an approximate 50% correction to world-wide TEC, for use in an advanced navigation system, has been developed by Klobuchar [1975].

All of the models listed here, and the list is by no means complete, are empirical models that attempt to correct for average TEC behavior only. However, the variability from average TEC behavior can be large and may be important to some radio wave systems that must propagate through the ionosphere.

### 10.9.2 Temporal Variability of TEC

#### 10.9.2.1 Variability from Monthly Mean TEC Values.

The ionosphere is a weakly ionized plasma and the resultant TEC is a function of many variables including solar ionizing radiation, neutral wind and electric field effects, neutral composition, and temperature changes. A monthly overplot

of curves of diurnal changes in TEC for a northern mid-latitude station for twelve months during a solar maximum period is shown in Figure 10-88. The standard deviation from monthly mean diurnal behavior is approximately 20%-25%, during the daytime hours when the absolute TEC values are greatest. Figure 10-89 shows the standard deviation from monthly average TEC behavior for the mid-day hours for a number of stations during the solar maximum period 1968-1969. Again 20%-25% is a good value for the standard deviation from the monthly average behavior. The standard deviation is somewhat higher during the nighttime hours, but the absolute TEC values are much lower during these periods.

If a satellite ranging system has error requirements such that it must correct for monthly average ionospheric time delay, but still can tolerate the approximate 20%-25% variability of TEC from monthly average conditions, approximately 70%-80% of the ionospheric effect on the system can be eliminated by the use of an average TEC model such as the one constructed by Bent [Llewellyn and Bent, 1973]. If the system only requires an approximate 50% rms correction of the ionospheric time delay, the algorithm developed by Klobuchar [1975] can be used. On the other hand, if corrections for some portion of the remainder of the ionospheric time delay are required, after a state of the art TEC

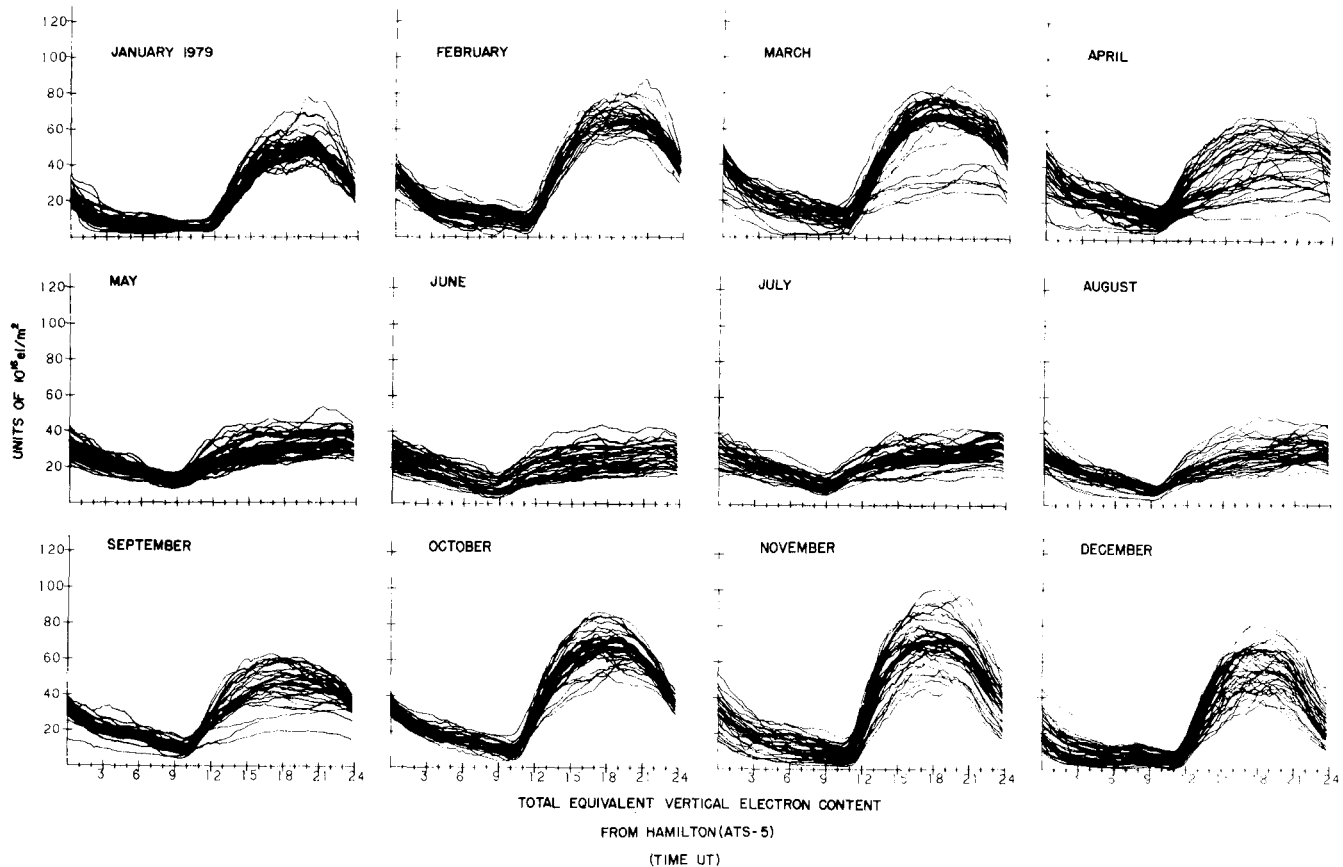


Figure 10-88 Monthly overplots of TEC diurnal curves for Hamilton, Mass. for 1979.

## CHAPTER 10

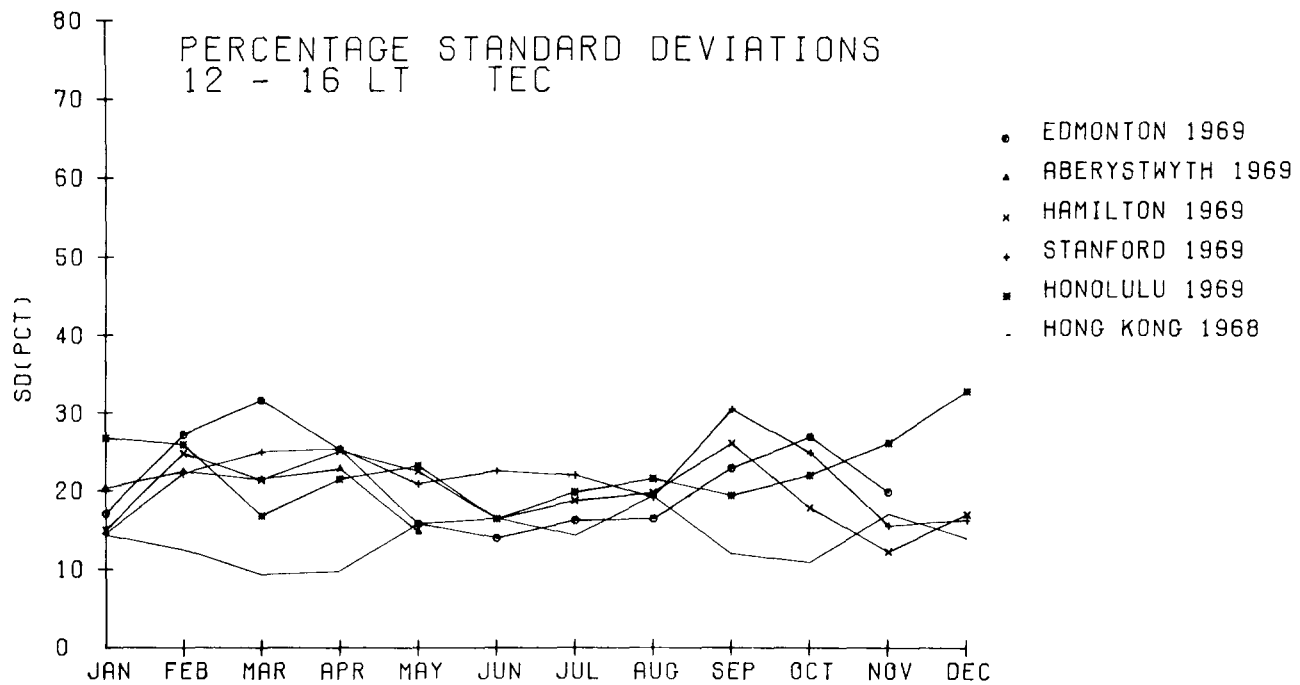


Figure 10-89. Percentage standard deviations for daytime TEC from the stations indicated.

model, such as the Bent one, has been used to take out the monthly mean TEC, then the short term (a few hours) temporal variability as well as the geographic variability, of TEC must be considered.

### 10.9.2.2 Short Term Temporal Variability of TEC.

The correlation time of departures of TEC from monthly average curves has been studied by Donatelli and Allen [1981]. They concluded, for the midlatitude station they studied, that the useful prediction time was a function of local time, season, and long term sunspot activity. However, in most cases they gained no significant improvement over the use of monthly mean predictions when they used actual data more than 3 hours old. The longest useful prediction interval occurred, fortunately, during solar maximum daytime hours when absolute TEC values are highest. During solar minimum periods their useful prediction time interval was often as short as one hour.

In their study, Donatelli and Allen [1981] predicted TEC data for the same geographic location and direction in the sky as their measurements. If the prediction is for a different location, the temporal correlation will be lower.

**10.9.2.3 Geographic Variability of TEC.** The variability of TEC at the same local time, but as a function of distance has been studied by Klobuchar and Johanson [1977]. They utilized TEC data from two sets of stations, one aligned approximately along an east-west direction, with the other set of stations aligned along an approximate north-south

direction. Their results are shown in Figures 10-90a and b for the east-west and the north-south station alignments, respectively. No significant difference in correlation distance was found with season.

The percent improvement, P.I., in TEC from the average value is related to the correlation coefficient  $r$  by

$$\text{P.I.} = 100 \times [1 - (1 - r^2)^{0.5}]$$

(see Gautier and Zacharisen, [1965]) (10.84)

Note that a correlation coefficient of 0.7 explains only 29% of the variance between the data at station pairs; hence a measurement at one station, with a correlation coefficient of 0.7 between data sets with a second station would result in an improvement at the second station over the average predicted value of only 29%.

### 10.9.3 TEC in the Near-Equatorial Region

All of the preceding sections have concentrated on the behavior of TEC in the midlatitude regions of the world, mainly because most of the available data are from that region. The near-equatorial region deserves special mention due to the fact that the highest TEC values in the world occur in this region, as shown in Figure 10-87. This region extends to approximately  $\pm 20^\circ$ - $25^\circ$  either side of the magnetic equator, with the highest TEC values not at the equator, but rather at the so called "equatorial anomaly" regions located at approximately  $\pm 15^\circ$  from the magnetic equator.

# IONOSPHERIC RADIO WAVE PROPAGATION

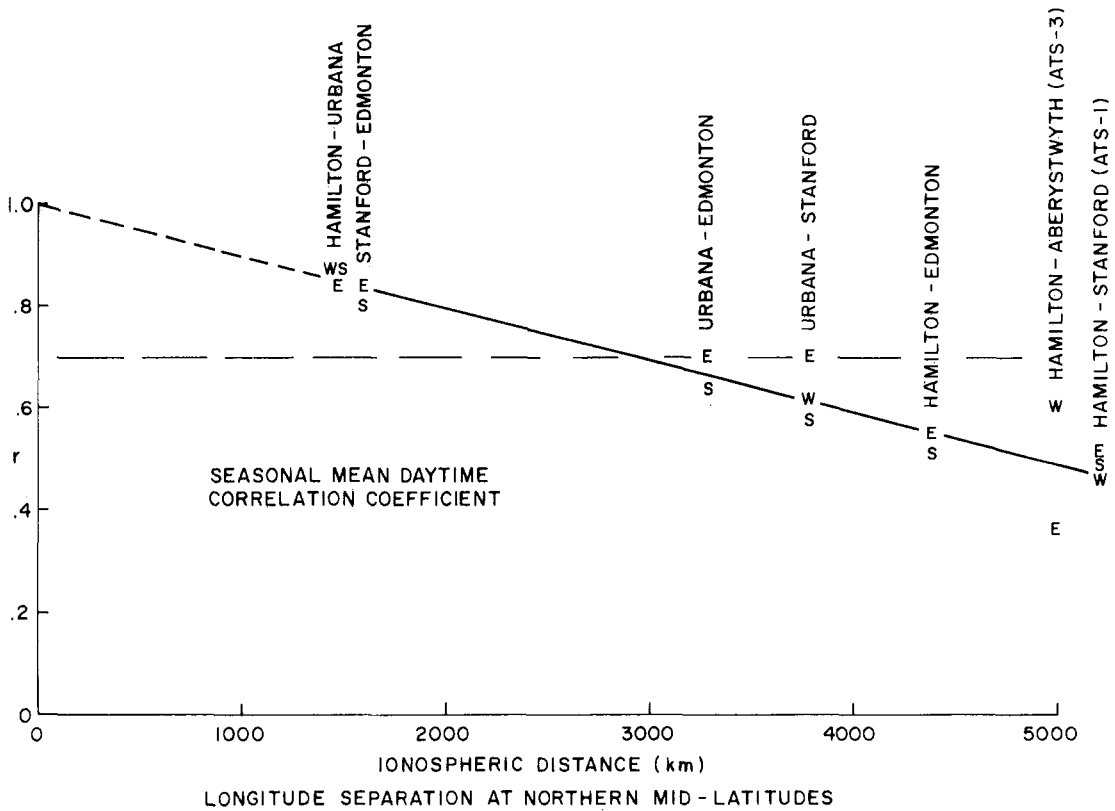
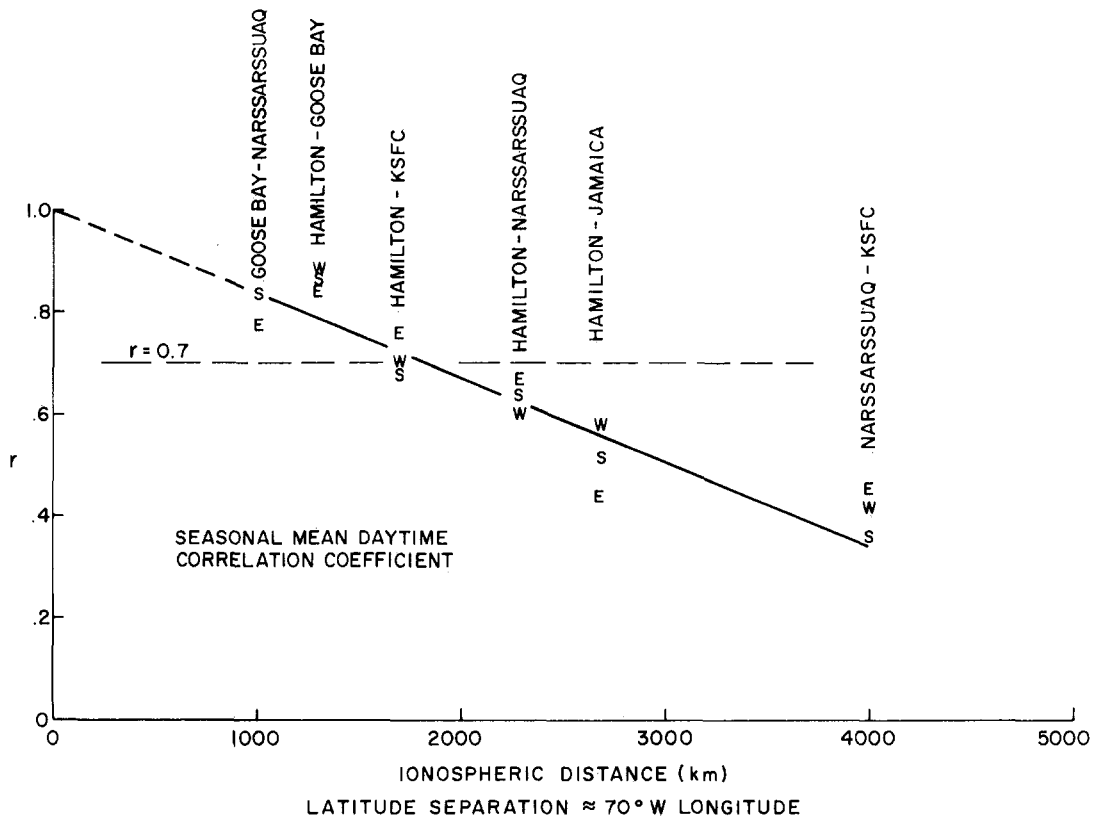


Figure 10-90. Correlation coefficient vs station separation in (a) latitude and (b) longitude.

## CHAPTER 10

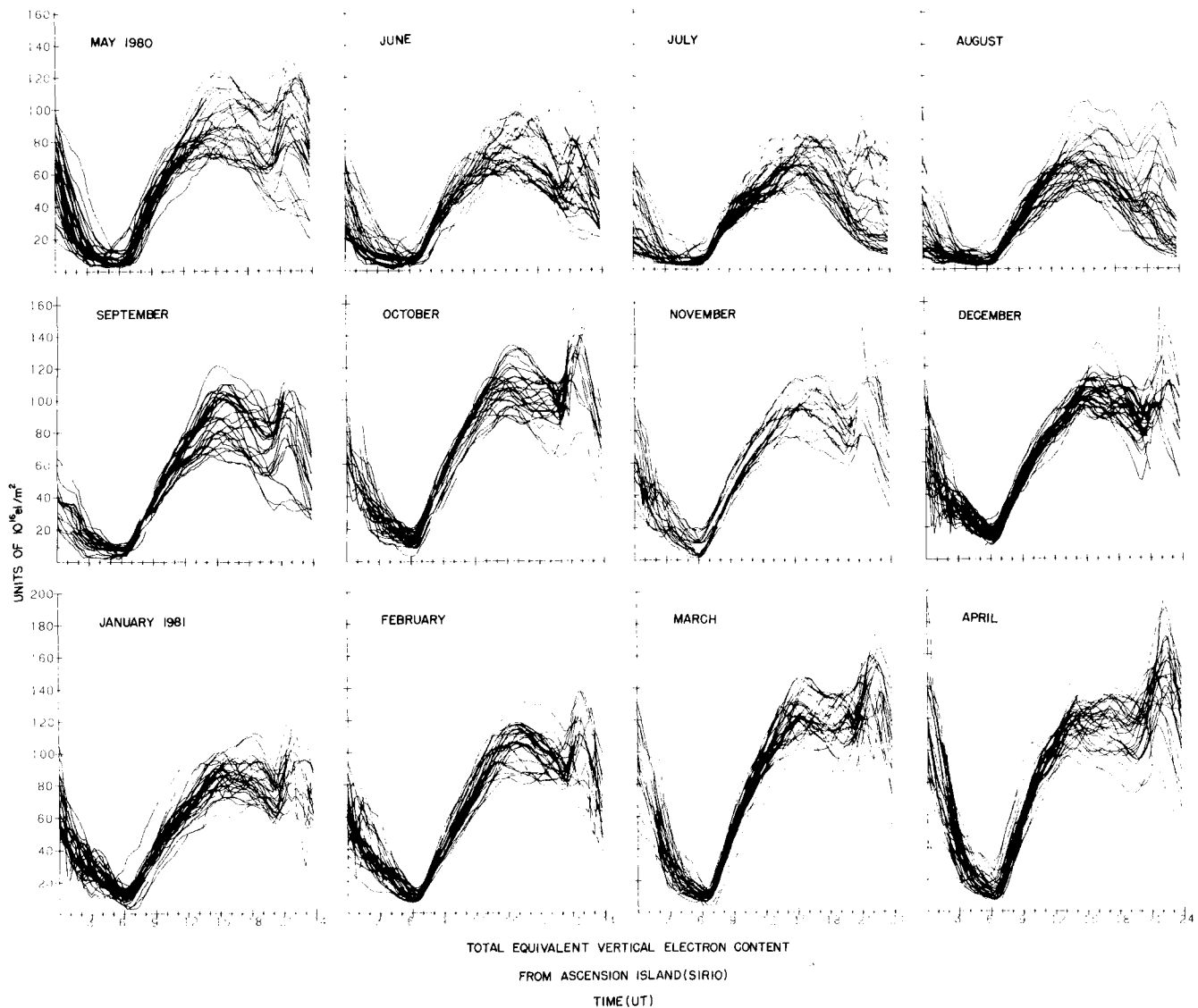


Figure 10-91. Monthly overplots of TEC diurnal curves for Ascension Island, May 1980–April 1981.

The regions of highest TEC values at 2000 hours UT are clearly seen in Figure 10-87 near 100° west longitude.

Most of the day-to-day geographic variability of TEC in the equatorial anomaly region during solar minimum conditions can be explained by the variability of equatorial electrojet strength. Unfortunately, no such similar TEC data are available for solar maximum.

An example of the high temporal variability of TEC for solar maximum conditions for Ascension Island, a station located near the peak of the southern TEC equatorial crest region, is shown in Figure 10-91. Note the extremely large day-to-day TEC variability in the afternoon and evening hours in some months. Any satellite ranging system requiring ionospheric TEC corrections in the near-equatorial region should not use the midlatitude standard deviation values of approximately 20%-25% to represent the variability of the near-equatorial region.

10-94

### 10.9.4 TEC in the Auroral and Polar Cap Regions

Since most available TEC values have been measured using radio signals transmitted from geostationary satellites, which can be viewed only at low elevation angles from high latitudes, knowledge of the variability of TEC in the auroral and polar cap regions is sparse. In the American longitude sector, where the magnetic latitudes are lowest for a given geographic latitude, there is considerable TEC data from Goose Bay, Labrador, over which the aurora passes southward, even during moderately magnetically disturbed periods. The behavior of TEC during those periods can be highly irregular, especially during the nighttime hours. TEC values often exhibit rapid changes and occasionally even exceed the daytime maximum values briefly. While the occurrence of general auroral activity may be predictable, the

## IONOSPHERIC RADIO WAVE PROPAGATION

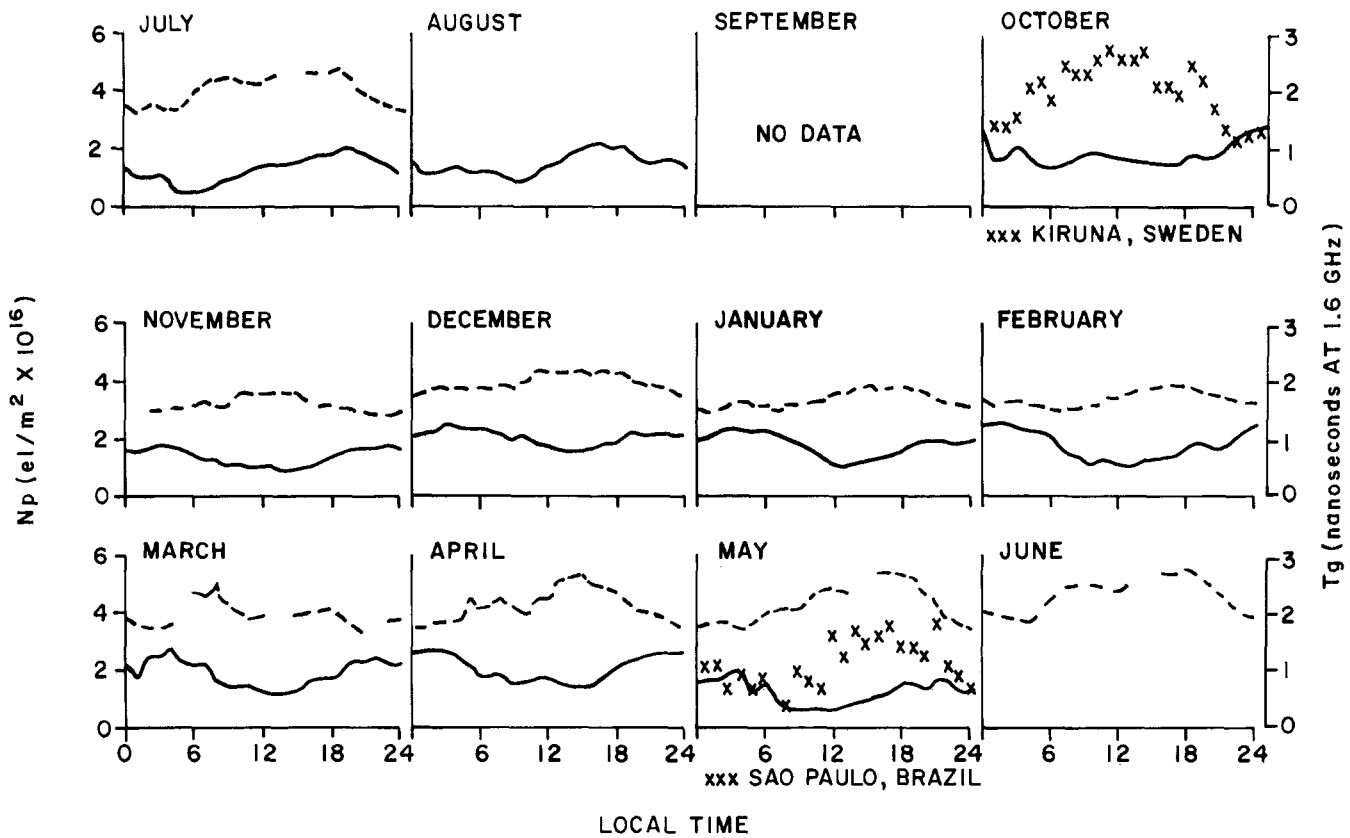


Figure 10-92. Monthly average plasmaspheric electron content vs. local time for Aberystwyth, Wales (dashed line) and for Hamilton, Mass. (solid line). Also plotted are values from Kiruna, Sweden for October 1975 and from Sao Paulo, Brazil for May 1975.

specific large increases in TEC, likely due to auroral precipitation, are not individually predictable, but may be statistically characterized as a function of magnetic activity.

In the polar cap region a negligible amount of TEC data exists. The absolute TEC values are probably lower in this region than in the midlatitudes, and the variability of the polar cap TEC is probably very high.

### 10.9.5 Protonospheric Electron Content

Most of the available TEC data has been taken by measurements of Faraday rotation of single frequency radio waves transmitted from geostationary satellites to ground observers. The electron content obtained from Faraday rotation observations, while made from radio waves transmitted from satellites at geostationary satellite height above the earth's surface, only includes the contribution of electrons up to heights of approximately 2000 km. This is because the integrated product of the longitudinal component of the earth's magnetic field times the electron density, above approximately 2000 km, is negligible. The only measurements of the additional contribution of electrons above the Faraday maximum height have been made using signals from an ionospheric beacon on the geostationary satellite ATS-6.

Davies [1980] has reviewed the overall results of the ATS-6 experiment. A summary of typical protonospheric electron content data is shown in Figure 10-92 taken from Klobuchar et. al. [1978]. Note that the protonospheric values are fairly low in absolute value.

During the nighttime hours when the ionospheric TEC is low, the protonospheric contribution may become a fairly large percentage of the total number of electrons between a satellite at geostationary height and an observer on, or near the earth's surface. Unfortunately, no protonospheric electron content data are available during solar maximum conditions.

### 10.9.6 Short Term Variations in TEC

The time rate of change of TEC, in addition to the normal diurnal variations, also has periodic variations due to perturbations of the ionospheric F region from various potential sources as geomagnetic substorms, meteorological sources such as weather fronts, shock waves from supersonic aircraft, volcanic explosions, rocket launches, and other miscellaneous sources. While these short term variations in TEC cover a large range of periods and amplitudes, common periods range from 20 to over 100 minutes with amplitudes

## CHAPTER 10

of a few percent of the background TEC. A 10% ionospheric disturbance with respect to the background TEC is uncommon, while a 1% TEC perturbation is common. Titheridge [1968] and Yeh [1972] have made studies of the statistics of traveling ionospheric disturbances (TIDs), in TEC for midlatitude regions.

A system that requires correction for the rate of change of TEC cannot rely on models of TEC to provide reliable information on short term rate of change of TEC information, and can use available TID information only in a statistical manner. The only recourse for a system significantly affected by rate of change of TEC is to use a dual frequency measurement technique to directly measure the ionospheric contribution to range rate.

### 10.9.7 Conclusions

There are at least three categories of systems potentially affected by ionospheric time delay. For the first category of user the potential systems effects may be small, at least under any naturally occurring worst case ionospheric conditions. In the second category, a user may require a nominal correction for average ionospheric time delay, but is able to tolerate the 20%-25% standard deviation from average conditions. He should expect at least a 50% correction for ionospheric time delay effects using a relatively simple time delay algorithm, and up to 70%-80% for a state of the art, fairly complex model. These model corrections can be improved by the use of actual ionospheric measurements within a reasonable temporal and spatial frame. For the third category of user ionospheric model corrections, even updated with near-real-time measurements, may not be sufficient to correct for ionospheric time delay, and the system must then make its own ionospheric correction. Fortunately, the ionosphere is a dispersive medium and the use of identical modulation on two, widely-spaced frequencies will allow a direct measurement to be made of ionospheric range delay. Two coherently-derived carrier frequencies may be used to obtain accurate time rate of change information for TEC. Details of measuring ionospheric effects directly by a system's use of multiple frequencies are available in Burns and Fremouw [1970].

## 10.10 ARTIFICIAL MODIFICATION

The field of ionospheric modifications is a subset of a more general class of research today called "Active Experiments" in space plasmas. This field was initiated early in the space program by using rocketborne chemical releases as tracers and/or modifiers of upper atmospheric processes. The physical basis for such experiments was reviewed in some detail by Haerendel [1976] during the first international meeting devoted entirely to artificial modification studies [Albrecht, 1976]. A second major symposium on Active

Experiments [Russell and Rycroft, 1980] dealt with a broad spectrum of experiments: energetic particle injections, plasma wave (VLF) injections, mass (neutral gas) injections, as well as with laboratory and computer simulation experiments. The most recent summary of Active Experiments in space treated particle beams, neutral gas injections, wave injections and high power heating experiments [Burke, 1983]. The common thread that binds all of these methods is the use of well-defined input/output experiments to probe the system response functions for specific atmospheric and space plasma systems.

In terms of purely ionospheric phenomena, the modification of ambient electrons and ions are most often achieved by chemical injections or by radiowave heating experiments. Each of these areas is treated in the following sections.

### 10.10.1 Chemical Releases

The history of chemical release experiments dates from the the earliest days of space exploration when, shortly after Sputnik-1 in 1957, rocket-borne payloads of highly reactive chemicals were injected into the upper atmosphere in attempts to use artificial perturbation techniques as a way of investigating the structure and dynamics of the neutral and ionized components of the upper atmosphere. The Air Force Cambridge Research Laboratories (ARCRL) carried out the initial work with *plasma cloud injections* [Marmo et al., 1959], and later a pioneering and comprehensive series of chemical injection experiments under PROJECT FIREFLY [Rosenberg, 1964]. Experiments using barium releases (or similar, easily ionized species) have formed the major activity in this field, tracing and/or modifying ionospheric processes from auroral locations [Holmgren et al., 1980] to the equator [Kelly et al. 1979]. The symposium proceedings referenced above [Albrecht, 1976; Russell and Rycroft, 1980; Burke, 1983] offer comprehensive summaries of these experiments.

The field of *neutral mass injections* was first concerned with the environmental impacts that might result from the larger and more powerful rockets being developed for space exploration [Kellogg, 1964]. In 1973, when the last Saturn V rocket to be used in the U.S. Space Program launched NASA's Skylab Workshop, the resultant deposition of approximately 1000 kg/s of H<sub>2</sub> and H<sub>2</sub>O exhaust molecules into the 200-440 km altitude region initiated a rapid and large-scale depletion of the ionosphere to an extent never seen before (see Figure 10-93). The artificially-created "ionospheric hole" amounted to nearly a 50% decrease in the total electron content (TEC) of the ionosphere over an area of approximately a million square kilometers. Mendillo et al. [1975 a,b] attributed the effect to the explosive expansion of an exhaust cloud of highly reactive molecules that initiated a rapid recombination of the ionospheric plasma.

The introduction of such typical rocket exhaust products as H<sub>2</sub>, H<sub>2</sub>O and CO<sub>2</sub> into the upper atmosphere causes the

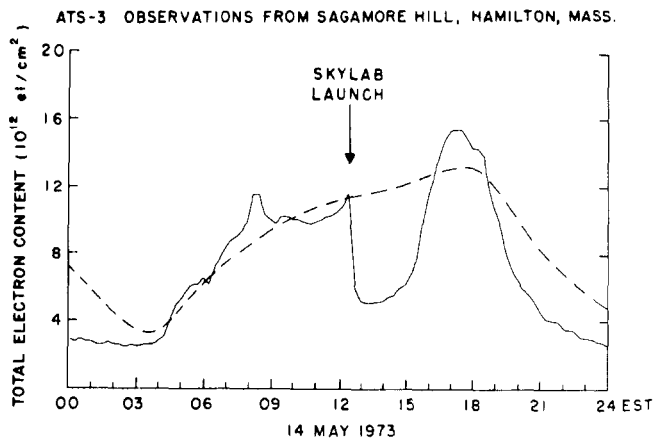
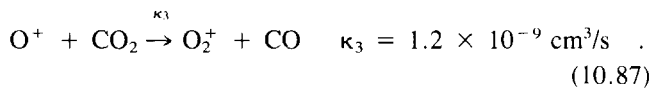
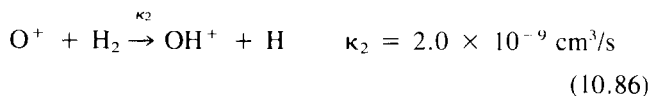
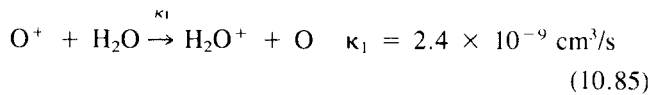


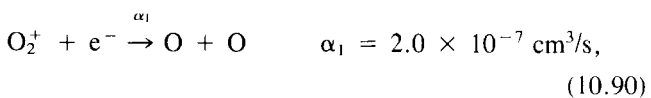
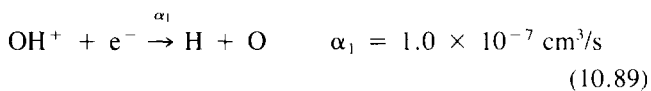
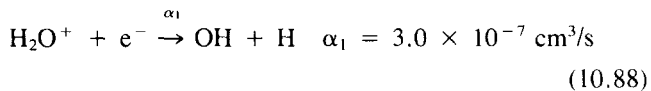
Figure 10-93. Total Electron Content (TEC) data used to detect the "SKYLAB effect" on 14 May 1973. The dashed curve gives the anticipated diurnal TEC behavior based upon a monthly median prediction updated for geomagnetic storm effects [Mendillo et al., 1975b].

atomic ion F region plasma to be transformed to a molecular ion plasma at rates 100 to 1000 times faster than occur with the naturally present molecules of nitrogen ( $N_2$ ) and oxygen ( $O_2$ ).

These important reactions are



Once a molecular ion is formed, its dissociative recombination with an ambient electron occurs rapidly,



and hence an "ionospheric hole" is formed. A review of rocket induced ionospheric disturbances has been given by Mendillo [1981].

Figure 10-94 contains a schematic showing the many physical and chemical processes associated with artificially-induced depletions in the F region. It should be noted that

the lack of large-scale/long-lived modification effects upon the lower regions of the ionosphere is due primarily to the high neutral densities and molecular ion chemistry already dominant at D and E region heights, as discussed in detail by Forbes [1980].

Computer simulation models for the F region effects have been constructed by Bernhardt et al. [1975], Mendillo and Forbes [1978], Anderson and Bernhardt [1978] and Zinn and Sutherland [1980]. The emphasis in these studies has ranged from environmental impacts of proposed in-space construction scenarios [Rote, 1979], to laboratory-in-space experiments using "dedicated engine-burns" of the space shuttle as part of the Spacelab-2 mission in 1985, to a series of chemical modification experiments planned for the Combined Release and Radiation Effects Satellite (CRRES) scheduled for the late 1980's. Some of these concepts have been tested using rocketborne chemical payloads during projects LAGOPEDO [Pongratz and Smith, 1978], WATERHOLE [Whalen et al., 1981], BIME [Narcisi, 1983] and COLOURED BUBBLES [Haerendel et al., 1983]. In the AFGL Ionospheric Modification Study [Narcisi, 1983], attempts were made to study effects associated with  $SF_6$  induced negative ion plasmas [Mendillo and Forbes, 1978]. During so-called "experiments of opportunity," where scheduled rocket launches are monitored by a variety of techniques, satellite radio beacon observations have been reported by Mendillo, et al. [1980] incoherent scatter measurements by Wand and Mendillo [1984], and optical diagnostics by Kofsky [1981] and Mendillo and Baumgardner [1982]. Figure 10-95 offers an example of the artificial airglow clouds associated with F region hole-making experiments.

### 10.10.2 High Power HF Transmissions

Ground based high power high frequency transmitters operating below the critical frequency of the ionosphere have been used to artificially modify the ionospheric electron thermal budget and plasma characteristics [Utlaut, 1970; Gordon et al., 1971; Shlyger, 1974; for comprehensive reviews, see Carlson and Duncan, 1977 and Gurevich and Fejer, 1979]. The power aperture product of these high power transmitters have been typically of the order of  $10^4 \text{ Mwm}^2$  providing power densities of about  $10\text{-}100 \mu\text{wm}^{-2}$  at ionospheric heights. The ionospheric "modification" or so-called "heating" experiments have been observed to cause not only the initially intended enhancements of electron gas temperature with associated plasma redistribution but give rise to a variety of nonlinear plasma phenomena. Figure 10-96 [after Carlson and Duncan, 1977] summarizes, in a schematic form, the striking variety of observed effects of ionospheric heating. The enhancements of electron gas temperature have been observed to be a few hundred degrees K [Gordon et al., 1971] caused by the deviative

SPACELAB-2 PLASMA DEPLETION EXPERIMENTS

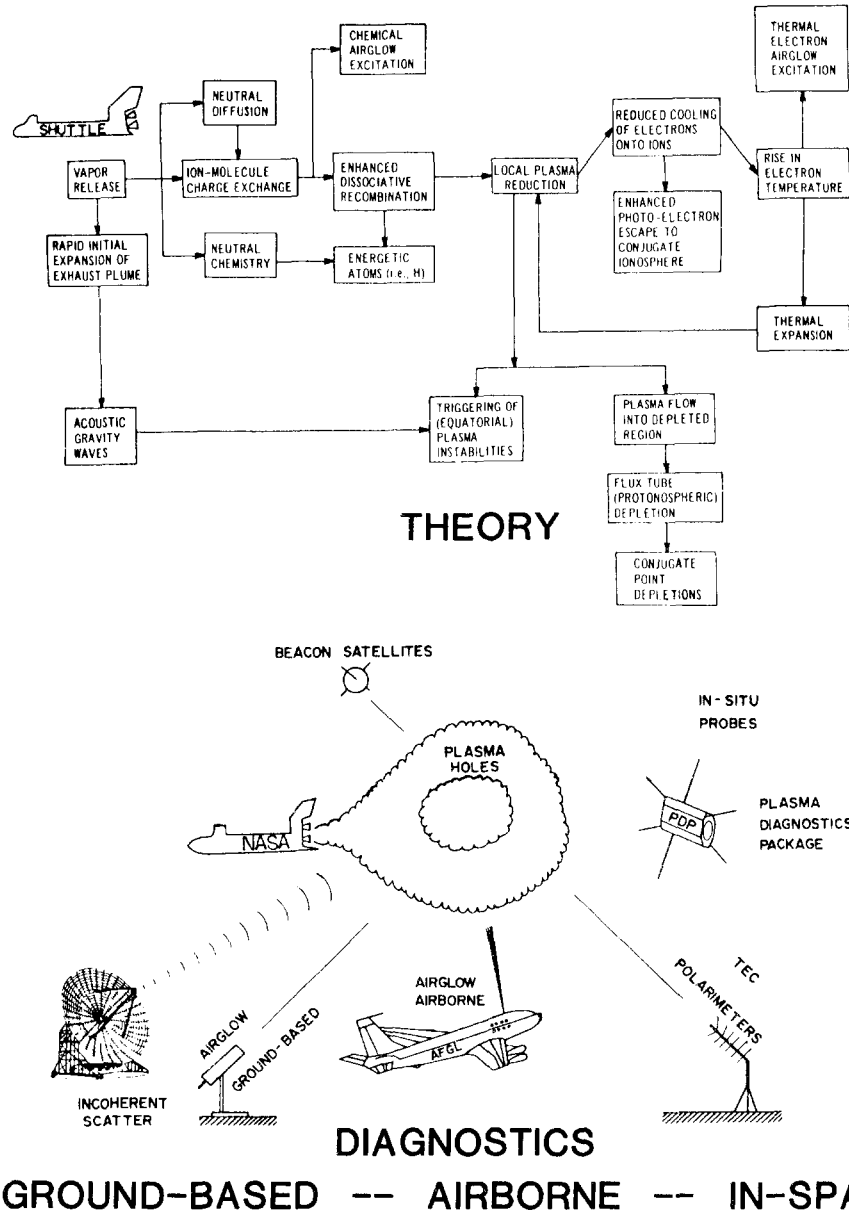


Figure 10-94. Schematic summary of possible rocket effluent effects upon the upper atmosphere ( $h > 200$  km), associated with the NASA Spacelab-2 mission scheduled for Spring-Summer 1985.

absorption of the heater wave near the altitude of HF reflection. The following manifestations of plasma instabilities have been observed: (1) artificially created spread F; (2) strongly enhanced radio wave absorption; (3) the creation of field-aligned density irregularities which scatter (this phenomenon is sometimes called field-aligned scatter of FAS) an incident HF, VHF, or UHF wave with virtually no frequency change and make certain types of scatter communication circuits possible; (4) scattering process in which the frequency of the scattered wave differs from the frequency of the incident wave by roughly the frequency of

the high-power HF transmissions; and (5) strongly enhanced airglow at  $6300 \text{ \AA}$ ; some enhancement at  $5577 \text{ \AA}$  is also observed (see the Special Issue of Radio Science, [1974]).

The short-wavelength (1 cm - 10 m) field-aligned irregularities produced by ionospheric heating are a result of parametric decay instability or wave interaction between the high power radio wave (pump) and the ion-acoustic and Langmuir waves. This was predicted from theory [Perkins and Kaw, 1971; Perkins et al., 1974; DuBois and Goldman, 1972] and experimentally confirmed at Arecibo [Carlson et al., 1972].

## IONOSPHERIC RADIO WAVE PROPAGATION

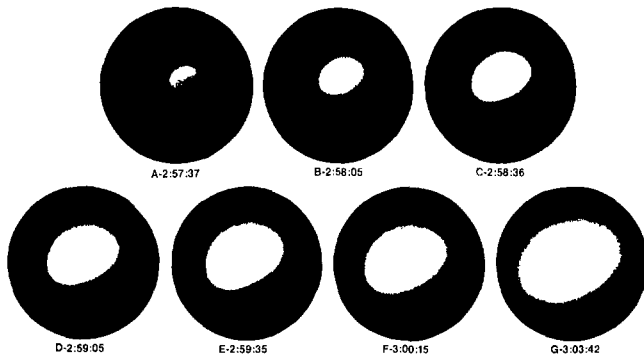


Figure 10-95. The growth of an ionospheric hole is shown in this sequence of image-intensified, wide-angle photographs of the expanding 6300 Å airglow cloud produced by excited oxygen atoms created from the recombination of free electrons and molecular ions ( $O_2^+$ ,  $OH^+$ ,  $H_2O^+$ ) produced by exhaust molecules ( $CO_2$ ,  $H_2$ ,  $H_2O$ ) and ambient atomic ions ( $O^+$ ). Times are a.m., PST [Mendillo and Baumgardner, 1982].

The long-wavelength ( $\sim 1$  km) field-aligned irregularities giving rise to artificial spread F [Utlaut et al., 1970; Utlaut and Violette, 1972; Wright, 1973] could not, however, be explained in terms of the above instability process. The causative mechanism for the generation of long wavelength irregularities remained obscure for quite a while and

is now attributed to either a thermal self-focusing mechanism [Perkins and Valeo, 1974; Thome and Perkins, 1974] or the alternative mechanisms of stimulated Brillouin scattering [Cragin and Fejer, 1974] and stimulated diffusion scattering [Goldman, 1974].

The above range of irregularity scale sizes has sufficient power spectral intensity to cause scintillation of radio signals received from radio stars and artificial satellites. This was demonstrated when VHF/UHF signals transmitted through the artificially heated ionospheric F region were found to exhibit scintillations [Rufenach, 1973; Pope and Fritz, 1974; Bowhill, 1974]. Radio star scintillation measurements at 26 MHz during ionospheric modification indicated the presence of either rapid and random or deep long-period ( $\sim 5$  mins) fluctuations. In order to avoid some of the difficulties of radio star observations, Bowhill [1974] performed scintillation measurements with both geostationary and orbiting satellites and established the field-aligned nature of the irregularities causing VHF and UHF scintillations, their transverse scale and drift speed. One feature common to all the above studies was the fact that the heater frequency was below the plasma frequency of the F region. The magnitude of scintillations observed on transionospheric communication channels is found to be of the order of 5 dB at 250 MHz when the nighttime F region is heated by an incident power density of about  $50 \mu\text{Wm}^{-2}$  [Basu et al., 1980a].

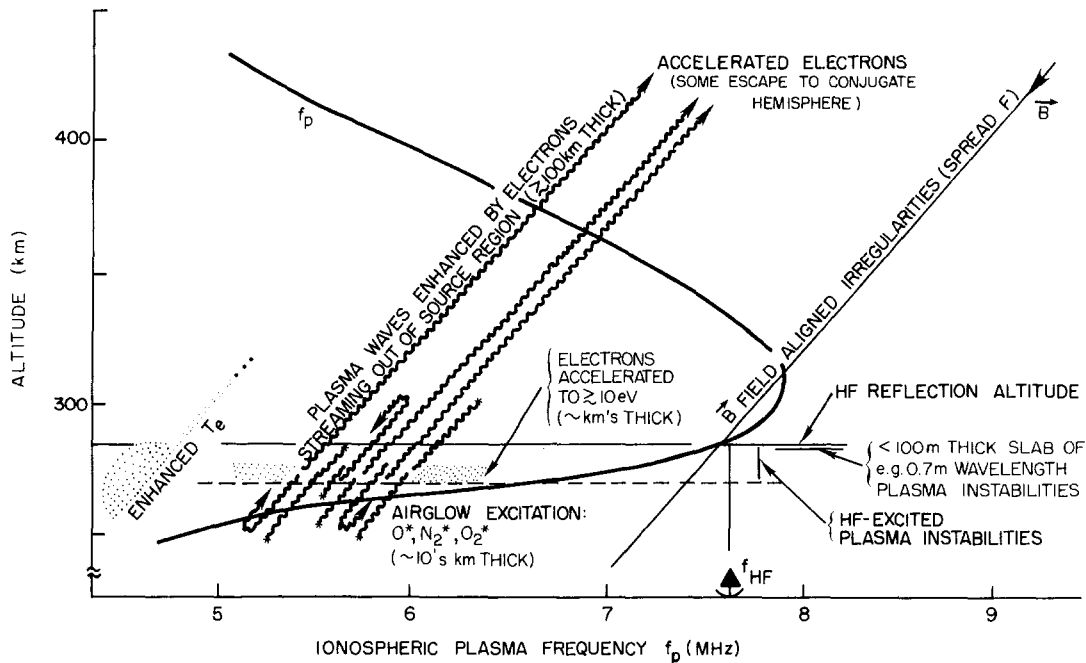


Figure 10-96. Effects produced by ground-based transmitter of power aperture of the order of  $10^4 \text{ Mwm}^2$  in the 4–12 MHz frequency range. Energy deposited in the ionospheric plasma alters both the thermal and nonthermal properties of its charged particle population. Controlled experiments have applications to aeronomy, chemical rates, atomic cross sections, communications, and a number of areas of plasma physics [Carlson and Duncan, 1977].

## CHAPTER 10

### REFERENCES

- Aarons, J., "A Descriptive Model of F-Layer High-Latitude Irregularities as Shown by Scintillation Observations," *J. Geophys. Res.*, **78**: 7441–7450, 1973.
- Aarons, J., "Equatorial Scintillations: A Review," *IEEE Trans. Antennas Propagat.*, **AP-25**, 729, 1977.
- Aarons, J., "Global Morphology of Ionospheric Scintillations," *Proc. IEEE*, **70**: 360–378, April 1982.
- Aarons, J. and R.S. Allen, "Scintillation Boundaries During Quiet and Disturbed Magnetic Conditions," *J. Geophys. Res.*, **76**: 170, 1971.
- Aarons, J. and E. Martin, "The Effects of the August 1972 Magnetic Storms on Ionospheric Scintillations," *Radio Sci.*, **10**: 547–554, 1975.
- Aarons, J., J.P. Mullen, and H.E. Whitney, "The Scintillation Boundary," *J. Geophys. Res.*, **74**: 884–889, 1969.
- Aarons, J., E. MacKenzie, and K. Bhavnani, "High-Latitude Analytical Formulas for Scintillation Levels," *Radio Sci.*, **15**: 115–127, 1980a.
- Aarons, J., J.P. Mullen, J.P. Koster, R.F. daSilva, J.R. Medeiros, R.T. Medeiros, A. Bushby, J. Pantoja, J. Lanat, and M.R. Paulson, "Seasonal and Geomagnetic Control of Equatorial Scintillations in Two Longitudinal Sectors," *J. Atmos. Terr. Phys.*, **42**: 861–866, 1980b.
- Aarons, J., E. MacKenzie, and S. Basu, "Microwave Equatorial Scintillation Intensity During Solar Maximum," *Radio Sci.*, **16**: 939–945, 1981a.
- Aarons, J., J.P. Mullen, H. Whitney, A. Johnson, and E. Weber, "VHF Scintillation Activity Over Polar Latitudes," *Geophys. Res. Lett.*, **8**: 277–280, 1981b.
- AGARD, "Modern HF Communications," *AGARD Lecture Series 127*, (avail. through NTIS, Springfield, Va) 1983.
- Akasofu, S.-I., "Midday Auroras and Polar Cap Auroras," *Geofysiske Publikasjoner* (Norske Videnskaps-Akademi i Oslo), **29**: 73–85, 1972.
- Albrecht, H.J., (ed.), *Artificial Modification of Propagation Media*, *AGARD Conf. Proc.* **192**, Brussels, 26–29 April 1976.
- Al'pert, Ia. L., "Ionospheric Propagation of Radio Waves," *Acad. of Sci. of USSR, Moscow, Section on Long Waves* (avail) as Translation T5-60, National Bureau of Standards, Boulder, 1960.
- Ames, J.W. and R.D. Egan, "Digital Recording and Short-Term Prediction of Oblique Ionospheric Propagation," *IEEE Trans. Antennas Propag.* **AP-15**: 382, 1967.
- Ames, J.W., R.D. Egan and G.F. McGintie, "Short-Term Prediction of HF Communication Circuit Performance" in *Ionospheric Forecasting*, *AGARD Conf. Proc.*, **49**, AD700896, 1970.
- Anderson, D.N., "Modelling the Ambient Low Latitude F-Region Ionosphere—A Review," *J. Atmos. Terr. Phys.*, **43**: 753, 1981.
- Anderson, D.N. and P.A. Bernhardt, "Modeling the Effects of an H Gas Release the Equatorial Ionosphere," *J. Geophys. Res.*, **83**: 4777, 1978.
- Appleton, E.V. and W.J.G. Beynon, "The Application of Ionospheric Data to Radio-Communication Problems: Part I," *Proc. Phys. Soc.*, **52**: 518, 1940.
- Baggaley, W.J., "Backscatter Observations of F-Region Field-Aligned Irregularities During the I.Q.S.Y.," *J. Geophys. Res.*, **75**: 152–158, 1970.
- Bain, W.C., "Models of the Mid Latitude D Region at Noon" in *Medium, Long and Very Long Wave Propagation*, *AGARD Conf. Proc.*, **305**: 34-1–34-8 ADA113969, 1982.
- Balsley, B.B. and W.L. Ecklund, "VHF Power Spectra of the Radar Aurora," *J. Geophys. Res.*, **77**: 4746–4760, 1972.
- Balsley, B.B., W.L. Ecklund, and R.A. Greenwald, "VHF Doppler Spectra of Radar Echoes Associated with a Visual Auroral Form: Observations and Implications," *J. Geophys. Res.*, **78**: 1681–1687, 1973.
- Bannister, P.R., "Variations in Extremely Low Frequency Propagation Parameters," *J. Atmos. Terr. Phys.*, **37**: 1203–1210, 1975.
- Bannister, P.R., "Extremely Low Frequency (ELF) Propagation," NUSC Scientific and Engineering Studies, Naval Underwater Systems Center, New London, Conn., February 1980.
- Bannister, P.R., "Overview of ELF Propagation," in *Medium, Long, and Very Long Wave Propagation*, *AGARD Conf. Proc.*, **305**: 10-1–10-13 ADA113969, 1982.
- Barghausen, A.L., J.W. Finney, L.L. Proctor, and L.D. Schultz, "Predicting Long-term Operational Parameters of High-Frequency Sky-Wave Telecommunication Systems," ESSA Tech. Rept. ERL 110-ITS 78, 1969.
- Barr, R., "The Effect of Sporadic E on the Nocturnal Propagation of ELF Radio Waves," *J. Atmos. Terr. Phys.*, **39**: 1379–1387, 1977.
- Barry, G.H., "A Low Power Vertical Incidence Ionosonde" *IEEE Trans. Geosci. Elect.*, **GE-9(2)**: 86–89, 1971.
- Basu, S. and Su. Basu, "Modeling of Equatorial Phase and Amplitude Scintillations from OGO-6 and AE Irregularity Data, Low Latitude Aeronomical Processes," *COSPAR Symposium Series*, **8**: 187–199, Pergamon Press 1980.
- Basu, S. and H.E. Whitney, "The Temporal Structure of Intensity Scintillation Near the Magnetic Equator," *Radio Sci.*, **18**: 263–271, 1983.
- Basu, S., Su. Basu, A.L. Johnson, J.A. Klobuchar, and C.M. Rush, "Preliminary Results of Scintillation Measurements Associated with Ionosphere Heating and Possible Implications for the Solar Power Satellite," *Geophys. Res. Lett.*, **7**: 609, 1980a.
- Basu, S., Su. Basu, J.P. Mullen, and A. Bushby, "Long-term 1.5 GHz Amplitude Scintillation Measurements at the Magnetic Equator," *Geophys. Res. Lett.*, **7**: 259–262, 1980b.
- Basu, S., J.P. McClure, Su. Basu, W.B. Hanson, and J. Aarons, "Coordinated Study of Equatorial Scintillation and in-situ and Radar Observations of Nighttime F Region Irregularities," *J. Geophys. Res.*, **85**: 5119–5130, 1980c.
- Basu, Su. and J. Aarons, "The Morphology of High-Latitude VHF Scintillation Near 70°W," *Radio Sci.*, **15**: 59–70, 1980.

## IONOSPHERIC RADIO WAVE PROPAGATION

- Basu, Su. and M.C. Kelley, "A Review of Recent Observations of Equatorial Scintillations and their Relationship to Current Theories of F-Region Irregularity Generation," *Radio Sci.*, **14**: 471, 1979.
- Basu, Su., R.L. Vesprini, and J. Aarons, "Field-Aligned Ionospheric E-Region Irregularities and Sporadic E," *Radio Sci.*, **8**: 235-246, 1973.
- Basu, Su., R.L. Vesprini, and J. Aarons, "F-Layer Irregularities as Determined by Backscatter Studies at 19 MHz over Half of a Solar Cycle," *Radio Sci.*, **9**: 355-371, 1974.
- Basu, Su., S. Basu, R.C. Livingston, E. MacKenzie, and H.E. Whitney, "Phase and Amplitude Scintillation Statistics at 244 MHz from Goose Bay using a Geostationary Satellite," AFGL TR-82-0222, ADA124291, 1982.
- Bates, H.F. and P.R. Albee, "Aspect Sensitivity of HF Auroral Echoes," *J. Geophys. Res.*, **74**: 1164-1168, 1969.
- Bates, H.F. and P.R. Albee, "Aspect Sensitivity of F-Layer HF Backscatter Echoes," *J. Geophys. Res.*, **75**: 165-170, 1970.
- Belrose, J.S., "Radio Wave Probing of the Ionosphere by the Partial Reflection of Radio Waves (From Heights below 100 km)," *J. Atmos. Terr. Phys.*, **32**: 567-596, 1970.
- Belrose, J.S., "COSPAR Symposium Record on D- and E-Region Ion Chemistry," *Aeron. Rept. No. 48*, Univ. of Illinois, Urbana, Ill., 1972.
- Belrose, J.S., "LF Propagation: An Overview" in *Medium, Long, & Very Long Wave Propagation*, AGARD Conf. Proc., **305**: 22-1-22-10 ADA113969, 1982.
- Belrose, J.S. and L. Thomas, "Ionization Changes in the Middle Latitude D-Region Associated with Geomagnetic Storms," *J. Geophys. Res.*, **30**: 1397-1413, 1968.
- Bennett, S.M. and A.B. Friedland, "Prediction of Daily Fluctuations of the F-Region Plasma Frequency," *Ionospheric Forecasting*, AGARD Conf. Proc., **49** AD700896, 1970.
- Bent, R.B., S.K. Llewellyn, and M.K. Walloch, "Description and Evaluation of the Bent Ionospheric Model," **I**, SAMSQ-TR-72-239, 1972.
- Bernhardt, P.A., C.G. Park, and P.M. Banks, "Depletion of the F Region Ionosphere and Protonosphere by the Release of Molecular Hydrogen," *Geophys. Res. Lett.*, **2**: 341, 1975.
- Bernstein, S.L., M.L. Burrows, J.E. Evans, A.S. Griffiths, D.A. McNeill, C.W. Neissen, I. Richer, D.P. White, and D.K. William, "Long Range Communication at Extremely Low Frequencies," *Proc. IEEE*, **62**(3), 292-312, 1974.
- Berry, L.A., "Wave Hop Theory of Long Distance Propagation of LF Radio Waves," *Radio Sci.*, **68D**: 1275-1282, 1964.
- Berry, L.A. and M.E. Chrisman, "The Path Integrals of LF/VLF Wave Hop Theory," *Radio Sci.*, **64D**: 1469-1480, 1965.
- Betts, J.A. and M. Darnell, "Real Time HF Channel Estimation by Phase Measurements on Low-Level Pilot Tones" in "Radar Systems and the Ionosphere," AGARD Conf. Proc., **173** ADA022439, 1975.
- Bibl, K., "Fixed and Variable Frequency Pulse Transmission at Oblique Ionospheric Incidence," AFCRL 64392 AD603045, 1963.
- Bibl, K. and B.W. Reinisch, "Digisonde 128 PS," University of Lowell, Center for Atmospheric Research, Lowell, Mass., 1978a.
- Bibl, K. and B.W. Reinisch, "The Universal Digital Ionosondes," *Radio Sci.*, **13**: 519-530, 1978b.
- Bickel, J.E., J.A. Ferguson, and G.V. Stanley, "Experimental Observations of Magnetic Field Effects on VLF Propagation at Night," *Radio Sci.*, **5**: 19-25, 1970.
- Bilitza, D., M. Noor Sheikh, and R. Eyfrig, "A Global Model for the Height of the F<sub>2</sub> Peak using M3000 Values from the CCIR Numerical Map," *Telecomm. J.*, **46**: 549-553, 1971.
- Black, H.D. "The Transit System, 1977; Performance, Plans and Potential," *Philos. Trans. R. Soc. Lond.* **A294**: 217-236, 1980.
- Booker, H.G., C.M. Crain, and E.C. Field, "Transmission of Electromagnetic Waves Through Normal and Disturbed Ionospheres," RAND Rept. R-558-PR, RAND Corp., Santa Monica, Calif., 1970.
- Booker, H.G. and G. MajidiAhi, "Theory of Refractive Scattering in Scintillation Phenomena," *J. Atmos. Terr. Phys.*, **43**: 1199, 1981.
- Bowhill, S.A., "Satellite Transmission Studies of Spread-F Produced by Artificial Heating of the Ionosphere," *Radio Sci.*, **9**: 975, 1974.
- Bowles, K.L., "Observations of Vertical Incidence Scatter from the Ionosphere at 41 Mc/sec," *Phys. Rev. Lett.*, **1**:454, 1958.
- Bowles, K.L. and Staff of Jicamarca Radio Observatory Institute, "Profiles of Electron Density Over the Magnetic Equator Obtained Using the Incoherent Scatter Technique," *Tech. Rept. Note 169*, National Bureau of Standards, Boulder, Colo., 1963.
- Bracewell, R.N. and W.C. Bain, "An Explanation of Radio Propagation at 16 kc/sec in Terms of Two Layers Below E Layer," *J. Atmos. Terr. Phys.*, **2**: 216-225, 1952.
- Bracewell, R.N., K.G. Budden, J.A. Ratcliff, T.W. Straker, and K. Weekes, "The Ionospheric Propagation of Low and Very Low Frequency Radio Waves Over Distances Less than 1000 km," *Proc. IEE*, **98**: 221, 1951.
- Bradley, P.A. and C. Bedford, "Prediction of HF Circuit Availability," *Elec. Lett.*, **12**: 32, 1976.
- Bradley, P.A. and J.R. Dudeney, "A Simple Model of the Vertical Distribution of Electron Concentration in the Ionosphere," *J. Atmos. Terr. Phys.*, **35**: 2131, 1973.
- Bramley, E.N., "Fluctuations in Direction and Amplitude of 136 MHz Signals from a Geostationary Satellite," *J. Atmos. Terr. Phys.*, **36**: 1503-1513, 1974.
- Breit, G. and M.A. Tuve, "A Test of the Existence of the Conducting Layer," *Phys. Rev.*, **28**: 554-575, 1926.
- Briggs, B.H. and I.A. Parkin, "On the Variation of Radio Star and Satellite Scintillation with Zenith Angle," *J. Atmos. Terr. Phys.*, **25**: 339-365, 1963.
- Brooks, D., "Observations of Radio Auroral Echoes and

## CHAPTER 10

- Simultaneous Magnetic Disturbances," *J. Atmos. Terr. Phys.*, **27**: 1151–1158, 1965.
- Brooks, D., "Observations of Auroral Echoes Following Worldwide Storm Sudden Commencements," *J. Atmos. Terr. Phys.*, **28**: 103–109, 1966.
- Buchau, J., W.N. Hall, B.W. Reinisch, and S. Smith, "Remote ionospheric Monitoring from Effects of the Ionosphere on Space and Terrestrial Systems," *Proc. IES (Ionospheric Effects Symposium)*, edited by John H. Goodman, U.S. Government Printing Office, Washington, D.C., 1978.
- Buchau, J., B.W. Reinisch, E.J. Weber, and J.G. Moore, "Structure and Dynamics of the Winter Polar Cap F Region," *Radio Sci.*, **19**: 995–1010, 1983.
- Budden, K.B., *Radio Waves in the Ionosphere*, Cambridge University Press, Cambridge, UK, 1961.
- Buneman, O., "Scattering of Radiation by the Fluctuations in a Non-Equilibrium Plasma," *J. Geophys. Res.*, **67**: 2050, 1962.
- Burke, W. (ed.), *Proceedings of International Symposium on Active Experiments in Space*, 23–29 May 1983, Alpbach, Austria, European Space Agency Report ESA-SP-195, Paris, 1983.
- Burns, A.A. and E.J. Fremouw, "A Real-Time Correction Technique for Transionospheric Ranging Error," *IEEE Trans. Antennas Propag.*, **AP-18**(6), Nov. 1970.
- Burrows, M.L., *ELF Communications Antennas*, Peter Pergrinus Ltd., Stevenage, England, 1978.
- Carlson, H.C. and L.M. Duncan, "HF Excited Instabilities in Space Plasmas," *Radio Sci.*, **12**: 1001, 1977.
- Carlson, H.C., W.E. Gordon, and R.L. Showen, "High Frequency Induced Enhancements of the Incoherent Scatter Spectrum at Arecibo," *J. Geophys. Res.*, **77**: 1242, 1972.
- CCIR (Comité Consultatif International des Radiocommunications = International Radio Consultative Committee), "World Distribution and Characteristics of Atmospheric Radio Noise," Report 332, Doc. Xth Plenary Ass., International Telecommunications Union (ITU), Geneva, 1963.
- CCIR, "CCIR Atlas of Ionospheric Characteristics," Report 340 and 340-2, Doc. XIth Plenary Ass., ITU, Geneva, 1966.
- CCIR, "Interim Method for Investigating Sky-Wave Field Strength and Transmission Loss at Frequencies Between the Approximate Limits of 2 and 30 MHz," Report 252-2, Doc. XIIth Plenary Ass., ITU, Geneva, 1970.
- CCIR, "Second CCIR Computer-Based Interim Method for Estimating Sky-Wave Field Strength and Transmission Loss Between 2 and 30 MHz," Suppl. Rept. 252-2, Doc. XIVth Plenary Ass., ITU, Geneva, 1978.
- CCIR, "Prediction of Sky-Wave Field Strength Between 150 and 1500 kHz," CCIR Recommendation 453-3, Doc. XIV Plenary Ass., ITU, Geneva, 1978.
- CCIR, "Special Properties of the High Latitude Ionosphere Affecting Radio-communications," Study Program 25B/6, Doc. 6/1005-E, 14 Oct 81, XVth Plenary Ass., ITU, Geneva, 1981a.
- CCIR, "Short-Term Forecasting of Operational Maximum Usable Frequencies and Total Electron Content," Study Program 27C/6, Doc. 6/1017-E, 14 Oct 81, XVth Plenary Ass., ITU, Geneva, 1981b.
- CCIR, "Short-Term Prediction of Solar-Induced Variations of Operational Parameters for Ionospheric Propagation," Study Program 27A/6, Doc. 6/1016-E, 14 Oct 81, XV Plenary Ass., ITU, Geneva, 1981c.
- CCIR, "Real-Time Channel Evaluation of Ionospheric Radio Circuits," Study Program 27B/6, Doc. 6/1018-E of XVth Plenary Ass., Geneva, 1981d.
- CCIR, "Prediction and Short-Term Forecasting of HF Radio Propagation Conditions at High Latitudes," Draft Report submitted ITU, Geneva, August 1983.
- Chan, K.L. and L. Colin, "Global Electron Density Distribution from Topside Soundings," *Proc. IEEE*, **57**: 6, 1969.
- Chapman, F.W., D.L. Jones, J.D.W. Todd, and R.A. Chalinor, "Observations on the Propagation Constant of the Earth-Ionosphere Waveguide in the Frequency Band 8 c/s to 16 kc/s," *Radio Sci.*, **1**(11), 1273–1282, 1966.
- Ching, B.K. and Chiu, Y.T., "A Phenomenological Model of Global Ionospheric Electron Density in the E, F<sub>1</sub>, and F<sub>2</sub> Regions," *J. Atmos. Terr. Phys.*, **35**: 1615, 1973.
- Chiu, Y.T., "An Improved Phenomenological Model of Ionospheric Density," *J. Atmos. Terr. Phys.*, **37**: 1563, 1975.
- Cole, D.G. and L.F. McNamara, "Variations of Spread-F Occurrence Rates at Near-Equatorial Stations in the Australian Zone," *Aust. J. Phys.*, **27**: 249, 1974.
- Cragin, B.L. and J.A. Fejer, "Generation of Large-Scale Field-Aligned Irregularities in Ionospheric Modification Experiments," *Radio Sci.*, **9**: 1071, 1974.
- Crain, C.M., "Ionospheric Probing with Long Wavelength Radio Waves," *J. Atmos. Terr. Phys.*, **32**: 551–566, 1970.
- Crane, R.K., "Spectra of Ionospheric Scintillation," *J. Geophys. Res.*, **81**: 2041–2050, 1976.
- Crane, R.K., "Ionospheric Scintillation," *Proc. IEEE*, **65**: 180, 1977.
- Cretcher, C.K., "Ionospheric Effects in NAVSTAR-GPS," in *Effects of the Ionosphere on Space Systems and Communications*, edited by J.M. Goodman, Naval Research Lab., Washington, D.C., U.S. Government Printing Office, Stock No. 08-051-00064-0, 1975.
- Czechowsky, P., W. Dieminger, and H. Kochan, "Backscatter Results from Lindau-I. Observations of Radio Auroras," *J. Atmos. Terr. Phys.*, **36**: 955–966, 1974.
- D'Accardi, R.J., "Time Series Modelling and Analysis of HF Vertical and Short-Path Oblique Incidence Ionospheric Soundings," U.S. Army Communications R & D Command Tech. Rept. CORADCOM 78-7, NTIS ADA058630, 1978.
- Dandekar, B.S., "Ionospheric Modeling," AFGL TR-82-0024, ADA 115243, 1982.
- Danielson, C., "Auroral Observations at Thule 1961-65," *Danish Met. Inst., Geophys. Papers R-9*, 1969.
- Darnell, M., "Channel Evaluation Techniques for HF Communication" in *Radio Systems and the Ionosphere*, *AGARD Conf. Proc.*, **173**, 1975a.
- Darnell, M., "Adaptive Signal Selection for Dispersive Channels and its Practical Implications in Communications System Design" in *Radio Systems and the Ionosphere*, *AGARD Conf. Proc.*, **173**, 1975b.
- Darnell, M., "Channel Evaluation Techniques for Dispersive Communications Paths," *Communication System*

## IONOSPHERIC RADIO WAVE PROPAGATION

- and *Random Process Theory*, edited by J.K. Skwirzynski, Sijthoff and Noordhoff, Alphen aan den Rijn, Holland, 1978.
- DasGupta, A., A. Maitra, and S. Basu, "Occurrence of Nighttime VHF Scintillations near the Equatorial Anomaly Crest in the Indian Sector," *Radio Sci.*, **16**: 1455–1458, 1981.
- David, P. and J. Voge, *Propagation of Waves*, Pergamon Press, London, U.K., 1969.
- Davies, K., *Ionospheric Radio Propagation*, National Bureau of Standards Monograph 80, U.S. Government Printing Office, Washington, D.C., 1966.
- Davies, K., *Ionospheric Radio Waves*, Blaisdell, Waltham, Mass., 1969.
- Davies, K., "Recent Progress in Satellite Radio Beacon Studies with Particular Emphasis on the ATS-6 Radio Beacon Experiment," *Space Sci. Rev.*, **25**: 357–430, 1980.
- Davis, T.N., "The Morphology of the Auroral Displays of 1957–1958. (2) Detailed Analysis of Alaska Data and Analysis of High Latitude Data," *J. Geophys. Res.* **67**: 75–110, 1962.
- Demaro, R.P., "NAVSTAR: The All-Purpose Satellite," *IEEE Spectrum*, **18**: 35–40, May 1981.
- Donatelli, D.C. and R.S. Allen, "Time Cells for Adaptive Predictions of Total Electron Content," *Radio Sci.*, **16**: 261–269, 1981.
- Donnelly, R.F., ed., *Solar Terrestrial Prediction Proceedings*, U.S. Dept. of Commerce, U.S. Government Printing Office, Washington, D.C. 20402
- Vol. 1 *Prediction Group Reports*, No. 003-023-0041-9, 1979.
- Vol. 2 *Working Group Reports and Reviews*, No. 003-017-00471-6, 1979.
- Vol. 3 *Solar Activity Predictions*, No. 003-017-00473-2, 1979.
- Vol. 4 *Predictions of Terrestrial Effects of Solar Activity*, No. 003-017-00479-1, 1980.
- Dougherty, J.P. and D.T. Farley, "A Theory of Incoherent Scattering of Radio Waves by a Plasma," *Proc. Roy. Soc. (London)*, **A259**: 79, 1960.
- Dubois, D.F. and M.V. Goldman, "Spectrum and anomalous Resistivity for the Saturated Parametric Instability," *Phys. Rev. Lett.*, **28**: 218, 1972.
- Ducharme, E.D., L.E. Petrie, and R. Eyfrig, "A Method for Predicting the  $F_1$  Critical Frequency," *Radio Sci.*, **6**: 369, 1971.
- Ducharme, E.D., L.E. Petrie, and R. Eyfrig, "A Method of Predicting the  $F_1$  Layer Critical Frequency Based on Zurich Smoothed Sunspot Number," *Radio Sci.*, **8**: 837–839, 1973.
- Dyson, P.L., J.P. McClure, and W.B. Hanson, "In situ Measurements of the Spectral Characteristics of Ionospheric Irregularities," *J. Geophys. Res.*, **79**: 1497, 1974.
- Eccles, D. and J.W. King, "A Review of Topside Sounder Studies of the Equatorial Ionosphere" *Proc. IEEE* **57**(6): 1012–1018, 1969.
- Evans, J.V., "Theory and Practice of Ionosphere Study by Thomson Scatter Radar," *Proc. IEEE*, **57**: 496, 1969.
- Evans, J.V., "Millstone Hill Radar Propagation Study" Scientific Results," Tech. Rept. 509; Joint Radar Propagation Study, Lincoln Laboratory, MIT, Lexington, Mass., 1973.
- Evans, J.V., "High-Power Radar Studies of the Ionosphere," *Proc. IEEE*, **63**: 12, 1636–1650, 1975.
- Eyfrig, R., "Contribution a l'Etude de l'Effect du Geomagnetisme sur le Couche  $F_1$ ," *Comptes Rendus Academie des Sciences*, **241**: 759–761, 1955.
- Fejer, J.A., "Scattering of Radiowaves by an Ionized Gas in Thermal Equilibrium," *Can. J. Phys.*, **38**: 1114, 1960; also *J. Geophys. Res.*, **65**: 2635, 1960.
- Fejer, J.A., "Radio Wave Probing of the Lower Ionosphere by Cross-Modulation Techniques," *J. Atmos. Terr. Phys.*, **32**: 597–607, 1970.
- Fejer, J.A., "Ionospheric Modification and Parametric Instabilities," *Rev. Geophys. Space Phys.*, **17**: 135, 1979.
- Feldstein, Y.I. and G.V. Starkov, "Dynamics of Auroral Belt and Polar Geomagnetic Disturbances," *Plan. Space Sci.*, **15**: 209–229, 1967.
- Ferguson, J.A., "Ionospheric Profiles for Predicting Nighttime VLF/LF Propagation," Tech. Rep. 530, Naval Ocean Systems Center, San Diego, Calif., 1980.
- Field, E.C., "Propagation of ELF Waves Under Normal and Naturally Disturbed Conditions," *J. Geophys. Res.*, **74**: 3639–3650, 1969.
- Field, E.C., "Low-Frequency Ground Wave Propagation Over Narrow Terrain Features," *IEEE Trans. Antennas Propag.*, **30**: 831–836, 1982a.
- Field, E.C., "ELF Propagation in Disturbed Environments" in *Medium, Long and Very Long Wave Propagation AGARD Conf. Proc.*, **305**: 11-1–11-10, ADA113969 1982b.
- Field, E.C., "VLF Propagation in Disturbed Environments" in *Medium, Long and Very Long Wave Propagation AGARD Conf. Proc.*, **305**: 17-1–17-10, ADA113969, 1982c.
- Field, E.C. and R.D. Engel, "The Detection of Daytime Nuclear Bursts Below 150 km by Prompt VLF Phase Anomalies," *Proc. IEEE*, **53**: 2009–2017, 1965.
- Field, E.C. and R.G. Joiner, "An Integral Equation Approach to Long Wave Propagation in a Non-Stratified Earth-Ionosphere Waveguide," *Radio Sci.*, **14**: 1057–1068, 1979.
- Field, E.C. and R.G. Joiner, "Effects of Lateral Ionospheric Gradients on ELF Propagation," *Radio Sci.*, **17**: 693–700, 1982.
- Field, E.C. and C.R. Warber, "Calculation of Ionospheric Electron Density Profiles by Inverting VLF/LF Reflection Data, 2. Anisotropic Propagation" RADC-TR-84-242, Rome Air Development Center, Griffiss AFB, N.Y., 1984.
- Field, E.C., M. Lewinstein, and M.A. Dore, "Effects of Antenna Elevation and Inclination on VLF/LF Signal Structure RADC-TR-76-375 ADA035510, 1976.
- Field, E.C., R.E. Warren, and C.R. Warber, "Calculation of Ionospheric Conductivity Profiles by Inverting VLF/LF Reflection Data, 1. Isotropic Propagation," *Radio Sci.*, **18**: 452–460, 1983.
- Flattery, T.W., T.F. Tascione, J.A. Secan, and J.W. Taylor, Jr., *A Four-Dimensional Ionospheric Model* (private communication).
- Flood, W.A. "Simultaneous VHF Auroral Backscatter Measurements," *J. Geophys. Res.*, **65**: 2261–2268, 1960.

## CHAPTER 10

- Forbes, J.M., "Upper Atmosphere Modifications Due to Chronic Discharges of Water Vapor from Space Vehicle Exhausts," in *Space Systems and their Interactions with Earth's Space Environment* edited by H.B. Garrett and C.P. Pike, American Institute of Aeronautics and Astronautics, New York, 1980.
- Franklin, C.A. and M.A. MacLean, "The Design of Swept Frequency Topside Sounders," *Proc. IEEE*, **57**(6): 897–929, 1969.
- Fremouw, E.J., "Geometrical Control of the Ratio of Intensity and Phase Scintillation Indices," *J. Atmos. Terr. Phys.*, **42**: 775–782, 1980.
- Fremouw, E.J. and J.F. Bates, "Worldwide Behavior of Average VHF-UHF Scintillation," *Radio Sci.*, **6**: 863–869, 1971.
- Fremouw, E.J. and C.L. Rino, "Modelling of Transionospheric Radio Propagation," RADC-TR-76-35, Rome Air Development Center, Griffiss AFB, NY, 1976.
- Fremouw, E.J.; C.L. Rino, A.R. Hessing, and V.E. Hatfield, "A Transionospheric Communication Channel Model," *Quart. Tech. Rep. 7*, SRI International (Stanford Research Institute), Menlo Park, Calif., 1977.
- Fremouw, E.J. and C.L. Rino, "A Signal-Statistical and Morphological Model of Ionospheric Scintillation," *Proc. AGARD Conf. Operational Modelling of the Aerospace Propagation Environment*, Ottawa, Canada, 1978.
- Fremouw, E.J., R.L. Leadabrand, R.C. Livingston, M.D. Cousins, C.L. Rino, B.C. Fair, and R.A. Long, "Early Results from the DNA Wideband Satellite Experiment-Complex Signal Scintillation," *Radio Sci.*, **13**: 167–187, 1978.
- Fremouw, E.J., R.C. Livingston, and D.A. Miller, "On the Statistics of Scintillating Signals," *J. Atmos. Terr. Phys.*, **43**: 717–731, 1980.
- Fremouw, E.J. and J.M. Lansinger, "Recent High Latitude Improvement in a Computer Based Scintillation Model," *Proc. Ionospheric Effects Symposium*, 3rd, 1981, Alexandria, Va., edited by J.M. Goodman, Naval Research Lab., Washington, D.C., 1982.
- Frisius, J., A. Ehmert, and D. Stratmann, "Effects of High Altitude Nuclear Tests on VLF-Propagation," *J. Atmos. Terr. Phys.*, **26**: 251–262, 1964.
- Galejs, J., *Terrestrial Propagation of Long Electromagnetic Waves*, Pergamon Press, Oxford, UK, 1972.
- Gallagher, P.B. and R.A. Barnes, "Radio-Frequency Backscatter of Artificial Electron Clouds," *J. Geophys. Res.*, **68**: 2987–3010, 1963.
- Gautier, T.N. and D.H. Zacharisen, "Use of Space and Time Correlations in Short-Term Ionospheric Predictions," Conference Record, 1st Annual IEEE Communications Convention, 671–676, 1965.
- Goldman, M.V., "Field Aligned Instability Due to Stimulated Scattering of Intense Radio Waves from Diffusion Quasimodes," *Radio Sci.*, **9**: 1077, 1974.
- Goodman, J.M., "A Survey of Ionospheric Models. A Preliminary Report on the Development of an Ionospheric Model Thesaurus and Users Guide," NRL Memorandum Report 4830, Naval Research Lab., Washington, D.C., 1982.
- Gordon, W.E., "Incoherent Scattering of Radio Waves by Free Electrons with Applications to Space Exploration by Radar," *Proc. IRE*, **46**: 1824, 1958.
- Gordon, W.E., H.C. Carlson, and R.L. Showen, "Ionospheric Heating at Arecibo: First Tests," *J. Geophys. Res.*, **76**: 7808, 1971.
- Gowell, R.W. and R.W. Whidden, "Ionospheric Sounders in Aircraft," AFCRL-68-0369, AD678047, 1968.
- Greenwald, R.A., W.L. Ecklund, and B.B. Balsley, "Diffuse Radar Aurora: Spectral Observations of Non-Two-Stream Irregularities," *J. Geophys. Res.*, **80**: 131–139, 1975.
- Griefinger, C. and P. Griefinger, "Approximate Method for Determining ELF Eigenvalues in the Earth-Ionosphere Waveguide," *Radio Sci.*, **13**: 831–837, 1978.
- Griefinger, C. and P. Griefinger, "On the Ionospheric Parameters which Govern High Latitude ELF Propagation in the Earth-Ionosphere Waveguide," *Radio Sci.*, **14**: 889–895, 1979.
- Grubb, R.N., "The NOAA SEL HF Radar Systems (Ionospheric Sounder)," NOAA Tech. Memo ERL SEL-55 NOAA Environmental Research Laboratories, Boulder, CO, 1979.
- Haerendel, G., "Modification of Ionized Media by Chemical Substances—A Review of Physical Processes," in *Artificial Modification of Propagation Media*, edited by H.J. Albrecht, *AGARD Conf. Proc.*, **192**, Brussels, 1976.
- Haerendel, G., O.H. Bauer, S. Cakir, H. Foppl, E. Reiger, and A. Valenzuela, "Coloured Bubbles—An Experiment for Triggering Equatorial Spread F," in *Active Experiments in Space* edited by W. Burke, European Space Agency Report **SP-195**: 295, 1983.
- Hagfors, T., "Density Fluctuations in a Plasma in a Magnetic Field with Applications to the Ionosphere," *J. Geophys. Res.*, **66**: 1699, 1961.
- Hagg, E.L., E.J. Hewens, and G.L. Nelms, "The Interpretation of Topside Sounder Ionograms," *Proc. IEEE*, **57**: 949–959, 1969.
- Haldoupis, C. and G. Sofko, "Doppler Spectrum of 42 MHz CW Auroral Backscatter," *Can. J. Phys.*, **54**: 1571, 1976.
- Hargreaves, J.K., *The Upper Atmosphere and Solar-Terrestrial Relations*, Van Nostrand Reinhold, New York, 1979.
- Harrison, R.P., J.L. Heckscher, and E.A. Lewis, "Helicopter Observations of Very Low Frequency Radio Waves Over Certain Mountains and Shorelines," *J. Atmos. Terr. Phys.*, **33**: 101–110, 1971.
- Harvey, R.P., R.B. Harrison, V.C. Fields, G.C. Hirst, P.A. Kossey, and E.A. Lewis, "Rocket Investigations of the VLF Ionospheric Transmission Window," AFCRL-TR-73-0293, AD767185, 1973.
- Haydon, G.W. and D.L. Lucas, "Predicting Ionosphere Electron Density Profiles," *Radio Sci.*, **3**: 111, 1968.
- Headrick, J.M. and M.I. Skolnik, "Over-the-Horizon Radar in the HF Band," *Proc. IEEE*, **62**: 664, 1974.
- Heckman, G., "Predictions of the Space Environment Services Center," *STPP*, (Solar Terrestrial Predictions Workshop) **1**: 322 (see R.F. Donnelly, ed.) 1979.
- Heckscher, J.L. and E.J. Tichovolsky, "Height-Gain Atlas for an Elemental Vertical Dipole Above a Flat Earth,"

- RADC-TR-81-39, Rome Air Development Center, Griffiss AFB, N.Y., 1981.
- Helliwell, R.A., *Whistlers and Related Ionospheric Phenomena*, Stanford University Press, Stanford, Calif., 1965.
- Herman, J.R., "Spread F and Ionospheric F-Region Irregularities," *Rev. Geophys.*, **4**: 244-299, 1966. (Includes important bibliography.)
- Heron, M.L. and L.F. McNamara, "Transequatorial VHF Propagation through Equatorial Plasma Bubbles," *Radio Sci.*, **14**, 897, 1979.
- Hill, D.A., and J.R. Wait, "Excitation of the Zenneck Surface Wave by a Vertical Aperture," *Radio Sci.*, **13**: 969-977, 1978.
- Hizal, A. and A.F. Fer, "Medium Wave Multi-Section Groundwave Propagation in Marmara and West Black-Sea Region—Numerical Results" in *Medium, Long & Very Long Wave Propagation AGARD Conf. Proc.*, **305**: 31-1-31-7, ADA113969 1982.
- Hofstee, J. and P.A. Forsyth, "Ion Acoustic Waves in the Auroral Plasma," *Can. J. Phys.*, **47**: 2797, 1969.
- Hollingworth, J., "The Propagation of Radio Waves," *J. IEE*, **64**: 579, 1926.
- Holmgren, G., R. Bostrom, M.C. Kelley, P.M. Kintner, R. Lundin, U.V. Fahlson, E.A. Bering, and W.R. Sheldon, "Trigger and Active Release Experiment that Stimulated Auroral Particle Precipitation and Wave Emissions," *J. Geophys. Res.*, **85**: 5043, 1980.
- Hower, G.L. and A.B. Makhijani, "Further Comparison of Spread-F and Backscatter Sounder Measurements," *J. Geophys. Res.*, **74**: 3723-3725, 1969.
- Hower, G.L., D.M. Ranz, and C.L. Allison, "Comparison of HF Radar Echoes and High-Latitude Spread-F Measurements," *J. Geophys. Res.*, **71**: 3215-3221, 1966.
- Hufford, G.A., "An Integral Equation Approach to the Problem of Wave Propagation Over an Irregular Surface," *Quart. Appl. Math.*, **9**: 391-403, 1952.
- Hultqvist, B., "Polar Cap Absorption and Ground Level Effects," in *Solar Flare and Research*, edited by G. de Jager and Z. Svestka, p. 216, North Holland, Amsterdam, 1969.
- Hunsucker, R.D., "Morphology and Phenomenology of the High Latitude E and F Regions," *STPP*, **2**:543 (see R.F. Donnelly, ed.), 1979.
- Hunsucker, R.D. (Chairman), "High Latitude E- and F-Region Ionospheric Predictions," *STPP*, **2**: 513 (see R.F. Donnelly, ed.), 1979.
- Hunsucker, R.D. and R.F. Bates, "Survey of Polar and Auroral Region Effects on HF Propagation," *Radio Sci.*, **4**: 347-365, 1969.
- Ichinose, M., R. Maeda and S. Ito, "MUF Short-Term Prediction for HF Radio Propagation Circuits over Japan Area," *J. Rad. Res. Labs. (Japan)*, **27**: 179, 1980.
- Inoue, Y. and S. Horowitz, "Numerical Solution of Full-Wave Equation with Mode Coupling," *Radio Sci.*, **1**: 957, 1968.
- Jelly, D.H. and L.E. Petrie, "The High-Latitude Ionosphere," *Proc. IEEE*, **57**: 1005-1018, 1969.
- Johler, J.R., "Concerning Limitations and Further Corrections to Geometric Optic Theory for LF, VLF Propagation Between the Ionosphere and the Ground," *Radio Sci.*, **68D**: 67-78, 1964.
- Johler, J.R., "Zonal Harmonics in Low Frequency Terrestrial Radio Wave Propagation," NBS Tech. Note TN335, U.S. Government Printing Office, Washington, D.C., 1966.
- Jones, T.B. and K. Mowforth, "A Review of the Analytical Techniques for Determining the Phase and Amplitude of a VLF Radio Wave Propagating in the Earth-Ionosphere Waveguide," in *Medium, Long, and Very Long Wave Propagation, AGARD Conf. Proc.*, **305**: 16-1-16-16 ADA113969, 1982.
- Jones, W.B. and R.M. Gallet, "Ionospheric Mapping by Numerical Methods," *ITU Telecomm. J.*, **12**: 260, 1960.
- Jones, W.B., R.P. Graham, and M. Leftin, *Advances in Ionospheric Mapping by Numerical Methods*, NBS Tech. Note 337, U.S. Government Printing Office, Washington, D.C., 1966.
- Kelley, M.C., K.D. Baker, and J.C. Ulwick, "Late Time Barium Cloud Striations and Their Possible Relationship to Equatorial Spread F," *J. Geophys. Res.*, **84**: 1898, 1979.
- Kellog, W.W. "Pollution of the Upper Atmosphere by Rockets," *Space Sci. Rev.*, **3**: 275, 1964.
- Kelso, J.M., *Radio Propagation in the Ionosphere*, McGraw Hill, New York, 1964.
- Kersley, L., "An Empirical Model of Ionospheric Slab Thickness," AGARD-CPP-284, May 1980.
- King, R.J. and J.R. Wait, "Electromagnetic Groundwave Theory and Experiment," *Symposia Mathematica* (Istituto Nazionale di Alta Matematica, Bologna, Italy), **18**: 107-208, 1976.
- Klobuchar, J.A., "Numerical Models of Total Electron Content over Europe and the Mediterranean and Multi-Station Scintillation Comparisons," AGARDOGRAPH: AG-166A, Nov. 1973.
- Klobuchar, J.A., "A First-Order, Worldwide, Ionospheric Time Delay Algorithm," AFCRL-TR-75-0502, ADA018862, Sep 1975.
- Klobuchar, J.A. and R.S. Allen, "A First-Order Prediction Model of Total-Electron-Content Group Path Delay for a Midlatitude Ionosphere," AFCRL-70-0403, AD711365 1970.
- Klobuchar, J.A., M.J. Buonsanto, M.J. Mendillo, and J.M. Johanson, "The Contribution of the Plasmasphere to Total Time Delay" in *Effects of the Ionosphere on Space and Terrestrial Systems*, edited by J.M. Goodman, U.S. Government Printing Office stock no. 008-051-00069-1, 1978.
- Klobuchar, J.A. and J.M. Johanson, "Correlation Distance for Mean Daytime Electron Content," AFGL TR-77-0185, ADA048117, 22 Aug 1977.
- Klobuchar, J.A., K.N. Iyer, H.O. Vats, and R.G. Rastogi, "A Numerical Model of Equatorial and Low Latitude Total Electron Content for use by Satellite Tracking Systems for Ionospheric Corrections," *Indian J. Radio Space Phys.*, **6**, 1977.
- Knight, P., "MF Propagation: A Wave-Hop Method for Ionospheric Field-Strength Prediction," *BBC Engineering*, **100**: 22-34, 1975.
- Knight, P., "Medium Frequency Propagation: A Survey," in *Medium, Long, and Very Long Wave Propagation*,

## CHAPTER 10

- AGARD Conf. Proc., **305**: 28-1–28-17, ADA113969 1982.
- Kofsky, I., "Further Evaluations of Infrared Simulation Data," Tech. Rept. DNA Contract 001-81-C-003, Photo Metrics, Inc., Woburn, Mass., 1981.
- Kohnlein, W., "Electron Density Models of the Ionosphere," *Rev. Geophys. Space Phys.*, **16**: 341, 1978.
- Kossey, P.A. and E.A. Lewis, "Detection and Classification of Solar X-Ray Flares Using VLF Phase and Amplitude Information," AFCRL-TR-74-0468, ADA003383 1974.
- Kossey, P.A., E.A. Lewis, and E.C. Field, "Relative Characteristics of TE/TM Waves Excited by Airborne VLF/LF Transmitters," in *Medium, Long, and Very Long Wave Propagation*, AGARD Conf. Proc., **305**: 19-1–19-10 ADA113969 1982.
- Kossey, P.A., J.E. Rasmussen, and E.A. Lewis, "VLF Pulse Ionosounder Measurements of the Reflection Properties of the Lower Ionosphere," COSPAR, *Lower Ionosphere Structure*, 133–138, Akademie Verlag, Berlin, 1974.
- Kossey, P.A., J.P. Turtle, R.P. Pagliarulo, W.I. Klemetti, and J.E. Rasmussen, "VLF Reflection Properties of the Normal and Disturbed Polar Ionosphere in Northern Greenland," *Radio Sci.*, **18**: 907–916, 1983.
- Koster, J.R., "Some Measurements of the Irregularities Giving Rise to Radio-Star Scintillations at the Equator," *J. Geophys. Res.*, **68**: 2579–2590, 1963.
- Kouba, J. "A Review of Geodetic and Geodynamic Satellite Doppler Positioning," *Rev. Geophys. and Space Phys.* **21**: 27–40, 1983.
- Kouris, S.S. and L.M. Muggleton, "Diurnal Variation in the E Layer Ionization," *J. Atmos. Terr. Phys.*, **35**: 133–139, 1973a.
- Kouris, S.S. and L.M. Muggleton, "A Proposed Prediction Method for Monthly Median foE," CCIR Report 252-2, Contrib. No. 6/3/07 to Interim Working Party 6/3, 1973b.
- Krause, G.E., R.J. D'Accardi, and E.L. Roswell III, "Field Test of a Near-Real-Time Ionospheric Forecasting Scheme (60 km)," U.S. Army ECOM Rept. 3345, 1970.
- Krause, G.E., R.J. D'Accardi, and E.L. Roswell III, "Field Test of a Near-Real-Time Ionospheric Forecasting Scheme (200 km)," U.S. Army ECOM Rept. 4144, 1973a.
- Krause, G.E., R.J. D'Accardi, and E.L. Roswell III, "Field Test of a Near-Real-Time Ionospheric Forecasting Scheme (500 km)," U.S. Army ECOM Rept. 4145, 1973b.
- Lakshmi, D.R., S. Aggarwal, P.K. Pasricha, and B.M. Reddy, "HF Communication Problems at Low Latitudes due to Steep Spatial and Temporal Gradients," *STPP*, **4**: D2-58 (see R.F. Donnelly, ed.), 1980.
- Larson, A.C. and J.C. Hodges, "VHF/UHF Auroral Radar Measurements," Stanford Research Institute International, Calif., June 1967.
- Leadabrand, R.L., A.G. Larson, and J.C. Hodges, "Preliminary Results on the Wavelength Dependence and Aspect Sensitivity of Radar Auroral Echoes Between 50 and 3000 MHz," *J. Geophys. Res.*, **72**: 3877–3887, 1967.
- Leadabrand, R.L., J.C. Schlobohm, and M.J. Baron, "Simultaneous Very High Frequency and Ultra High Frequency Observations of the Aurora at Fraserburgh, Scotland," *J. Geophys. Res.*, **70**: 4235–4284, 1965.
- Lee, M.C., A. DasGupta, J.A. Klobuchar, S. Basu, and S. Basu, "Depolarization of VHF Geostationary Satellite Signals near the Equatorial Anomaly Crest," *Radio Sci.*, **17**: 399, 1982.
- Leftin, M., "Numerical Representation of Monthly Median Critical Frequencies of the Regular E Region (F<sub>o</sub>E)," OT Rept. 76-88k, U.S. Office of Telecommunications, Boulder, Colo., 1976.
- Leftin, M., S.M. Ostrow, and C. Preston, "Numerical Maps of foE<sub>s</sub> for Solar Cycle Minimum and Maximum," ESSA Tech Rept. ERL 73-ITS-63, Boulder, Colo., 1968.
- Leiphart, J.P., R.W. Zeek, L.S. Bearce, and E. Toth, "Penetration of the Ionosphere by Very-Low-Frequency Radio Signals-Interim Results of the LOFTI I Experiment," *Proc. IRE*, **50**: 6-17, 1962.
- Lewis, E.A. and P.A. Kossey, "POWERFLUX I: A Method of Estimating Wave Intensities at Large Distances from Ground-Based Low Frequency Transmitters," AFCRL-TR-75-0338, ADA014787, 1975.
- Lewis, E.A., J.E. Rasmussen, and P.A. Kossey, "Measurements of Ionospheric Reflectivity from 6 to 35 kHz," *J. Geophys. Res.*, **78**: 3903–3911, 1973.
- Lewis, R.L., "The Wave-Hop fields for an Inclined Dipole Over a Spherical Earth with an Anisotropic Ionosphere," Tech Rept. OT/ITS RR 5, Institute for Telecommunication Sciences, Boulder, Colo., 1970.
- Lied, F., (ed.), *H.F. Radio Communications*, Technivision, Maidenhead, UK, 1967.
- Lincoln, J.V. and R.O. Conkright (eds.), "International Reference Ionosphere-IRI 79," Report UAG-82, World Data Center A for Solar-Terrestrial Physics, Boulder, Colo., 1981.
- Llewellyn, S.K. and R.B. Bent, "Documentation and Description of the Bent Ionospheric Model," AFCRL-TR-73-0657, AD 772733, 1973.
- Lloyd, J.S., G.W. Haydon, D.L. Lucas, and L.R. Teters, *Estimating the Performance of Telecommunication Systems Using the Ionospheric Transmission Channel*, National Telecommunications and Information Administration, Boulder, Colo., 1978.
- Lyakhova, L.N., "Short-Range Forecasting of the State of the Ionosphere," *Trudy IZMIRAN*, **17**: 240, 1960.
- Lyakhova, L.N. and L.I. Kostina, "On Quantitative Ionospheric Forecasting," *Geomag. Aeron.*, **13**: 50, 1973.
- Maeda, K.I., "Study on Electron Density in the Lower Ionosphere," *J. Geomag. Geoelect.*, **23**: 133–159, 1971.
- Malik, C. and J. Aarons, "A Study of Auroral Echoes at 19.4 Megacycles per Second," *J. Geophys. Res.*, **69**: 2731–2736, 1964.
- Marmo, F.F., L.M. Ashcenbrand, and J. Pressman, "Artificial Electron Clouds—I, Planet," *Space Sci.*, **1**: 277, 1959.
- Martin, E. and J. Aarons, "F-Layer Scintillation and the Aurora," *J. Geophys. Res.*, **82**: 2717, 1977.
- McNamara, L.F., "Ionospheric Predictions on Transequatorial Circuits," *Proc. IREE (Aust.)*, **35**: 17, 1974a.
- McNamara, L.F., "Unusual Nighttime Propagation Modes

- on the Guam and Manila—N.W. Cape Circuits," Ionospheric Prediction Service Series R Reports, IPS-R27, Sydney, Australia, 1974b.
- McNamara, L.F., "Short-Term Forecasting of foF<sub>2</sub>," Ionospheric Prediction Service Series R Reports, IPS-R33, Sydney, Australia, 1976.
- McNamara, L.F., "The Use of Ionospheric Indices to Make Real and Near Real Time Predictions of foF<sub>2</sub> Around Australia," *STPP*, **1**: 249 (see R.F. Donnelly, ed.), 1979.
- Mendillo, M., "The Effect of Rocket Launches on the Ionosphere," *Adv. Space Res.*, **1**: 275, 1981.
- Mendillo, M. and J. Baumgardner, "Optical Signature of an Ionospheric Hole," *Geophys. Res. Lett.*, **9**: 215, 1982.
- Mendillo, M. and J.M. Forbes, "Artificially Created Holes in the Ionosphere," *J. Geophys. Res.*, **83**: 151, 1978.
- Mendillo, M. and J. Forbes, "Theory and Observation of a Dynamically Evolving Negative Ion Plasma," *J. Geophys. Res.*, **87**: 8273, 1982.
- Mendillo, M., G.S. Hawkins, and J.A. Klobuchar, "A Large-Scale Hole in the Ionosphere Caused by the Launch of Skylab," *Science*, **187**: 343, 1975a.
- Mendillo, M., G.S. Hawkins, and J.A. Klobuchar, "A Sudden Vanishing of the Ionospheric F-Region Due to the Launch of Skylab," *J. Geophys. Res.*, **80**: 2217, 1975b.
- Mendillo, M. D. Rote, and P. Bernhardt, "Preliminary Report on the HEAO-Hole in the Ionosphere," *Eos, Trans. AGU*, **61**: 529, 1980.
- Mikkelsen, I.S., J. Aarons, and E. Martin, "Geometrical Considerations of 136 MHz Amplitude Scintillation in the Auroral Oval," *J. Atmos. Terr. Phys.*, **40**: 479-483, 1978.
- Milliken, R.J. and C.J. Zaller, "Principle of Operation of NAVSTAR and System Characteristics," *Navigation: J. Institute of Navigation*, **25**(2): 95-106 Summer 1978.
- Millington, G., "Ground-Wave Propagation Over an Inhomogeneous Smooth Earth," *Proc. IEE*, **96**, Part III: 53-64, 1949.
- Millman, G.H. *Modern Radar*, ed. R.S. Berkowitz, Wiley, New York, 1965.
- Millman, G.H., "An Evaluation of HF Ionospheric Backscatter Echoes," G.E. Tech. Information Series Rept. No. R75EMH19, Nov 1975.
- Millman, G.H. and C.D. Bell, "Ionospheric Dispersion of an FM Electromagnetic Pulse," *IEEE Trans. Antennas Propag.*, **AP-19**(1), Jan 1971.
- Millman, G.H. and G.M. Reinsmith, "An Analysis of the Incoherent Scatter-Faraday Rotation Technique for Ionospheric Propagation Error Correction," Rept. No. R74EMH2, G.E., New York, Feb 1974.
- Minnis, C.M. and G.H. Bazzard, "A Monthly Ionospheric Index of Solar Activity Based on F<sub>2</sub>-Layer Ionization at Eleven Stations," *J. Atmos. Terr. Phys.*, **18**: 297, 1960.
- Mitra, A.P., *Ionospheric Effects of Solar Flares*, D. Reidel, Dordrecht, Holland, 1974.
- Morfitt, D.G., "Effective Electron Density Distributions Describing VLF/LF Propagation Data," Tech. Rept. 141, Naval Ocean Systems Center, San Diego, Calif., 1977.
- Morfitt, D.G., J.A. Ferguson, and F.P. Snyder, "Numerical Modeling of the Propagation Medium at ELF/VLF/LF," in *Medium, Long and Very Long Wave Propagation, AGARD Conf. Proc.*, **305**: ADA113969 32-1-32-14, 1982.
- Muggleton, L.M., "Solar Cycle Control of N<sub>m</sub>(E)," *J. Atmos. Terr. Phys.*, **33**: 1307, 1971.
- Mullen, J.P., "Sensitivity of Equatorial Scintillation to Magnetic Activity," *J. Atmos. Terr. Phys.*, **35**: 1187, 1973.
- Muldrew, D.B., "F-Layer Ionization Troughs Deduced from Alouette Data," *J. Geophys. Res.*, **70**(11): 2635-2650, 1965.
- Narcisi, R.S., "Overview of Project BIME (Brazil Ionospheric Modification Experiments)," in *Active Experiments in Space* edited by W. Burke, European Space Agency Report SP-195, p. 295, 1983.
- Newman, P. (ed.), "Spread F and its Effects upon Radiowave Propagation and Communication," Technivision, Maidenhead, UK, 1966. (Also AGARDOGRAPH 90).
- Nielsen, E. and J. Aarons, "Satellite Scintillation Observations over the Northern High Latitude Regions," *J. Atmos. Terr. Phys.*, **36**: 159-165, 1974.
- Nielson, D.L. and M. Crochet, "Ionospheric Propagation of HF and VHF Radio Waves Across the Geomagnetic Equator," *Rev. Geophys. Space Phys.*, **12**: 688, 1974.
- Nisbet, J.S., "On the Construction and use of a Simple Ionospheric Model," *Radio Sci.*, **6**: 437, 1971.
- Norton, K.A., "The Calculation of Ground-Wave Field Intensity Over a Finitely Conducting Spherical Earth," *Proc. IRE*, **29**: 623-639, 1941.
- Noxon, J.F. and A.F. Johanson, "Effects of Magnetically Conjugate Photoelectrons on OI (6300 Å)," *Planet. Space Sci.*, **18**: 1367, 1970.
- Oelbermann, E., "Solar Particle Effects on Polar Cap VLF Propagation," *J. Franklin Inst., Special Issue on the Polar Cap*, **290**: 281-296, 1970.
- Oksman, J., H.G. Moller, and R. Greenwald, "Comparisons between Strong HF Backscatter and VHF Radar Aurora," *Radio Sci.*, **14**: 1121-1133, 1979.
- Oran, E.S. and T.R. Young, "Numerical Modeling of Ionospheric Chemistry and Transport Processes," *J. Phys. Chem.*, **81**: 2463, 1977.
- Oran, E.S., T.R. Young, D.V. Anderson, T.P. Coffey, P.C. Kepple, A.W. Ali., and D.F. Strobel, *A Numerical Model of the Mid-Latitude Ionosphere*, Naval Research Laboratory Memorandum Rept. No. 2839, 1974.
- Orsak, L.E., L.H. Rorden, G.B. Carpenter, and B.P. Ficklin, "VLF Propagation and Noise in the Ionosphere Observed by Sounding Rockets," Final Report on Contract NASr-49(01), Stanford Research Institute, Menlo Park, Calif., 1965.
- Pappert, R.A., "A Numerical Study of VLF Mode Structure and Polarization Below an Anisotropic Ionosphere," *Radio Sci.*, **3**: 219-233, 1968.
- Pappert, R.A., "Effects of a Large Patch of Sporadic E on Nighttime Propagation at Lower ELF," *J. Atmos. Terr. Phys.*, **42**: 417-425, 1980.
- Pappert, R.A., "LF Daytime Earth Ionosphere Waveguide Calculations," Tech. Rept. 647, Naval Ocean Systems Center, San Diego, Calif., 1981.
- Pappert, R.A. and J.E. Bickel, "Vertical and Horizontal

## CHAPTER 10

- VLF Fields Excited by Dipoles of Arbitrary Orientation and Elevation," *Radio Sci.*, **35**: 1445–1452, 1970.
- Pappert, R.A. and W.F. Moler, "A Theoretical Study of ELF Normal Mode Reflection and Absorption Produced by Nighttime Ionospheres," *J. Atmos. Terr. Phys.*, **40**: 1031–1045, 1978.
- Patenaude, J., K. Bibl, and B.W. Reinisch, "Direct Digital Graphics," *American Lab.*, **9**:5–101, 1973.
- Paul, A.K., "Processing of Digital Ionograms," NOSC-TD-529, Naval Ocean Systems Center, San Diego, 1982.
- Penndorf, R., "Geographic Distribution of Spread-F in the Arctic," *J. Geophys. Res.*, **67**: 2274–2288, 1962.
- Perkins, F.W. and P.K. Kaw, "On the Role of Plasma Instabilities in Ionospheric Heating by Radio Waves," *J. Geophys. Res.*, **76**: 282, 1971.
- Perkins, F.W. and E.J. Valeo, "Thermal Self-Focusing of Electromagnetic Waves in Plasma," *Phys. Res. Lett.*, **32**: 1234, 1974.
- Perkins, F.W., C. Oberman, and E.J. Valeo, "Parametric Instabilities and Ionospheric Modification," *J. Geophys. Res.*, **79**: 1478, 1974.
- Peterson, A.M., O.G. Villard, R.L. Leadbrand, and P.B. Gallagher, "Regularly Observable Aspect-Sensitive Radio Reflections from Ionization Aligned with the Earth's Magnetic Field and Located within the Ionosphere Layer at Middle Latitudes," *J. Geophys. Res.*, **60**: 497–512, 1955.
- Petrie, L.E. and E.S. Warren, "The Propagation of High Frequency Waves on the Winnipeg-Resolute Bay Oblique Sounder Circuit," in *Ionospheric Radio Communications*, Plenum, New York, 1968.
- Picquenard, A., *Radio Wave Propagation*, MacMillan, 1974.
- Piggot, R.W. and K. Rawer, "URSI Handbook of Ionogram Interpretation and Reduction," Report UAG-23 and UAG-23A, World Data Center A for Solar-Terrestrial Physics, NOAA, Boulder, Colo., 1972.
- Pike, C.P., "An Analytical Model of the Main F-Layer Trough," AFGL-TR-76-0098, ADA026031, 1976.
- Pitteway, M.L.V., "The Numerical Calculation of Wave Fields, Reflection Coefficients and Polarizations for Long Radio Waves in the Lower Ionosphere, I," *Phil. Trans. Roy. Soc.*, **A275**: 219–241, 1965.
- Phelps, A.D.R. and Sagalyn R.C. "Plasma Density Irregularities in the High Latitude Topside Ionosphere," *J. Geophys. Res.*, **81**: 515 1976.
- Pongratz, M.B. and G.M. Smith, "The LAGOPEDO Experiments—An Overview," *Eos, Trans. AGU*, **59**: 334, 1978.
- Pope, J.H. and R.B. Fritz, "Observations of Artificially Produced Scintillation using Satellite Transmissions," *J. Geophys. Res.*, **79**: 1074, 1974.
- Potemra, T.A. and T.J. Rosenberg, "VLF Propagation Disturbances and Electron Precipitation at Mid-Latitudes," *J. Geophys. Res.*, **78**: 1572–1580, 1973.
- Proceedings IEEE*, **57**(6), 1969.
- Radinov, Ya. S., "Autocorrelative Characteristics of Critical Frequency and Ionization Density Fluctuations," *Geomag. Aeron.*, **3**: 985, 1963.
- Radio Science*, **2**(10), 1967.
- Radio Science*, **9**(11), 1974.
- Ramakrishnan, S., D. Bilitza, and H. Thiemann, *Limitations of the IRI-78 Model*, presented at COSPAR General Assembly, Bangalore, India, 1979.
- Rasmussen, J.E., P.A. Kossey, and E.A. Lewis, "Evidence of an Ionospheric Reflecting Layer Below the Classical D region," *J. Geophys. Res.*, **85**: 3037–3044, 1980.
- Rasmussen, J.E., P.A. Kossey, and J.P. Turtle, "VLF/LF Pulse Reflections from Layers Below the Ionospheric D-Region," *AGARD Conf. Proc.*, **305**: 5-1–5-10 ADA 113969, 1982.
- Rastogi, R.G., "Seasonal and Solar Cycle Variations of Equatorial Spread-F in the American Zone," *J. Atmos. Terr. Phys.*, **42**: 593–597, 1980.
- Ratcliffe, J.A., "The Magneto-Ionic Theory and its Application to the Ionosphere," Cambridge University Press, London, 1959.
- Ratcliffe, J.A., *Sun, Earth and Radio*, World University Library, London, 1970.
- Rawer, K., "Propagation of Decameter Waves (HF-Bands)" in *Dynamical and Chemical Coupling between the Neutral and Ionized Atmosphere*, edited by B. Grandal and J.A. Holtlet, Reidel, Dordrecht, Holland, 1963.
- Rawer, K., "The Historical Development of Forecasting Weather for Ionospheric Propagation of HF Waves," *Radio Sci.*, **10**(7): 669–679, 1975.
- Rawer, K., *International Reference Ionosphere—IRI-79*, edited by J.V. Lincoln and R.O. Conkright, World Data Center A, for Solar Terrestrial Physics (STP), NOAA, Boulder, Colo., 1981.
- Rawer, K. and K. Suchy, "Radio Observations of the Ionosphere," in *Encyclopedia of Physics*, edited by S. Flugge, Springer-Verlag, New York, 1967.
- Reddy, C.A. and M.M. Rao, "On the Physical Significance of the Es Parameters fbEs, fEs and foEs," *J. Geophys. Res.*, **73**: 215, 1968.
- Reder, F.H., "VLF Propagation Phenomena Observed During Low and High Solar Activity," XVI General Assembly of URSI, Ottawa, Canada, 1969.
- Reilly, M.H., L.O. Harnish, and J.M. Goodman, "Polarimetry Studies of Ionospheric Modifications by Rocket Boosters," NRL Mem. Rpt. No. 4517, Naval Research Laboratory, Washington, D.C., 1981.
- Reinisch, B.W. and H. Xuequin, "Automatic Calculations of Electron Density Profiles from Digital Ionograms. 1. Automatic O and X Trace Identification for Topside Ionograms," *Radio Sci.*, **17**: 421–434, 1982.
- Reinisch, B.W. and H. Xuequin, "Automatic Calculation of Electron Density Profiles from Digital Ionograms. 3. Processing of Bottomside Ionograms," *Radio Sci.*, **18**: 477–492, 1983.
- Reinisch, B.S., J.S. Tang, W.N. Hall, and J. Buchau, "Automatic Ionogram Processing Shows Seasonal Variations in the Auroral Ionosphere," AFGL-TR-82-0122, ADA 119911, 1982a.
- Reinisch, B.W., J.S. Tang, and R.R. Gamache, "Automatic Scaling of Digisonde Ionograms," Test and Evaluation Report, AFGL TR-82-0324, ADA121666, 1982b.
- Richmond, A.D. and S.V. Venkateswaran, "Geomagnetic Crochets and Associated Ionospheric Current Systems," *Radio Sci.*, **6**: 139, 1971.
- Rino, C.L. and S.J. Matthews, "On the Morphology of

## IONOSPHERIC RADIO WAVE PROPAGATION

- Auroral Zone Radio Wave Scintillation," *J. Geophys. Res.*, **85**: 4139, 1980.
- Rino, C.L. and J. Owen, "The Structure of Localized Night-time Auroral Zone Enhancements," *J. Geophys. Res.*, **85**: 2941-2948, 1980.
- Rino, C.L. and J. Owen, "On the Temporal Coherence Loss of Strongly Scintillating Signals," *Radio Sci.*, **16**: 31, 1981.
- Rino, C.L., R.C. Livingston, and S.J. Matthews, "Evidence for Sheet-Like Auroral Ionospheric Irregularities," *Geophys. Res. Lett.*, **5**: 1039, 1978.
- Rishbeth, H. and O.K. Garriott, *Introduction to Ionospheric Physics*, Academic Press, 1969.
- Rosenberg, N.W. (ed.) *PROJECT FIREFLY 1962-1963*, AFCRL-64-364, 1964.
- Rosich, R.K. and W.B. Jones, "The Numerical Representation of the Critical Frequency of the F<sub>1</sub> Region of the Ionosphere," OT Rept. 73-22, Boulder, Colo., 1973.
- Rote, D.M., "Proceedings of the Workshop on Ionospheric and Magnetospheric Effects of Satellite Power Systems (SPS)," Conf. Rept. No. 7807115, U.S. Department of Energy, December 1979.
- Rufenach, C.L., "Radio Scintillation of Stellar Signals during Artificial Ionospheric Modification," *J. Geophys. Res.*, **78**: 5611, 1973.
- Rush, C.M., "Improvements in Ionospheric Forecasting Capability," AFCRL-72-0138, AD742258 1972.
- Rush, C.M., "An Ionospheric Observation Network for use in Short-Term Propagation Predictions," *Telecomm. J.*, **43**: 544, 1976.
- Rush, C.M. and J. Gibbs, "Predicting the Day-to-Day Variability of the Mid-Latitude Ionosphere for Application to HF Propagation Predictions," AFCRL-TR-73-0335, AD764711 1973.
- Rush, C.M., M. Pokempner, D.N. Anderson, F.G. Steward, and J. Perry, "Improving Ionospheric Maps using Theoretically Derived Values of foF<sub>2</sub>," *Radio Sci.*, **18**: 95, 1983.
- Russell, C.T. and M.J. Rycroft (eds.), *Active Experiments in Space Plasmas*, Proc. Sym. 9, COSPAR XXIII, Budapest, 2-14 June 1980, Pergamon Press, 1980.
- Sagalyn, R.C., M. Smiddy, and J. Wisnia, "Measurements and Interpretation of Ion Density Distribution in the Daytime F-Region," *J. Geophys. Res.*, **68**: 199, 1963.
- Sagalyn, R.C., M. Smiddy, and M. Ahmed, "High Latitude Irregularities in the Topside ionosphere based on ISIS—Thermal Probe Data," *J. Geophys. Res.*, **79**: 4252, 1974.
- Saltpeper, E.E., "Electron Density Fluctuations in a Plasma," *Phys. Rev.*, **120**: 1528, 1960; also *J. Geophys. Res.*, **65**: 1851, 1960.
- Shea, M.A., S.A. Militello, and H.E. Coffey, "Directory of Solar-Terrestrial physics Monitoring Stations," MONSEE Special Publication No. 2, AFGL TR 84-0237, 1984.
- Shellman, C.H., "Electron Density Distributions in the Lower Ionosphere with Associated Error Limits Derived from VLF and LF Sounder Data," *Radio Sci.*, **5**: 1127-1135, 1970.
- Shimazaki, T., "World Wide Variations in the Height of the Maximum Electron Density of the Ionospheric F<sub>2</sub> Layer," *J. Radio Res. Labs. (Japan)*, **2**: 86, 1955.
- Shlyger, I.S., "Self-Modulation of a Powerful Electromagnetic Pulse Reflection from the Upper Layers of the Ionosphere," *JETP (Engl. Transl.)*, **19**: 162, 1974.
- Singh, M., E.P. Szuszczewicz, and J.C. Holmes, "The STP/S3-4 Satellite Experiment," Equatorial F-Region Irregularities," Proc—Ionospheric Effects Symposium 1981, Alexandria, Va. edited by J.M. Goodman, Naval Research Lab., Washington D.C., 1982.
- Singleton, D.G., "The Morphology of Spread F Occurrence over Half a Sunspot Cycle," *J. Geophys. Res.*, **73**: 295-308, 1968.
- Singleton, D.G., "Dependence of Satellite Scintillations on Zenith Angle and Azimuth," *J. Atmos. Terr. Phys.*, **32**: 789-803, 1970.
- Singleton, D.G., "Transionsospheric Propagation Prediction. An Improved Ionospheric Irregularity Model," *STPP*, **4**: D1-1 (see R.F. Donnelly, ed.), 1980.
- Sinno, K. and M. Kan, "Ionospheric Scintillation and Fluctuations of Faraday Rotation Caused by Spread-F and Sporadic-E over Kokobunji, Japan," *J. Radio Res. Lab.*, **27**: 53-77, 1980.
- Sommerfeld, A., "The Propagation of Waves in Wireless Telegraphy," *Ann. Physik*, **28**: 665, 1909.
- Sprenger, K. and K. Glöde, "Some Properties of Radio Aurorae in Medium Latitudes," *J. Atmos. Terr. Phys.*, **26**: 193-198, 1964.
- Storey, L.R.O., "An Investigation of Whistling Atmospherics," *Phil. Trans. Roy. Soc., London*, **A246**: 113-141, 1953.
- Stratton, J.A., *Electromagnetic Theory*, McGraw-Hill, New York, 1941.
- Strobel, D.F. and M.B. McElroy, "The F<sub>2</sub> Layer at Middle Latitudes," *Planet. Space Sci.*, **18**: 1181, 1970.
- Stubbe, P., "Simultaneous Solution of the Time Dependent Coupled Continuity Equations, and Equations of Motion for a System Consisting of a Neutral Gas, and Electron Gas, and a four Component Ion Gas," *J. Atmos. Terr. Phys.*, **32**: 865, 1970.
- Svennesson, J., "Effects on VLF Propagation During Ionospheric Substorms," *J. Atmos. Terr. Phys.*, **35**: 761-773, 1973.
- Swenson, E.M., "Aspect-Sensitive Reflections from Ionization Irregularities in the F-Region," *J. Atmos. Terr. Phys.*, **34**: 1469-1476, 1972.
- Tascione, T.F., T.W. Flattery, V.G. Patterson, J.A. Secan, and J.W. Taylor, Jr., "Ionospheric Modelling at Air Force Global Weather Central," *STPP*, **1**: 367 (see R.F. Donnelly, Ed.) 1979.
- Tellegen, B.D.H., "Interaction Between Radio Waves," *Nature*, **131**: 840, 1933.
- Thomas, J.O. and M.K. Andrews, "Transpolar Exospheric Plasma," *J. Geophys. Res.*, **73**: 7407-7417, 1968.
- Thomas, J.O. and M.H. Rycroft, "The Exospheric Plasma During the International Years of the Quiet Sun," *Planet. Space Sci.*, **18**: 41-63, 1970.
- Thome, G.D. and F.W. Perkins, "Production of Ionospheric Striations by Self-Focusing of Intense Radio Waves," *Phys. Rev. Lett.*, **32**: 1238, 1974.
- Thompson, R.L. and J.A. Secan, "Geophysical Forecasting

## CHAPTER 10

- at AFGWC," *STPP*, **1**: 355 (see R.F. Donnelly, ed.), 1979.
- Thomson, J.J., *Conduction of Electricity Through Gases*, p. 321, Cambridge University Press, London, 1906.
- Thrane, E.V. (Chairman), "D-Region Predictions," *STPP*, **2**: 573 (see R.F. Donnelly, ed.), 1979.
- Tinsley, B.A., A.B. Christensen, J.A. Bittencourt, P.D. Angreji, and H. Takahashi, "Excitation of Oxygen Permitted Emissions in the Tropical Nightglow," *J. Geophys. Res.*, **78**: 1174, 1973.
- Titheridge, J.E., "Periodic Disturbances in the Ionosphere," *J. Geophys. Res.*, **73**: 243–252, 1968.
- Trizna, D.B. and J.M. Headrick, "Ionospheric Effects on HF Over-the Horizon Radar," in *Effects of the Ionosphere on Radiowave Systems*, Proc. Ionospheric Effects Symposium 1981, Alexandria, Va. edited by J.M. Goodman, Naval Research Lab., Washington, D.C., 1982.
- Tsunoda, R.T., "On the Spatial Relationship of 1-m Equatorial Spread F Irregularities and Plasma Bubbles," *J. Geophys. Res.*, **85**: 185, 1980.
- Tsunoda, R.T., R.C. Livingston, J.P. McClure, and W.B. Hanson, "Equatorial Plasma Bubbles" Vertically Elongated Wedges from the Bottomside F-Layer," *J. Geophys. Res.*, **387**: 9171, 1982.
- Turner, J.F., "The Development of the Ionospheric Index T," Ionospheric Prediction Science Series R Reports, IPS-R12, Sydney, Australia, 1968.
- Turner, J.F. and P.J. Wilkinson, "A Weekly Ionospheric Index," *STPP*, **1**: 279 (edited by R.F. Donnelly), 1979.
- UAG Report 10, *Atlas of Ionograms*, (avail. World Data Center A, U.S. Dept. of Commerce, NOAA/EDIS, Boulder, Colo.), 1970.
- UAG Report 23, *URSI Handbook of Ionogram Interpretation and Reduction*, (avail. World Data Center A, U.S. Dept. of Commerce, NOAA/EDIS, Boulder, Colo.), 1972.
- UAG Report 23a, *URSI Handbook of Ionogram Interpretation and Reduction, Revision of Chapters 1–4*, (avail. World Data Center A, U.S. Dept. of Commerce, NOAA/EDIS, Boulder, Colo.), 1978.
- UAG Report 50, *High Latitude Supplement to the URSI Handbook of Ionogram Interpretation and Reduction*, (avail. World Data Center A, U.S. Dept. of Commerce, NOAA/EDIS, Boulder, Colo.), 1975.
- UAG-85 *Catalogue of Vertical Ionosphere Soundings Data*, (avail. World Data Center A, U.S. Dept. of Commerce, NOAA/EDIS, Boulder, Colo.), 1982.
- Uffelmann, D.R. and L.O. Harnish, "Initial Results from HF Propagation Studies During Solid Shield," Naval Research Lab. Memorandum Report 4849, 1982.
- Utlaut, W.F., "An Ionospheric Modification Experiment using Very High Power, High-Frequency Transmission," *J. Geophys. Res.*, **75**: 6402, 1970.
- Utlaut, W.F. and E.J. Violette, "Further Observations of Ionospheric Modification by a High-Powered HF Transmitter," *J. Geophys. Res.*, **77**: 6804, 1972.
- Utlaut, W.F., E.J. Violette, and A.K. Paul, "Some Ionospheric Observations of Ionospheric Modification by Very High Power High-Frequency Ground-Based Transmission," *J. Geophys. Res.*, **25**: 6429, 1970.
- Van der Pol, B. and H. Bremmer, "The Diffraction of Electromagnetic Waves from an Electrical Point Source Round a Finitely Conducting Sphere," *Phil. Mag. Series 7*, **24**: 141–176, 1937; **24**: 825–864, 1937; **25**: 817–834, 1938; and **26**: 262–275, 1938.
- Vickery, J.F., C.L. Rino, and T.A. Potemra, "Chatanika Triad Observations of Unstable Ionization Enhancements in the Auroral F-Region," *Geophys. Res. Lett.*, **7**: 789–792, 1980.
- Videberg, J.I. and G.S. Sales, "Long Range Survivable MF Radio Communication Study Using High Altitude Whispering Gallery Modes," AFCRL-TR-73-0552, AD774989, 1973.
- Villard, O.G. Jr., "The Ionospheric Sounder and Its Place in the History of Radio Science," *Radio Sci.*, **11**: 847–860, 1976.
- von Flotow, C.S., "Ionospheric Forecasting at Air Force Global Weather Central," in *Effects of the Ionosphere on Space and Terrestrial Systems*, edited by J.M. Goodman, U.S. Government Printing Office, Stock No. 008-051-00069-1, Jan 1978.
- Wait, J.R., "Radiation from a Ground Antenna," *Can. J. Tech.*, **32**: 1–9, 1954.
- Wait, J.R., "Mixed-Path Ground Wave Propagation, I. Short Distances," *J. Res. NBS*, **57**: 1–15, 1956.
- Wait, J.R., "Excitation of Surface Waves on Conducting, Stratified, Dielectric-Clad, and Corrugated Surfaces," *J. Res. NBS*, **59**: 365–377, 1957.
- Wait, J.R., "The Electromagnetic Fields of a Horizontal Dipole in the Presence of a Conducting Half-Space," *Can. J. Phys.*, **39**: 1017–1028, 1961.
- Wait, J.R., *Electromagnetic Waves in Stratified Media*, Pergamon Press, New York, 1970.
- Wait, J.R., (ed.), *Electromagnetic Probing in Geophysics*, The Golem Press, Boulder, Colo., 163–207, 1971.
- Wait, J.R., (ed.) "Special Issue on Extremely Low Frequency (ELF) Communications," *IEEE Trans. Commun.*, COM-22, 1974.
- Wait, J.R., "Propagation of ELF Electromagnetic Waves and Project Sanguine/Seafarer," *IEEE J. Ocean. Eng.*, **OE-2**: 161–172, 1977.
- Wait, J.R. and H.H. Howe, "Amplitude and Phase Curves for Ground Wave Propagation in the Band 200 Cycles per Second to 500 Kilocycles," NBS Circular 574, National Bureau of Standards, Washington, D.C., U.S. Government Printing Office, 1956.
- Wait, J.R. and A. Murphy, "Influence of a Ridge on the Low Frequency Ground Wave," *J. Res. NBS*, **58**: 1–5, 1957.
- Wait, J.R. and A. Murphy, "Further Studies of the Influence of a Ridge on the Low Frequency Ground Wave," *J. Res. NBS*, **61**: 57–60, 1958.
- Wait, J.R. and K.P. Spies, "Characteristics of the Earth-Ionosphere Waveguide for VLF Radio Waves," NBS Tech. Note 300, National Bureau of Standards, Washington, D.C., U.S. Government Printing Office, 1964.
- Wait, J.R. and L.C. Walters, "Curves for Ground Wave Propagation Over Mixed Land and Sea Paths," *IEEE Trans. Antennas Propag.*, **11**: 38–45, 1963.
- Wand, R.H. and J.V. Evans, "Morphology of Ionospheric Scintillation in the Auroral Zone," in *Effect of the Ionosphere on Space systems and Communications*, edited

## IONOSPHERIC RADIO WAVE PROPAGATION

- by J. Goodman, NTIS CSCL 04/1 N75-30714, Naval Research Laboratory, Washington, D.C., 1975.
- Wand, R.H. and M. Mendillo, "Incoherent Scatter Observations of an Artificially Modified Ionosphere," *J. Geophys. Res.*, **89**: 203, 1984.
- Watson, G.N., "The Transmission of Electric Waves Round the Earth," *Proc. Roy. Soc.*, **95**: 546–563, 1919.
- Watt, A.D., *VLF Radio Engineering*, Pergamon Press, New York, 1967.
- Weaver, P.F., "Backscatter Echoes from Field-Aligned Irregularities in the F-Region," *J. Geophys. Res.*, **70**: 5425–5432, 1965.
- Weber, E.J. and J. Buchau, "Polar Cap F-Layer Auroras," *Geophys. Res. Lett.* **8**:125, 1981.
- Weber, E.J., J. Buchau, R.H. Eather, and S.B. Mende, "North-South Aligned Equatorial Airglow Depletions," *J. Geophys. Res.*, **83**: 712, 1978.
- Weber, E.J., J. Buchau, and J.G. Moore, "Airborne Studies of Equatorial F-Layer Ionospheric Irregularities," *J. Geophys. Res.*, **85**: 4631–4641, 1980.
- Weber, E.J., H.C. Brinton, J. Buchau, and J.G. Moore, "Coordinated Airborne and Satellite Measurements of Equatorial Plasma Depletions," *J. Geophys. Res.*, **87**: 503–510, 513, 1982.
- Wernik, A.W., C.H. Liu, and K.C. Yeh, "Model Computations of Radio Wave Scintillation caused by Equatorial Ionospheric Bubbles," *Radio Sci.*, **15**: 559, 1980.
- Weyl, H., "Propagation of Electromagnetic Waves Above a Plane Conductor," *Ann. Physik*, **60**: 481–500, 1919.
- Whalen, B.A., et al., "Preliminary Results from Project Waterhole—An Auroral Modification Experiment," *Can. J. Phys.*, **59**: 1175, 1981.
- Whitney, H.E., C. Malik, and J. Aarons, "A Proposed Index for Measuring Ionospheric Scintillation," *Planet. Space Sci.*, **17**: 1069–1073, 1969.
- Whitney, H.E., J. Aarons, R.S. Allen, and D.R. Seemann, "Estimation of the Cumulative Amplitude Probability Distribution Function of Ionospheric Scintillations," *Radio Sci.*, **7**: 1095–1104, 1972.
- Wilkinson, P.J., "Prediction Limits for foF2," *STPP*, **1**: 259 (see R.F. Donnelly ed.), 1979.
- Wilkinson, P.J., "A Comparison of Monthly Indices of the Ionospheric F-Region," Ionospheric Prediction Service Series R Reports, IPS-R41, Sydney, Australia, 1982.
- Winkler, C., "Radio Wave Guidance at VHF Through Equatorial Plasma Bubbles," *J. Atmos. Terr. Phys.*, **43**: 307, 1981.
- Wright, J.W., "Kinesonde Observations of Ionosphere Modification by Intense Electromagnetic Fields from Platteville, Colorado," *J. Geophys. Res.*, **78**: 5622, 1973.
- Wright, J.W. and A.K. Paul, "Toward Global Monitoring of the Ionosphere in Real Time by a Modern Ionosonde Network: The Geophysical Requirements and Technological Opportunity," NOAA Special Report, Space Environment Lab., July 1981.
- Wright, J.W. and M.L.V. Pitteway, "Real-Time Data Acquisition and Interpretation Capabilities of the Dynasonde, 1. Data Acquisition and Real Time Display, 2. Determination of Magnetosonic Mode and Echolocation using a Small Spaced Receiving Array," *Radio Sci.*, **14**, 815–835, 1979.
- Wright, J.W. and M.L.V. Pitteway, "Data Processing for the Dynasonde: The Dopplionogram," *J. Geophys. Res.*, **87**: 1589, 1982.
- Yeh, K.C., "Travelling Ionospheric Disturbances as a Diagnostic Tool for Thermospheric Dynamics," *J. Geophys. Res.*, **77**: 709–719, 1972.
- Yeh, K.C. and C.H. Liu, "Ionospheric Effects on Radio Communication and Ranging Pulses," *IEEE Trans. Antennas Propag.*, **AP-27**(6), Nov 1979.
- Yeh, K.C. and C.H. Liu, "Radio Wave Scintillations in the Ionosphere," *Proc. IEEE*, **70**, 1982.
- Yeh, K.C., H. Soicher, and C.H. Liu, "Observations of Equatorial Ionospheric Bubbles by the Radio Propagation Method," *J. Geophys. Res.*, **84**: 6589, 1979.
- Zacharisen, D.M., "Space-Time Correlation Coefficients for use in Short-Term Ionospheric Predictions," NBS Report 8811, 1965.
- Zevakina, R.A. E.V., Lavrova, and L.N. Lyakhova, *Manual on Short-Term Predictions of Ionospheric Geomagnetic Storms and Radio-Propagation Forecasting*, (text in Russian) Nauka, Moscow, 1967.
- Zinn, J. and C.D. Sutherland, "Effects of Rocket Exhaust Products in the Thermosphere and Ionosphere," *Space Solar Power Rev.*, **1**: 109, 1980.
- Zinn, J., C.D. Sutherland, S. Stove, and L. Duncan, "Ionospheric Effect of Rocket Exhaust Products: HEAO-C and Skylab," *J. Atmos. Terr. Phys.*, **44**: 1143, 1982.